Institute for Circuit Theory and Signal Processing
Munich University of Technology

Filter Bank based Multicarrier Systems for Wireless Communications

Leonardo Gomes Baltar

Vollständiger Abdruck der von der Fakultät für Elektrotechnik und Informationstechnik der Technischen Universität München zur Erlangung des akademischen Grades eines

Doktor-Ingenieurs

genehmigten Dissertation.

Vorsitzender: Prof. Dr. sc. techn. Gerhard Kramer
Prüfer der Dissertation:

1. Prof. Dr. techn. Dr. h. c. Josef A. Nossek
2. Prof. Paulo S. Ramirez Diniz, Ph.D.

Die Dissertation wurde am 14.06.2017 bei der Technischen Universität München eingereicht und durch die Fakultät für Elektrotechnik und Informationstechnik am 21.11.2017 angenommen.

Acknowledgements

In the first place, I would like to say a big thank you to Prof. Josef A. Nossek for accepting me in his institute, his supervision, his guidance, the work and projects we did together, and his friendship. I also would like to thank Prof. Paulo S. R. Diniz—o mestre—for accepting to be my second examiner after already being my M.Sc. supervisor and examiner, for being a mentor and also a long-term friend. Those professors are role models for me in profession and in life! I also would like to thank Prof. Gerhard Kramer for accepting to coordinate my examination at the Department of Electrical and Computer Engineering of the Technische Universitaet Muenchen (TUM).

During the development of the research presented in this work and the time I spent at the Institute for Circuit Theory and Signal Processing (NWS) from the TUM, I had the opportunity to meet, exchange and work with different people with various backgrounds, coming from multiple cultures, each with her or his particular life story. I really learned a lot, not only from the technical expertise, but also about life, its good and not so good parts, about people and culture.

Special thanks go to Sergey Fedorov, Manuel Stein, Dirk Waldhauser for our friendship inside and outside of the institute, the many opportunities to spent our coffee and lunch time together discussing the big and small problems of mankind, and for the chance to work together. Further special thanks for Mario Castaneda—our latin american affinity does not need further explanations, grande amigo, Amine Mezghani—for the support on endless technical discussions that strongly influenced the direction of my research and for the friedship for life, Israa Slim—the countless discussions on filter bank shaped a great part of this work and our roots in Brazil connected us in a special way—and David Schmidt—the continuous friendship inside and outside the institute and for introducing me to the best of Munich (read Wiesn!). Thanks also for all my colleagues from the institute that in a way or another, directly or indirectly, helped me, provided me inspiration and support along the way, those are Kilian Roth, Felix Antreich, Hela Jedda, Jawad Munir, Hans Brunner, Qing Bai, Bernhard Lehmeyer, Peter Breun, Michael Joham, Michel Ivrlac and Prof. Wolfgang Utschick.

I have also counted with the creativity and endurance of a number of students—at that time—during my time at the institute. The supervision of those students not only improved the quality of my research, but provided decisive insights and different views to the problems. Many thanks specifically to Tobias Laas, Oliver De Candido, Michael Newinger, Johannes Herdegen, Stefan Dierks, Alexander Gullueglu, Christoph Schwarz, Niklas Winter, Lilia Smaoui, Mingqian Cui and Richard Ziehut.

Thanks for the administrative and technical support of Ali Yilmazcan—Guter Mann—, Ulrike Heer, Elizabeth Soeder, Hartmut Peters, Lidmila Barth and Dr. Rainer Pauli.

I would also like to acknowledge some fellows and research partners external to TUM, who also influenced this work, my research in general and I had the pleasure to collaborate for publications

and projects, those are Prof. Markku Renfors, Prof. Eleftherios Kofidis, Prof. Martin Haardt, Dr. Frank Scheich, Prof. Maurice Bellanger, Prof. Faouzi Bader, Dr. Xavier Mestre, Prof. Didier Le Ruyet, Prof. Lee Swindlehurst, Prof. Juan Cousseau, Prof. Fernando Gregorio and Prof. Tadeu Nagashima.

During the latest phases in the development of this work I counted with the strong support of Michael Faerber—thank you very much for that!

Last but not least, I would like to thank my wife Tatiana for her boundless and absolute support, her incredible patience and enormous love. Moreover, I would also thank my parents Jose—my first engineer friend—and Leda—super mom—for their unrestricted support and for educating me to make this world a better place to live, and my sister Ana Carolina, who was always there when I needed and who I admire as a person and professional.

This thesis is first dedicated to my wife Tatiana and my kids Karina and Nicolas. You are the best I have in life, I love you!

This thesis is also dedicated *in memoriam* to my uncle Jose Roberto, who was always an inspiration and a motivator for my career.

Contents

List of Figures

List of Tables

1. Introduction

In recent years multi-carrier systems have been at the forefront of broadband communication systems due to their attractive properties at high data rates. OFDM with a Cyclic Prefix (CP) is a widely implemented solution for multi-carrier systems already included in wireless communications standards such as Institute of Electrical and Electronics Engineers (IEEE) 802.11 and 3rd Generation Partnership Project (3GPP) Long-Term Evolution (LTE), but also for wired communications such as Asymmetric Digital Subscriber Line (ADSL) and Very-high-bit-rate digital subscriber line (VDSL). Its popularity is partly due to the simple equalization enabled by the CP, the efficient implementation using Fast Fourier Transform (FFT) and the flexibility on allocating the time and frequency resources between sources. However, some of those advantages come at the price of a loss in spectral efficiency due to the CP, which is extremely long in the presence of highly frequency selective channels. Moreover, CP-OFDM systems suffer from high out-of-band emissions, which also reduces the spectral efficiency and requires additional processing either in the digital or in the analog domain that increases design and implementation complexity. In addition to that, CP-OFDM systems have a high sensitivity to imperfect time and frequency synchronization.

In future wireless mobile communication systems [51] not only broadband transmissions are envisioned, but also narrowband machine type communications, for the so-called Internet of Things (IoT), and ultra reliable low latency, also known as mission critical communications. The range of device types considered for those systems is very wide and it covers from small form factor low power sensors to high end high data rate hungry handhelds and vehicles moving at high speed. Increased degrees of freedom are necessary to implement those systems, among others, flexible choice of the subcarrier spacing and bandwidth, i.e. broader subcarriers for lower latency and narrower subcarriers for very low rate sensor data, frequency and time multiplexing of sources with different subcarrier spacing, robustness to the deployment on a wide range of carrier frequencies, including those in the range of centimeter and millimeter wavelength. The disadvantages of CP-OFDM become more evident when those future systems are considered.

An alternative solution to CP-OFDM are FBMC/OQAM which are a strong contender for future mobile communication systems [12]. FBMC/OQAM systems have improved spectral efficiency because they do not employ a CP and due to the improved per-subcarrier filtering employed at the transmitter and receiver [68], which guarantees higher selectivity in the frequency domain and a much lower out-of-band radiation compared with CP-OFDM [9]. This form of pulse shaping limits the Inter-carrier Interference (ICI), while simultaneously attributing to more Inter-symbol Interference (ISI) within each individual sub-carrier. Furthermore, FBMC/OQAM systems are extremely efficient in the presence of highly frequency selective channels. These advantages over

CP-OFDM come at the cost of slightly higher computational complexity, however, this is not problematic [8].

1.1 Historical Review of Multicarrier Communications

The basic idea of multicarrier systems is to divide a wide-band frequency selective transmission channel into narrowband orthogonal subchannels[1] that, although overlapping in the frequency domain, are simpler to equalize. The orthogonal functions used to shape each subchannel will directly determine the flexibility of the system, its performance, the spectral occupation and the implementation complexity. Those functions will also determine the number of degrees of freedom for the system design. We can classify the multicarrier modulation schemes, based on the length of the shaping functions, into memoryless block transmission, when the functions have the duration of one symbol, or overlapped block transmission systems, when the functions are longer than the symbol period, what also means that the blocks overlap in time domain.

A basic requirement for each subchannel is that, at the receiver side, the symbols are free from ISI and ICI. The first descriptions of multicarrier systems in accordance with those requirements were presented in continuous time or, equivalently, with analog implementation [20, 21, 64] of the multicarrier modulation. The system in [64] differed from the others as it used a staggered or OQAM on each subcarrier. In those systems, the modulation functions were considered longer than the symbol period. An analog per sub-channel equalization strategy for those systems was later proposed in [33].

In [78] a digital efficient implementation of the orthogonal individual sub-carrier modulation, based on the Discrete Fourier Transform (DFT) is presented. But in this case the duration of the functions are equal to the symbol period and had a rectangular shape. This originated the system known today as OFDM. Afterwards, in [34] it was also shown an efficient implementation based on the DFT, but for shaping functions longer than the symbol period, what originated what we call FBMC/OQAM.

Based on the results from [34] some authors classify the systems based on overlapped (in time) functions as a special case of OFDM, what they call OFDM/OQAM, differing to the traditional memoryless system, which they call OFDM/Quadrature Amplitude Modulation (QAM) [48].

After the development of the theory of multirate systems and filter banks [28,71], some authors applied it to multicarrier systems [27]. Particularly, for the special case of modulated filter banks, where the sub-channels shaping functions are modulated versions of a prototype filter, powerful tools are provided to analyze and design multicarrier systems. The application of those tools consists basically on the use of efficient structures with the polyphase decompositions, design of the shaping function and evaluation (if existing) of distortions on each sub-channel. When the theory of filter banks is applied to multicarrier systems, the name TMUX is usually employed. The mathematical equivalence of OFDM/OQAM and TMUX systems based on modulated filter banks was presented on [68].

The concept of Perfect Reconstruction (PR) once introduced for filter bank systems is also successfully applied to TMUX systems. Perfect reconstruction means that the signal at the output of the filter bank, when compared to the signal at the input, has no amplitude distortion, no phase distortion and no aliasing, if no operation is performed between the analysis and the synthesis bank [28,71]. This also means that, if a prototype designed for a perfect reconstruction filter bank is

[1] In this work we will use the words subcarrier and subchannels interchangeably.

employed in a TMUX system with ideal transmission channel, the resulting orthogonal multicarrier system is ICI and ISI free [68].

One example of TMUX structure equivalent to the OFDM/OQAM is based on the filter bank called Modified Discrete Fourier Transform (MDFT) [28]. It consists of using a DFT filter bank together with an OQAM modulation on each sub-carrier. The MDFT TMUX can be realized efficiently depending on the length of the prototype filter [42].

The choice of the TMUX prototype filter offers many possibilities. Assuming an ideal transmission channel, ISI and ICI free transmissions are accomplished, if a RRC filter is used as prototype. But those filters have infinite impulse response and for practical implementations they have to be truncated or windowed, resulting in a TMUX free from ICI but not free from ISI. Assuming the non-existence of ideal transmission channel and considering small tolerable ISI and ICI, some authors rely on the use of Gaussian or extended Gaussian functions [41, 48]. There exists no closed formula leading to ICI or ISI free modulated TMUX or, equivalently, to PR modulated filter banks with more than 2 sub-channels. Neverthless, the PR condition can still be reached if nonlinear optimization routines are employed [29–31]. The only exception is for the case when the polyphase components have length 2, where the ELT can be applied and it has a closed-form [50].

Another approach for filter bank based multicarrier systems encountered in the current literature is based on the so called Exponentially Modulated Filter Banks (EMFB), which consists of one cosine and one sine modulated filter bank at the transmitter and, for proper equalization, two Cosine Modulated Filter Bank (CMFB) and two Sine Modulated Filter Bank (SMFB) at the receiver [38, 74]. It is worth mentioning that this approach is not based on the concept of OQAM but it has similar properties. In [73] it is claimed that the EMFB can be more efficiently realized than the MDFT filter bank.

Under the realistic assumption that the transmission channel is not ideal, that is ISI and ICI will occur anyway, one possibility is the design of optimal prototypes for near-perfect reconstruction filter banks [29–31]. In any case a equalizer has to be employed at each subcarrier due to frequency selectivity.

The TMUX equalization is still an open problem, although there are some works about this topic [38, 76, 79]. If the equalization is performed at a higher sampling rate as the symbol rate, for example, twice the symbol rate, it is highly dependent on the structure employed.

1.2 Overview and Contributions

FBMC systems provide on the other hand an effective alternative to CP-OFDM. FBMC systems based on OQAM, in particular, have properties which allows to fulfill a number of the requirements for advanced wireless communications. Due to the lack of CP and the orthogonal or near-orthogonal overlapping of the subcarriers, an improved spectral and energy efficiency is achieved. The use of a pulse shaping in each subcarrier tailored to fulfill stricter frequency and time domain requirements allows to improve the spectral containment and increase the robustness to synchronization errors. Furthermore, the pulse shaping can be flexibly chosen to convey the transmission of different categories of communications traffic.

This dissertation covers different aspects of FBMC systems based on OQAM with the objective to bring further maturity to the combination of classical digital signal processing building blocks and pave its way into wireless standards and future technology.

In the first part, in Chapter 2, the basic theory and fundamental operations of FBMC systems is presented. Different structures for the realization of the system are presented. They allow to ef-

ficiently perform the per-subcarrier filtering, modulation and combination of all subcarrier signals. The presentation of the structures is followed by a complexity analysis and comparison. Finally, some options for the choice of the filter employed in each subcarrier are presented.

It is important to consider in detail the complexity of the synthesis and analysis of the multi-carrier signals. In advanced cellular systems, like 3GPP standardized systems as LTE-Advanced and 5G, for example, the so-called carrier aggregation is utilized. Moreover, if multiple antennas are employed one SFB and one AFB is necessary for each antenna in typical applications. In both cases, multiple AFB and SFB need to be implemented in both mobile and base stations, scaling the complexity linearly with the number of carriers and with the number of antennas.

In the second part, in Chapter 3, different procedures are presented for the estimation of the propagation channel under which the system operates. In addition to the need of schemes that differ from the ones used in CP-OFDM, FBMC systems also require appropriate subcarrier signal models that are tailored to the channel estimation scheme chosen.

In the final part, in Chapter 4, methods to compensate and mitigate the effects of the propagation channel are presented. The channel equalization or precoding in FBMC systems also has to be adapted to the underlying signal model. An extension from systems which involve single antenna at the transmitter and single antenna at the receiver, to systems with multiple antennas in both sides is also discussed in this work.

1.3 Notation and Definitions

In this work vectors are represented as bold small letters and matrices as bold capital letters. Scalar can be either small or capital letters in roman. Where not otherwise stated, we assume in the course of this work that all signals are complex valued.

Given a discrete-time Finite Impulse Response (FIR) filter $g[k]$ operating in the sampling rate $1/T_\mathrm{s}$ and its impulse response of degree $(L_g - 1)$ and duration $(L_g - 1)T_\mathrm{s}$

$$g[k] = g_0\delta[k] + g_1\delta[k-1] + ... + g_{L_g-1}\delta[k - L_g + 1], \tag{1.1}$$

its corresponding $\mathcal{Z}$-domain polynomial description is $G(z) = g_0 + g_1 z^{-1} + ... + g_{L_g-1} z^{-L_g+1}$. The complex frequency variable z is related to the continuous-time frequency variable s by the relation $z = e^{sT_\mathrm{s}}$, where $s = \sigma + \mathrm{j}\omega$ and $\omega = 2\pi f$ is the angular frequency in rad/s and f the technical frequency in Hz. Given also an input sequence $x[k]$ and its $\mathcal{Z}$-transform $X(z)$, the output sequence $y[k]$, and its $\mathcal{Z}$-transform $Y(z)$, is calculated by the discrete-time convolution given by[2]

$$y[k] = (g * x)[k] = \sum_{\tau=0}^{L_g} g_\tau x[k-\tau]. \tag{1.2}$$

Equivalently, given the polynomials $G(z)$ and $X(z)$, the output polynomial $Y(z)$ is obtained by the product $Y(z) = G(z) \cdot X(z)$.

In the course of this work we will deal with signals and filters that are defined, described and processed in multiple sampling rates, the so-called multirate signal processing. If we now define a new input signal $x'[l]$, a filter $g'[l]$ and an output signal $y'[l]$ and describe them in a lower sampling rate $1/MT_\mathrm{s}$, we also need a new $z' = e^{sT_\mathrm{s}M} = z^M$. A more convenient choice is to call $z' = z^M = z_M$, where the subscript indicates that M delays of T_s seconds can be substituted by

[2] Mathematicians call the discrete convolution the Cauchy product of two sequences.

one delay of MT_s seconds. Then we could write $Y'(z') = G'(z') \cdot X'(z') = Y'(z^M) = G'(z^M) \cdot X'(z^M) = Y'(z_M) = G'(z_M) \cdot X'(z_M)$. For convenience, we define z for the highest sampling rate in our system description and for lower sampling rates we include the corresponding subscript or exponent.

If in (1.2) the input sequence $x[k]$ has finite duration with L_x samples, then the output sequence $y[k]$ will have $L_y = L_x + L_g - 1$ samples. We can now stack the filter coefficients, input and output sequences in the vectors

$$\mathbf{g} = \begin{bmatrix} g_1 & g_0 & \cdots & g_{L_g-1} \end{bmatrix}^\mathrm{T} \in \mathbb{C}^{L_g}, \tag{1.3}$$

$$\mathbf{x}[k] = \begin{bmatrix} x[k] & x[k-1] & \cdots & x[L_x-1] \end{bmatrix}^\mathrm{T} \in \mathbb{C}^{L_x} \text{ and} \tag{1.4}$$

$$\mathbf{y}[k] = \begin{bmatrix} y[k] & y[k-1] & \cdots & y[L_y-1] \end{bmatrix}^\mathrm{T} \in \mathbb{C}^{L_y}. \tag{1.5}$$

In the course of this work we will frequently drop the time index k to simplify the notation as in the definitions that follow.

We can now define the output vector by

$$\mathbf{y} = \begin{bmatrix} g_0 & 0 & \cdots & 0 \\ g_1 & g_0 & \cdots & \vdots \\ \vdots & \vdots & \ddots & \vdots \\ g_{L_g-1} & g_{L_g-2} & \cdots & 0 \\ 0 & g_{L_g-1} & \cdots & g_0 \\ \vdots & \vdots & \ddots & \vdots \\ 0 & 0 & \cdots & g_{L_g-1} \end{bmatrix} \mathbf{x} = \mathbf{G}\mathbf{x}, \tag{1.6}$$

where the Toeplitz matrix $\mathbf{G} \in \mathbb{C}^{L_y \times L_x}$ is the usually so-called *convolution matrix* and given the vector $\mathbf{g}$, it can be generated by

$$\mathbf{G} = \sum_{i=1}^{L_x} \mathbf{D}_i \mathbf{g} \mathbf{e}_i^\mathrm{T}, \tag{1.7}$$

where $\mathbf{e}_i \in \{0,1\}^{L_x}$ has the i-th element equal to one and the other elements equal to zero, and $\mathbf{D}_i \in \{0,1\}^{L_y \times L_g}$ is defined as

$$\mathbf{D}_i = \begin{bmatrix} \mathbf{0}_{(i-1)\times L_g} \\ \mathbf{I}_{L_g} \\ \mathbf{0}_{(L_x-i)\times L_g} \end{bmatrix}, \tag{1.8}$$

where $\mathbf{0}_{(i-1)\times L_g} \in \{0\}^{(i-1)\times L_g}$ is the all zero matrix and $\mathbf{I}_{L_g} \in \{0,1\}^{L_g \times L_g}$ is the identity matrix. We can note that the dimensions L_x and L_g have independent magnitudes.

In (1.6), we have assumed that the memory of the FIR filter is empty at the beginning and at the end of the convolution operation, i.e. it includes the precursors and postcursors (transients) in addition to the steady-state. This is equivalent to assume that the input $x[k]$ has a relatively short duration and we are interested on observing the influence of the whole input sequence into the output sequences.

For the design of some system blocks such as channel equalizers and precoders, as we will show in Chapter 4, we are mostly interested on considering the outputs after the steady-state has been

reached. This is particularly useful when the input sequence $x[k]$ has a much longer duration than the impulse response of the filter $G(z)$. In this case, we define an observations vector $\mathbf{y}_\mathrm{o} \in \mathbb{C}^{L_\mathrm{o}}$, which is given by

$$\mathbf{y}_\mathrm{o} = \begin{bmatrix} g_0 & g_1 & \cdots & g_{L_g-1} & 0 & \cdots & 0 \\ 0 & g_0 & \cdots & g_{L_g-2} & g_{L_g-1} & \cdots & 0 \\ \vdots & \vdots & \ddots & \vdots & \vdots & \ddots & \vdots \\ 0 & \cdots & \cdots & 0 & g_0 & \cdots & g_{L_g-1} \end{bmatrix} \mathbf{x}' = \mathbf{G}'\mathbf{x}', \tag{1.9}$$

where now the dimension of $\mathbf{x}' \in \mathbb{C}^{L'_x}$ depends on the number of observations L_o, which is the dimension of $\mathbf{y}_\mathrm{o}$, and on the impulse response length L_g, i.e. $L'_x = L_\mathrm{o} + L_g - 1$. Moreover, we can also express the Toeplitz matrix $\mathbf{G}' \in \mathbb{C}^{L_\mathrm{o} \times L'_x}$ as a function of $\mathbf{g}$ as

$$\mathbf{G}' = \sum_{i=1}^{L'_x} \mathbf{e}'_i \mathbf{g}^\mathrm{T} \mathbf{D}'_i, \tag{1.10}$$

where now $\mathbf{e}'_i \in \{0,1\}^{L'_x}$ and $\mathbf{D}'_i \in \{0,1\}^{L_g \times L'_x}$ is defined as

$$\mathbf{D}'_i = \begin{bmatrix} \mathbf{0}_{L_g \times (i-1)} & \mathbf{I}_{L_g} & \mathbf{0}_{L_g \times (L'_x - i)} \end{bmatrix}. \tag{1.11}$$

We can see that matrix $\mathbf{G}'$ is a *transposed convolution matrix* and, if and only if $L_\mathrm{o} = L_x$ then $\mathbf{G}' = \mathbf{G}^\mathrm{T}$, because $L'_x = L_y$.

For other processing blocks such as channel estimation, as we will show in Chapter 3, we need to rewrite (1.9) by exchanging the roles of $\mathbf{G}'$ and $\mathbf{x}'$. An alternative expression for the filter output is then

$$\mathbf{y}_\mathrm{o} = \begin{bmatrix} x[k] & x[k-1] & \cdots & x[k-L_g+1] \\ x[k-1] & x[k-2] & \cdots & x[k-L_g] \\ \vdots & \vdots & \ddots & \vdots \\ x[k-L_\mathrm{o}+1] & x[k-L_\mathrm{o}] & \cdots & x[k-L_\mathrm{o}-L_g+1] \end{bmatrix} \mathbf{g} = \mathbf{X}\mathbf{g}, \tag{1.12}$$

where $\mathbf{X} \in \mathbb{C}^{L_\mathrm{o} \times L_g}$ is a Hankel matrix given by

$$\mathbf{X} = \sum_{i=1}^{L_g} \mathbf{D}''_i \mathbf{x}' \mathbf{e}''^\mathrm{T}_i, \tag{1.13}$$

where now $\mathbf{e}''_i \in \{0,1\}^{L_g}$ and $\mathbf{D}''_i \in \{0,1\}^{L_o \times L'_x}$ is defined as

$$\mathbf{D}''_i = \begin{bmatrix} \mathbf{0}_{L_\mathrm{o} \times (i-1)} & \mathbf{I}_{L_\mathrm{o}} & \mathbf{0}_{L_\mathrm{o} \times (L'_x - i)} \end{bmatrix}. \tag{1.14}$$

It is worth noting that also in both (1.9) and (1.12), we can choose the dimension L_o independent of L_g.

2. Exponentially Modulated Filter Banks

2.1 Introduction

We begin this chapter with the introduction of the basic multirate signal processing concepts of interpolation and decimation, including the sub-blocks of upsampling and downsampling. Moreover, we show how discrete-time modulation can be incorporated to the interpolation and decimation process by a frequency shift of the corresponding filter. After that we will show how interpolation and decimation can be efficiently implemented using two different approaches: the first one based on the polyphase decomposition of the interpolation filter and the second one based on the frequency domain implementation of the linear convolution, where a basic building block is the FFT. We will then compare the computational complexity of the different structures and finally present some prototype filter designs.

2.2 Basic Multirate Operations and Structures

In this section we introduce the basic processing and the building blocks of multicarrier modulation based on filter banks. The generation of the multicarrier signal at the transmitter side is performed by discrete-time modulation (a.k.a. mixing) obtained as a combination of sampling rate increase,i.e. upsampling and filtering. The recovery of the multicarrier signals is performed by discrete-time demodulation (a.k.a. de-mixing), filtering and sampling rate decrease, i.e. downsampling.

2.2.1 Upsampling, Interpolation and Discrete-time Modulation

We call interpolation the process of converting a signal from a sampling rate into a higher one. The process of interpolation is divided into two steps: upsampling and filtering as depicted in Fig. 2.1. First, given an input signal $x[k]$ with sampling period T and an upsampling factor M, we define the upsampled signal $x_{\text{us}}[l]$ with a shorter sampling period $T_{\text{s}} = T/M$ by inserting $(M-1)$ zero-valued samples between each of the original samples of $x[k]$. In time domain, the upsampling is

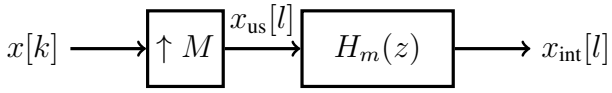

Fig. 2.1. Interpolation: Upsampling and Filtering

given by

$$x_{\text{us}}[l] = \begin{cases} x[k], & l = kM \\ 0, & \text{otherwise.} \end{cases} \tag{2.1}$$

Given the $\mathcal{Z}$-transform of the input $X(z_M) = \sum_{k=-\infty}^{+\infty} x[k] z_M^{-k}$ and (2.1), the output of the upsampler (or expander) is given by

$$X_{\text{us}}(z) = \sum_{l=-\infty}^{+\infty} x_{\text{us}}[l] z^{-l} = \sum_{k=-\infty}^{+\infty} x[k] z^{-kM} = X(z^M). \tag{2.2}$$

We can see that the $\mathcal{Z}$-transform of the output is nearly the same function of z as the $\mathcal{Z}$-transform of the input signal with only a substitution of the variable z by z^M, i.e. no distortion or fundamental change in the shape of the function occurs in the process of upsampling. By evaluating $X(z_M)$ along the unit circle, i.e. $z_M = e^{\text{j}\omega T}$, to obtain the frequency or Fourier domain representation, we can see that, after the upsampling, the uniqueness domain[1] of the frequency variable is extended from $\omega \in [-\pi/T, \pi/T]$ to $\omega \in [-\pi M/T, \pi M/T]$. We have now a discrete-time signal that has multiple equally shaped spectral components, also called spectrum images [26, 71].

To illustrate the process described above, in the upper diagram of Fig. 2.2 we first depict the magnitude of the frequency domain representation $X(e^{\text{j}\omega T})$ of a band limited complex signal $x[k]$. The spectra represented with dashed lines are outside the uniqueness domain given by the sampling rate $1/T$ and are just periodical repetitions of the spectrum contained in the interval $[-\pi/T, \pi/T]$. After upsampling, in the second graphic from the top in Fig. 2.2, we illustrate the same spectra but for the new uniqueness domain with sampling rate $1/T_{\text{s}} = 4/T$, i.e. an upsamplig factor of $M = 4$.

Now, the frequency domain representation contain redundancies (images) inside the uniqueness domain that are generated by the insertion of the zero-valued samples in the time domain. The images can now be filtered out, what results in a smoother time domain signal course, i.e. the zero-valued samples will acquire non-zero values. If the input signal posses mainly lower frequency components, a low-pass filter can be applied to remove the spectral repetitions and keep the original signal properties in the high rate output signal. In the third graphic of Fig. 2.2 we depict the magnitudes of the frequency domain representation of two filters: $H_0(z)$ in solid lines is a low-pass and $H_1(z)$ in dashed lines is a band-pass filter. The latter is obtained by exponentially modulating the former, i.e. $H_1(z) = H_0(ze^{-\text{j}\frac{2\pi}{M}}) = H_0(ze^{-\text{j}\frac{\pi}{2}})$. The second spectrum from the bottom shows the output of the interpolation when $x_{\text{us}}[l]$ is filtered by $H_0(z)$.

As will be shown later in this work, for frequency division multiplexing it is necessary to generate a frequency shifted version of the input signal $x[k]$. We can then take advantage of the fact that, after the upsampling operation, frequency shifted spectral repetitions of the input signal are available. We just need to substitute the low-pass interpolation filter $H_0(e^{\text{j}\omega T})$ by a band-pass filter, for example $H_1(e^{\text{j}\omega T})$. In the last graphic of Fig. 2.2 we can see the result of filtering $x_{\text{us}}[l]$ by $H_1(z)$.

In the current literature of multirate signal processing, filter banks and multicarrier modulation, an alternative for the approach previously described is the frequency shift (exponential modulation) of the signal after low-pass filtering. In order to derive efficient implementations of the interpolation operation, as will be shown later, it appears to be more convenient to utilize the approach presented in this section.

[1] We define uniqueness domain as the frequency range in which the discrete-time signal can be fully described and manipulated by a subsequent filter.

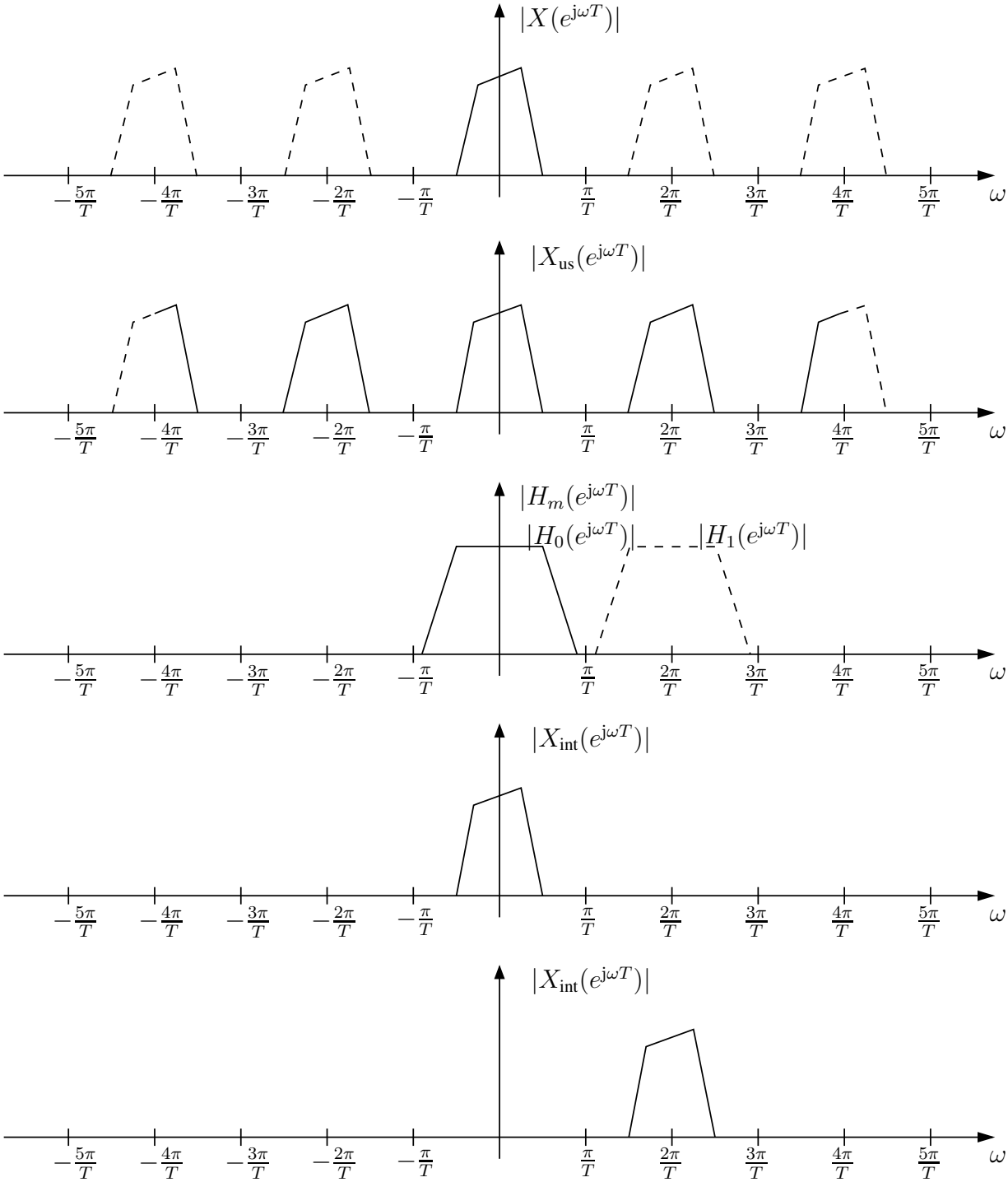

Fig. 2.2. Illustration of interpolation with upsampling followed by low-pass and band-pass filtering

2.2.2 Downsampling, Decimation and Discrete-time Demodulation

We call decimation the process of converting a signal from a higher sampling rate into a lower one. As in the interpolation, it is also divided into two basic steps, but this time, first a filtering and second a downsampling, as depicted in Fig. 2.3. Given a signal $x[l]$ in a short sampling period $T_s = T/M$, a filter $F_m(z)$ will limit its spectrum to avoid the so-called alias effect. To better

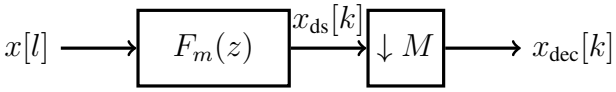

Fig. 2.3. Decimation: Filtering and down-sampling

understand the necessity of first filtering the signal, we need first to look at the downsampling operation in more detail.

In the downsampling by M every M-th sample of the input $x[l]$ is retained and the $M-1$ samples in between are not further processed, i. e. they are scrapped. In time domain the output of the downsampling by M is given by

$$x_{\text{ds}}[k] = x[lM]. \tag{2.3}$$

It is then clear that information may be lost during the downsampling operation, in other words downsampling may generate signal distortions, unlike to the upsampling, where no information loss or distortions to the signal occurs. For every M samples of $x[l]$, there are M possibilities which sample to keep. As a consequence a time offset μ for the downsampling operation should be defined. The resulting signal $x_{\text{ds}}[k] = x[lM+\mu]$ will be slightly different according to the offset choice. As a consequence we can conclude that the downsampling operation is periodically time variant. Without loss of generality, we make the usual assumption that the time offset is $\mu = 0$. In this case, the $\mathcal{Z}$-transform of the resulting signal after downsampling is given by

$$X_{\text{ds}}(z_M) = \frac{1}{M}\sum_{l=0}^{M-1} X(ze^{-\mathrm{j}\frac{2\pi l}{M}}). \tag{2.4}$$

We can see from (2.4) that the output of the downsampling operation is the sum of frequency shifted versions of the input signal. If the frequency response of $X(z)$ has a broad magnitude or it has many strong frequency components spread over the whole uniqueness domain, then, during the downsamplig operation, parts of the spectrum will overlap and the resulting signal will have a new frequency response. It may not be possible to recover the original signal from this new one. The distortion caused by the addition of overlapping frequency components is called aliasing effect [26, 71].

To avoid aliasing, it is necessary to apply a filter to limit the band of the input signal before the downsampling operation. To illustrate the whole decimation operation and also the joint decimation and demodulation (de-mixing), we depict an example in Fig. 2.4 for $M = 4$. In the first plot, the input signal $X(z)$ sampled in a high rate $4/T$ Hz has multiple frequency components and can be interpreted as a frequency multiplexing of multiple signals. In this example we have four signals centralized around the frequencies 0, $2\pi/T$, $-2\pi/T$ and $4\pi/T$ rad/s, or equivalently $-4\pi/T$ rad/s. In the second plot, the frequency responses of a low-pass filter $F_0(z)$ and a band-pass filter $F_1(z) = F_0(ze^{-\mathrm{j}\frac{2\pi}{M}}) = F_0(ze^{-\mathrm{j}\frac{\pi}{2}})$ are represented. The output of $F_0(z)$ is shown in the third plot, while the output of the whole decimation process, i.e. after filtering by $F_0(z)$ and downsampling, is represented in the fourth plot. We can see that now the uniqueness domain is reduced to the range $[-\pi/T, \pi/T]$ and the periodical spectral repetitions outside of this range correspond to the spectral component originally localized around the frequency 0. In the fifth plot we depict the resulting signal when the filter $F_1(z)$ is employed before the downsampling. The same signal after the downsampling is depicted in the sixth and last plot. One can see now that the resulting spectrum only contains the signal that was originally centralized around $2\pi/T$ rad/s in the first plot.

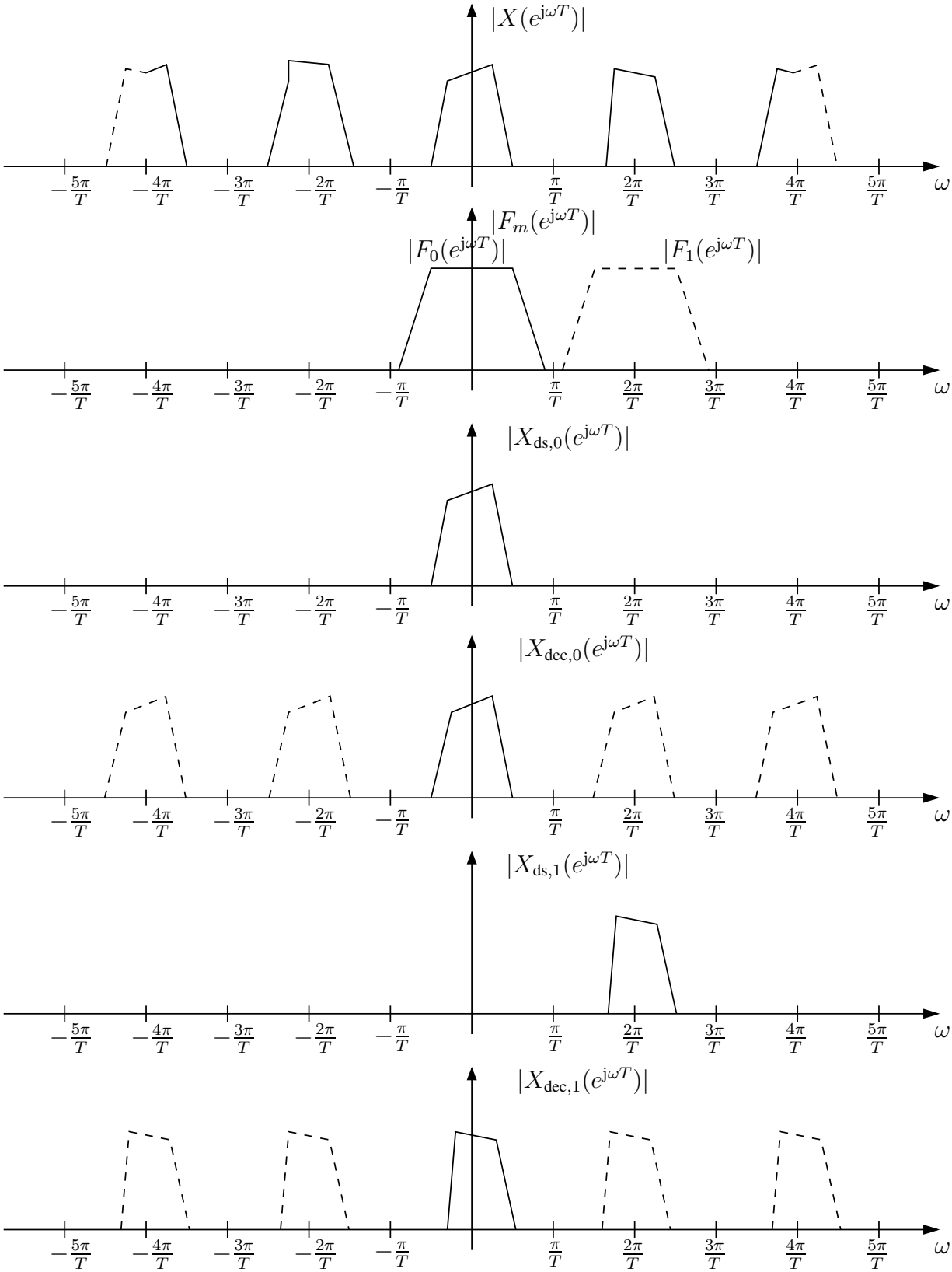

Fig. 2.4. Illustration of decimation with low-pass and band-pass filtering followed by downsampling

The decimation process depicted in Fig. 2.4 can be interpreted as a representation of a frequency demultiplexing, as will be explained later.

2.2.3 Efficient Realizations

The realization of the interpolation and decimation processes based on the block diagrams from Figs. 2.2 and 2.4 is not efficient. In the case of the interpolation, one can see that the input of the filter contains many zero-valued samples in a high sampling rate. The filter has to generate output samples in the same high sampling rate, although only a fraction of the coefficients (every M-th) are effectively being multiplied by non-zero input samples. In the case of decimation, the filter is also operating in the higher sampling rate, although this time not necessarily with zero valued input samples, but many of its output samples are not retained by the downsampling operation.

In the section that follows, we will present two possible implementations for both interpolation and decimation. The first one is based on the polyphase decomposition of the filter and the second on a frequency domain based filtering, i.e. FFT based fast convolution, and sampling rate conversion.

2.2.3.1 Polyphase Structures

Let us assume that the FIR interpolation filter $H_0(z)$ has $L_\mathrm{P} = KM$ coefficients[2] and its transfer function is given by

$$H_0(z) = \sum_{p=0}^{L_\mathrm{P}-1} h_p z^{-p}. \tag{2.5}$$

By defininining $p = \mu + \kappa M$, the type-1 polyphase decomposition of this filter is given by

$$H_0(z) = \sum_{\mu=0}^{M-1}\sum_{\kappa=0}^{K-1} h_{\mu+\kappa M} z^{-(\mu+\kappa M)} = \sum_{\mu=0}^{M-1} z^{-\mu}\left(\sum_{\kappa=0}^{K-1} h_{\mu+\kappa M} z^{-\kappa M}\right) = \sum_{\mu=0}^{M-1} z^{-\mu} G_\mu(z^M), \tag{2.6}$$

where the transfer functions $G_\mu(z^M) = \sum_{\kappa=0}^{K-1} h_{\mu+\kappa M} z^{-\kappa M}$ are the so-called polyphase components each with K non-zero-valued coefficients. We can see that each of the M polyphase components is constructed by taking every M-th sample of the filter in a similar fashion to what we did in the downsampling operation with signals. The difference between the polyphase components is then the time offset μ in which we start the downsampling of the filter. Moreover, the definition in (2.6) suggests to arrange the polyphase components in a parallel structure, i.e. the same input signal is filtered each polyphase component, and their outputs are added together before the upsampling and after a delay dependent on the branch index.

In the case of modulated filters, we can incorporate the frequency shift as

$$H_m(z) = H_0(ze^{-\mathrm{j}\frac{2\pi}{M}m}) = \sum_{p=0}^{L_\mathrm{P}-1} h_p z^{-p} e^{\mathrm{j}\frac{2\pi}{M}mp} \tag{2.7}$$

[2]This is a special case of the more general filter length $P = KM + s$, with $0 < s < M$, which implies the polyphase components have different lengths.

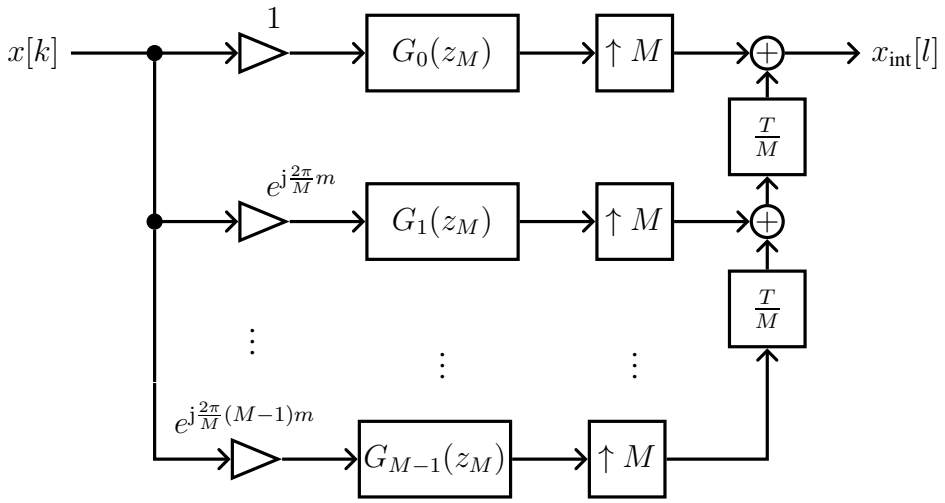

Fig. 2.5. Efficient realization of interpolation with modulation based on polyphase decompositions

and the polyphase decomposition can now be defined as

$$H_m(z) = \sum_{\mu=0}^{M-1}\sum_{\kappa=0}^{K-1} h_{\mu+\kappa M} z^{-(\mu+\kappa M)} e^{\mathrm{j}\frac{2\pi}{M}m(\mu+\kappa M)} = \sum_{\mu=0}^{M-1} z^{-\mu}\left(\sum_{\kappa=0}^{K-1} h_{\mu+\kappa M} z^{-\kappa M}\right) e^{\mathrm{j}\frac{2\pi}{M}m\mu}$$
$$= \sum_{\mu=0}^{M-1} z^{-\mu} G_\mu(z^M) e^{\mathrm{j}\frac{2\pi}{M}m\mu}, \tag{2.8}$$

where we should highlight that the same polyphase components from the non-shifted filter is employed here, in addition to the exponential modulation. Also here, a parallel structure appears to be straightforward from (2.8), with the difference that a multiplication by an exponential is applied before each polyphase component.

Up to now, we have just substituted the linear convolution with a single filter with KM coefficients by a parallel structure with M filters each with K coefficients. A final step is still missing to improve the efficiency of the whole interpolation operation. We need to move the upsampling operation after each of the polyphase components. Furthermore, we observe that the Noble Identity [26, 71] for interpolation can be applied due to the definition of the polyphase components. Then, we can rewrite (2.8) as

$$H_m(z) = \sum_{\mu=0}^{M-1} z^{-\mu} G_\mu(z_M) e^{\mathrm{j}\frac{2\pi}{M}m\mu}, \tag{2.9}$$

which is then translated to the block diagram shown in Fig. 2.5. We can observe that both frequency translation and filtering by the polyphase components are executed in the lower sampling rate. As a consequence, although the total number of multiplications has not effectively changed, in the polyphase structure the multiplications are paralleled and executed in a lower sampling rate, compared to the original interpolation procedure.

In the case of the decimation, similar steps can be performed. By first defining the decimation filter as

$$F_0(z) = \sum_{p=0}^{L_{\text{P}}-1} f_p z^{-p}, \tag{2.10}$$

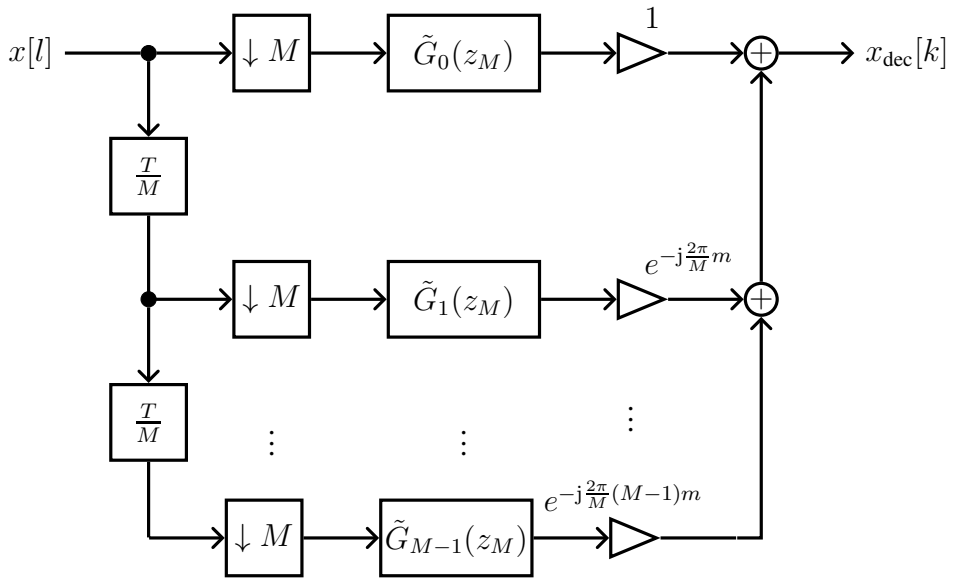

Fig. 2.6. Efficient realization of demodulation and decimation based on polyphase decompositions

we can analogously define the polyphase components as $\tilde{G}_\mu(z^M) = \sum_{\kappa=0}^{K-1} f_{\mu+\kappa M} z^{-\kappa M}$. Similar to what we did with the interpolation filter, we can incorporate the frequency shift to the definition of the filters

$$F_m(z) = F_0(ze^{\mathrm{j}\frac{2\pi}{M}m}) = \sum_{p=0}^{L_\mathrm{P}-1} f_p z^{-p} e^{-\mathrm{j}\frac{2\pi}{M}mp} \tag{2.11}$$

and to the polyphase decomposition. The main difference comes from the fact that the downsampling has to be moved from the right to the left. After using the Noble Identity [26, 71] for decimation the following definition holds

$$F_m(z) = \sum_{\mu=0}^{M-1} e^{-\mathrm{j}\frac{2\pi}{M}m\mu} \tilde{G}_\mu(z_M) z^{-\mu}, \tag{2.12}$$

which is actually very similar to (2.9), but just written in a different way to represent the corresponding final frequency shifted polyphase structure shown in Fig. 2.6. We can also see here that the filters operate now in a parallel structure in the lower sampling rate as well as the multiplications by exponentials.

2.2.3.2 Frequency Domain Fast Convolution

The two steps to perform an interpolation represented by the operations in Fig. 2.1 and illustrated in Fig. 2.2 can also be realized in the frequency domain with the help of the so-called fast convolution algorithms OS or OA [59]. These algorithms realize a linear convolution operation based on the use of the FFT and the cyclic convolution, i.e. a point-by-point multiplication in the frequency domain.

Beginning with the interpolation, let us start with the second operation, i.e. we first implement the time domain linear convolution with an OS algorithm, and keep the upsampling in the time domain. This means that after the upsampling we take overlapping blocks of the signal, transform

with an FFT, multiply by the DFT of the impulse response of the filter, transform with an Inverse Fast Fourier Transform (IFFT) and serialize part of its output samples.

The sizes of the FFT/IFFT can be freely chosen above a minimum value and, typically depend on the filter impulse response length and a time-domain overlapping factor which is a free design parameter. Let us assume a filter of impulse response length L_p, then the FFT/IFFT size N_FFT in the OS method is given by $N_\mathrm{FFT} = N_\mathrm{new} + L_\mathrm{p} - 1$. N_new is the number of new input samples in each block entering the FFT and $(L_\mathrm{p} - 1)$ samples are repeated in each block entering the FFT and the overlapping factor is given by the ratio $\gamma_\mathrm{OF} = (L_\mathrm{p} - 1)/N_\mathrm{FFT}$.

We can now transfer the operation upsampling by M to the frequency domain, realize it also with the help of the FFT/IFFT and combine it with the filter multiplication in the frequency domain. In this case, to realize the upsampling in the frequency domain, we reduce the FFT size to N_FFT/M, repeat M-times the output samples of the FFT, i.e. include a ramification of each FFT output into M signals, and keep the IFFT size of N_FFT. The structure for the efficient interpolation and modulation realization based on the OS algorithm is depicted in Fig. 2.7, where $H_{m,q}$ is obtained by evaluating the transfer function $H_m(z)$ at the corresponding frequency bin, i.e.

$$H_{m,q} = H_m(z)|_{z=\mathrm{e}^{j\omega_q}} = H_m(\mathrm{e}^{j\omega_q}), \text{ where } \omega_q = \frac{2\pi M q}{T N_\mathrm{FFT}} \tag{2.13}$$

or by approximating it with the corresponding DFT sample of the filter impulse response $H_m(z)$. It is clear that for this efficient implementation both the N_FFT and the filter order $(L_\mathrm{p} - 1)$ need to be multiple of the upsampling factor M. Consequently, N_new should also be a multiple of M, with the exception of the special case when $N_\mathrm{new} = 1$ as we will see later in this sub-section, where actually L_p should be a multiple of M.

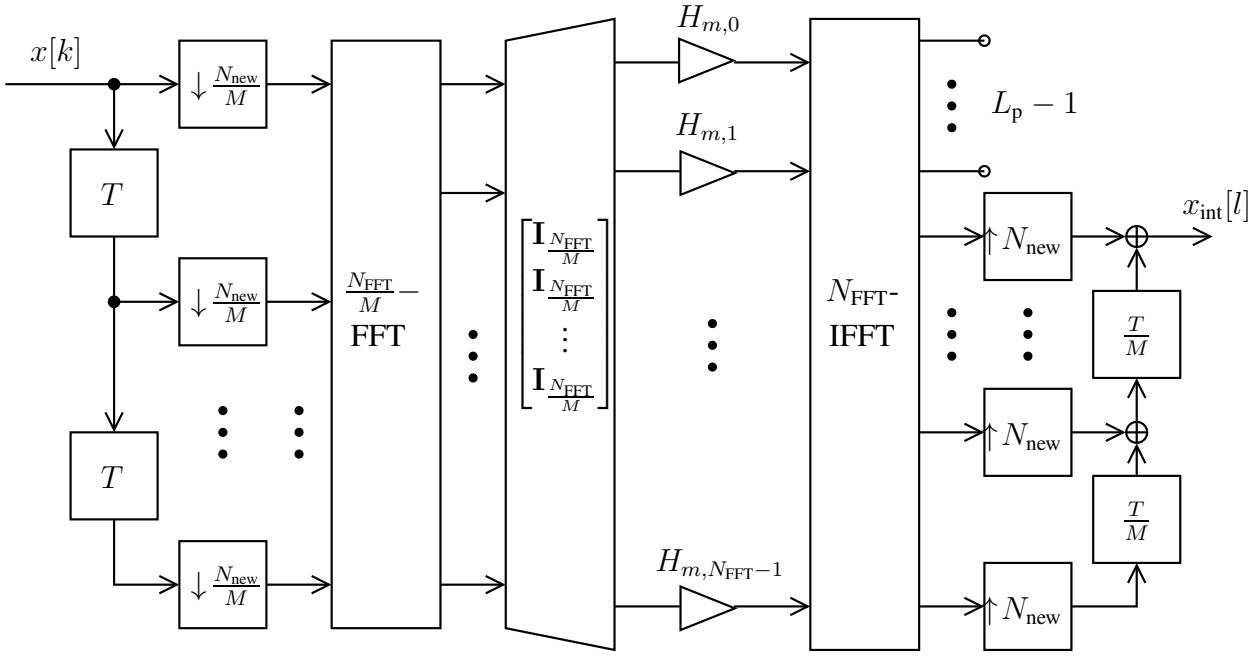

Fig. 2.7. Efficient interpolation and modulation realization based on OS algorithm for upsampling factor M.

Furthermore, the operation of modulation is obtained by circularly shifting the vector with the frequency domain samples of the interpolation filter. Let us assume the vector $\mathbf{h}_0 \in \mathbb{C}^{N_\mathrm{FFT}}$ contains

the $H_{0,q}$ samples, i.e. $\mathbf{h}_0 = [H_{0,0}, H_{0,1}, ..., H_{0,N_{\text{FFT}}-1}]^{\text{T}}$, with $H_{0,q}$ as defined in (2.13) for $m = 0$. The circularly shifted version $\mathbf{h}_m$ is given by

$$\mathbf{h}_m = \text{circshift}\left(\mathbf{h}_0, m_{\text{rot}}(m)\right) = \begin{bmatrix} \mathbf{0}_{m_{\text{rot}} \times (N_{\text{FFT}} - m_{\text{rot}})} & \mathbf{I}_{m_{\text{rot}}} \\ \mathbf{I}_{N_{\text{FFT}} - m_{\text{rot}}} & \mathbf{0}_{(N_{\text{FFT}} - m_{\text{rot}}) \times m_{\text{rot}}} \end{bmatrix} \mathbf{h}_0, \tag{2.14}$$

where the number of frequency bin shifts $m_{\text{rot}}(m)$ is given by

$$m_{\text{rot}}(m) = \text{round}\left(\frac{\gamma_{\text{OF}} N_{\text{FFT}} m}{M}\right) \frac{1}{\gamma_{\text{OF}}} = \text{round}\left(\frac{(L_{\text{p}} - 1)m}{M}\right) \frac{N_{\text{FFT}}}{(L_{\text{p}} - 1)}, \tag{2.15}$$

where round $(\bullet)$ represents rounding to the nearest integer. Moreover, we can see that $m_{\text{rot}}(m)$ will only be integer if N_{FFT} is a multiple of $(L_{\text{p}} - 1)$, which is always true if both are multiples of M as stated before. As a consequence, under our assumptions (2.15) simplifies to

$$m_{\text{rot}}(m) = \frac{m N_{\text{FFT}}}{M}. \tag{2.16}$$

However, for the special case when $N_{\text{new}} = 1$, $N_{\text{FFT}} = L_{\text{p}}$ and the number of frequency bin shifts is then given by $m_{\text{rot}}(m) = mL_{\text{p}}/M$, which is an integer provided that L_{p} is a multiple of M.

Similarly, one can realize the interpolation and modulation using the OA algorithm. In this case a serial-to-parallel operation is done and a zero-padding of $(L_{\text{p}} - 1)/M$ is applied before the small FFT. Between the small FFT and the large IFFT the same processing as in OS variant is employed. After the large IFFT a block overlapping of $(L_{\text{p}} - 1)$ samples according to the corresponding factor is performed. The structure for the efficient interpolation and modulation realization based on the OA algorithm is depicted in Fig. 2.8. It is worth noting that the upsampling, modulation

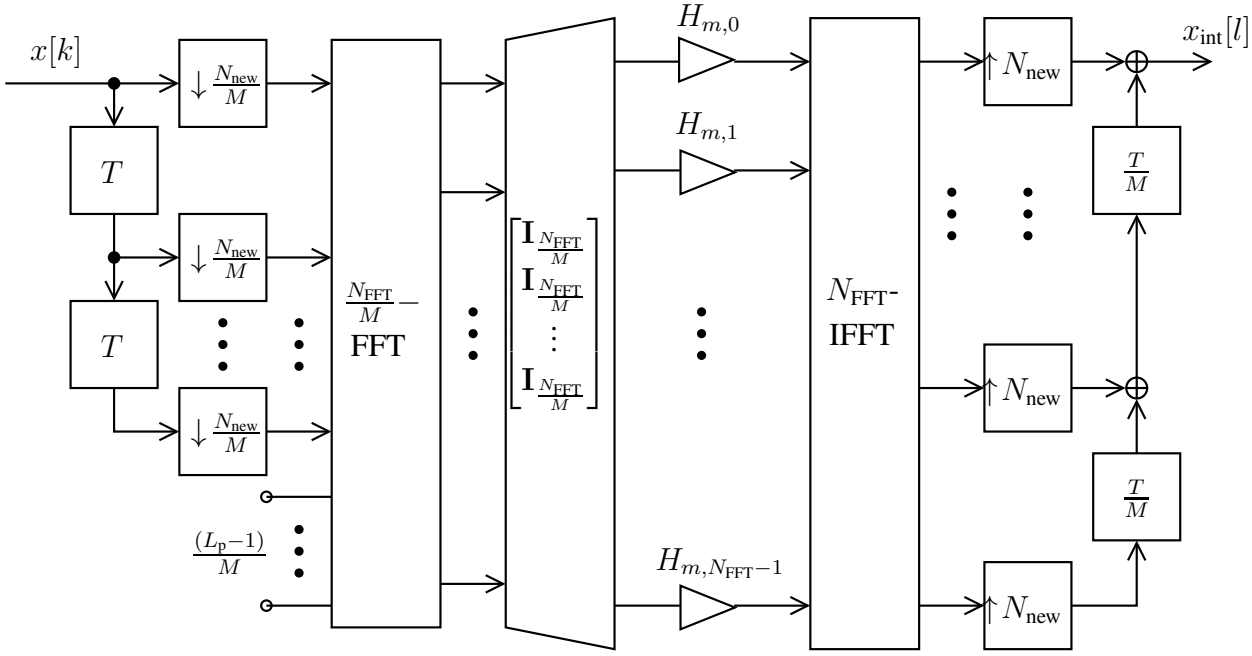

Fig. 2.8. Efficient interpolation and modulation realization based on OA algorithm for upsampling factor M

and filtering operations with the discrete frequency domain samples shown in Figs. 2.7 and 2.8

resembles a discrete frequency implementation of the steps depicted in Fig. 2.2. In addition to that, in practical implementations it is clear that the magnitude of many of the $H_{m,\bullet}$s will be very small and those coefficients may not need to be implemented. In this case only the coefficients in the surroundings of the passband and in the passband itself need to be implemented. The structures presented here show the steps to achieve the strict equivalence to the time domain interpolation.

The decimation can be realized by performing the transposed operations of the interpolation, but now with a downsampling by M. But now, first a large FFT of size N_{FFT} is applied by taking blocks of $(L_{\text{p}}-1)$ overlapping samples for OS and with serial-to-parallel of N_{new} samples plus zero-padding of $(L_{\text{p}}-1)$ samples for OA. After the multiplications by the frequency response of the filter, the decimation is obtained by wrapping and adding the spectral components to be aliased. This is obtained by M adders which then generate $\frac{N_{\text{FFT}}}{M}$ signals to be converted by a small IFFT of size $\frac{N_{\text{FFT}}}{M}$. Finally, only $\frac{N_{\text{new}}}{M}$ outputs of the small IFFT are serialized for the OS method and a block overlapping of $(L_{\text{p}}-1)/M$ IFFT outputs are necessary for the OA.

The structures for the efficient modulation and decimation realizations based on the OS and OA algorithms are depicted in Figs. 2.9 and 2.10. We can observe that the OS-based decimation

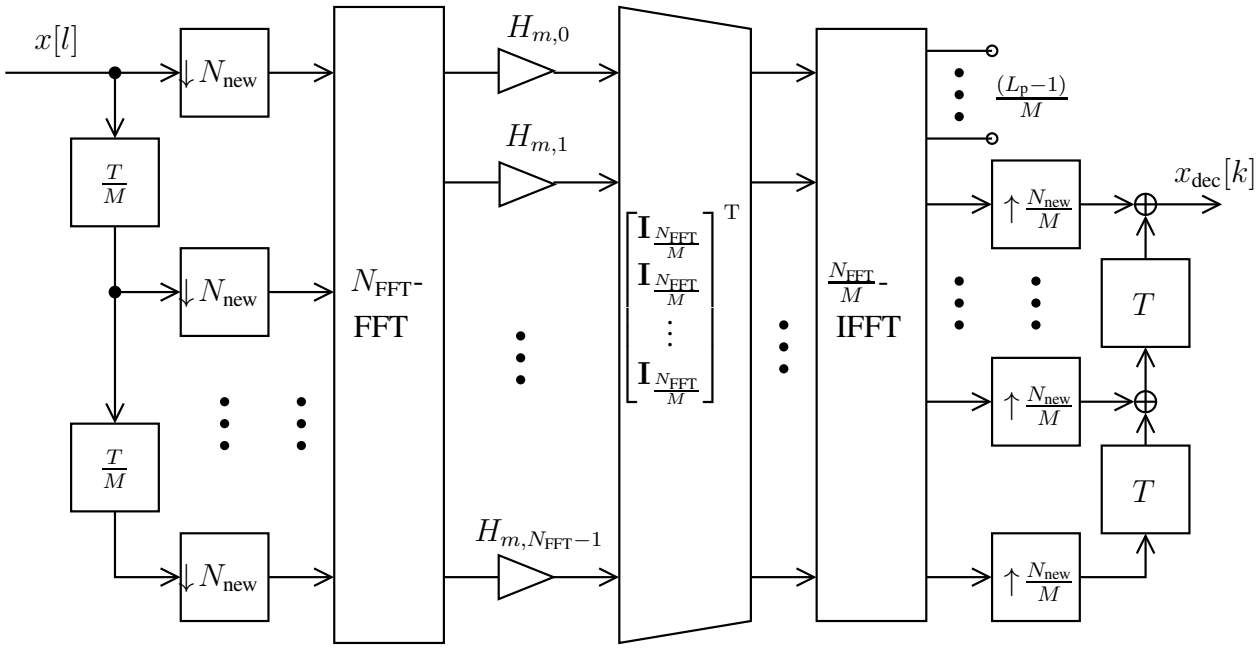

Fig. 2.9. Efficient modulation and decimation realization based on OS algorithm for downsampling factor M

implementation in Fig. 2.9 contains the transposed or dual operations of the OA-based interpolation in Fig. 2.8, while the OA-based decimation in Fig. 2.10 contains transposed or dual operations of the OS-based interpolation in Fig. 2.7. Again here many of the frequency domain coefficients of the filter may be very small and not only those coefficients may be neglected, but also a number of additions from the spectral warping.

One particular structure of interest is the special case when $N_{\text{new}} = 1$, especially if we consider the OA algorithm for the interpolation with modulation, and OS for the decimation with modulation. Because in OA-based interpolation only one small-FFT input is different from zero and in OS-based decimation only one small-IFFT output is further processed, the corresponding DFT and Inverse Discrete Fourier Transform (IDFT) matrices are simplified to a all-ones column

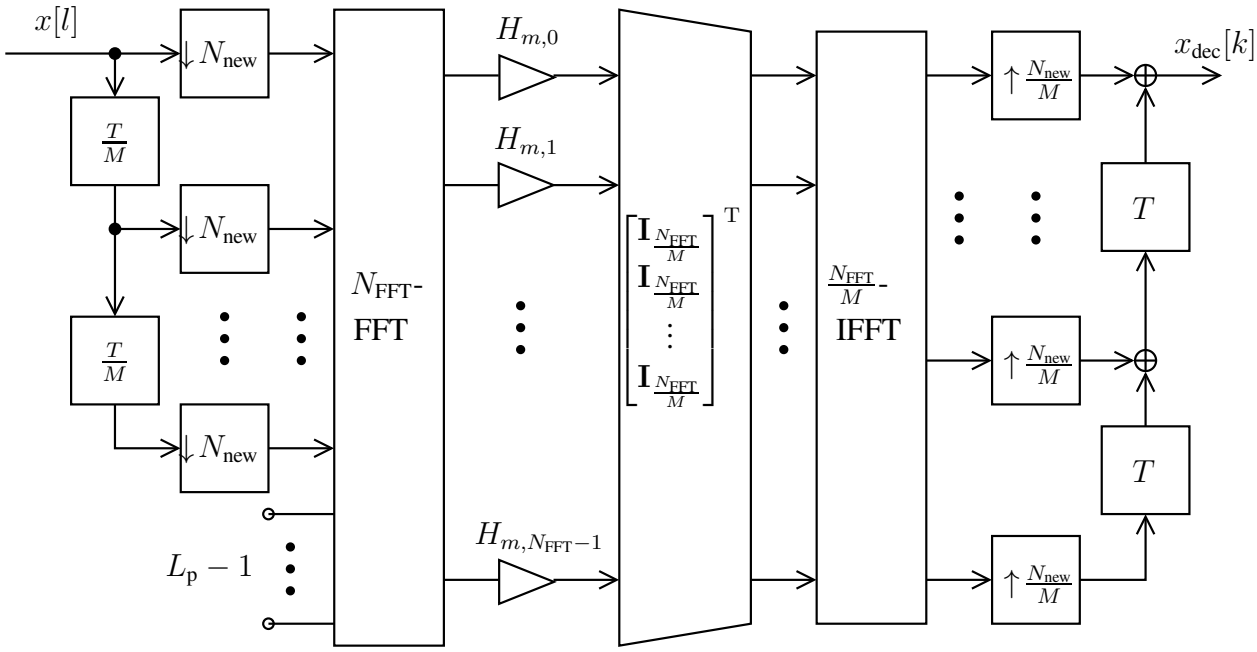

Fig. 2.10. Efficient modulation and decimation realization based on OA algorithm for downsampling factor M

vector $\mathbf{1}$ and row vector $\mathbf{1}^{\text{T}}$. As a consequence, in both cases the small FFT and IFFT, combined with the spectral repetition and wrapping, boil down to the trivial operations of ramification into and addition of N_{FFT} signals. Moreover, the upsampling operations can be moved to the right and downsampling to the left in the corresponding structures. The resulting interpolation and decimation structures are depicted in Figs. 2.11 and 2.12. Also here, for practical implementations, many of the filter coefficients may be neglected and the inputs of the big IFFT will be zero, simplifying its implementation, for the OA-based interpolation. For the OS-based decimation, many of the FFT outputs may not need to be calculated and many of the additions do not need to be implemented.

Let us take a look at some interesting examples of different ovelapping factors, FFT/IFFT sizes and new input samples N_{new}, namely with $N_{\text{new}} = 1$, $N_{\text{new}} = L_{\text{p}} - 1$, $N_{\text{new}} = 2(L_{\text{p}} - 1)$ and $N_{\text{new}} = 3(L_{\text{p}} - 1)$:

1) $N_{\text{new}} = 1$: FFT/IFFT size is $N_{\text{FFT}} = L_{\text{p}}$ and the overlapping factor is $\gamma_{\text{OF}} = (L_{\text{p}} - 1)/L_{\text{p}} = 1 - 1/L_{\text{p}} \approx 1$ or nearly 100% for typical filter lengths. If we assume $L_{\text{p}} = KM$, we obtain $N_{\text{FFT}} = KM$ and $m_{\text{rot}}(m) = mK$ as defined in (2.16).
2) $N_{\text{new}} = L_{\text{p}} - 1$: FFT/IFFT size is $N_{\text{FFT}} = 2(L_{\text{p}} - 1)$ and the overlapping factor is $\gamma_{\text{OF}} = \frac{L_{\text{p}}-1}{2(L_{\text{p}}-1)} = 1/2 = 0.5$ or exactly 50%. If we assume $L_{\text{p}} = KM + 1$, we obtain $N_{\text{new}} = KM$, $N_{\text{FFT}} = 2KM$ and $m_{\text{rot}}(m) = m2K$.
3) $N_{\text{new}} = 2(L_{\text{p}} - 1)$: FFT/IFFT size is $N_{\text{FFT}} = 3(L_{\text{p}} - 1)$ and the overlapping factor is $\gamma_{\text{OF}} = \frac{L_{\text{p}}-1}{3(L_{\text{p}}-1)} = 1/3 = 0.333$ or 33.33%. If we assume $L_{\text{p}} = KM + 1$, we obtain $N_{\text{new}} = 2KM$, $N_{\text{FFT}} = 3KM$ and $m_{\text{rot}}(m) = m3K$.
4) $N_{\text{new}} = 3(L_{\text{p}} - 1)$: FFT/IFFT size is $N_{\text{FFT}} = 4(L_{\text{p}} - 1)$ and the overlapping factor is $\gamma_{\text{OF}} = \frac{L_{\text{p}}-1}{4(L_{\text{p}}-1)} = 1/4 = 0.25$ or exactly 25%. If we assume $L_{\text{p}} = KM + 1$, we obtain $N_{\text{new}} = 3KM$, $N_{\text{FFT}} = 4KM$ and $m_{\text{rot}}(m) = m4K$.

Given the examples above, the following facts can be derived:

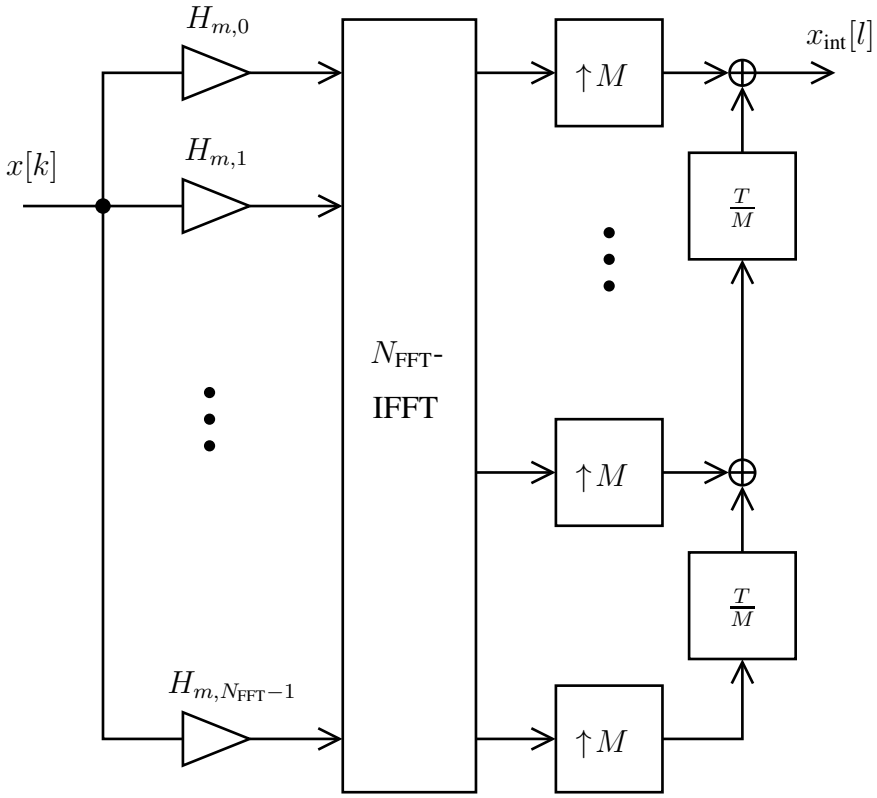

Fig. 2.11. Efficient interpolation and modulation realization based on OA algorithm for upsampling factor M and $N_{\text{new}} = 1$

- Example 1 has the smallest FFT size $N_{\text{FFT}} = KM$ and only one large FFT/IFFT, but the transform runs in the low sampling rate $1/T$ of the input signal.
- Example 2 has a two-times larger FFT size $N_{\text{FFT}} = 2KM$ and one small FFT/IFFT of size $N_{\text{FFT}}/M = 2K$, but all transforms run in the rate $1/KT$, i.e. K-times smaller then the sampling rate of the input signal for SFB and output signal for AFB.
- Example 3 has a three-times larger FFT size $N_{\text{FFT}} = 3KM$ and one small FFT/IFFT of size $N_{\text{FFT}}/M = 3K$, but all transforms run in the rate $1/2KT$, i.e. $2K$-times smaller then the sampling rate of the input or output signal. On the downside the large FFT size is not a power of two, as frequently desired.
- Example 4 has a four-times larger FFT size $N_{\text{FFT}} = 4KM$ and one small FFT/IFFT of size $N_{\text{FFT}}/M = 4K$, but all transforms run in the rate $1/3KT$, i.e. $3K$-times smaller then the sampling rate of the input or output signal.
- By evaluating the total number of multiplications necessary to process or generate N_{new} samples of the low rate input or output signal, one can conclude that Example 4 has the lowest complexity and Example 1 has the highest. In other words, a higher ovelapping factor results in a higher number of multiplications per time unit. We provide numerical examples later in this chapter that support this assessment.

But the choice of the parameters for the fast convolution scheme depends also on the architecture and the hardware properties than on the total number of multiplications per time unit. A larger N_{new} implies in a larger FFT, which then requires more memory, and also increases the processing latency.

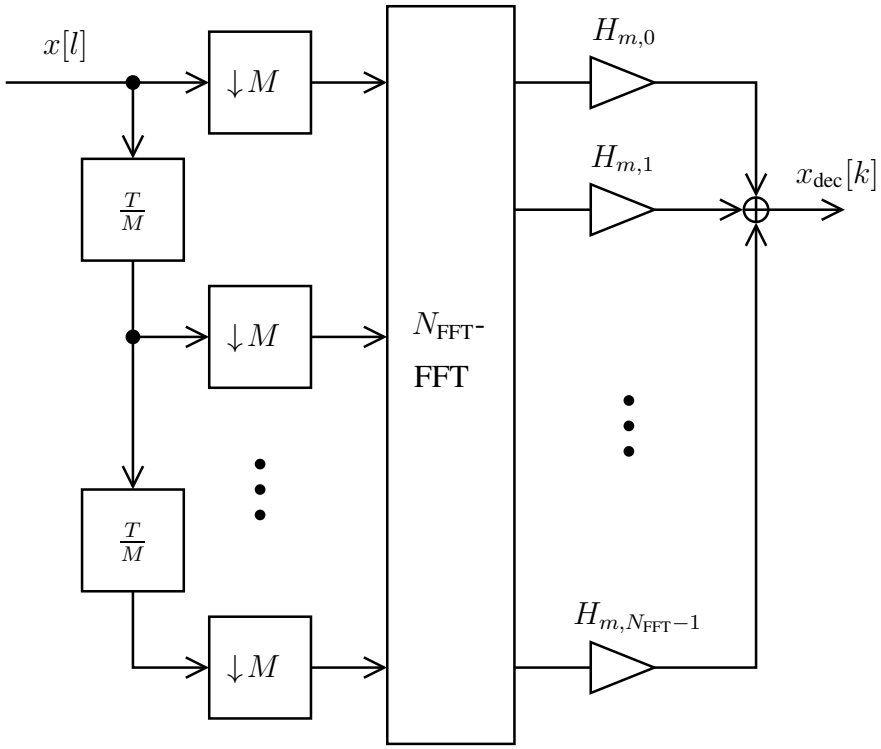

Fig. 2.12. Efficient modulation and decimation realization based on OS algorithm for downsampling factor M and $N_{\text{new}} = 1$

It is worth noting that we have not considered here non-integer rational upsampling or downsampling factor M. In this case a higher flexibility on the choice of the parameters exist for a given filter length.

2.3 Orthogonal Uniform Filter Banks

Until now we have presented multirate structures that generate either one high rate signal from one low rate signal through interpolation, or generate one low rate signal from one high rate signal through decimation. Moreover, we have considered the possibility of including a discrete time frequency modulation or translation in the process and also presented efficient structures for the implementation.

In the case of the interpolation process including discrete time modulation presented in Section 2.2.1, we can apply the same procedure to a number, for example M, of low rate narrowband signals. If the modulation frequency chosen for each of the signals is properly chosen, i.e. different frequency for each narrowband signal with sufficient distance between them, we can added up the interpolated signals. The results is broadband signal that multiplexes the original signals in the frequency domain, the so-called Frequency-Division Multiplexing (FDM)[3]. The resulting structure is the so-called SFB and the resulting synthesis operation is the basic principle of MultiCarrier (MC) modulation as we will further detail in this chapter. If the frequency modulated narrowband

[3]We do not differentiate here if the low rate signals are coming from a single source or from multiple sources, i.e. the signals may originate from a single or multiple applications from one user or also from different users. In this last case the term Frequency-Division Multiple Access (FDMA) is commonly employed.

signals are uniformly distributed in frequency domain and they all have the same bandwidth-and the same sampling rate $1/T$, we call the system a uniform filter bank. For an interpolation factor M in all branches and a multiplexing of M low rate signals, we denote the SFB as uniform critically sampled and a general model of it is shown in Fig. 2.13. The output signal $x_{\text{SFB}}[l]$ has a sampling

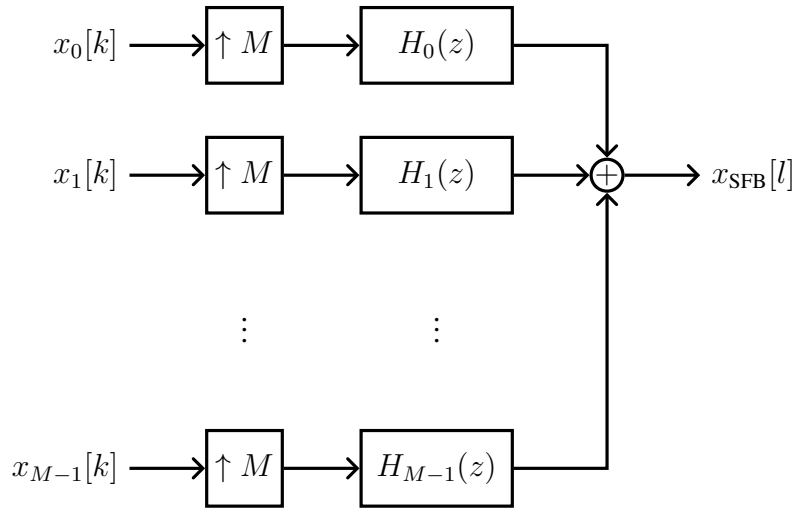

Fig. 2.13. General structure of a uniform critically sampled synthesis filter bank

rate of $\frac{1}{T_s} = \frac{M}{T}$. Because the sub-filters in a uniform critically sampled SFB were assumed here to be generated by a modulation or frequency translation, we call them modulated uniform critically sampled filter banks.

It is important to mention here that the upsampling or interpolation factor can be greater than the number of signals to be frequency multiplexed. In this case we speak of an oversampled SFB, which allows to improve the frequency separation between the narrowband signals with consequent increase in the overall broadband signal bandwidth. MC signals based on oversampled filter banks are frequently called Filtered Multitone (FMT). In some aspects FMT may simplify the overall implementation and looses some requirements, but on the other side it reduces the spectral and energy efficiency of the systems. The focus of this work is on critically sampled filter banks.

The resulting FDM or multicarrier baseband signal can then be further processed and prepared to be transmitted through a wireless or wired channel, or be stored in some media. Then at some other point in time and/or space, the low rate signals need to be recovered or analysed. In this case a frequency division demultiplexing needs to be performed with a so-called AFB, which is a transposed SFB. We apply in parallel multiple decimation operations with a factor M to a single broadband signal and use frequency demodulations that match to those used in the synthesis part. A general model of the uniform critically sampled AFB is shown in Fig. 2.14. The input signal $y_{\text{AFB}}[l]$ has a sampling rate of $\frac{1}{T_s} = \frac{M}{T}$ and the output signals $y_m[k]$ have a sampling rate of $1/T$.

We should note here that the inverse sequence of operations can also be performed, i.e. AFB is employed to decompose a broadband signal into narrowband signals and an SFB is then employed to generate a broadband signal. This configuration is classically called Sub-band Coding (SBC). Our multicarrier approach is classically known as TMUX [71].

The general structure for an MC system involving SFB at transmitter side and AFB at receiver side is shown in Fig. 2.15. For general input signals $x_m[k]$, the channel and noise do not necessarily allow us to perfectly recover them from the received signals $y_m[k]$. But if the $x_m[k]$ belong to a set of symbols known or estimated by the receiver, it is possible to find the actual transmitted symbols

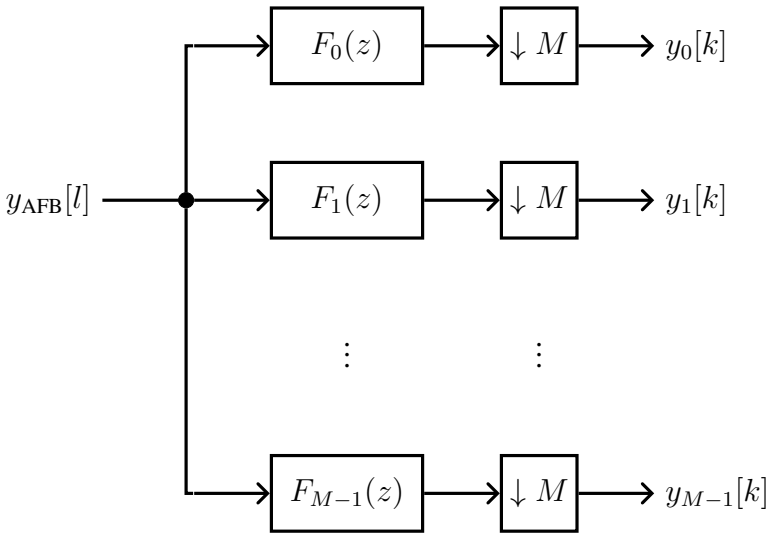

Fig. 2.14. General structure of a uniform critically sampled analysis filter bank

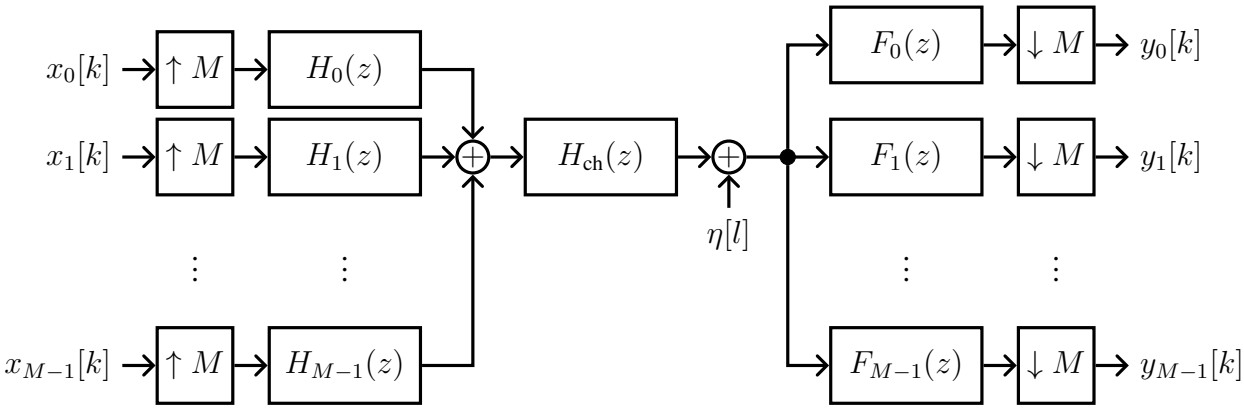

Fig. 2.15. General Multicarrier System Model based on a TMUX

with a certain probability and reliability. The overall performance will depend on the choice of the set of symbols, the noise power, the channel and the resulting transfer function of the filter bank. We will concentrate here on the latter, i.e. on how to design and implement the filter banks, such that their influence on the quality or reliability of the overall transmission is minimized. In the later chapters we present methods that compensate the influences of the channel adapted to the assumption that the MC structures presented in this chapter are employed.

Let us assume for the moment that the transmission channel is ideal, i.e. it does not distort the amplitude and phase of the transmitted signal. Moreover, we assume that the noise power is zero, such that we can only observe the influences of SFB and AFB. If the sub-filters are designed in such a way that the received signals $y_m[k]$ are scaled and delayed versions of the input signals, i.e.

$$y_m[k] = c_{\text{TMUX}} x_m[k + \tau_{\text{TMUX}}], \tag{2.17}$$

we can say that the filter bank is orthogonal, or at least biorthogonal [26], and that fulfills the PR conditions. If on the other hand the received signal is influenced by previous or succeeding $x_m[k]$, we say that the received symbol contains ISI, and if it is influenced by the signals from the other subcarriers, we say that it contains ICI. In the cases where the ISI and ICI are very small we can say that the filter bank is nearly-orthogonal or Near Perfect Reconstruction (NPR).

For real valued input signals $x_m[k]$, CMFB and SMFB [26, 50, 71] are examples of uniform modulated filter banks with the general structure shown in Figs. 2.13 and 2.14 that can be designed to be either PR or NPR [26, 29–31]. It should be clear at this point that the structures in Figs. 2.13, 2.14 and 2.15 are not computationally efficient, because the filters are applied in the higher sampling rate as explained in Section 2.2.3. Moreover, we should note that CMFB and SMFB have very efficient structures based on the same methods presented later in this work, i.e. polyphase decompositions and frequency domain filtering.

In wireless communications, especially in multicarrier communications, it is in general assumed that the inputs $x_m[k]$ are complex valued, i.e. they convey information in the amplitude and phase. In this case, CMFB and SMFB may not be the best option to be individually employed, but it is better to combine both into an exponentially modulated filter bank EMFB or to directly use the class of DFT filter banks.

The issue with exponentially modulated SFB and AFB when combined with complex valued inputs is that orthogonality, biorthogonality and PR cannot be achieved with a single step upsampling and downsampling by M as in Figs. 2.13, 2.14 and 2.15. Back in [64], it has already been identified in the context of multicarrier modulation that the complex input signals needed to be modified to achieve full or near orthogonality between the subcarriers or subchannels. Later other authors [43, 68] confirmed that result by utilizing filter banks theory. The solution employed is the staggering of the real and imaginary parts of the complex inputs $x_m[k]$ by a period of $\frac{T}{2}$. The resulting signal receives the name OQAM, because the real and the imaginary parts of $x_m[k]$ have such a time offset. Moreover, it is necessary that adjacent subcarriers have alternating real and imaginary parts staggering as explained in more detail in the following.

In Fig. 2.16 we have depicted the block diagram $\mathcal{O}_m$ of an OQAM-staggering or mapping operation for subcarriers with even numbered index m. The blocks labeled $\text{Re}\{\bullet\}$ and $\text{jIm}\{\bullet\}$ represent the operation of taking the real and imaginary parts from the input samples and providing them at the output. Then an upsampling by a factor 2 is performed and a delay of $\frac{T}{2}$ is included in the lower branch. In Fig. 2.17 we have a similar operation for the subcarriers with odd numbered index m, which is obtained by exchanging the blocks labeled $\text{Re}\{\bullet\}$ and $\text{jIm}\{\bullet\}$ in Fig. 2.16. We can see that the resulting signal is an interleaved version of the real and imaginary parts of the

input signal $x_m[k]$ and that the sampling rate has increased by a factor 2. It is important to note

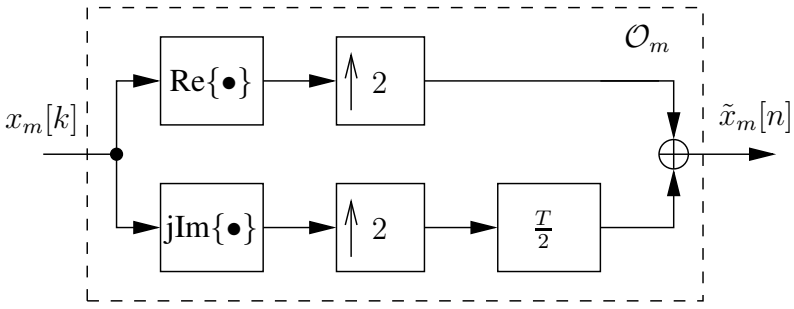

Fig. 2.16. OQAM-Staggering for even subcarrier index m

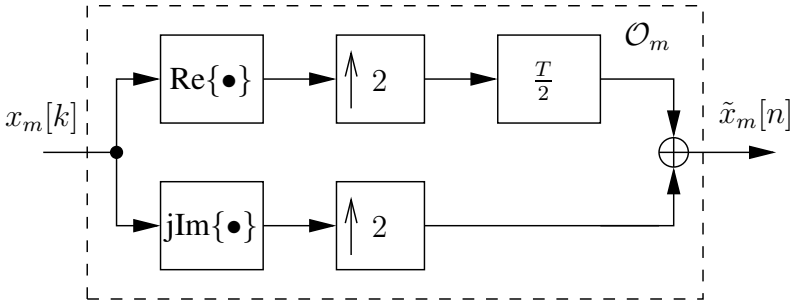

Fig. 2.17. OQAM-Staggering for odd subcarrier index m

that the use of OQAM fully guarantees the orthogonality between adjacent subcarriers and all other subcarriers with oposite phase in the staggering. The subcarriers with the same staggering will be decoupled by the stop-band attenuation or through a PR design.

Following the OQAM-staggering we can perform the interpolation and exponential modulation in each subcarrier, but because the sampling rate is already increased by a factor of 2, now the upsampling factor of the interpolation is $\frac{M}{2}$. The resulting orthogonal or nearly orthogonal exponentially modulated SFB is depicted in Fig. 2.18. It is clear now that M has to be even and later we will see that preferably also a power of 2.

The corresponding orthogonal or nearly orthogonal exponentially modulated AFB is shown in Fig. 2.19, The filtered signals at the AFB are downsampled by the block $\downarrow \frac{M}{2}$ that lowers the rate by a factor $\frac{M}{2}$. The block $\mathcal{O}'_m$ represent the OQAM de-staggering. In Fig. 2.20 we show the OQAM de-staggering operation for subcarriers with even index m and Fig. 2.21 for odd index m, respectively.

It is clear now that the AFB subfilters $F_m(z)$ have to be matched to the SFB subfilters $H_m(z)$. Moreover, in order to avoid any phase distortion in the subcarrier signals, the subfilters are designed to be strictly linear phase. Both $H_m(z)$ and $F_m(z)$ are obtained my exponentially modulating the same prototype filter, which is denoted as $H_{\mathrm{P}}(z)$ and is also strictly linear phase. The subfilters $H_m(z)$ and $F_m(z)$ are calculated as follows [43]

$$H_m(z) = F_m(z) = H_{\mathrm{P}}(zW_M^m)d^m, \quad m = 0, 1, \ldots, M-1, \tag{2.18}$$

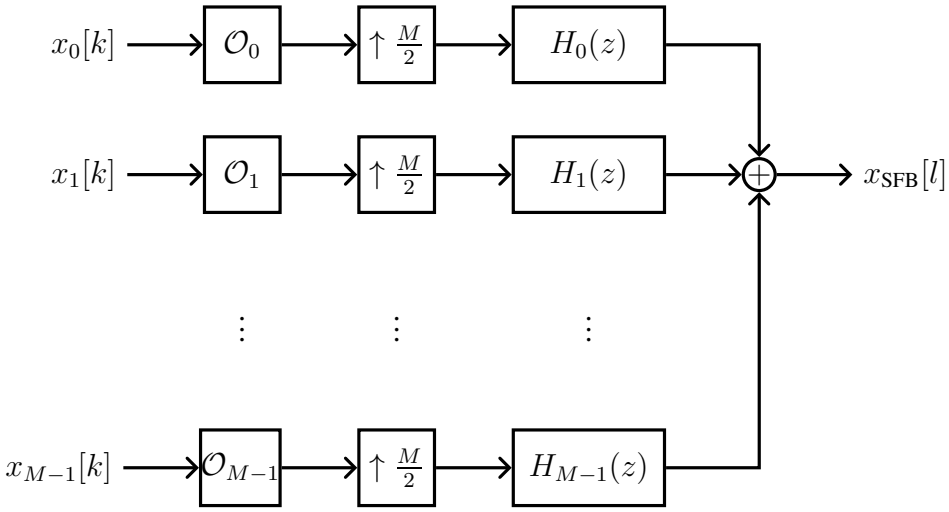

Fig. 2.18. Exponentially Modulated SFB

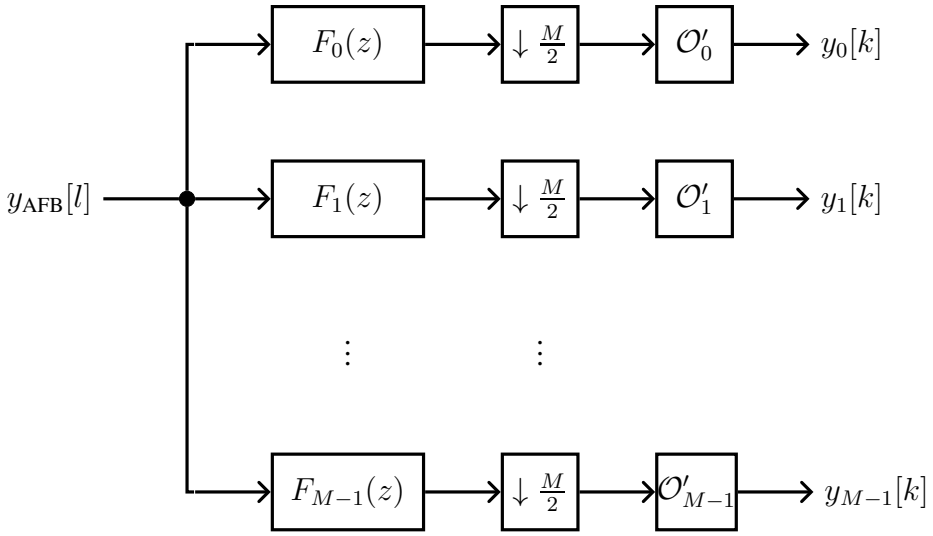

Fig. 2.19. Basics of Exponentially Modulated AFB

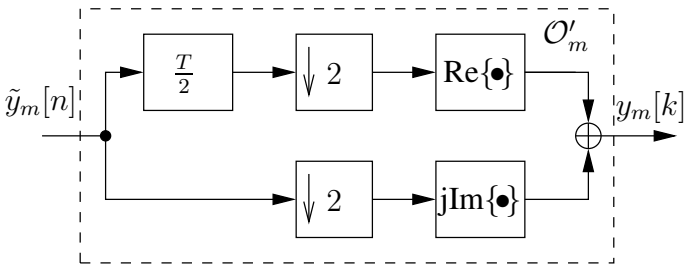

Fig. 2.20. OQAM de-staggering for even subcarrier index m

where

$$H_{\text{P}}(z) = H_0(z) = \sum_{p=0}^{L_{\text{P}}-1} h_p z^{-p},$$

$$H_m(z) = F_m(z) = \sum_{p=0}^{L_{\text{P}}-1} h_{m,p} z^{-l} = \sum_{p=0}^{L_{\text{P}}-1} h_{\text{P},p} W_M^{-m\left(p-\frac{L_{\text{P}}-1}{2}\right)} z^{-p},$$

$$\text{where } h_{m,p} = h_{\text{P},p} W_M^{-m\left(p-\frac{L_{\text{P}}-1}{2}\right)}, \tag{2.19}$$

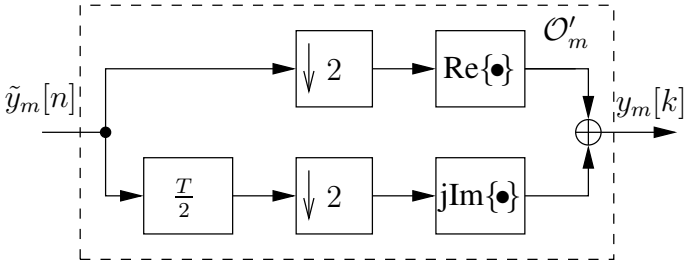

Fig. 2.21. OQAM de-staggering for odd subcarrier index m

with $W_M = e^{-\mathrm{j}\frac{2\pi}{M}}$ and $d = e^{-\mathrm{j}\frac{2\pi}{M}\frac{P-1}{2}} = W_M^{\frac{L_\mathrm{P}-1}{2}}$. The phase rotation factor d is has to be included in the exponential modulation in order to achieve strictly linear phase in the subfilters. We can, for example, assume here, without loss of generality, that the length of the prototype is $L_\mathrm{P} = KM$ or $L_\mathrm{P} = KM + 1$, where K is the time overlapping factor and determines not only the complexity of the filter bank, but also its memory.

We should note that, the structures presented in Figs. 2.18 and 2.19 are not efficient in terms of computational complexity, because either signal samples that are filtered at a high rate are thrown away or signals with samples equal to zero are filtered at a high rate just as discussed in Section 2.2.3.

2.4 Efficient Structures

The SFB and AFB shown in Figs. 2.18 and 2.19 can also be efficiently realized following a similar procedure as shown in Section 2.2.3 for single channel interpolation and decimation. We will also show here two families of efficient structures: First those based on a time domain filtering that uses the polyphase decompositions and second those based on frequency domain filtering using OA and OS.

2.4.1 Polyphase Decomposition based Structures

As we did for a single channel in Section 2.2.3, we start here by decomposing the the prototype filter in its polyphase components as a first step. We define $G_\mu\left(z_{\frac{M}{2}}\right), \mu = 0, ..., M-1$, as the μ-th type-1 polyphase component [26, 28, 71] of $H_\mathrm{P}(z)$ and is given by the relation

$$H_\mathrm{P}(z) = \sum_{\kappa=0}^{K-1}\sum_{\mu=0}^{M-1} h_\mathrm{P}[\kappa M + \mu] z^{-(\kappa M+\mu)} = \sum_{\mu=0}^{M-1} G_\mu(z^M) z^{-\mu}, \tag{2.20}$$

with $G_\mu(z_M) = \sum_{\kappa=0}^{K-1} h_\mathrm{P}[\kappa M + \mu] z_M^{-\kappa}$ and, by assuming without loss of generality that the prototype has $L_\mathrm{P} = KM$ coefficients, each polyphase component has K non-zero coefficients.

By plugging (2.20) into (2.18), the subfilters are then given by

$$H_m(z) = F_m(z) = \sum_{\mu=0}^{M-1} G_\mu(z^M W_M^{Mm}) z^{-\mu} W_M^{-m\mu} d^m = \sum_{\mu=0}^{M-1} G_\mu(z^M) z^{-\mu} W_M^{-m\mu} d^m. \tag{2.21}$$

We can now define the following vectors

$$\mathbf{h}(z) = \begin{bmatrix} H_0(z) & H_1(z) & \cdots & H_{M-1}(z) \end{bmatrix}^{\mathrm{T}}, \tag{2.22}$$

$$\mathbf{f}(z) = \begin{bmatrix} F_0(z) & F_1(z) & \cdots & F_{M-1}(z) \end{bmatrix}^{\mathrm{T}}, \tag{2.23}$$

$$\mathbf{a}(z) = \begin{bmatrix} 1 & z^{-1} & \cdots & z^{-(M-1)} \end{bmatrix}^{\mathrm{T}}, \tag{2.24}$$

$$\tilde{\mathbf{x}}(z) = \begin{bmatrix} \tilde{X}_0(z^M) & \tilde{X}_1(z^M) & \cdots & \tilde{X}_{M-1}(z^M) \end{bmatrix}^{\mathrm{T}}, \tag{2.25}$$

$$\tilde{\mathbf{y}}(z) = \begin{bmatrix} \tilde{Y}_0(z^M) & \tilde{Y}_1(z^M) & \cdots & \tilde{Y}_{M-1}(z^M) \end{bmatrix}^{\mathrm{T}}. \tag{2.26}$$

Furthermore, we have then the following input-output relations for the SFB and AFB

$$X_{\mathrm{SFB}}(z) = \mathbf{f}^{\mathrm{T}}(z)\tilde{\mathbf{x}}(z), \tag{2.27}$$

$$\tilde{\mathbf{y}}(z) = \mathbf{h}(z)Y_{\mathrm{AFB}}(z), \tag{2.28}$$

where the following relations holds

$$\mathbf{h}(z) = \mathbf{D}\mathbf{W}_M^{\mathrm{H}}\mathbf{G}(z^M)\mathbf{a}(z), \tag{2.29}$$

$$\mathbf{f}^{\mathrm{T}}(z) = \mathbf{a}^{\mathrm{T}}(z)\mathbf{G}(z^M)\mathbf{W}_M\mathbf{D}, \tag{2.30}$$

with the definitions $\mathbf{D} = \mathrm{diag}\,(1, d, ..., d^{M-1})$, $\mathbf{G}(z^M) = \mathrm{diag}\,(G_0(z^M), G_1(z^M), ..., G_{M-1}(z^M))$. Moreover, $\mathbf{W}_M$ and $\mathbf{W}_M^{\mathrm{H}}$ are the M size unitary DFT and IDFT matrix. The DFT or IDFT can be efficiently implemented using FFT algorithms [26, 59], which are very efficient especially if M is a power of 2.

Eqs. (2.29) and (2.30) can be further developed if we apply the Noble identities, which then allows us to move the upsampling by $\frac{M}{2}$ to the output of the polyphase components and before the delay chain described by $\mathbf{a}(z)$. We can now combined the input of the SFB with the OQAM-staggering to come up with the efficient structure shown in Fig. 2.22 [28]. We should note that

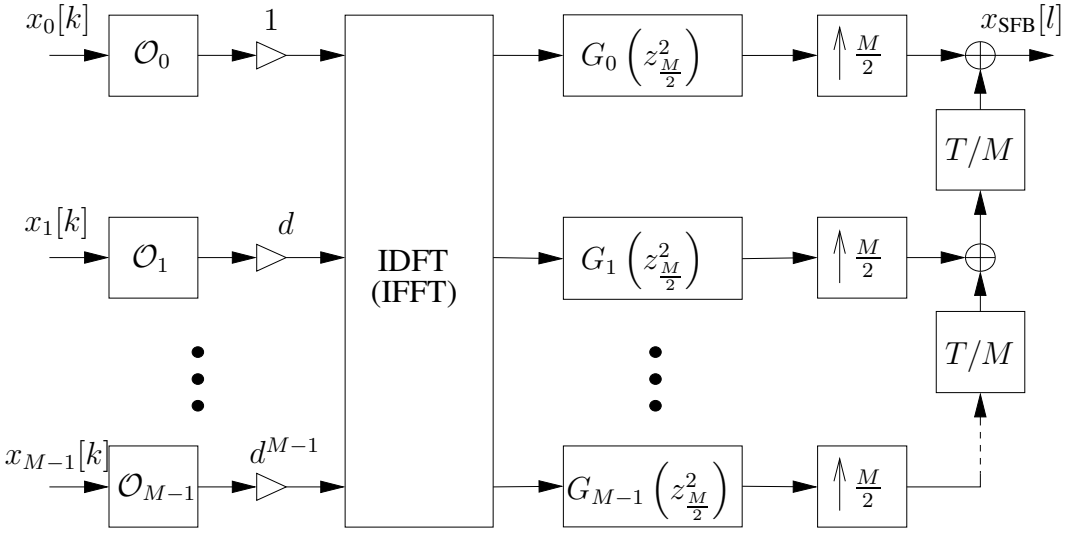

Fig. 2.22. Efficient structure of the SFB based on the polyphase decomposition of **type 1**

$G_\mu\left(z^2_{\frac{M}{2}}\right)$ is the μ-th type-1 polyphase component of the prototype upsampled by a factor of 2 and

the parallel samples at the outputs of the polyphase components are transformed to a serial signal by means of a block overlapping parallel to serial conversion with 50% overlapping.

The prototype filter $H_{\mathrm{P}}(z)$ can be designed such that PR conditions [26, 28, 71] are fulfilled. In this case, the constraints on the polyphase componens for PR are given by [43, 68]

$$G_{\mu}\left(z_{\frac{M}{2}}^{2}\right) G_{M-1-\mu}\left(z_{\frac{M}{2}}^{2}\right) + G_{\mu+\frac{M}{2}}\left(z_{\frac{M}{2}}^{2}\right) G_{\frac{M}{2}-1-\mu}\left(z_{\frac{M}{2}}^{2}\right) = \frac{2}{M} z_{\frac{M}{2}}^{-2(K-1)}, \tag{2.31}$$

where now $\mu = 0, ..., \frac{M}{4} - 1$, i.e. there are in total $\frac{M}{4}$ constraints. It is worth noting that because of the symmetry of the prototype impulse response the following equality holds

$$G_{M-1-\mu}\left(z_{\frac{M}{2}}^{2}\right) = z_{\frac{M}{2}}^{-2(K-1)} G_{\mu}\left(z_{\frac{M}{2}}^{-2}\right) = \tilde{G}_{\mu}\left(z_{\frac{M}{2}}^{2}\right), \tag{2.32}$$

where the right hand side is called the causal para-conjugate of the transfer function $G_{\mu}\left(z_{\frac{M}{2}}^{2}\right)$.

It is worth noting that although the prototype has a symmetrical impulse response, which is necessary to achieve PR, one multiplier per prototype filter coefficient has to be realized in the polyphase network presented above. This was a particularity of this polyphase components based filter bank structure until now. In the next paragraphs we will show that this will not be necessary later with a new proposed architecture.

Regarding Fig. 2.22, (2.31) and (2.32), it can be concluded that $M/2$ pairs of polyphase components are power complementary [28, 71]. The components $G_{\mu}(z^2)$ and $G_{\mu+\frac{M}{2}}\left(z_{\frac{M}{2}}^{2}\right)$ as well as their para-conjugates $G_{M-1-\mu}(z^2)$ and $G_{\frac{M}{2}-1-\mu}\left(z_{\frac{M}{2}}^{2}\right)$ possess this property and thus can be grouped as shown in Fig. 2.23, where we define the vectors of transfer functions

$$\mathbf{g}_{\mu}\left(z_{\frac{M}{2}}^{2}\right) = \begin{bmatrix} G_{\mu}\left(z_{\frac{M}{2}}^{2}\right) \\ G_{\mu+\frac{M}{2}}\left(z_{\frac{M}{2}}^{2}\right) \end{bmatrix}, \quad \mathbf{g}_{M-1-\mu}\left(z_{\frac{M}{2}}^{2}\right) = \begin{bmatrix} G_{M-1-\mu}\left(z_{\frac{M}{2}}^{2}\right) \\ G_{\frac{M}{2}-1-\mu}\left(z_{\frac{M}{2}}^{2}\right) \end{bmatrix}, \tag{2.33}$$

$$\text{for} \quad \mu = 0, ..., M/4 - 1. \tag{2.34}$$

We can see in Fig. 2.23 that it is necessary to reorganize the IDFT outputs. Moreover, for each polyphase component pair the outputs are added at the lower sampling rate. The delay that is necessary for the output of the polyphase component with highest index in each pair is transfered to the lower sampling rate and then to the front of the filter block. Finally, the outputs of the polyphase components pairs in Fig. 2.23 are serialized, different to Fig.2.22 where instead of being directly serialized the outputs of the two power complementary polyphase components are added at the higher rate, resulting in a block overlap and add procedure.

Now, the power complementary polyphase components pairs can be either implemented in a direct form as two separate transfer functions or they can be jointly implemented using, for example, a non-recursive lattice structure [44, 71]. A lattice structure provides several advantages like, for example, robustness to coefficient quantization, a modular and scalable structure, facilitate PR fulfilling design, etc. The lattice structure is composed of consecutive Givens rotations $\mathbf{R}_{\mu,i}, i = 0, \cdots, K-1$, and delay sections $\mathbf{\Lambda}\left(z_{\frac{M}{2}}^{2}\right)$ with

$$\mathbf{R}_{k,i} = \begin{bmatrix} \cos\Theta_{\mu,i} & \sin\Theta_{\mu,i} \\ -\sin\Theta_{\mu,i} & \cos\Theta_{\mu,i} \end{bmatrix}, \quad \mathbf{\Lambda}\left(z_{\frac{M}{2}}^{2}\right) = \begin{bmatrix} 1 & 0 \\ 0 & z_{\frac{M}{2}}^{-2} \end{bmatrix} = \begin{bmatrix} 1 & 0 \\ 0 & z_{M}^{-1} \end{bmatrix}, \tag{2.35}$$

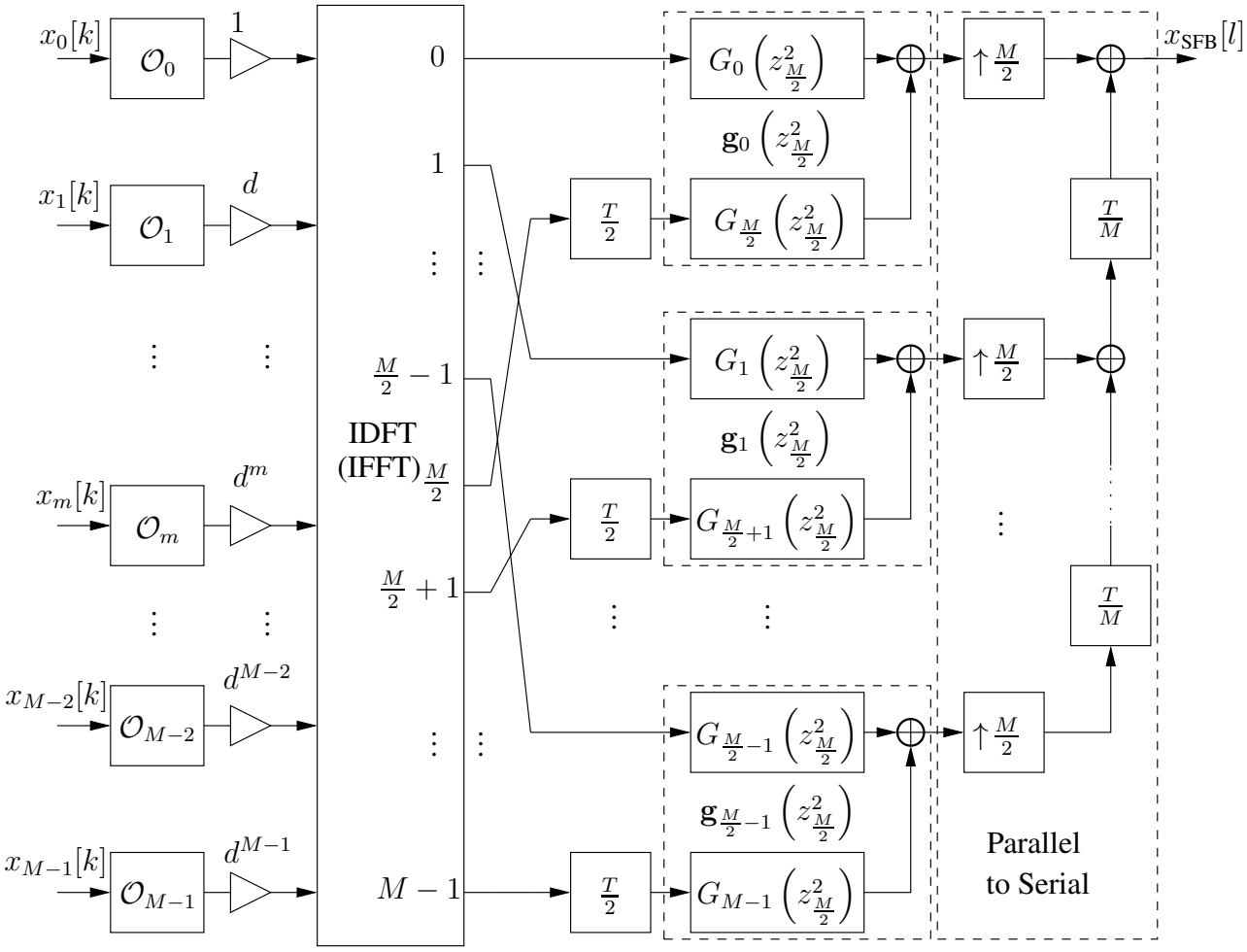

Fig. 2.23. Efficient SFB implementation with polyphase components of **type 1** reordered and grouped in power complementary pairs

and

$$\mathbf{g}_{\mu}^{\mathrm{T}}\left(z^2_{\frac{M}{2}}\right) = \begin{bmatrix}\cos\Theta_{\mu,K-1} & \sin\Theta_{\mu,K-1}\end{bmatrix}\mathbf{\Lambda}\left(z^2_{\frac{M}{2}}\right)\mathbf{R}_{\mu,K-2}\ldots\mathbf{\Lambda}\left(z^2_{\frac{M}{2}}\right)\mathbf{R}_{\mu,0}, \tag{2.36}$$

$$\mathbf{g}_{M-1-\mu}^{\mathrm{T}}\left(z^2_{\frac{M}{2}}\right) = \begin{bmatrix}\sin\Theta_{\mu,K-1} & \cos\Theta_{\mu,K-1}\end{bmatrix}\mathbf{\Lambda}\left(z^2_{\frac{M}{2}}\right)\mathbf{R}_{\mu,K-2}\ldots\mathbf{\Lambda}\left(z^2_{\frac{M}{2}}\right)\mathbf{R}_{\mu,0}, \tag{2.37}$$

where $\mu = 0, \ldots, M/4-1$.

The lattice structure for each $\mathbf{g}_{\mu}\left(z^2_{\frac{M}{2}}\right)$ is shown in Fig. 2.24. The rotation angles $\Theta_{\mu,i}$'s can be found from the coefficients of the polyphase pairs in $\mathbf{g}_{\mu}\left(z^2_{\frac{M}{2}}\right)$ by a successive polynomial degree reduction [71]. In Fig. 2.25 shows the lattice structure for the pair $\mathbf{g}_{M-1-\mu}\left(z^2_{\frac{M}{2}}\right)$, that has many similarities to the one in Fig. 2.24, like the same $\Theta_{\mu,i}$'s, for example. The reason for those similarities lie in the fact that the two transfer functions in $\mathbf{g}_{M-1-\mu}\left(z^2_{\frac{M}{2}}\right)$ are para-conjugate of the ones in $\mathbf{g}_{\mu}\left(z^2_{\frac{M}{2}}\right)$. Another important detail is that the last rotor in both cases has only one branch, to generate the single output.

Now, if a full rotor is implemented in the last lattice stage, we would obtain a lattice structure with two inputs and two outputs. This 2×2 lattice structure is depicted in Fig. 2.26, where 4

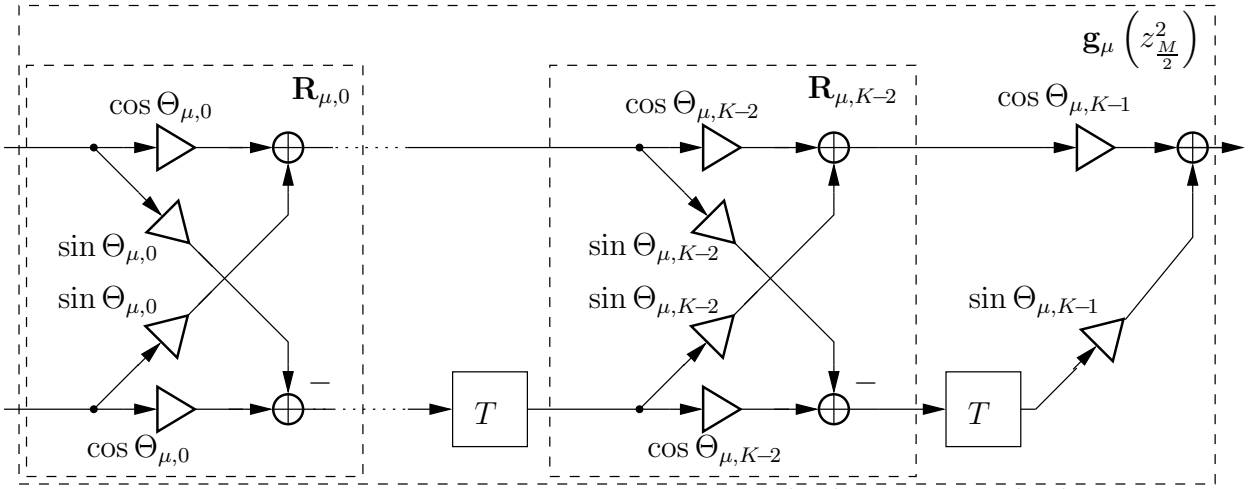

Fig. 2.24. Lattice realization of polyphase pair $G_\mu\left(z^2_{\frac{M}{2}}\right)$ and $G_{\mu+\frac{M}{2}}\left(z^2_{\frac{M}{2}}\right)$

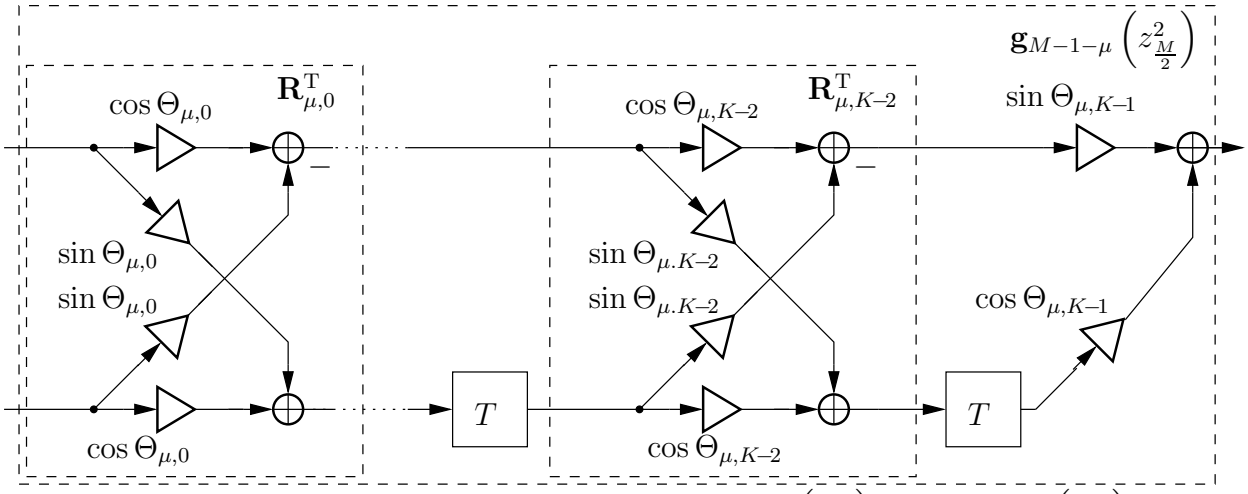

Fig. 2.25. Lattice realization of polyphase pair $G_{M-1-\mu}\left(z^2_{\frac{M}{2}}\right)$ and $G_{\frac{M}{2}-1-\mu}\left(z^2_{\frac{M}{2}}\right)$

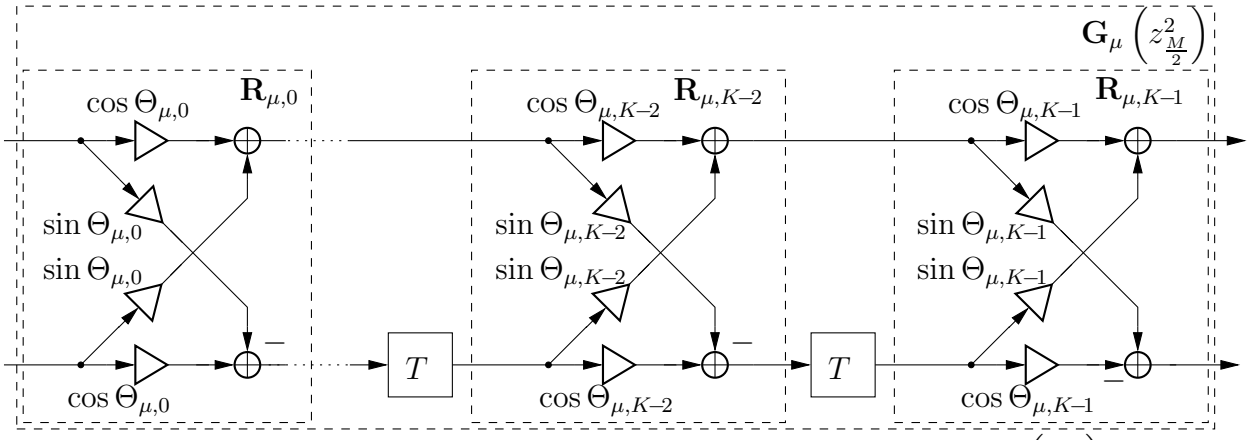

Fig. 2.26. Lattice realization of the 2×2 orthogonal transfer function $\mathbf{G}_\mu\left(z^2_{\frac{M}{2}}\right)$

different transfer functions are obtained and described by the transfer function matrix

$$\mathbf{G}_\mu\left(z^2_{\frac{M}{2}}\right) = \begin{bmatrix} G_\mu\left(z^2_{\frac{M}{2}}\right) & G_{\frac{M}{2}+\mu}\left(z^2_{\frac{M}{2}}\right) \\ G_{\frac{M}{2}-1-\mu}\left(z^2_{\frac{M}{2}}\right) & -G_{M-1-\mu}\left(z^2_{\frac{M}{2}}\right) \end{bmatrix}, \quad \mu = 0, ..., M/4-1. \tag{2.38}$$

Here two pairs of power complementary polyphase components are implemented in one non-recursive 2×2 lattice. The 2×2 lattice structure is one of the best known implementation of an orthogonal filter. This structure will be an important building block of the new structure we will present in the next section.

By considering again the structures in Figs. 2.24 and 2.25 we can conclude that they contain more coefficient multiplications than if the two polyphase components are implemented separately in a direct form each. However, the full rotors can be modified in order to have only two multipliers each and, in addition to that, two multipliers for each polyphase component pair output. This low complexity lattice structure is presented in Fig. 2.27 for the 2×1 lattice, were $\kappa_\mu = \prod_{i=0}^{K-1} \cos\Theta_{k,i}$.

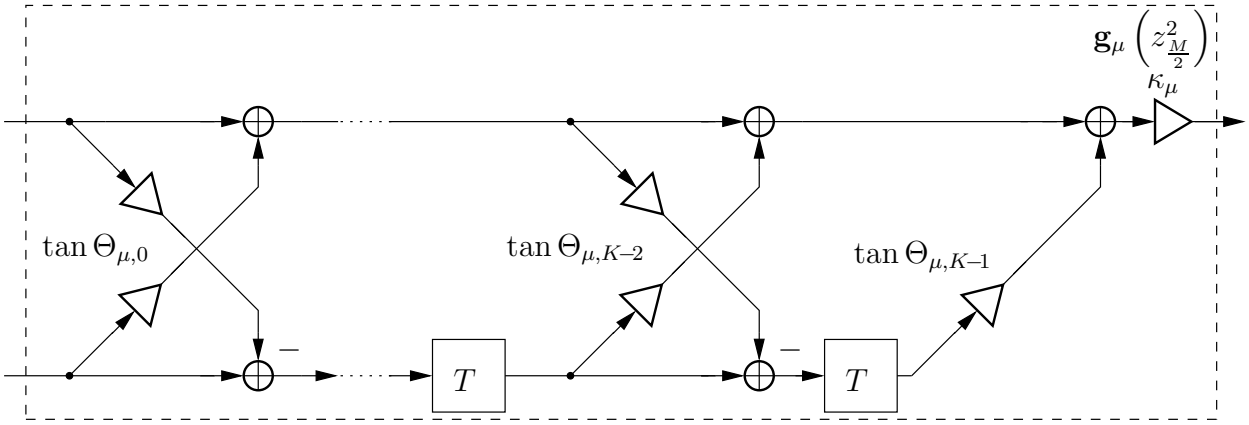

Fig. 2.27. Efficient 2×1 lattice structure with two-multiplier rotors

Now the lattice rotors with only two multipliers reduce the complexity almost to the same as the direct form.

We could say that the state-of-the-art structure for exponentially modulated SFBs based on the prototype polyphase decomposition of type 1 is the one in Fig. 2.23, with the polyphase components pairs either implemented in direct form or as 2×1 lattices as in Fig. 2.27.

Furthermore, the same simplification of the rotors can be applied to the 2×2 lattice, resulting in the structure shown in Fig. 2.28. Although derived in a different way and following a parallel development to the filter banks theory, the lapped transforms [50] have a fast implementation that is also based on the lattice structures. Actually, we will see in the next section that our proposed architecture corresponds to the exponential modulated filter bank in terms of complexity and efficient realization, as the fast lapped transform corresponds to CMFB and SMFB.

One alternative to the lattice structure of Fig. 2.26 that also reduces the complexity, and has similar advantages, is achieved with the so called lifting steps [25, 60], or ladder structure, and it is presented in Fig. 2.29, where each rotor is now substituted by 3 multipliers.

We have shown until now state-of-the-art structures of the SFB and only for the prototype polyphase decomposition of type 1. Similar structures can be derived based on polyphase decompositions of type 2 shown in Fig. 2.30, where the multipliers before the DFT are redefined to $d' = dW_M = W_M^{\frac{L_p+1}{2}}$, and for polyphase decompositions of type 3, as shown in Fig. 2.31. Fi-

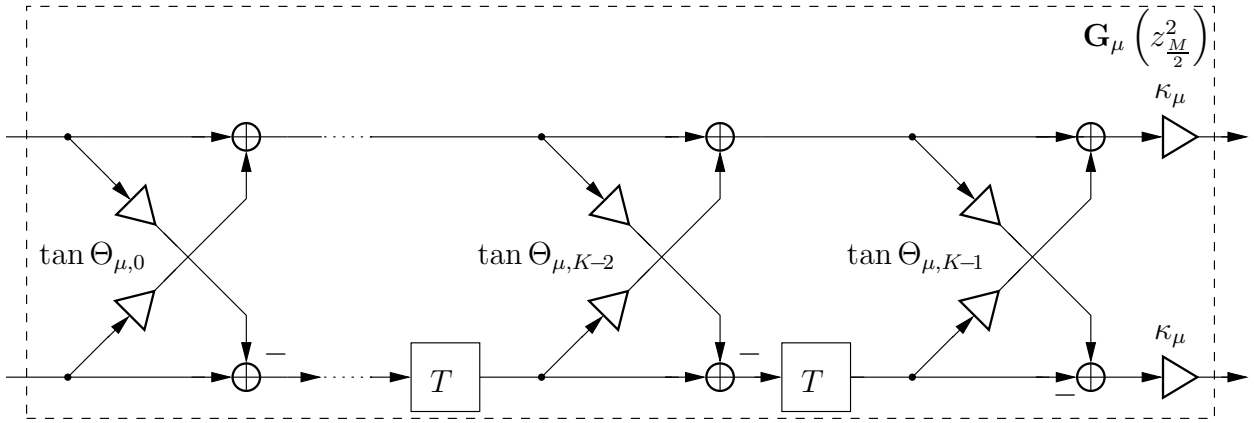

Fig. 2.28. Efficient 2×2 lattice structure with two-multiplier rotors

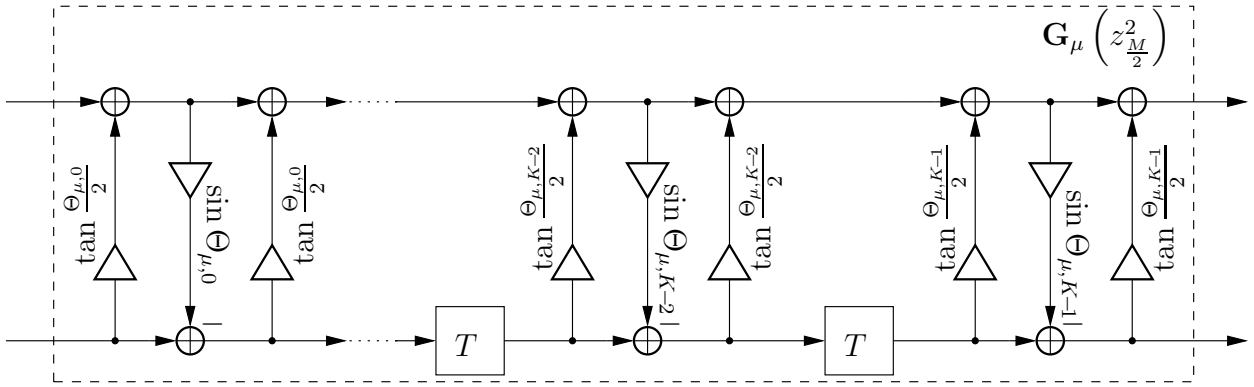

Fig. 2.29. Orthogonal 2×2 polyphase components structure based on lifting steps

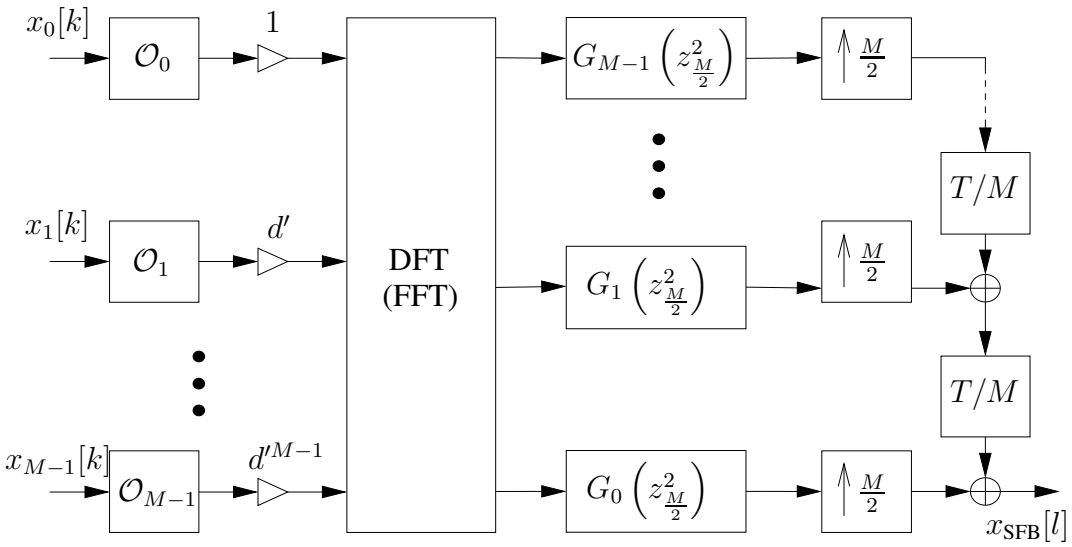

Fig. 2.30. Efficient structure of the SFB based on the polyphase decomposition of **type 2**

nally, for the AFB there are equivalent corresponding structures for all three types of polyphase decompositions and for the pairs of polyphase components as direct form, low complexity lattice or lifting steps available.

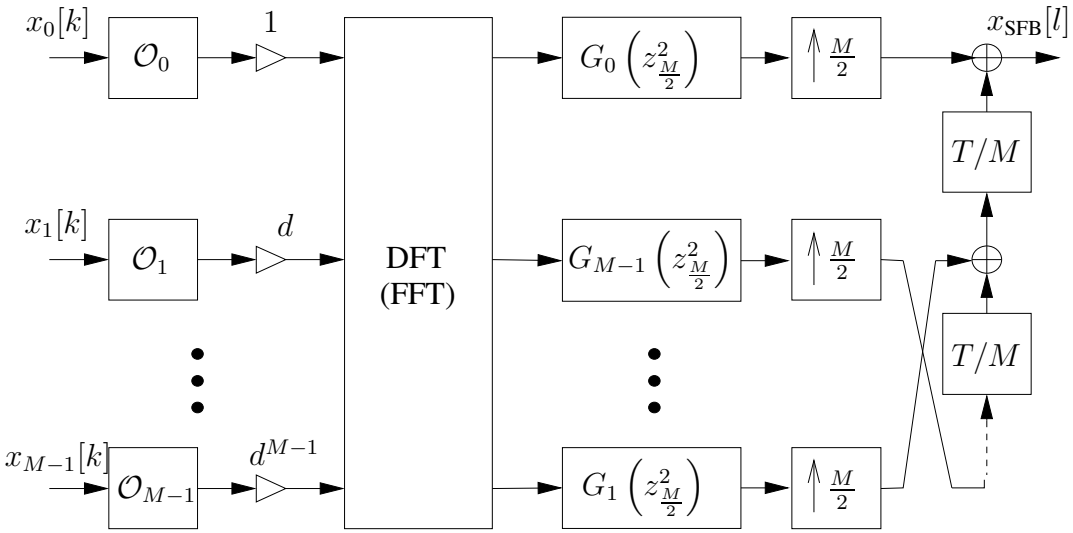

Fig. 2.31. Efficient structure of the SFB based on the polyphase decomposition of **type 3**

The new structures that we propose in this work are depicted in Figs. 2.32, 2.33, 2.34, for the SFB based on polyphase decompositions of type 1, 2 and 3, and in Figs. 2.35, 2.36, 2.37, for the AFB also based on polyphase decompositions of type 1, 2 and 3. Where for the structures based on type 2 decomposition we use the definition

$$\mathbf{G}'_{\mu}\left(z^2_{\frac{M}{2}}\right) = \begin{bmatrix} G_{M-1-\mu}\left(z^2_{\frac{M}{2}}\right) & G_{\frac{M}{2}-1-\mu}\left(z^2_{\frac{M}{2}}\right) \\ G_{\frac{M}{2}+\mu}\left(z^2_{\frac{M}{2}}\right) & -G_{\mu}\left(z^2_{\frac{M}{2}}\right) \end{bmatrix}, \quad \mu = 0, ..., M/4-1. \tag{2.39}$$

The new structures are based on the further development of the polyphase networks from Figs. 2.23 for the corresponding FB and decomposition type. As mentioned in the former section, because the prototype filter has a symmetric impulse response, there are pairs of polyphase components that have the same coefficients but in a reverse order. In other words they are pairs of para-conjugate filters. As shown in Fig. 2.28 and 2.29 and in Eqs. (2.38) and Eqs. (2.39), the 2×2 lattice or lifting structures provide four of the polyphase components. Now only $M/4$ such structures are necessary where each of them has $2(K+1)$ multipliers for the case of lattice and $3K$ for the case of lifting steps.

But there are two other important issues that the new structures solve. They are related on how to connect the DFTs and IDFTs to the polyphase filters and to the polyphase matrix contents itself. We will focus here on the SFBs. First, the negative sign in one of the transfer functions in the matrix in (2.38) that is obtained automatically from the lattice structure. This is solved with the periodic sign inversion for even time instants represented by the multiplier -1^{m+1}. It can be shown that the impulse responses in the second row are applied in a time interleaving fashion and by this alternation of the samples sign, only the impulse response with the inversed sign is reverted to its original value.

The second issue is that the DFT or IDFT provide M outputs, but now only $M/2$ inputs exist in the new polyphase network. It can be demonstrated that because of the special characteristics of the signals at the input of the DFT or IDFT, the outputs actually show many redundancies. In other words, as it will be shown below, the outputs of the IDFT have the following properties $Y_{\frac{M}{2}-n-1} = \pm Y^*_n$ and $Y_{M-n-1} = \pm Y^*_{\frac{M}{2}+n}$ for $0 < n < \frac{M}{4} - 1$. As a consequence, half of the

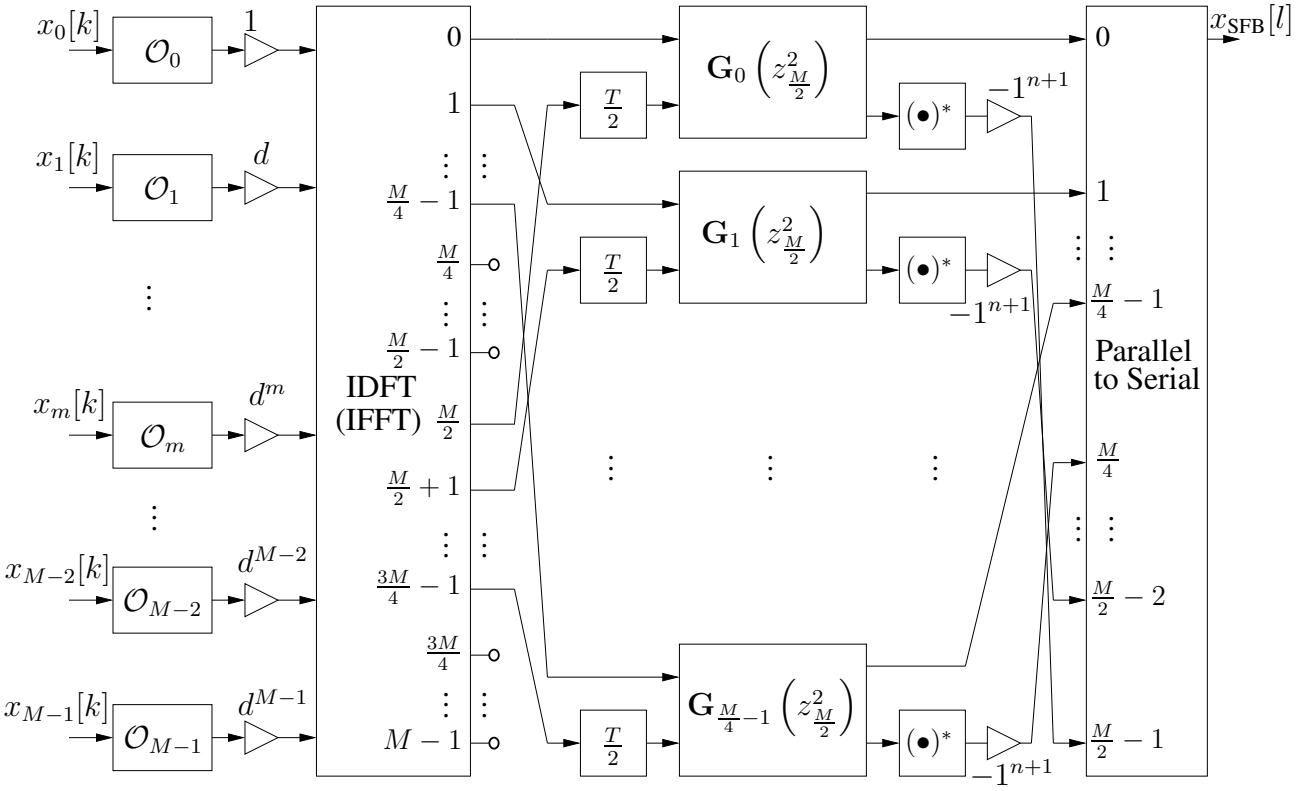

Fig. 2.32. New efficient SFB implementation based on the polyphase decomposition of **type 1** organized as orthogonal 2×2 transfer functions

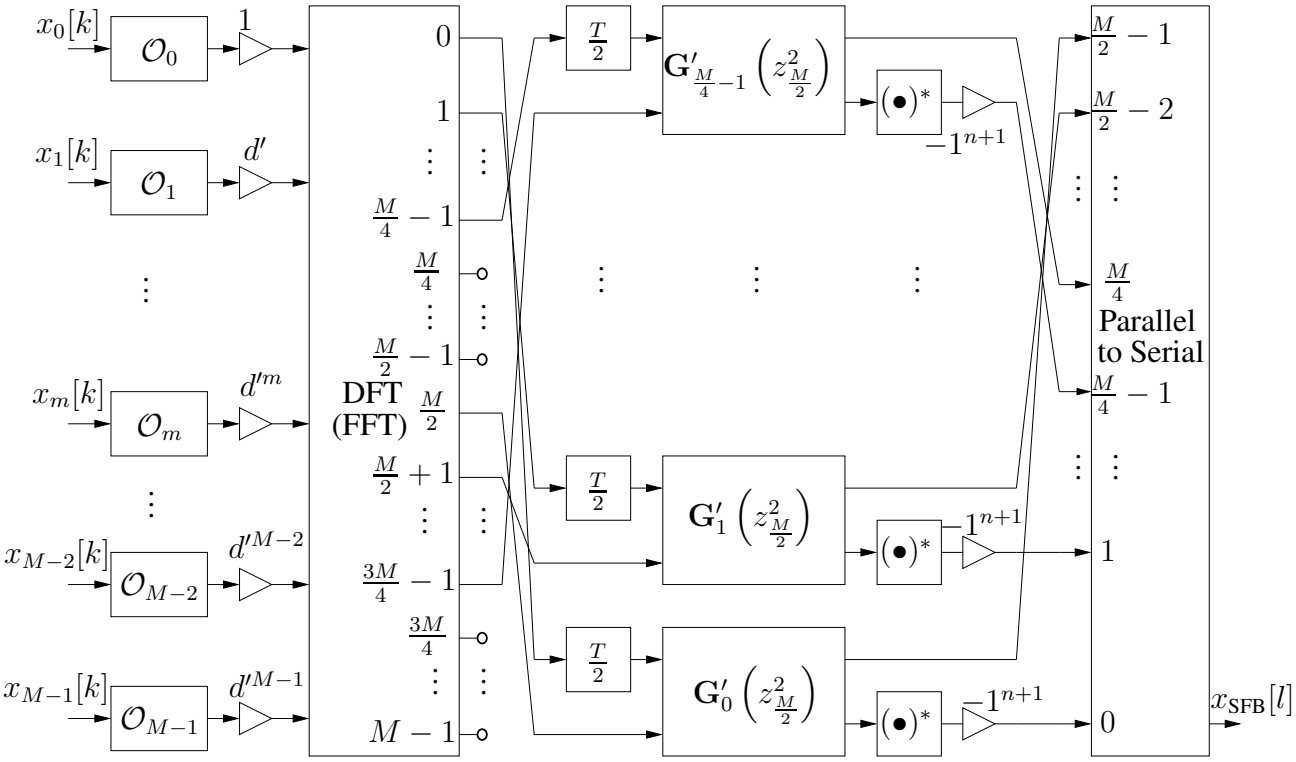

Fig. 2.33. New efficient SFB implementation based on the polyphase decomposition of **type 2** organized as orthogonal 2×2 transfer functions

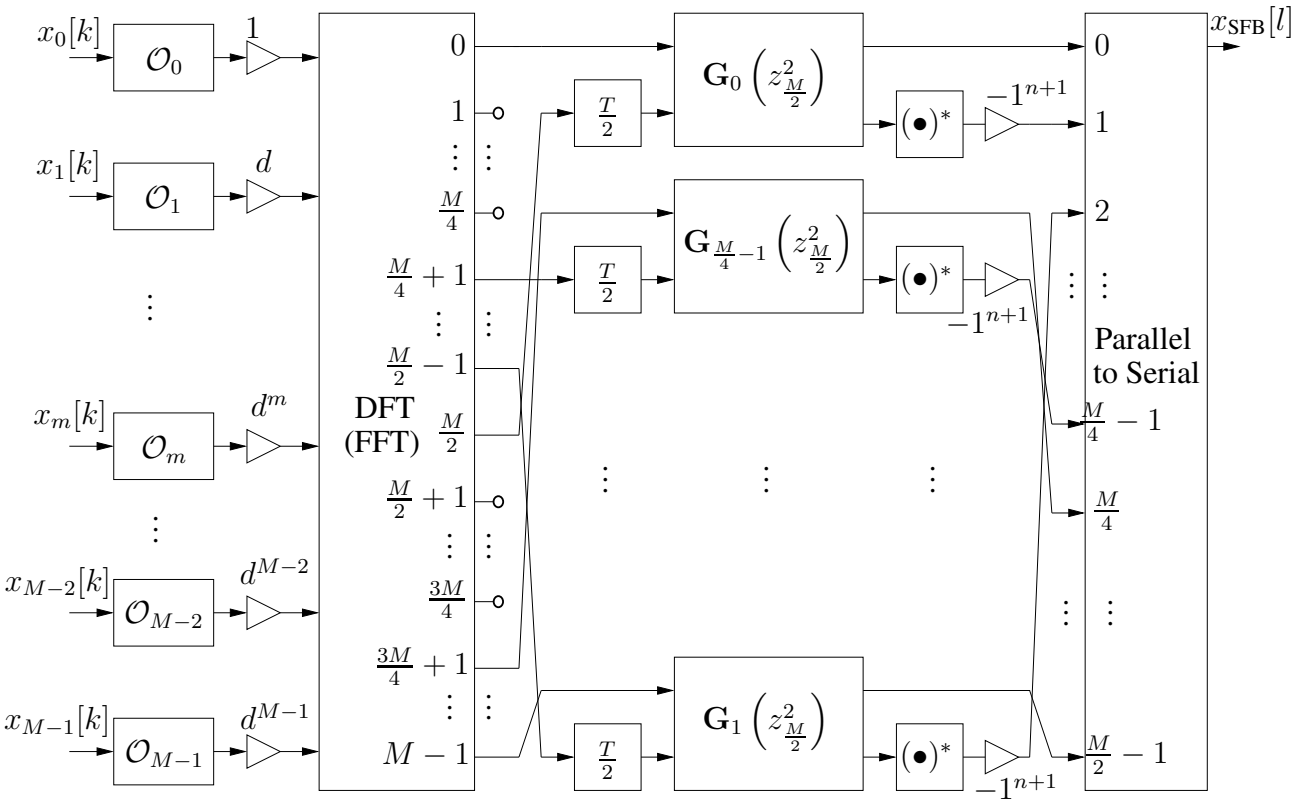

Fig. 2.34. New efficient SFB implementation based on the polyphase decomposition of **type 3** organized as orthogonal 2×2 transfer functions

outputs are positive or negative complex conjugated versions of the other half. With this in mind, one can see that all the necessary signals are generated by half of the DFT or IDFT outputs. We just need to take the positive or negative complex conjugate signal and from one of the outputs of each polyphase sets. Since all coefficients of the polyphase components are real valued, this is equivalent to take the positive or negative complex conjugate of the two input signals. This means that half of the outputs of the DFT or IDFT do not need to be calculated, reducing even more the total computational complexity.

Let us assume the SFB structure based on type 1 polyphase decompositions. Given the IDFT input samples X_m and the phase rotations $d^m = \mathrm{e}^{-\mathrm{j}\frac{2\pi}{M}\frac{KM-1}{2}m}$, we can now prove that the IDFT output samples Y_n contain redundancies, if the input samples are purely real or purely imaginary, i.e. are OQAM-like. We will show that $Y_{\frac{M}{2}-n-1} = \pm Y_n^*$ for $0 < n < \frac{M}{4} - 1$ and, similarly, it can be shown that $Y_{M-n-1} = \pm Y^*_{\frac{M}{2}+n}$. First, we need to find an expression for Y_n to help our proof as follows

$$\begin{aligned} Y_n &= \frac{1}{\sqrt{M}} \sum_{m=0}^{M-1} X_m \mathrm{e}^{-\mathrm{j}\frac{2\pi}{M}\frac{KM-1}{2}m} \mathrm{e}^{\mathrm{j}\frac{2\pi}{M}mn} \\ &= \frac{1}{\sqrt{M}} \sum_{m=0}^{M-1} X_m \mathrm{e}^{-\mathrm{j}\pi Km} \mathrm{e}^{\mathrm{j}\frac{2\pi}{M}m(n+\frac{1}{2})}. \end{aligned} \tag{2.40}$$

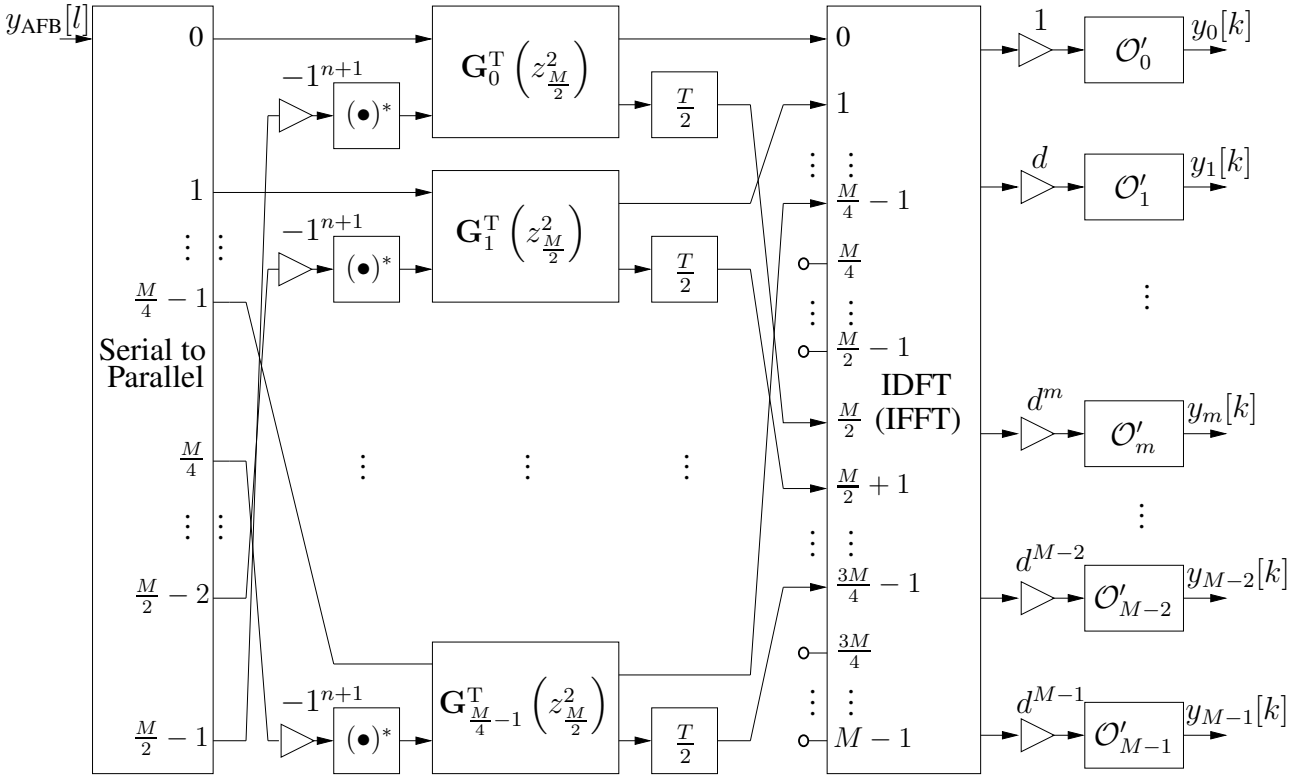

Fig. 2.35. New efficient AFB implementation based on the polyphase decomposition of **type 1** organized as orthogonal 2×2 transfer functions

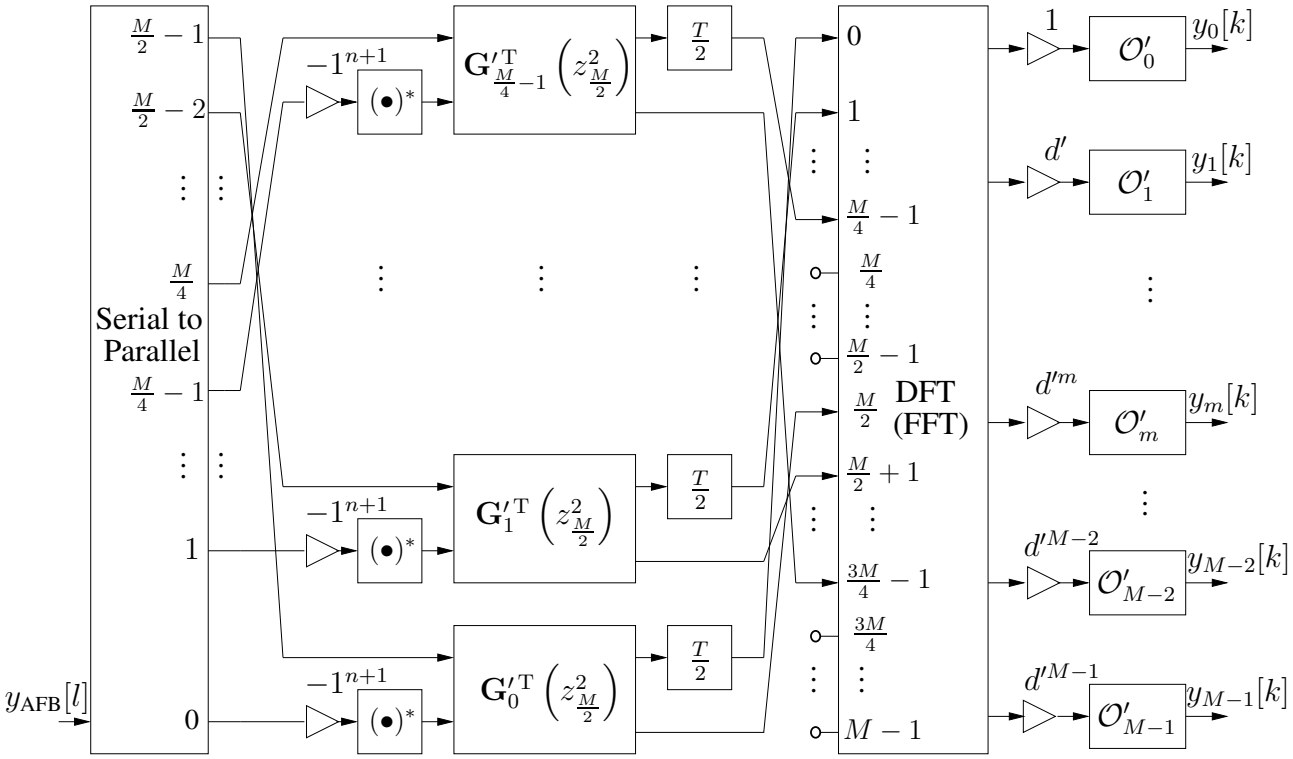

Fig. 2.36. New efficient AFB implementation based on the polyphase decomposition of **type 2** organized as orthogonal 2×2 transfer functions

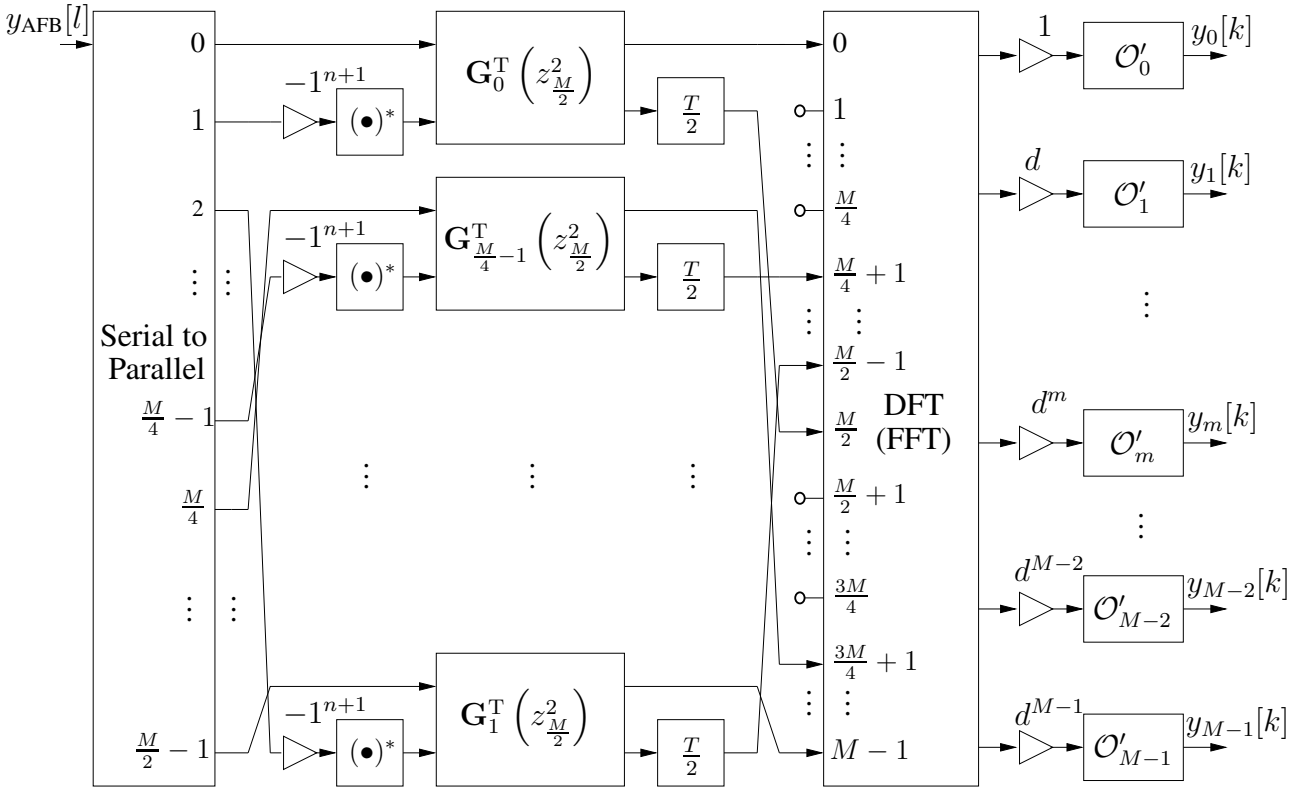

Fig. 2.37. New efficient AFB implementation based on the polyphase decomposition of **type 3** organized as orthogonal 2×2 transfer functions

Then we take the complex conjugate of (2.40) and further develop the expression as follows

$$\begin{aligned} Y_n^* &= \frac{1}{\sqrt{M}} \sum_{m=0}^{M-1} X_m^* \mathrm{e}^{\mathrm{j}\pi K m} \mathrm{e}^{-\mathrm{j}\frac{2\pi}{M} m(n+\frac{1}{2})} \\ &= \frac{1}{\sqrt{M}} \sum_{\ell=0}^{\frac{M}{2}-1} \left(X_{2\ell}^* \mathrm{e}^{\mathrm{j}2\pi K \ell} \mathrm{e}^{-\mathrm{j}\frac{2\pi}{M} 2\ell(n+\frac{1}{2})} + X_{2\ell+1}^* \mathrm{e}^{\mathrm{j}\pi K(2\ell+1)} \mathrm{e}^{-\mathrm{j}\frac{2\pi}{M}(2\ell+1)(n+\frac{1}{2})} \right) \\ &= \frac{1}{\sqrt{M}} \sum_{\ell=0}^{\frac{M}{2}-1} \left(X_{2\ell}^* + X_{2\ell+1}^* \mathrm{e}^{\mathrm{j}\pi K} \mathrm{e}^{-\mathrm{j}\frac{2\pi}{M}(n+\frac{1}{2})} \right) \mathrm{e}^{-\mathrm{j}\frac{4\pi}{M}\ell(n+\frac{1}{2})}, \end{aligned} \tag{2.41}$$

where we decomposed the expression into the even and odd input contributions, and used $\mathrm{e}^{\mathrm{j}2\pi K\ell} = 1$. Now, we use (2.40) to derive an expression for $Y_{\frac{M}{2}-n-1}$ as follows

$$\begin{aligned} Y_{\frac{M}{2}-n-1} &= \frac{1}{\sqrt{M}} \sum_{m=0}^{M-1} X_m \mathrm{e}^{-\mathrm{j}\pi K m} \mathrm{e}^{\mathrm{j}\frac{2\pi}{M} m(\frac{M}{2}-n-1+\frac{1}{2})} \\ &= \frac{1}{\sqrt{M}} \sum_{m=0}^{M-1} X_m \mathrm{e}^{\mathrm{j}\pi K m} \mathrm{e}^{\mathrm{j}\pi m} \mathrm{e}^{-\mathrm{j}\frac{2\pi}{M} m(n+\frac{1}{2})}, \quad \text{because} \quad \mathrm{e}^{-\mathrm{j}\pi K m} = \mathrm{e}^{\mathrm{j}\pi K m} \\ &= \frac{1}{\sqrt{M}} \sum_{\ell=0}^{\frac{M}{2}-1} \left(X_{2\ell} - X_{2\ell+1} \mathrm{e}^{\mathrm{j}\pi K} \mathrm{e}^{-\mathrm{j}\frac{2\pi}{M}(n+\frac{1}{2})} \right) \mathrm{e}^{-\mathrm{j}\frac{4\pi}{M}\ell(n+\frac{1}{2})} \end{aligned} \tag{2.42}$$

Finally, we can see that if $X_{2\ell}$ is purely real and $X_{2\ell+1}$ is purely imaginary, then (2.42) is equal to (2.41), i.e. $Y_{\frac{M}{2}-n-1} = Y_n^*$, and if on the contrary $X_{2\ell}$ is purely imaginary and $X_{2\ell+1}$ is purely real, then (2.42) is equal to minus (2.41), i.e. $Y_{\frac{M}{2}-n-1} = -Y_n^*$.

Because the AFB is the transposed of the SFB, the corresponding identities exist in reversed order and the corresponding solutions can be seen in the structures proposed.

As we mentioned before, structures with similar complexity to the efficient lattice were developed for CMFBs and SMFBs and received the name fast extended lapped transforms [50]. They were originally not derived as an extension of the polyphase decomposition of the prototype, but it is worth mention that they can be derived in similar way as shown here. In [73] the authors propose an efficient structure for exponentially MFBs that is based on a combination of CMFBs and SMFBs, then they just assume that those can be implemented as a fast lapped transform. In the case of exponentially MFBs combined with OQAM staggering, to the best of our knowledge, there is no equivalent structures, specially for those based on the DFT/IDFT.

2.4.2 Frequency Spread/Fast Convolution based Structures

In Section 2.2.3.2 we have presented an efficient structure to combine interpolation and modulation based on frequency domain filtering and the so-called fast convolution methods OA and OS. An SFB can be also efficiently realized using the same structures and by taking advantage of commonalities between different subchannels. If we take, for example, the structure in Fig. 2.8, it can be observed that the frequency multiplexing of the different subchannels can be performed before the IFFT of size N_{FFT} by adding the frequency bins of each subchannel. As already mentioned, most of the filter coefficients in frequency domain will have very low magnitude - or even zero magnitude - allowing to have much less multiplications per subchannel than the general structure shown in Fig. 2.8. The protoype filter can be either designed to have zero magnitude in some frequency bins or have its stop-band behavior modified by forcing to zero the frequency bins in this region on implementation phase. Fig. 2.38 shows a pictorial representation of two subchannel filters, which could correspond to subcarriers $m-1$ and m. Both continuous and sampled frequency representation are depicted for each of the subchannel filters. For the prototype filter represented, seven frequency bins have magnitude different from zero and the rest is equal to zero.

One particular structure that became very popular recently is the commonly called Frequency Spread-FBMC implementation. This structure was introduced in [15, 16] based on the original work of [52] and it was inspired by the original frequency sampling filter design from Martin-Bellanger [13, 52]. The FS-FBMC structure can be derived by implementing interpolation and modulation as shown in Fig. 2.11. In this case the OA method is chosen for the SFB and it uses $N_{\text{new}} = 1$, such that, for a prototype of length $L_{\text{p}} = KM$, we have $N_{\text{FFT}} = KM$. But now, in the SFB the small FFT before the upsampling in the frequency domain has size $2K$ because the upsampling factor is now $M/2$, due to the combination with OQAM. Only one element of the FFT input signal block is different from zero and only the first column of the DFT matrix needs to be implemented. The DFT can then substituted by a repetition of $2K$ times the input different from zero. We then just add the bins of the different subchannels after multiplying each of them by the corresponding frequency domain filter coefficient. Because each subchannel typically overlapps only with the adjacent ones, each frequency bin is only added to one frequency bin, i.e. simple two element adders are necessary. Finally, the IFFT of size $N_{\text{FFT}} = KM$ is applied and a block overlapping is performed, where the last $(K-1/2)M$ samples of each block are added to the first $(K-1/2)M$ samples of the subsequent block and the blocks are serialized. In Fig. 2.39 a

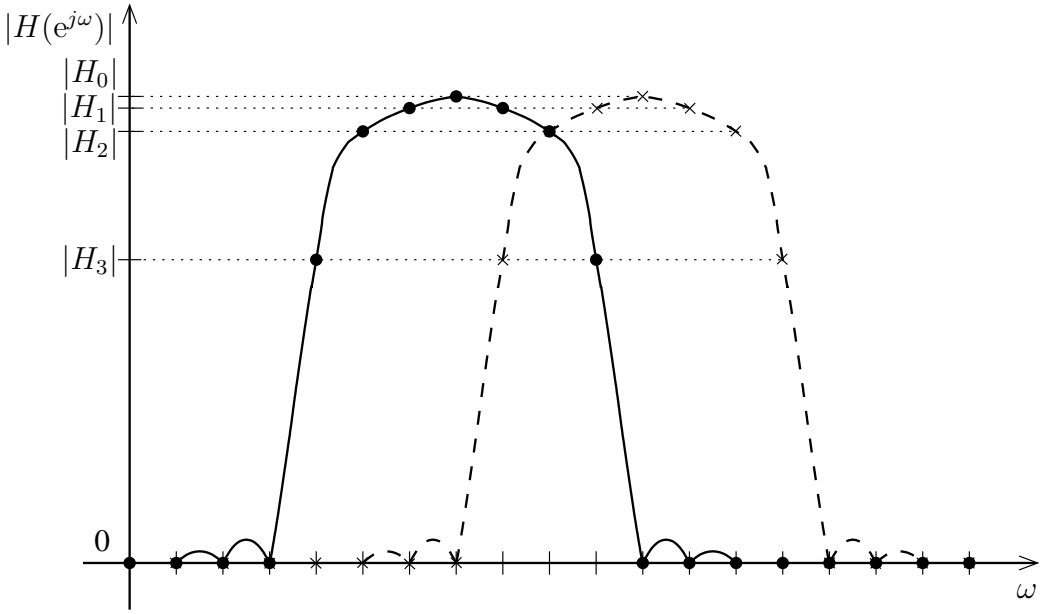

Fig. 2.38. Two subchannel filters in continuous and frequency sampled representation.

representation of the SFB using the FS-FBMC structure is shown. We have assumed here that only $2K-1$ frequency domain filter coefficients are different from zero, that the prototype has a symmetric frequency response and that $H_0 = 1$. Moreover, the frequency domain filtering and combination of different subcarriers can be described by the matrix $\mathbf{H} = [\mathbf{h}_0 \cdots \mathbf{h}_{M-1}] \in \mathbb{C}^{KM \times M}$, where the $\mathbf{h}_m$ are defined as in (2.14).

In the case of the AFB based on the FS-FBMC structure, the OS method is employed as shown in Fig. 2.12. The resulting AFB structure is a transposed of the SFB and is shown in Fig. 2.40, where the input signal is segmented into overlapping blocks of size KM, where the first $(K - 1/2)M$ samples of a new block are a repetition of the last $(K-1/2)M$ samples of the previous block. An FFT of size $N_{\text{FFT}} = KM$ is applied to the blocks and after it, the frequency bins are multiplied by the corresponding frequency domain filter coefficient. The frequency bins are then combined, phase corrected and OQAM de-staggered. It is worth noting, that in the AFB case, the small IDFT of size $2K$ is reduced to a sum of the different frequency bins. In Fig. 2.40 we have also assumed that $2K-1$ frequency domain coefficients are different from zero.

The FS-FBMC structure is a special case for the more general FB structure based on fast convolution algorithms OA and OS. It is important also to see the differences and later compare the complexity between different cases of FC based FBs. Based on the combined modulation with interpolation and decimation structures shown in Figs. 2.7, 2.8, 2.9 and 2.10, we can also derive the general SFB and AFB structures or just take some specific examples. We will assume here the case where $N_{\text{new}} = 3KM$, i.e. an overlapping factor of 25%. In this case we assume a prototype length of $L_{\text{p}} = KM + 1$ and an FFT of size $N_{\text{FFT}} = 4KM$. In Fig.2.41, we show the resulting SFB structure based on the OS method. For each of the M subcarriers, we first need to collect the OQAM symbols in overlapping blocks of length $8K$, where the first $2K$ symbols of each block are a repetition of the last $2K$ symbols of the previous block, and it is necessary to employ one FFT of size $8K$. Then the frequency bins are multiplied by the corresponding frequency domain filter coefficients and the frequency bins of different subcarriers are added, represented here by the matrix $\mathbf{H}_{\text{A}}$. Again here the adders have only two inputs. Then the IFFT of size $N_{\text{FFT}} = 4KM$ is

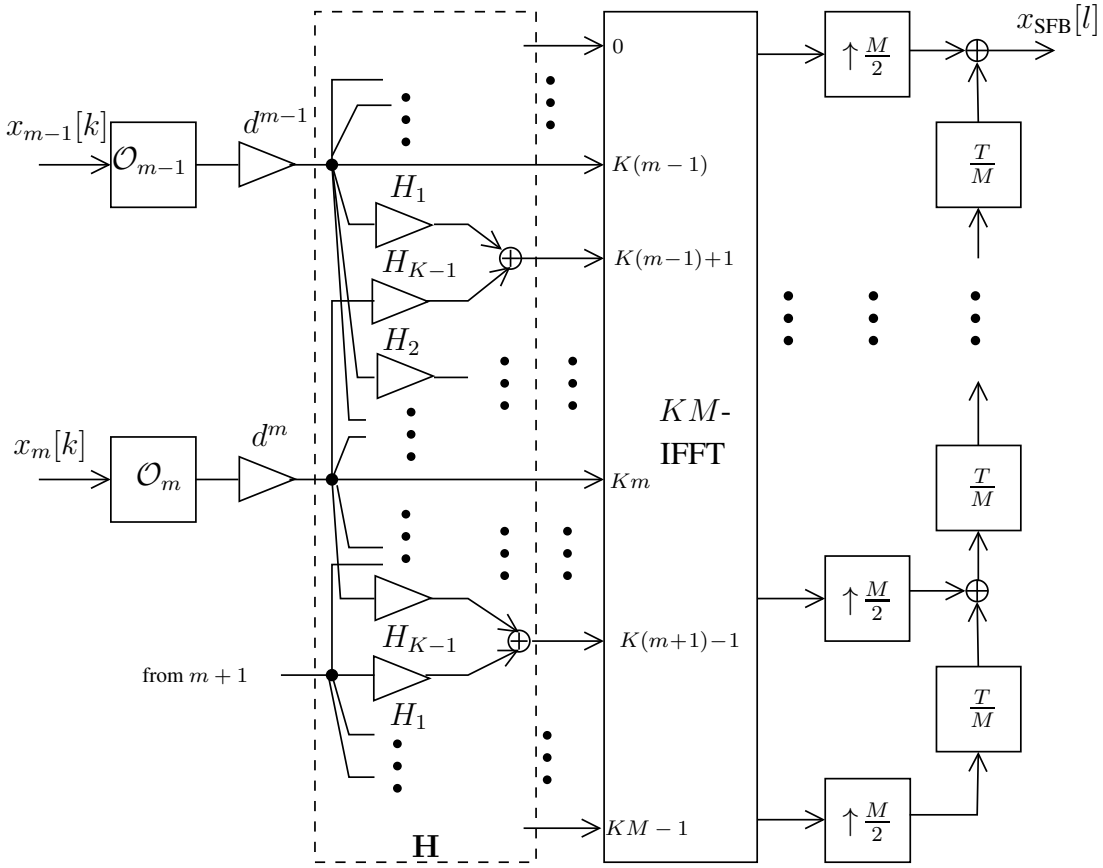

Fig. 2.39. Frequency domain SFB realization for $N_{\text{new}} = 1$, aka FS-FBMC

applied to combine the signals of all subcarriers and only $3KM$ samples of the output block are serialized, i.e. KM or $1/4$ of the output samples do not need to be calculated. It is worth noting, that we assume here that a maximum of $8K$ frequency domain filter coefficients are different from zero. Moreover, the frequency domain filtering and combination of different subcarriers can be described by the matrix $\mathbf{H}_{\text{A}} \in \mathbb{C}^{4KM \times 8KM}$.

The corresponding SFB structure based on the OA algorithm from Fig. 2.8 is similar to Fig. 2.41, but with the difference that the input OQAM symbols are just taken in blocks of size $6K$ in a simple serial-to-parallel operation, with the remaining $2K$ FFT inputs set to zero, as in Fig. 2.8, and the blocks at the output of the IFFT overlap have KM samples that overlap.

In Fig. 2.42 we have depicted the corresponding AFB structure based on the OA algorithm from Fig. 2.10. The input signal is segmented in blocks of length $3KM$, which are zero padded and transformed with the FFT of size $N_{\text{FFT}} = 4KM$. Then the frequency bins are multiplied by the frequency domain filter coefficients for each subchannel, represented here by the matrix $\mathbf{H}_{\text{A}}^T$. Then the IFFT of size $8K$ is applied and the blocks are overlapped by $2K$ samples and added to finally be serialized.

Now one can straightforwardly derive similar structures to the Figs. 2.41 and 2.42 for the case where $N_{\text{new}} = KM$ and an overlap of 50% is desired. In this case $N_{\text{FFT}} = 2KM$ and the prototype filter can be assumed again to have length $L_{\text{p}} = KM + 1$. For the SFB, the downsampling factors before the small FFT of size $4K$ are then $2K$ and the upsampling factor after the large IFFT are KM. For the AFB, the downsampling factor before the large FFT are KM and the upsampling factors after the small FFT of size $4K$ are $2K$.

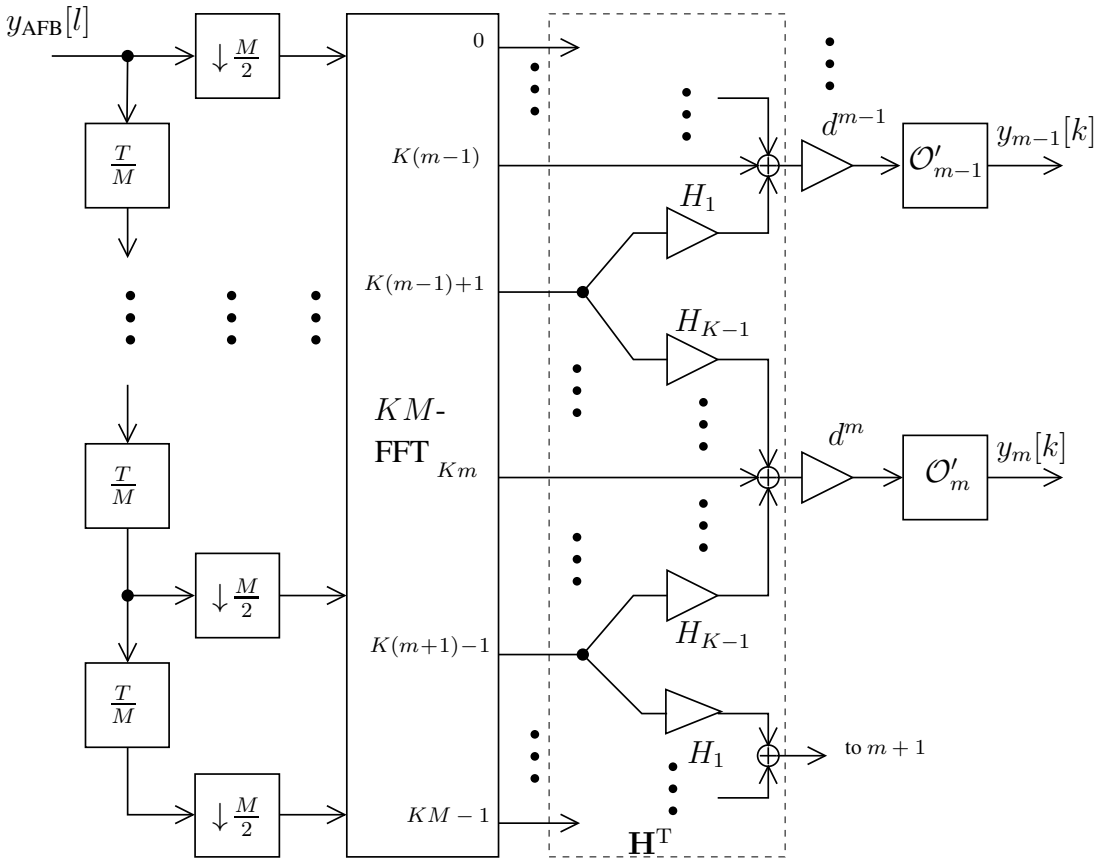

Fig. 2.40. Frequency domain AFB realization for $N_{\text{new}} = 1$, aka FS-FBMC

The implementation based on frequency domain filtering presents some advantages compared to the one based on the polyphase decompositions. First, some of the existing algorithms for channel estimation, channel equalization and MIMO processing utilized in CP-OFDM in a subcarrier symbol level can be reused here in the individual frequency bins instead. Second, the main building block is the FFT, which has many available and efficient implementations in ASICS, ASIPS and DSPs. Finaly, in exeptional cases, different filters may be employed in different subcarriers, for example, if subcarriers have different bandwidth or different overlap behavior is desired.

2.4.3 OQAM De-staggering Combined with Linear Equalizer

In some applications of exponentially modulated, for example, wired and wireless communications, an additional filter, an equalizer or a precoder, has to be included before the OQAM de-staggering for each subchannel in the AFB or after the staggering in the SFB. One good example is the channel equalization in multicarrier modulation schemes [33, 77], where one multitap filter is included before the OQAM demapping for each subcarrier in the AFB in order to compensate for the frequency selectivity of the channel. In Fig. 2.43 we have a new definition for the block $\mathcal{O}'_m$ in the odd subcarrier m that already includes the FIR equalizer. An equivalent scheme can be drawn for the even subchannels and a corresponding one for the SFB. We will concentrate here on the structure for odd m and only for the AFB.

In addition to the new polyphase network for AFB and SFB structures, we also can improve the subchannel processing, by making use of the real and imaginary staggering. Since there are

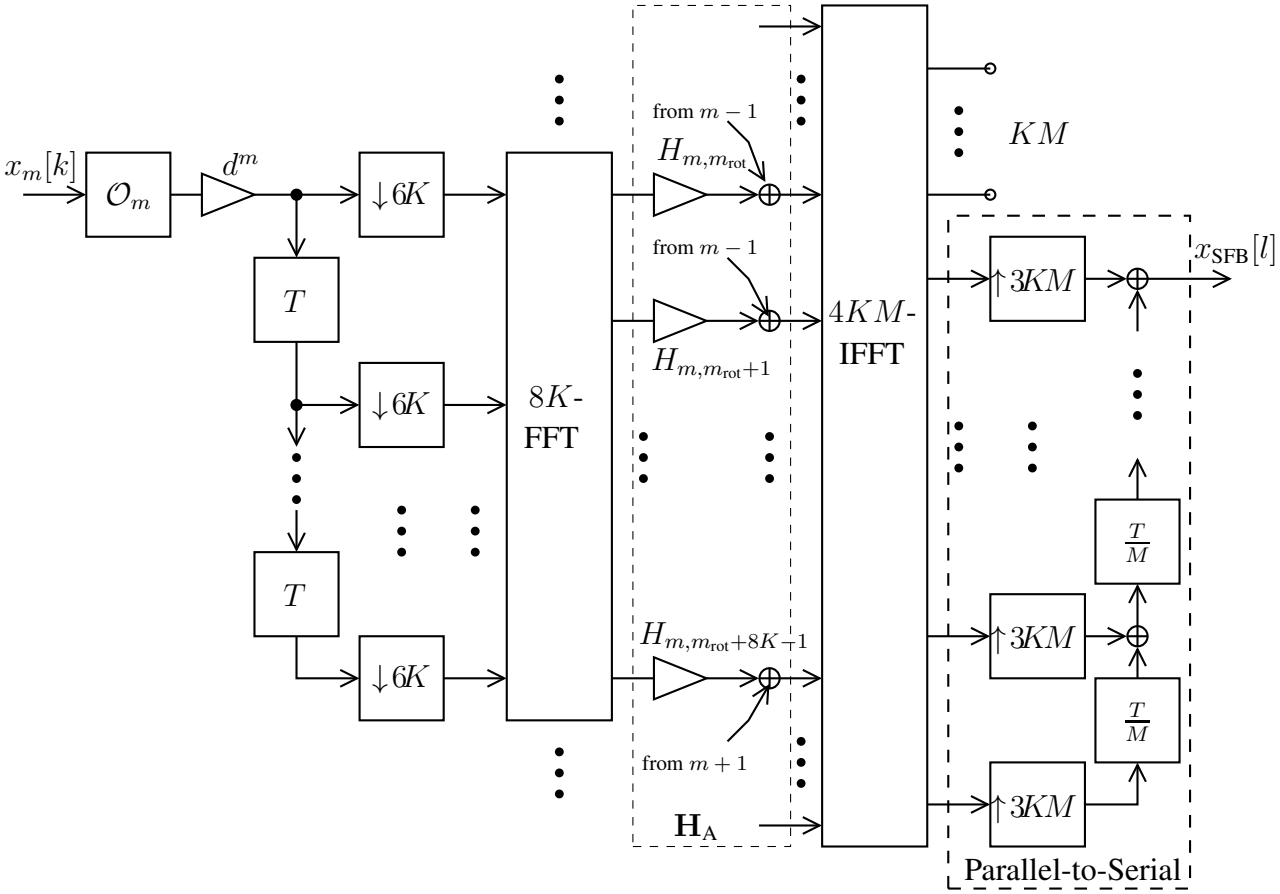

Fig. 2.41. Frequency domain SFB realization based on OS algorithm for $N_{\text{new}} = 3KM$ (25 % overlap).

operations involving real and imaginary part removal and downsampling, we can make use of some multirate processing identities to reduce the complexity [26, 28, 71].

If the subchannel filter is a single complex coefficient w_m, it can be jointly implemented with the OQAM de-staggering with the structure shown in Fig. 2.44, where $w_m = w_m^{(\text{R})} + jw_m^{(\text{I})}$. It is worth noting that the multipliers ds in the AFB structures shown before can always be incorporated into the subchannel equalizer.

However, the subchannel equalizers will be multitap in general, so we can decompose the into their polyphase components also. For each subchannel m we decompose the equalizer in two components as follows

$$W_m\left(z_{\frac{M}{2}}\right) = V_{0,m}\left(z_{\frac{M}{2}}^2\right) + V_{1,m}\left(z_{\frac{M}{2}}^2\right) z_{\frac{M}{2}}^{-1} \tag{2.43}$$

with $V_{0,m}(z_M) = V_{0,m}^{(\text{R})}(z_M) + jV_{0,m}^{(\text{I})}(z_M)$, where $V_{0,m}^{(\text{R})}(z_M)$ and $V_{0,m}^{(\text{I})}(z_M)$ contain the real and imaginary parts of the coefficients of $V_{0,m}(z_M)$.

Now we are able to jointly realize the subchannel equalizers and the OQAM de-staggering as shown in Fig. 2.45 This new proposed subchannel filtering structure reduces to the half the number of multiplications per output sample.

As mentioned before it is trivial to show the corresponding structures for even m and for precoders in the SFB.

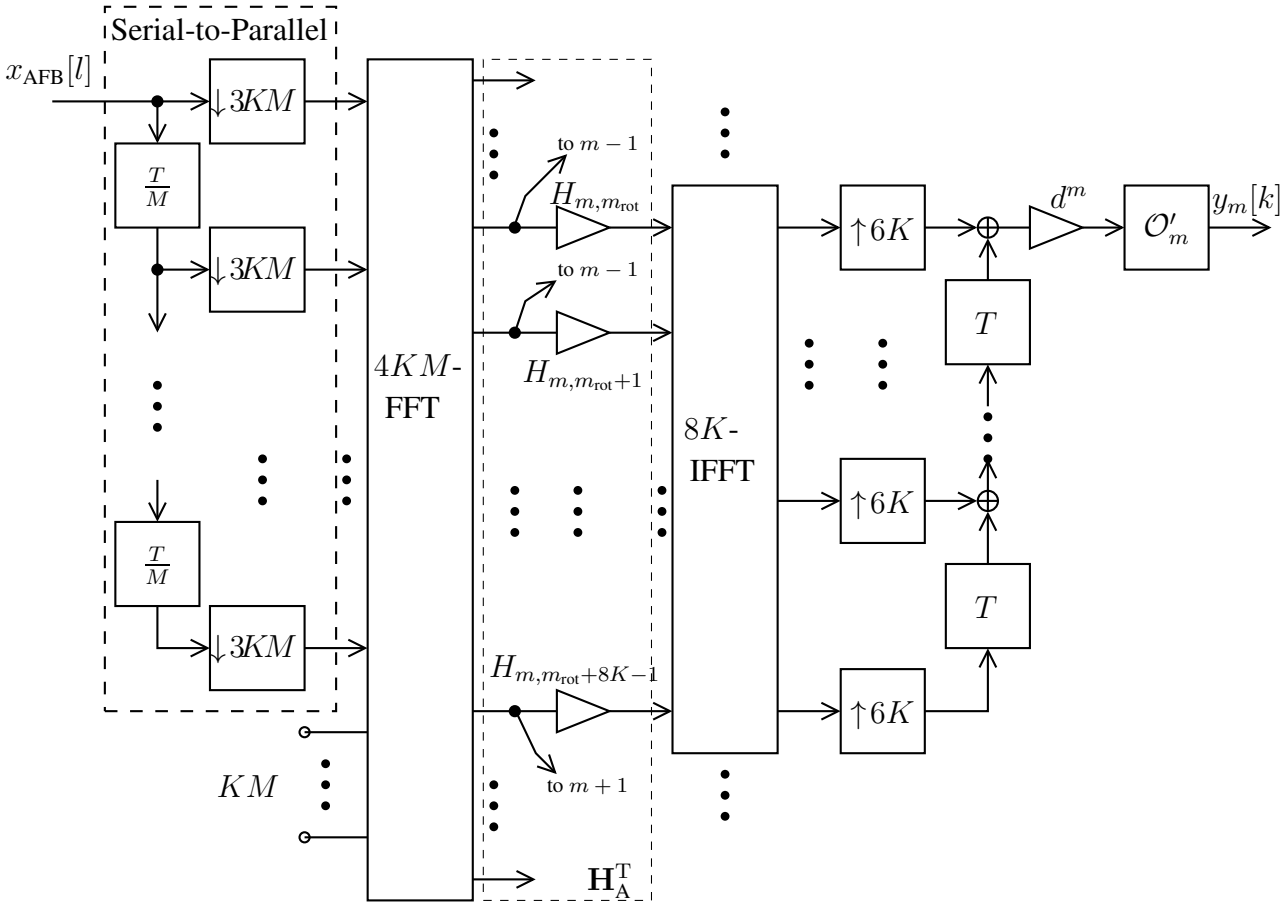

Fig. 2.42. Frequency domain AFB realization based on OA algorithm for $N_{\text{new}} = 3KM$ (25 % overlap).

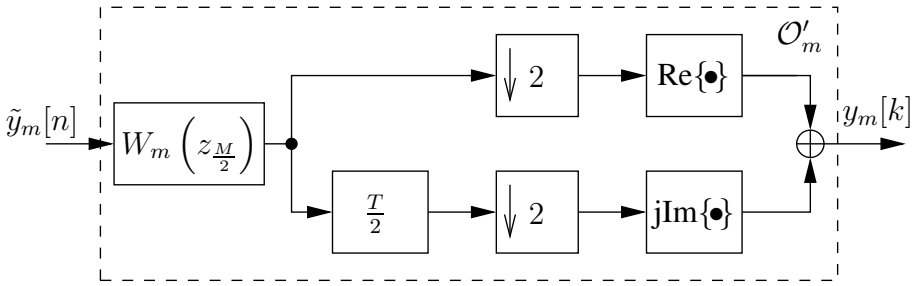

Fig. 2.43. Equalizer followed by OQAM-Destaggering for odd m

2.4.4 Complexity Analysis and Comparison

Complexity analysis of the different structures and comparison for different parametrization. (Also compare the complexity by considering quantization of the prototype filter coefficients.)

We will analyse the complexity in terms of number of real multiplications and additions to be executed during one OQAM period of $T/2$ in the steady state, where $1/T$ is the complex QAM symbol rate. Moreover, we assume that each multiplication between two complex numbers corresponds to four real-valued multiplications and two real valued additions. Each complex valued addition corresponds to two real valued additions. We further assume that the multicarrier mod-

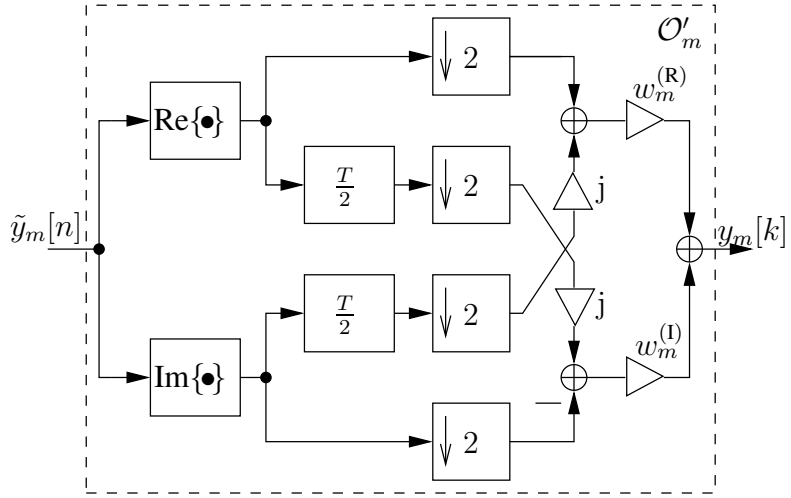

Fig. 2.44. Single tap equalizer jointly realized with OQAM De-staggering for odd m

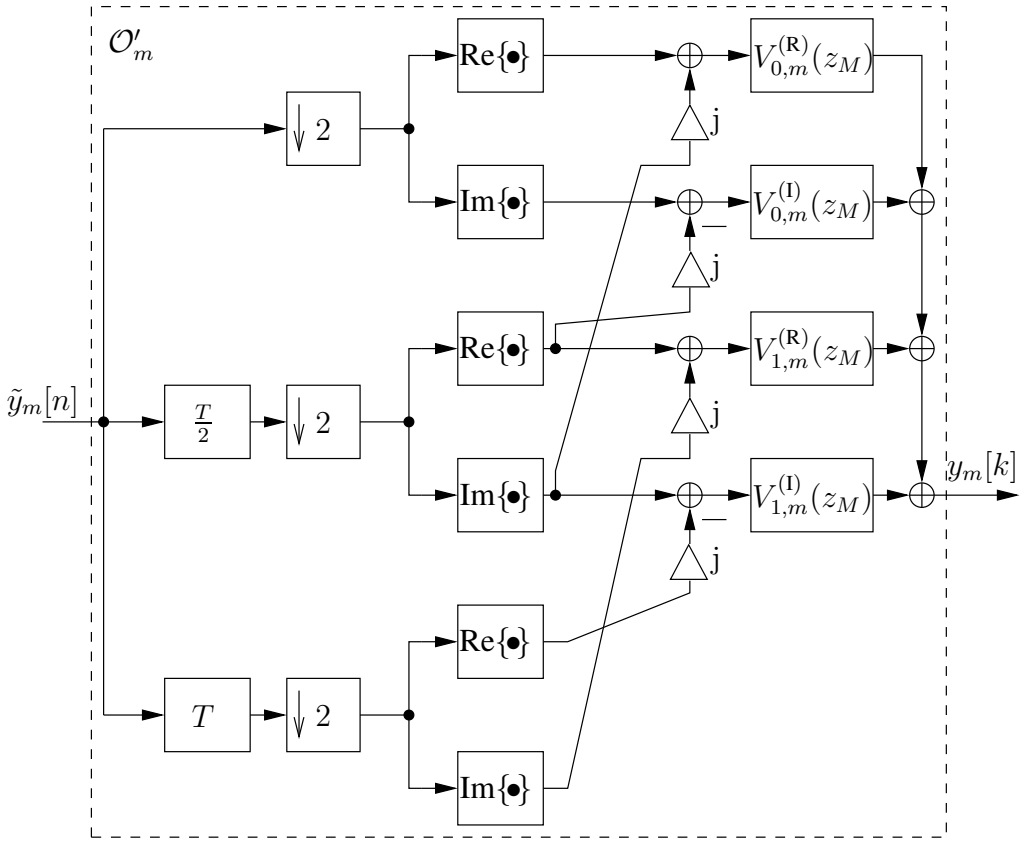

Fig. 2.45. Multitap equalizer jointly realized with OQAM De-staggering for odd m

ulation is the only baseband signal processing at the transmit side or, in other words, there is no channel dependent transmit processing, e.g. linear precoders.

The total number of real multiplications and additions for an M-point (I)DFT using an FFT Split-Radix algorithm are given by

$$\mathcal{C}_{\mathrm{FFT}}(M) = M(\log_2(M) - 3) + 4 \quad \text{and} \tag{2.44}$$
$$\mathcal{A}_{\mathrm{FFT}}(M) = 3M(\log_2(M) - 1) + 4, \tag{2.45}$$

respectively. In realizations of the FFT where many of its inputs or outputs are equal to zero or not further utilized, a so-called pruned FFT can be utilized. By comparing the different structures presented in this chapter, a pruned FFT may be utilized, for example, if a small number of the subcarriers are occupied. This typically occurs when multiple mobile stations are allocated a small amount of frequency resources at the same time. Either receiver or transmitter of the mobile station could then reduce the complexity of the FFT to reduce the energy consumption. The total number of real multiplications and additions for an M-point pruned FFT with L zero-valued inputs or non-utilized outputs are given by

$$\mathcal{C}_{\mathrm{FFT}}(M) = M(\log_2(L) - 3) + 4 \quad \text{and} \tag{2.46}$$
$$\mathcal{A}_{\mathrm{FFT}}(M) = 3M(\log_2(L) - 1) + 4. \tag{2.47}$$

Our benchmark is a conventional CP-OFDM MC system with a CP length L_{CP} and a CP-length ratio relative to the block length of $R_{\mathrm{CP}} = L_{\mathrm{CP}}/M$. At the transmitter side of a CP-OFDM system, the total number of real operations depends only from $\mathcal{C}_{\mathrm{FFT}}$ and $\mathcal{A}_{\mathrm{FFT}}$.

$$\mathcal{C}_{\mathrm{OFDM,Tx}} = \frac{(1 + R_{\mathrm{CP}})\mathcal{C}_{\mathrm{FFT}}}{2} \tag{2.48}$$
$$\mathcal{A}_{\mathrm{OFDM,Tx}} = \frac{(1 + R_{\mathrm{CP}})\mathcal{A}_{\mathrm{FFT}}}{2}, \tag{2.49}$$

where the factor $(1 + R_{\mathrm{CP}})$ comes from the fact that for the period of one QAM symbol, the MC blocks has to be generated and the CP has to be attached. Because the CP depends on the same MC block it has to be attached to and this can only happen after all the MC modulation operations have been performed, the QAM symbol period in a CP-OFDM system is extended by a factor $(1 + R_{\mathrm{CP}})$ compared to OQAM FBMC systems that have no CP, or, if FBMC and CP-OFDM have the same symbol period, in CP-OFDM the MC modulation need to be processed faster by the same factor. The factor $1/2$ is necessary because our reference is half a symbol period $T/2$, but in CP-OFDM the operations are executed in the symbol period T. If we consider M_{f} subcarriers are occupied, the rest has zero or no data symbols, and a complex-valued single-tap channel equalizer per subcarrier is employed, the complexity at the receiver side is given by

$$\mathcal{C}_{\mathrm{OFDM,Rx}} = \frac{(1 + R_{\mathrm{CP}})(\mathcal{C}_{\mathrm{FFT}} + 4M_{\mathrm{f}})}{2} \tag{2.50}$$
$$\mathcal{A}_{\mathrm{OFDM,Rx}} = \frac{(1 + R_{\mathrm{CP}})(\mathcal{A}_{\mathrm{FFT}} + 2M_{\mathrm{f}})}{2}. \tag{2.51}$$

For the FBMC system, we have multiple options for the efficient structures as shown in the previous sub-sections. We will analyse here the complexity of the polyphase components based structure with the frequency domain filtering, including the FS-FBMC structure.

For the time-domain filtering, both SFB and AFB structures are composed by the filtering through polyphase components, by an FFT/IFFT, by the phase rotations and, at the receiver, by the

linear equalizers. We will consider first a comparison between the different possibilities to realize the polyphase components. We will then take the one with the lowest complexity to compare with the frequency domain filtering.

At the SFB we need M_{f} complex-valued multiplications for the phase rotations, $\mathcal{C}_{\mathrm{FFT}}(M)$ real-valued multiplications for the IFFT and $\mathcal{C}_{\mathrm{poly}}$ for the polyphase network, which we will explain further bellow. The number of real multiplications is then given by

$$\mathcal{C}_{\mathrm{PC-SFB}} = 4M_{\mathrm{f}} + \mathcal{C}_{\mathrm{FFT}}(M) + \mathcal{C}_{\mathrm{poly}}, \tag{2.52}$$

and the corresponding number of real-valued additions is

$$\mathcal{A}_{\mathrm{PC-SFB}} = 2M_{\mathrm{f}} + \mathcal{A}_{\mathrm{FFT}}(M) + \mathcal{A}_{\mathrm{poly}} \tag{2.53}$$

In the AFB we have the similar operations as in the SFB, but in the inverse order. Moreover, we consider the use of a multi-tap linear equalizer in each subcarrier and that the phase rotations can be incorporated into the equalizer. The total number of real-valued multiplications in the AFB is

$$\mathcal{C}_{\mathrm{PC-AFB}} = \mathcal{C}_{\mathrm{poly}} + \mathcal{C}_{\mathrm{FFT}}(M) + 2L_{\mathrm{eq}}M_{\mathrm{f}}, \tag{2.54}$$

where L_{eq} is the length of the equalizer. We have assumed here the realization of a multi-tap equalizer as in Fig. 2.45. The corresponding number of real-valued additions is

$$\mathcal{A}_{\mathrm{PC-AFB}} = \mathcal{A}_{\mathrm{poly}} + \mathcal{A}_{\mathrm{FFT}}(M) + (2L_{\mathrm{eq}} - 1)M_{\mathrm{f}}, \tag{2.55}$$

In both SFB and AFB structures based on polyphase components we have first the well known structure shown, for example, in Fig. 2.23, where the M polyphase components can be realized individually using a direct form, or can be grouped into $M/2$ power complementary pairs and implemented as lattice or ladder (lifting steps) structures. In addition to that, to further reduce complexity, we can also realize SFB and AFB using the newer structures shown in Figs. 2.32, 2.33, 2.34, Figs. 2.35, 2.36 and 2.37, where the polyphase components are grouped into $M/4$ two-input two-output filters. We should further emphasize here that all polyphase components have real-valued coefficients that multiply complex valued signals. In this case each multiplier consists of two real-valued multiplications and each adder consists of two additions.

The total number of real-valued multiplications for the polyphase filtering step for the structure in Fig. 2.23 by considering the three different possibilities for the realization of the polyphase components pairs is given by:

- Direct form: $\mathcal{C}_{\mathrm{poly}} = 2KM$ and $\mathcal{A}_{\mathrm{poly}} = (2K-1)M$
- Low complexity lattice (Fig. 2.27): $\mathcal{C}_{\mathrm{poly}} = (2K+1)M$ and $\mathcal{A}_{\mathrm{poly}} = (2K-1)M$
- Ladder or lifting steps (Fig. 2.29): $\mathcal{C}_{\mathrm{poly}} = (3K-1)M$ and $\mathcal{A}_{\mathrm{poly}} = (3K-1)M$

For the SFB structures in Figs. 2.32, 2.33 and 2.34, and AFB structures in Figs. 2.35, 2.36 and 2.37, we can realize the polyphase components with the lattice and ladder (lifting steps), because for the direct form we would need to implement four transfer functions for each of the $M/4$ modules resulting in the same complexity as presented above. The resulting number of operations for this new polyphase network are the following:

- Low complexity lattice (Fig. 2.28): $\mathcal{C}_{\mathrm{poly}} = (K+1)M$, $\mathcal{A}_{\mathrm{poly}} = KM$
- Lifting steps (Fig. 2.29): $\mathcal{C}_{\mathrm{poly}} = 3KM/2$, $\mathcal{A}_{\mathrm{poly}} = 3KM/2$

Now we will analyse the complexity of the structures based on frequency domain filtering shown in Figs. 2.39, 2.40, 2.41 and 2.42. It is important to note that for frequency domain filtering the length of the prototype will not be directly expressed in the complexity, but rather how many non-zero frequency domain filter coefficients are implemented.

The M_{f} complex-valued multiplications for the phase rotations can be incorporated in the frequency domain filters in both SFB and AFB. We can further assume that the channel equalization in the AFB is also performed in the frequency domain and no further multiplication or addition is necessary, because the equalizer coefficients can also be pre-multiplied by the frequency domain filter coefficients and phase rotations.

The SFB of FS-FBMC contains $2K-1$ complex valued multiplications for each of the M_{f} subcarriers for the combined frequency domain coefficients and phase rotations. But because this operation is preceded by an OQAM staggering, those multipliers can be simplified in a similar way as shown in Fig. 2.44. The total number of real valued multiplications for the SFB of the FS-FMBC implementation is given by

$$\mathcal{C}_{\mathrm{FS-SFB}} = (4K-2)M_{\mathrm{f}} + \mathcal{C}_{\mathrm{FFT}}(KM), \tag{2.56}$$

and the corresponding total number of real-valued additions

$$\mathcal{A}_{\mathrm{FS-SFB}} = (3K-1)M_{\mathrm{f}} + \mathcal{A}_{\mathrm{FFT}}(KM) + (K-1/2)M \tag{2.57}$$

For the AFB of the FS-FBMC structure including the merge of frequency domain filtering, phase rotations and equalizers, and including the $(2K-1)$ complex valued additions to combine the frequency bins in each subcarrier, we get the following number of real-valued multiplications

$$\mathcal{C}_{\mathrm{FS-AFB}} = \mathcal{C}_{\mathrm{FFT}}(KM) + (4K-2)M_{\mathrm{f}}, \tag{2.58}$$

and number of real-valued additions

$$\mathcal{A}_{\mathrm{FS-AFB}} = \mathcal{A}_{\mathrm{FFT}}(KM) + (4K-2)M_{\mathrm{f}}. \tag{2.59}$$

In the case of the more general structure for Frequency Domain FBMC/OQAM (FD-FBMC), exemplified for the case $N_{\mathrm{new}} = 3KM$ in Figs. 2.41 and 2.42, we have to take into account the small and the large (I)FFTs, but also that both operate in a lower rate than the twice the symbol rate. In this case we will not combine the phase rotations with the frequency domain filtering, but we still assume that in the AFB the equalizers are implemented in the frequency domain and, as such, is combined with the filter coefficients. We also assume that the phase rotations can still be combined with the OQAM staggering and destaggering.

By assuming a small (I)FFT size of $2N_{\mathrm{FFT}}/M$, a large (I)FFT size of N_{FFT} and the OS based FD-FBMC SFB implementation has the following number of real-valued multiplications

$$\mathcal{C}_{\mathrm{FD-SFB}} = 2M_{\mathrm{f}} + \frac{M_{\mathrm{f}}\mathcal{C}_{\mathrm{FFT}}(2N_{\mathrm{FFT}}/M) + (8N_{\mathrm{FFT}}M_{\mathrm{f}}/M) + \mathcal{C}_{\mathrm{FFT}}(N_{\mathrm{FFT}})}{(2N_{\mathrm{new}}/M)}, \tag{2.60}$$

and the corresponding real-valued number of additions is as follows

$$\mathcal{A}_{\mathrm{FD-SFB}} = M_{\mathrm{f}} + \frac{M_{\mathrm{f}}\mathcal{A}_{\mathrm{FFT}}(2N_{\mathrm{FFT}}/M) + (16N_{\mathrm{FFT}}M_{\mathrm{f}}/M) + 2N_{\mathrm{FFT}} + \mathcal{A}_{\mathrm{FFT}}(N_{\mathrm{FFT}})}{(2N_{\mathrm{new}}/M)}, \tag{2.61}$$

where the factor $M/2N_{\text{new}}$ indicates that the operations are executed in a rate $2N_{\text{new}}/M$ times lower than $T/2$.

For the OA based FD-FBMC AFB implementation the number of real-valued multiplications is given by

$$\mathcal{C}_{\text{FD-AFB}} = \frac{M_{\text{f}}\mathcal{C}_{\text{FFT}}(2N_{\text{FFT}}/M) + (8N_{\text{FFT}}M_{\text{f}}/M) + \mathcal{C}_{\text{FFT}}(N_{\text{FFT}})}{2N_{\text{new}}/M} + 2M_{\text{f}}, \tag{2.62}$$

and the corresponding real-valued number of additions is as follows

$$\mathcal{A}_{\text{FD-AFB}} = \frac{M_{\text{f}}\mathcal{A}_{\text{FFT}}(2N_{\text{FFT}}/M) + (16N_{\text{FFT}}M_{\text{f}}/M) + \mathcal{A}_{\text{FFT}}(N_{\text{FFT}})}{2N_{\text{new}}/M} + M_{\text{f}}. \tag{2.63}$$

For example, for the SFB structure in Fig. 2.41, where $N_{\text{new}} = 3KM$ and $N_{\text{FFT}} = 4KM$, the number of real-valued multiplications is given by

$$\mathcal{C}_{\text{FD-SFB}} = 2M_{\text{f}} + \frac{M_{\text{f}}\mathcal{C}_{\text{FFT}}(8K) + (32KM_{\text{f}}) + \mathcal{C}_{\text{FFT}}(4KM)}{6K} \tag{2.64}$$

Now we will perform a numerical comparison of the different FBMC structures. For the numerical examples we will consider the SFB or AFB complexity as the total number of real operations per OQAM symbol, which is the sum of the number of real multiplications and real additions divided by M_{f}. We will also assume a pruned (I)FFT realization for the cases where many of their inputs or outputs are not utilized. We will consider the different structures presented previously in this chapter and vary the three main paramenters that have a stronger influence in the complexity, namely, K, M and M_{f}.

We will start comparing the different time-domain filtering structures, where the main difference between them is the structure employed to realize the polyphase components. We will consider only the complexity of the SFB in this first comparison, to emphasize the effect of the different polyphase components structures, i.e. the complexity of the equalizer is not considered, because it has the same complexity for all of them.

In Fig. 2.46 we show the number of real operations as a function of K, the length of polyphase components. We considered a total number of subcarriers of $M = 4096$, out of which $M_{\text{f}} = 3300$ are occupied, what corresponds to 80% of subcarrier occupation. We can observe that the complexity linearly increases with K, as verified by the complexity equations. For the applications in mobile communications, the lower values of K from 2 to 4 are of higher interest. In this range, there is no significant difference on the complexity of the various polyphase implementations. But the difference between the different structures increases with K.

Now we consider Fig. 2.47, where the total number of subcarriers M is varied between 128 and 8192, but the relation $M_{\text{f}}/M \approx 0.8$ is kept constant and $K = 4$. The corresponding values of M and M_{f} are shown in Table 2.1 The complexity linearly increases with $\log_2(M)$, but the relative number of operations between different polyphase components structures remain constant independent of M.

In Fig. 2.48 we have varied the number of occupied subcarriers M_{f} for constant $K = 4$ and $M = 4096$. The relative subcarrier occupation is varied between 8% and 80%, what corresponds to $M_{\text{f}} = 330, 660, ..., 3300$. We can observe that the complexity exponentially reduces and the relative complexity between the different polyphase components structures also reduces as M_{f} increases.

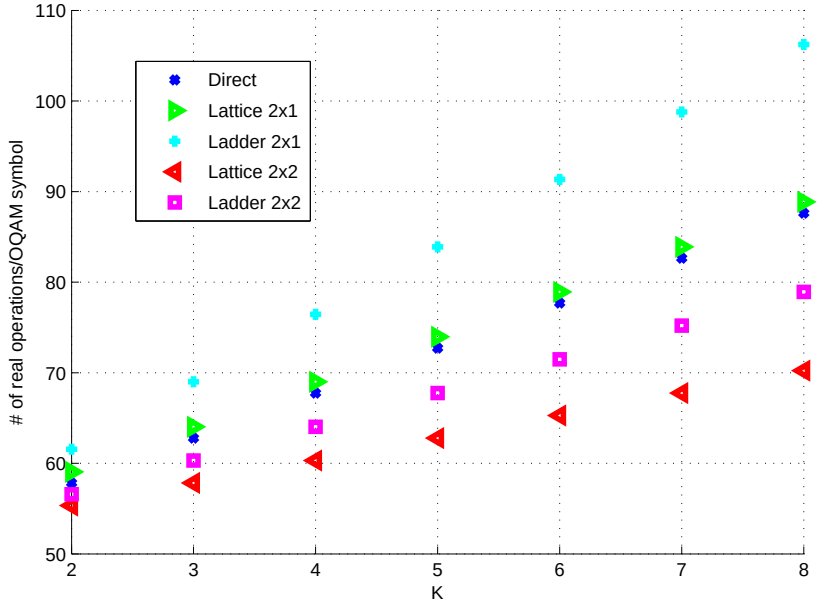

Fig. 2.46. Complexity of the SFB with different polyphase components realizations, $M = 4096$ and $M_f = 3300$.

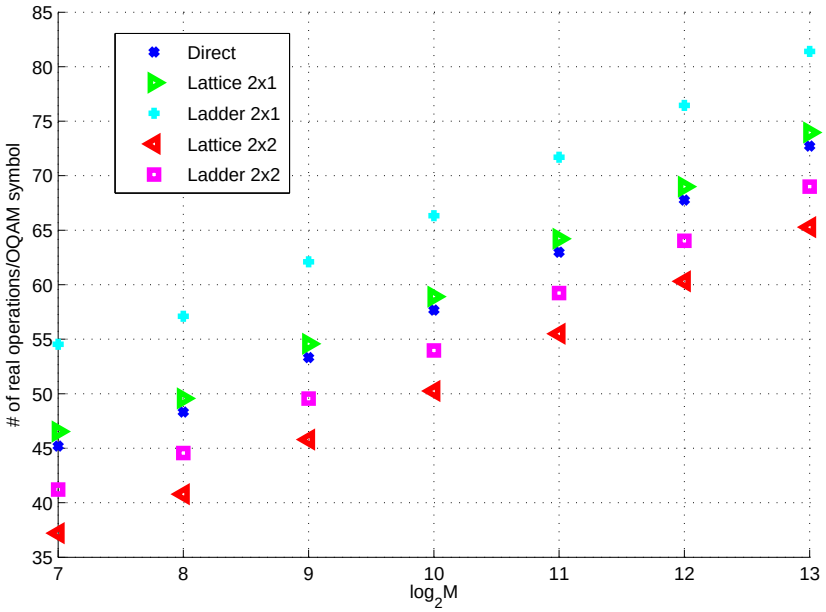

Fig. 2.47. Complexity of the SFB with different polyphase components realizations, $K = 4$ and $M_\mathrm{f}/M \approx 0.8$.

Table 2.1. Values employed in the numerical evaluation of Fig. 2.47

$\log_2(M)$	7	8	9	10	11	12	13
M	128	256	512	1024	2048	4096	8192
M_f	96	204	408	828	1644	3300	6600

As expected, in the numerical examples shown in Figs. 2.46, 2.47 and 2.48, the polyphase components implementations with two inputs and two outputs using ladder and lattice structures have the lowest complexity with a slightly advantage for the lattice based implementation.

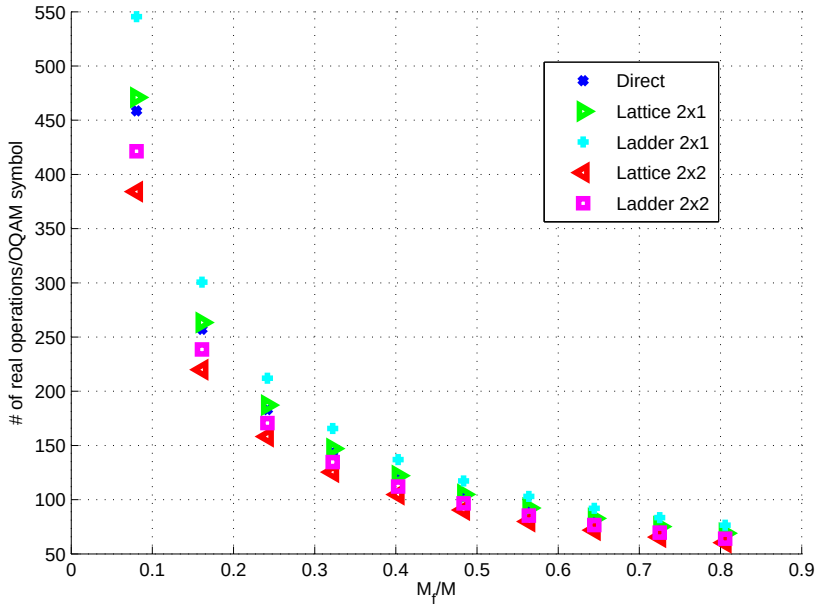

Fig. 2.48. Complexity of the SFB with different polyphase components realizations, $K = 4$ and $M = 4096$.

We continue the numerical complexity analysis by comparing the polyphase decomposition based structure with the frequency domain filtering based structures. For the polyphase decomposition based structure we will only consider the one with the lowest complexity, as concluded above, i.e. the 2 lattice. For the frequency domain filtering with consider the frequency spread approach, i.e. $N_{\text{new}} = 1$, and with the overlapping of 25% and 50%, i.e. $N_{\text{new}} = KM$ and $N_{\text{new}} = 3KM$. As a benchmark we have also considered the complexity of CP-OFDM with $R_{\text{CP}} = 1/8$, although it is worth noting that compared to the FBMC system a lower spectral efficiency is achieved due to the CP and to the poor spectral containment. We will show separate numerical results for the SFB and AFB, and for the latter, we assume an equalizer length $L_{\text{eq}} = 4$ for the FBMC with polyphase components based structure and that the equalizer is realized in frequency domain and merged with the filter coefficients for the frequency domain filtering structures. This last consideration is equivalent to have $2N/M$ frequency domain equalizer coefficients that can be designed and very efficiently implemented in frequency domain.

In Fig. 2.49 we show the numerical complexity results as a function of K for the SFB with $M = 4096$ and $M_f = 3300$. The smaller plot is a zoom at the region with low values of K, which are of more interest for wireless communications applications. We can observe that the complexity of all FBMC structures linearly increases with K and there is no significant difference between the lattice and the frequency domain - for 25% and 50% overlap - based structures. The lattice based structure has a slightly lower complexity, up to 15% less operations, than the frequency domain filtering structures. On the other hand the frequency spread approach - less than 1% overlap - possesses a significant higher complexity than all the other structures even for lower values of K. Although not shown in the plot, one can see by comparing the equations that only for $K = 1$, which is a special case, the frequency spread structure has a similar complexity to the the lattice based one. But still in this case the lattice based has a slightly lower complexity.

For the AFB, we have the complexity numerical results for the different FBMC structure in Fig. 2.50, where we can see a similar general relation between the different structures and also a similar individual behavior as a function of K.

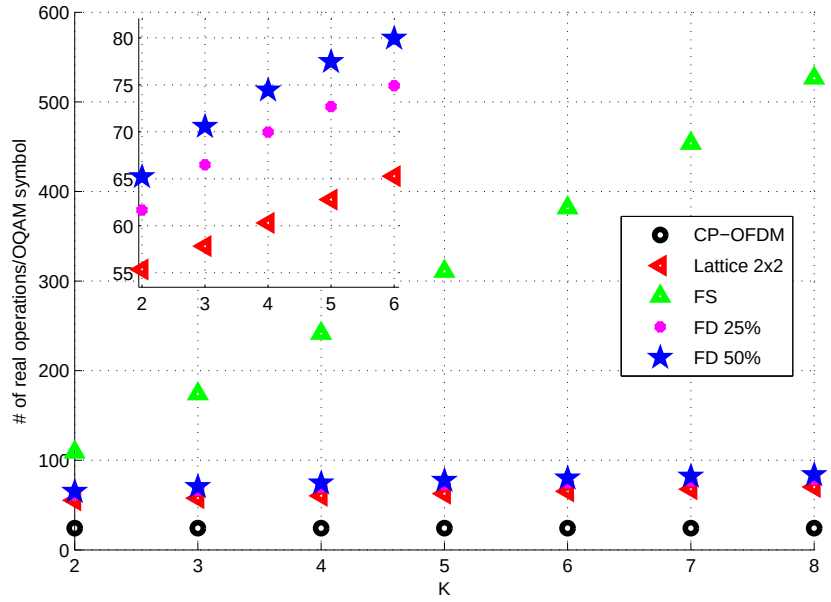

Fig. 2.49. Complexity of SFB for different FBMC structures and CP-OFDM Tx with $R_{\text{CP}} = 1/8$, $M = 4096$ and $M_f = 3300$.

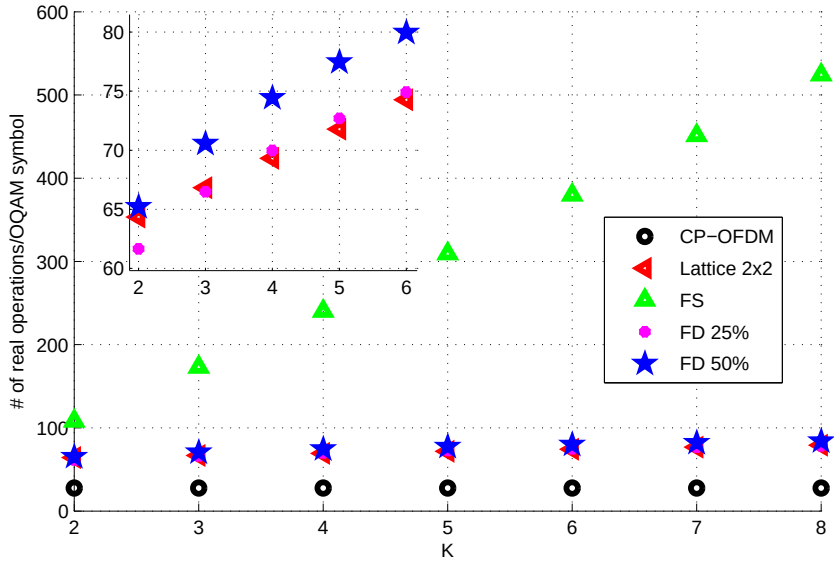

Fig. 2.50. Complexity of AFB for different FBMC structures and CP-OFDM Rx with $R_{\text{CP}} = 1/8$, $M = 4096$, $M_f = 3300$ and $L_{\text{eq}} = 4$.

In Fig. 2.51, we show the number of operations of the different structures as a function of $\log_2(M)$ for $K = 4$ and a constant relation $M_f/M \approx 0.8$ with the values shown in Table 2.1. We can observe a small advantage, from 7% up to 36% less operations, for the lattice based structure for smaller values of M, while the frequency spread approach has a significant higher complexity for all the values.

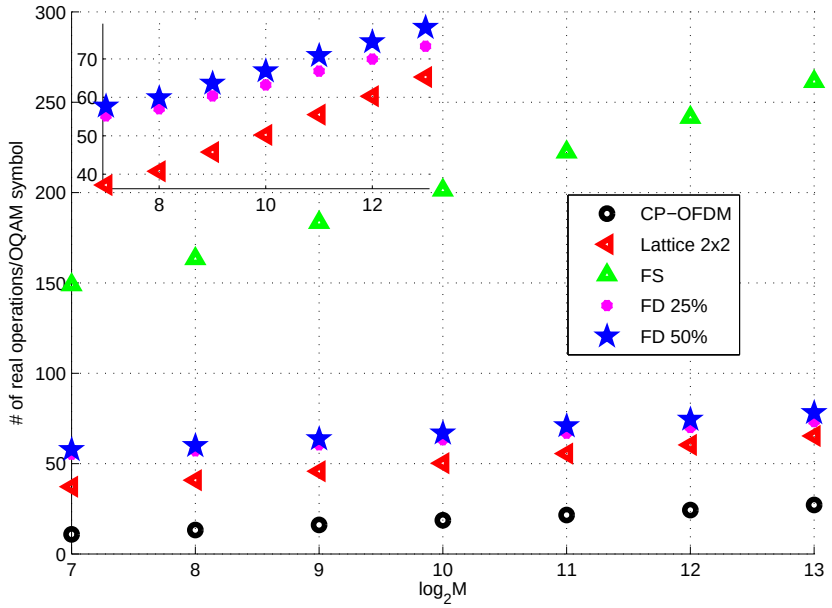

Fig. 2.51. Complexity of SFB for different FBMC structures and CP-OFDM Tx with $R_{\text{CP}} = 1/8$, $K = 4$ and $M_f/M \approx 0.8$.

A very similar behavior as the one observed for the SFB can be observed for the AFB in Fig. 2.52 for the complexity as a function of $\log_2(M)$, with the main difference that the small advantage of the lattice structure is slightly reduced, from 0% up to 34% less operations.

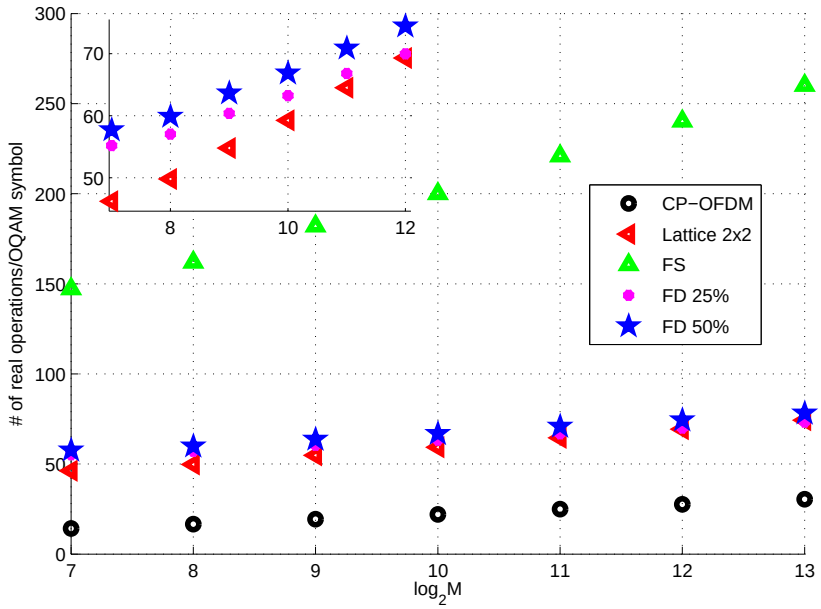

Fig. 2.52. Complexity of AFB for different FBMC structures and CP-OFDM Rx with $R_{\text{CP}} = 1/8$, $K = 4$, $M_f/M \approx 0.8$ and $L_{\text{eq}} = 4$.

In Fig. 2.53 we have the SFB complexity of the different structures as a function of M_{f}, for $K = 4$ and $M = 4096$, where again the values $M_{\text{f}} = 330, 660, ..., 3300$ were employed. We can

observe here again that the complexity exponentially reduces with the subcarrier occupation. Again the frequency spread structure is significantly higher than all the other structures. For very low subcarrier occupancy, there is no significant difference between the other FBMC structures, whereas for higher subcarrier occupancy we can see a small advantage for the lattice based structure.

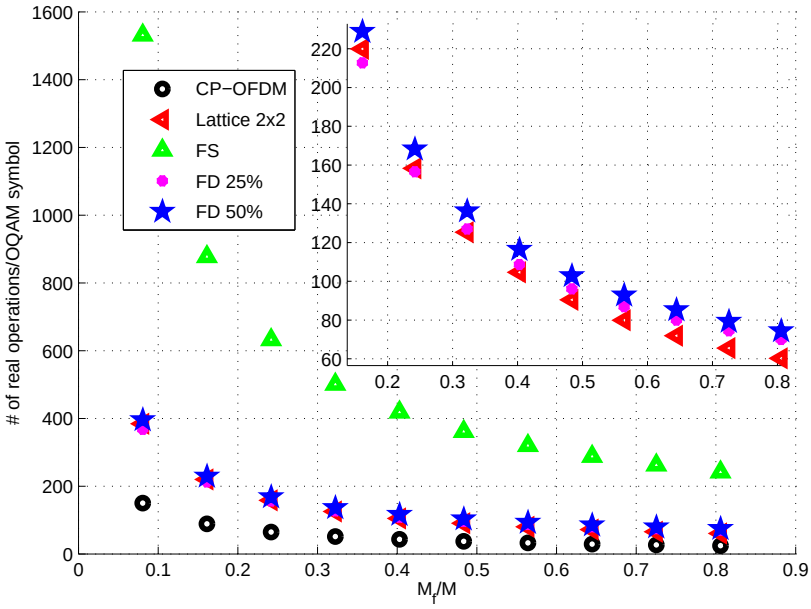

Fig. 2.53. Complexity of SFB for different FBMC structures and CP-OFDM Tx with $R_{\text{CP}} = 1/8$, $K = 4$ and $M = 4096$.

For the AFB complexity, we show in Fig. 2.54 a similar performance to the SFB shown before with the main difference that the lattice structure does not show any further advantage and, apart from the frequency sampling approach, all the other FBMC structures show similar complexity.

From the complexity analysis presented in this section we can conclude that FS is the least attractive option for the realization of FBMC systems, while other frequency domain filtering based structures have a much more competitive complexity compared to polyphase network based structures. We did not considered here a more detailed comparison with CP-OFDM, especially the more significant case when a different subcarrier bandwidth is employed in each system. More specifically, in FBMC we can take broader subcarriers to reduce latency and Peak-to-Average Power Ratio (PAPR), at the cost of higher equalizer complexity. In [8] we have shown a detailed comparison between the complexity of FBMC and CP-OFDM including turbo coding and decoding, and also different subcarrier bandwidth. The systems are assumed to have the same throughput.

2.5 Prototype Filter Designs

In this section we will give an overview of a few well known prototype design methods found in the multicarrier and filter banks literature. We will show how their design works, discuss their advantages and drawbacks depending on which structure is employed to realized the filter banks.

It is important to note that, in wireless communications, the prototype filter does not necessarily needs to fulfill the PR constraints, because noise, interference, quantization, synchronization errors, among other effects will already increase the noise floor and mask most of the imperfection of an NPR prototype filter. Nevertheless, some PR designs may be useful if specific structures

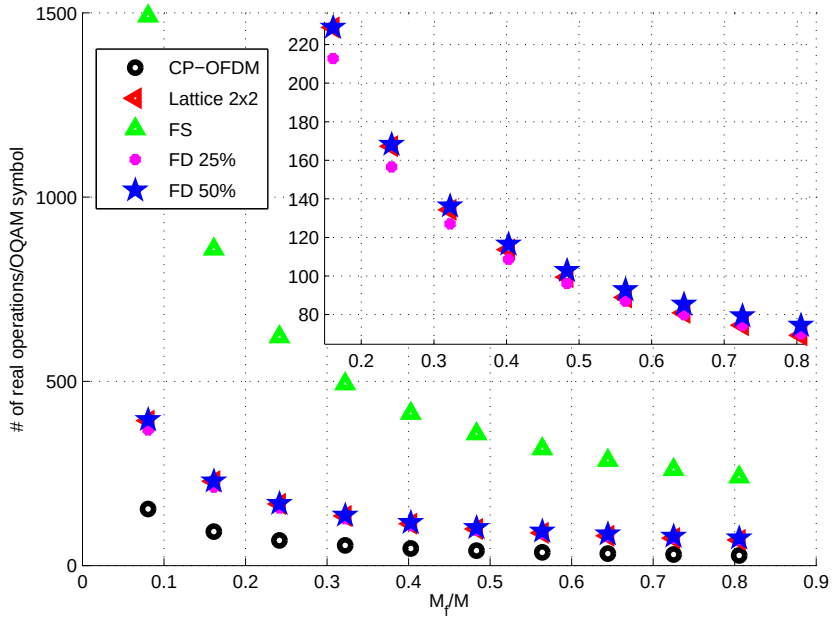

Fig. 2.54. Complexity of AFB for different FBMC structures and CP-OFDM Rx with $R_{\text{CP}} = 1/8$, $K = 4$, $M = 4096$ and $L_{\text{eq}} = 4$.

are envisioned, some examples are the polyphase structures based on lattice modules with their inherent advantages as described in the previous sections.

2.5.1 RRC Filter

The RRC Filter is one of the most known classical filter described in communications theory and has been employed in a number of practical systems [61]. Nevertheless, the RRC as a prototype filter for FBMC is frequently neglected in the literature, although it is one of the most straightforward solutions and simple to design.

The RRC, as its name states, is the square root of the frequency response of the Raised Cosine (RC) filter, which is a Nyquist filter, i.e. an ISI-free filter. An RC filter allows to limit the bandwidth of a signal composed by a sequence of symbols and, when properly designed, do not superpose subsequent symbols due to the time-domain zero crossings at the symbol period. By splitting the RC in two, we obtain two RRC filter which are employed in Tx and Rx. Because Rx filter is the matched filter of the transmitter filter, it maximizes the Signal-to-Noise Ratio (SNR) in the presence of noise.

In practice, the RC or RRC filters cannot be implemented in an exact way when a linear phase behavior is desired. In the case of digital implementations it is possible to design and implement both RC and RRC filters as IIR filters with exact amplitude behavior, but the phase of the individual filters will not be exact linear and ISI will occur. In the case of an FIR filter, as used in FBMC systems, an approximation of the RRC is obtained by truncating the impulse response.

When employed in FBMC, the RRC in SFB convolves with the RRC in the AFB resulting in an RC subcarrier transfer function. The bandwidth of the RRC is equal to the QAM symbol rate, i.e. equal to subcarrier spacing. Here we assume that given the total number of subcarriers M and the time-overlap factor K, the RRC is truncated to the length $L_{\text{P}} = KM + 1$.

The symbol period and the roll-off factor ρ will determine the shape of the RRC filter. A smaller ρ implies in a stronger concentration in frequency but a longer impulse response is necessary to get a better approximation of the original infinite length RRC filter, because the impulse response slowly decays. On the other hand, a larger ρ implies in less frequency domain concentration but faster impulse response decay. For FBMC applications the typical roll-off is $\rho = 1$, which means that the transition band approximately ends in the frequency point where the middle of the adjacent subcarrier is located and, it can be shown, that the main lobe is similar to the main lobe of the Dirichlet kernel used to filter the subcarriers in conventional OFDM. But the sidelobes of the RRC filter decay much faster and have much lower amplitude than the Dirichlet kernel.

By assuming T is the QAM symbol period used in each subcarrier, i.e. subcarrier distance of $1/T$, the frequency response is given by

$$H_{\mathrm{P}}(f) = \begin{cases} 1, & |f| \leq \frac{1-\rho}{2T} \\ \cos\left(\frac{\pi T}{2\rho}\left(|f| - \frac{1-\rho}{2T}\right)\right), & \frac{1-\rho}{2T} < |f| \leq \frac{1+\rho}{2T} \\ 0, & \text{otherwise} \end{cases} \tag{2.65}$$

and the continuous time impulse response of the RRC prototype filter would be given by

$$h_{\mathrm{P}}(t) = \begin{cases} \frac{1}{\sqrt{T}}\left(1-\rho+4\frac{\rho}{\pi}\right), & t = 0 \\ \frac{\rho}{\sqrt{2T}}\left[\left(1+\frac{2}{\pi}\right)\sin\left(\frac{\pi}{4\rho}\right)+\left(1-\frac{2}{\pi}\right)\cos\left(\frac{\pi}{4\rho}\right)\right], & t = \pm\frac{T}{4\rho} \\ \frac{1}{\sqrt{T}}\dfrac{\sin\left[\pi\frac{t}{T}(1-\rho)\right]+4\rho\frac{t}{T}\cos\left[\pi\frac{t}{T}(1+\rho)\right]}{\pi\frac{t}{T}\left[1-\left(4\rho\frac{t}{T}\right)^2\right]}, & \text{otherwise} \end{cases} \tag{2.66}$$

For a given total number of subcarriers M, we need to sample the RRC filter with a period $T_{\mathrm{s}} = \frac{T}{M}$. We then substitute $t = lT_{\mathrm{s}}$ to obtain the discrete time coefficients with

$$h_{\mathrm{P},l} = \begin{cases} \frac{1}{\sqrt{T}}\left(1-\rho+4\frac{\rho}{\pi}\right), & l = 0 \\ \frac{\rho}{\sqrt{2T}}\left[\left(1+\frac{2}{\pi}\right)\sin\left(\frac{\pi}{4\rho}\right)+\left(1-\frac{2}{\pi}\right)\cos\left(\frac{\pi}{4\rho}\right)\right], & l = \pm\frac{M}{4\rho} \\ \frac{1}{\sqrt{T}}\dfrac{\sin\left[\pi\frac{l}{M}(1-\rho)\right]+4\rho\frac{l}{M}\cos\left[\pi\frac{l}{M}(1+\rho)\right]}{\pi\frac{l}{M}\left[1-\left(4\rho\frac{l}{M}\right)^2\right]}, & \text{otherwise} \end{cases} \tag{2.67}$$

Finally, we truncate the discrete time filter to the interval $\frac{-KM}{2} \leq l \leq \frac{KM}{2}$. We can see that K and M will determine how good will be the approximation of the infinite length RRC.

Now the convolution of RRC in SFB and AFB are not exactly RC, so that a residual ISI is left, i.e. the PR conditions are not strictly fulfilled. The practical RRC is then an NPR prototype filter.

After obtaining the FIR RRC filter one can decide which SFB and AFB structure to be employed. But depending on the structure choice it may be convenient to sample or resample the

impulse response. For example, it may be convenient to have a length KM, in that case the sampling interval has to be shifted by $T_s/2$ compared to the one we employed above.

For the case of a time-domain filtering based structure, the decomposition of the impulse response into the polyphase components is straightforward as shown earlier in this chapter. For a frequency domain filtering structure, there are two possibilities: The first is to transform the impulse response with a DFT of size N_{FFT} and then set $(N_{\text{FFT}}+1-2N_{\text{FFT}}/M)$ of the N_{FFT} frequency domain coefficients, which are already very small, to zero to reduce the complexity. The second is to use the analytical expression for the frequency response of the RRC filter and evaluate for the specific frequencies that are sampled, i.e. we define $H_q = H(f)|_{f=f_q}$, where $f_q = \frac{qM}{TN_{\text{FFT}}}$ are the sampled frequencies. The resulting frequency domain coefficients are given by

$$H_q = H(f_q) = \begin{cases} 1, & q = 0 \\ \cos\left(\frac{\pi T}{2\rho}\left(\frac{qM}{TN_{\text{FFT}}} - \frac{1-\rho}{2T}\right)\right), & 1 \le q \le \frac{2N_{\text{FFT}}}{M} - 1 \\ 0, & \text{otherwise} \end{cases} \tag{2.68}$$

In order to exemplify the RRC prototype and to compare the time and frequency properties achieved when using different structures, in Fig. 2.55 we have plotted the impulse response after the time domain sampling and after the frequency domain sampling with the zero-valued coefficients. We show the numerical examples for $N_{\text{FFT}} = 2KM$ and for $N_{\text{FFT}} = 4KM$, whereby $M = 16$ and $K = 4$. We have not shown here the results for $N_{\text{FFT}} = KM$, i.e. the frequency spread approach, because our prototype length is $L_{\text{P}} = KM + 1$ and the combination would not fulfill the requirements for strictly linear convolution. We can see that the impulse responses are visually

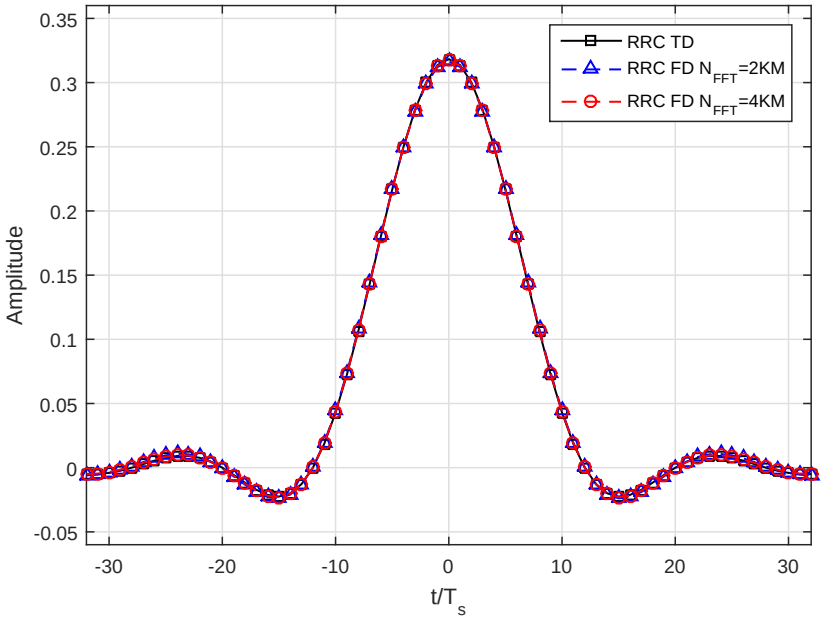

Fig. 2.55. Impulse responses of the RRC prototype filter for $K = 4$, $M = 16$, $\rho = 1$ and different frequency truncation.

very similar. It is important to mention that the impulse responses after the frequency domain sampling with zeroing of coefficients is not strictly limited to the length $L_{\mathbf{P}}$, but actually it is now N_{FFT}. But the coefficients with index higher than $L_{\mathbf{P}} - 1$ have negligible amplitude for the chosen

parameters and, for this reason, not shown in Fig. 2.55. Moreover, strictly speaking the filter is not anymore linear phase and for the deployment of the frequency domain structure, depending on the requirements of the system and the parameters available, those imperfections need to be carefully considered during design phase.

In Fig. 2.56 we have depicted the corresponding frequency domain magnitude responses. We can also see here that any visual deviation is very small and can be neglected for the parameters chosen.

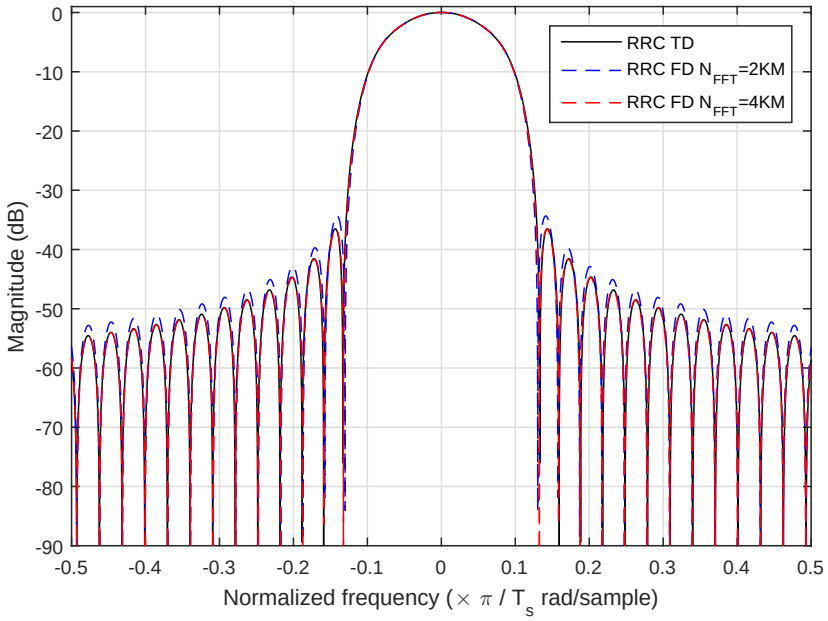

Fig. 2.56. Frequency response of the RRC prototype filter for $K = 4$, $M = 16$, $\rho = 1$ and different frequency truncation.

We finally evaluate the frequency domain behavior by generating the PSD when $M_{\mathrm{f}} = 204$ subcarriers out of $M = 256$ are occupied. The PSD are depicted in Fig. 2.57, where we have again used $K = 4$. When looking at the out-of-band emissions, we can now see a more evident gap between the different configurations, although they are of only a few dBs for a power density below -55dB/Hz.

From the examples shown, we can conclude that the RRC filter is a viable candidate for both time and frequency domain filtering structures.

2.5.2 Frequency Sampling based Filter Design according to Martin-Bellanger

We will describe here the prototype design based on the frequency sampling approach that was proposed in [13] and inspired on the scheme initially presented in [52]. The idea is to generate an NPR prototype that has a very high stop-band attenuation and it is designed based on the same principles as the Lerner filters [49, 52] initially designed with analog lumped components. This prototype has been very frequently considered in recent years and is frequently called "PHYDYAS filter" due to its intensive use in the PHYDYAS EU FP7 project [1].

It is assumed that the frequency response of the prototype filter can be uniformly sampled as shown in Fig. 2.38. The design is based on directly finding the discrete samples of the frequency response and then converting the frequency response to the time domain to obtain the impulse

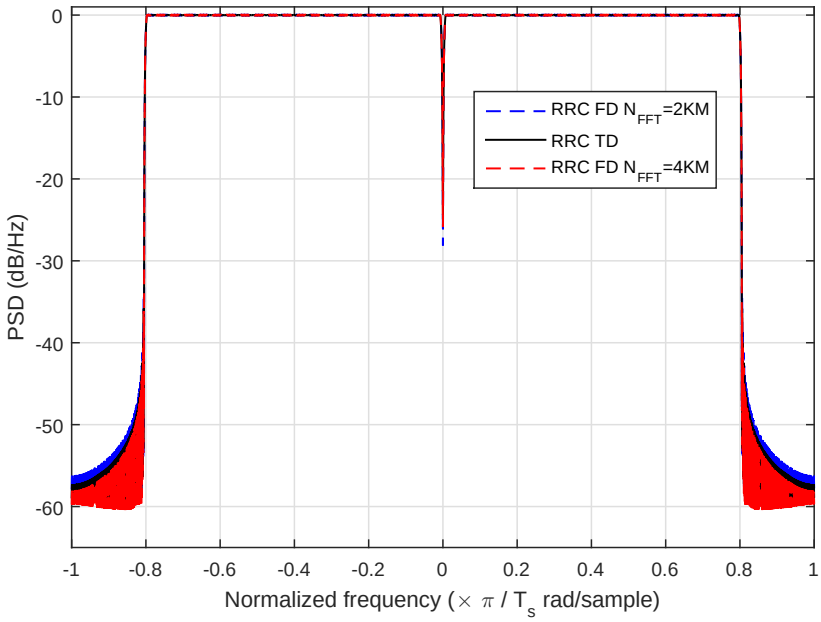

Fig. 2.57. PSD of the RRC prototype filter for $K = 4$, $M = 256$, $M_\mathrm{f} = 204$, $\rho = 1$ and different frequency truncation.

response with the help of the IDFT. If a frequency sampling structure as presented in Section 2.2.3.2 is employed, then the frequency samples are directly utilized in the filter bank structure.

The prototype filter impulse response of length $L_\mathrm{p} = KM$ is obtained by applying an IDFT to the frequency samples H_q

$$h_{\mathrm{P},l} = \frac{1}{KM} \sum_{q=0}^{KM-1} H_q \mathrm{e}^{\mathrm{j}\frac{2\pi kl}{KM}}, \quad \text{for } 0 \leq l \leq KM-1. \tag{2.69}$$

But some constraints are imposed to the H_q. The first is that $K(M-2)+1$ of the KM samples of H_q are equal to zero as illustrated in Fig. 2.38, i.e. only $2K-1$ need to be calculated. The second constraint is that the frequency samples are symmetric about the center of the passband. The third constraint is that the sum of the frequency samples is equal to zero, in order to get a high stopband attenuation. The effect of this constraint is that the side lobes of the continuous frequency representation of the discrete frequency coefficients that are added together, approximately cancel each other, and the further is the frequency from the passband, the stronger is the cancellation. It is worth noting that setting the sum of the frequency coefficients to zero is equivalent to set to zero the first coefficient of the prototype filter impulse response. The fourth and last constraint was the major contribution of [52], and it sets the condition under which the H_q allow the cascade SFB and AFB to satisfy the Nyquist criteria, i.e. it guarantees a symmetric transitions band of the resulting transfer function. Finally, without loss of generality, it is assumed that $H_0 = 1$.

We can now mathematically summarize the constraints as follows

$$\begin{cases} H_q = 0, & \text{for } K \leq q \leq KM-K, \\ H_{KM-q} = H_q, & \text{for } 1 \leq q \leq K-1, \\ H_0 + 2\sum_{q=1}^{K-1} H_q = 0, & \\ H_q^2 + H_{K-q}^2 = 1, & \text{for } 1 \leq q \leq K-1, \end{cases} \tag{2.70}$$

Given the values of K and M, one has to solve this system of partially non-linear equations to obtain the H_q. There are $K-1$ unknowns, one linear equation and $\lceil (K-1)/2 \rceil$ non-linear equations. It can be observed that the system of equations does not depend on the total number of subcarriers M. This means that for a given K, the H_q can be used for any M and the range of K of interest for wireless applications is very limited.

With the symmetry assumption, the IDFT in (2.69) can be re-written as

$$h_{\mathrm{P},l} = \frac{1}{KM}\left(H_0 + 2\sum_{q=1}^{K-1} H_q \cos\left(\frac{2\pi q l}{KM}\right)\right), \quad \text{for } 0 \leq l \leq KM-1 \tag{2.71}$$

In [13] the numerical values of H_q were given for $K=3$ and $K=4$, and the filters obtained for the latter value was made well known in [16] from where it got the nickname "PHYDYAS filter". The values came originally from [52], where further values for $K=6$ and $K=8$ are given.

If we take $K=3$, we only have to solve the following system of equations

$$H_1 + H_2 = -\frac{1}{2}, \tag{2.72}$$

$$H_1^2 + H_2^2 = 1, \tag{2.73}$$

where we just need to substitute the value of H_1 or H_2 in the second equation and find the roots of the polynomial of 2nd degree, which then results in $H_1 = -0.91143783$ and $H_2 = 0.41143783$. By taking $K=4$, we end-up with another system of equations

$$H_1 + H_2 + H_3 = -\frac{1}{2}, \tag{2.74}$$

$$H_1^2 + H_3^2 = 1, \tag{2.75}$$

$$2H_2^2 = 1, \tag{2.76}$$

where $H_2 = \sqrt{2}/2$ is straightforward and together with the second equation can be pluged-in the first one, and again the roots of polynomial of 2nd degree need to be find, which results in $H_1 = -0.97195983$ and $H_3 = -0.23514695$.

In Table I of [52], it is possible find the H_q values for $K = 3, 4, 6$ and 8. For $K \geq 5$ there is no close form solution and in [52] a problem formulation is presented, where a numerical optimization is used to calculate the H_q.

We can further extend constraints in (2.70) for the case of the more general frequency domain structure based on OA and OS, and where $N_{\text{new}} > 1$, as follows

$$\begin{cases} H_q = 0, & \text{for } \frac{N_{\text{FFT}}}{M} \leq q \leq N_{\text{FFT}} - \frac{N_{\text{FFT}}}{M}, \\ H_{N_{\text{FFT}}-q} = H_q, & \text{for } 1 \leq q \leq \frac{N_{\text{FFT}}}{M} - 1, \\ H_0 + 2\sum_{q=1}^{\frac{N_{\text{FFT}}}{M}-1} H_q = 0, & \\ H_q^2 + H_{\frac{N_{\text{FFT}}}{M}-q}^2 = 1, & \text{for } 1 \leq q \leq \frac{N_{\text{FFT}}}{M} - 1, \end{cases} \tag{2.77}$$

where we have now $\frac{N_{\text{FFT}}}{M} - 1$ unknowns and have to solve a system of equations with one linear equation and $\lceil \left(\frac{N_{\text{FFT}}}{M} - 1\right)/2 \rceil$ non-linear equations.

The impulse response of the prototype is given by

$$h_{\mathrm{P},l} = \frac{1}{N_{\mathrm{FFT}}} \left(H_0 + 2 \sum_{q=1}^{\frac{N_{\mathrm{FFT}}}{M}-1} H_q \cos\left(\frac{2\pi q l}{N_{\mathrm{FFT}}} \right) \right), \quad \text{for } 0 \leq l \leq L_{\mathrm{p}} - 1. \tag{2.78}$$

To compare and exemplify the implementation of the design based on frequency sampling we have depicted in Fig. 2.58 the impulse responses for the different structures, $K = 4$ and $M = 16$ And in Fig. 2.59 we have the corresponding subcarrier frequency responses for the time-domain

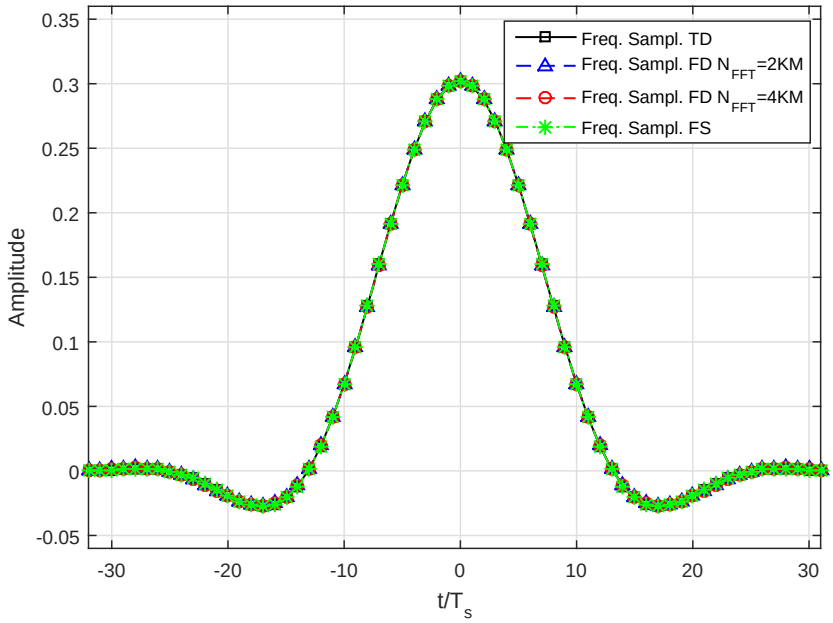

Fig. 2.58. Impulse responses of the frequency sampling based prototype filter for $K = 4$, $M = 16$ and different frequency truncation.

and the different frequency domain implementations.

The PSD for $K = 4$, $M = 256$ and $M_{\mathrm{f}} = 204$ is shown in Fig. 2.60.

2.5.3 ELT and LS optimized

For the specific cases when the prototype filter has a lengths of $L_{\mathrm{P}} = M$ or $L_{\mathrm{P}} = 2M$, i.e. $K = 1$ and $K = 2$, there exists closed form expressions for the filter coefficients $h_{\mathrm{P},l}$ that filfill the PR conditions and are known ELT [50]. Those closed form expressions are obtained from the assumption that the polyphase components can be realized with a lattice structure as explained earlier in this chapter. The theory of Lapped transforms is closely related to the real valued CMFB and SMFB.

For $K = 1$ the ELT prototype is given by

$$h_{\mathrm{P},l} = \pm \sin\left(\frac{\pi}{M} \left(l + \frac{1}{2} \right) \right), \quad l = 0, \cdots, M-1. \tag{2.79}$$

and for $K = 2$ is given by

$$h_{\mathrm{P},l} = \mp \frac{\sqrt{2}}{4} \pm \frac{1}{2} \cos\left(\frac{\pi}{M} \left(l + \frac{1}{2} \right) \right), \quad l = 0, \cdots, 2M-1. \tag{2.80}$$

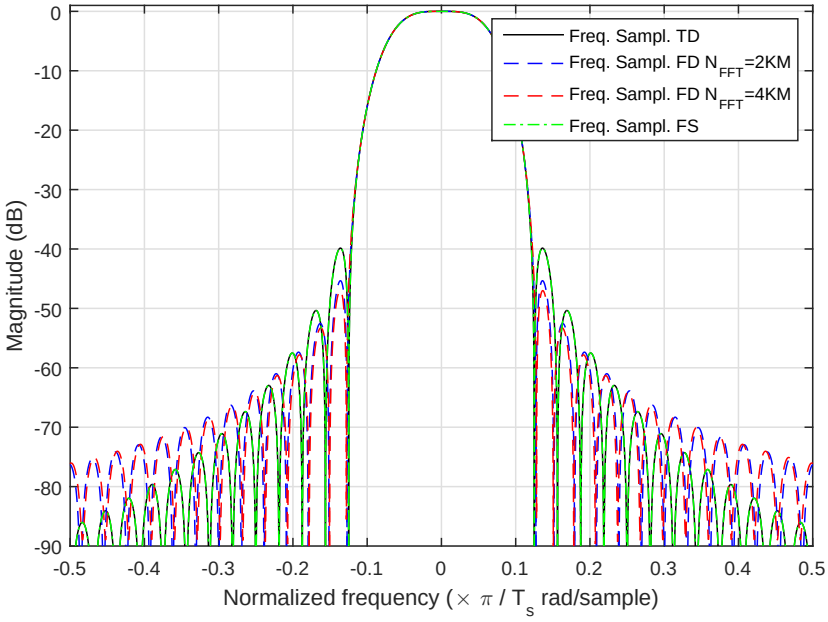

Fig. 2.59. Frequency response of the frequency sampling based prototype filter for $K = 4$, $M = 16$ and different frequency truncation.

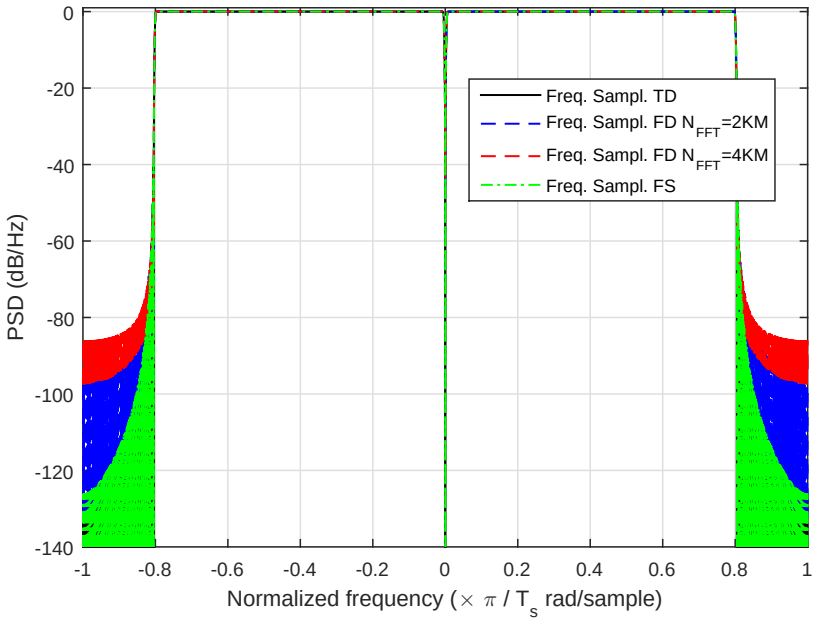

Fig. 2.60. PSD of the frequency sampling based prototype filter for $K = 4$, $M = 256$, $M_{\mathrm{f}} = 204$ and different frequency truncation.

In Fig. 2.61 we have plotted the impulse responses for the ELT when assuming both time-domain and frequency domain filtering structures with truncation of the frequency domain coefficients to reduce the complexity. The corresponding subcarrier frequency domain responses are depicted in Fig. 2.62. The PSD of a multicarrier signal with $K = 2$, $M = 256$, $M_{\mathrm{f}} = 204$ and for different frequency truncation factors is shown in Fig. 2.63.

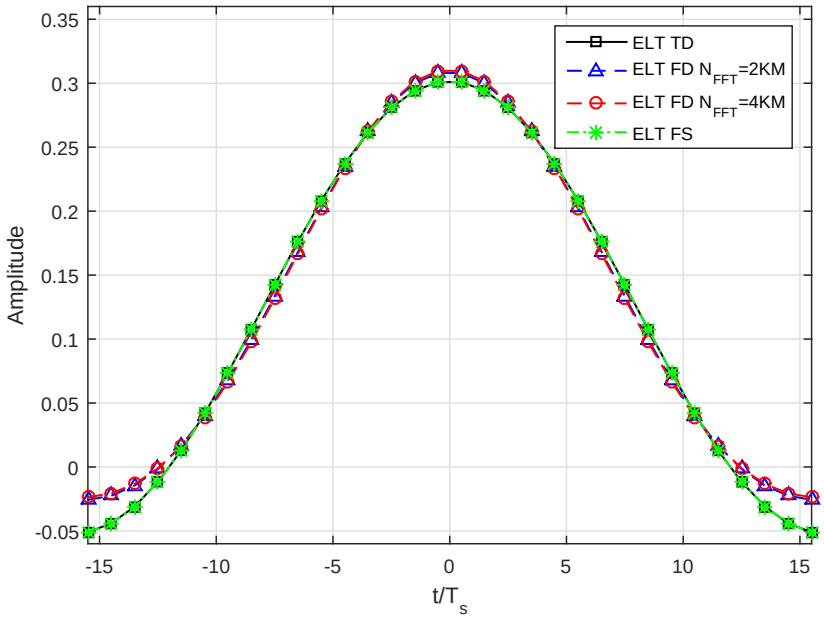

Fig. 2.61. Impulse responses of the ELT prototype filter for $K = 2$, $M = 16$ and different frequency truncation.

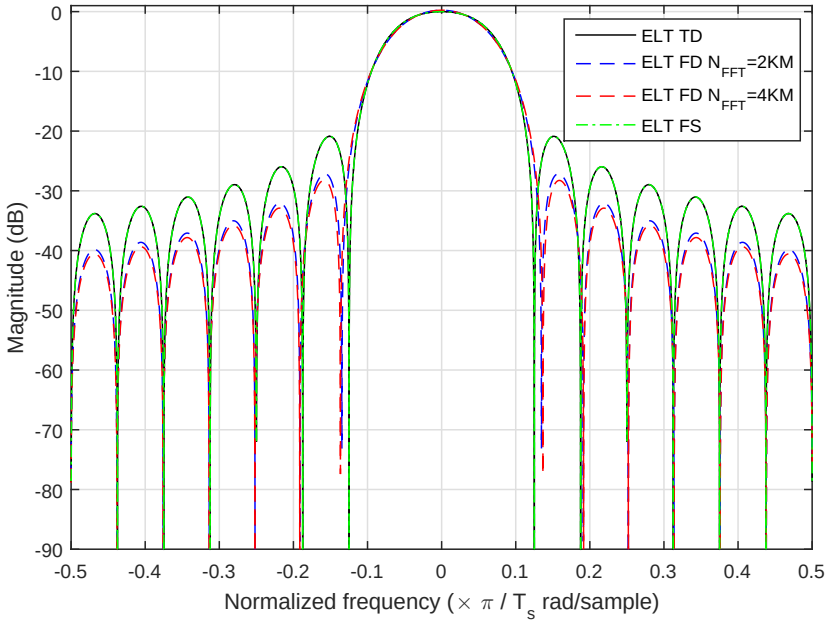

Fig. 2.62. Frequency response of the ELT prototype filter for $K = 2$, $M = 16$ and different frequency truncation.

For the cases where $K > 2$ there is no closed form solution to directly obtain the prototype coefficients. One possibility is to obtain the prototype by numerical optimization methods [29–31, 65, 72]. Given a certain design criteria for the optimization of $H_P(z)$, e.g. minimization of the stop-band in a least squares sense, the $\frac{M}{4}$ equations in (2.31) can be employed in a constrained optimization method. It is worth noting that the constraints are non-linear relations on the prototype

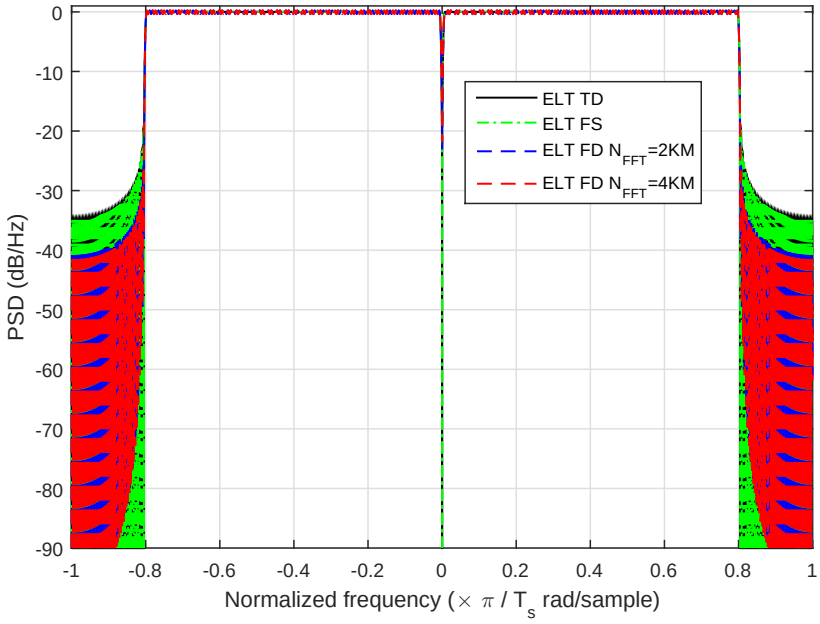

Fig. 2.63. PSD of the ELT prototype filter for $K = 2$, $M = 256$, $M_{\mathrm{f}} = 204$ and different frequency truncation.

filter coefficients. The typical objective function will usually also be a non-linear function of the prototype coefficients.

There exits other different optimization criteria in the literature. For example, minimization of the maximum stop-band ripples, i.e. minimax criteria, or the so-called peak-constrained [30], where a number of stop-band ripples are optimized in the minimax sense and the rest is minimized in the LS sense. The minimax strategy results in constant stop-band amplitude, which is not desired in FBMC applications. A continually decreasing stop-band is preferable in order to maximize interference rejection from external sources and minimize noise leakage into subcarriers with stronger fading. Subcarriers which are separated far apart would then become uncoupled. So LS or Peak-constrained objectives seem to be more appropriate, although we will only further consider here the LS optimized prototypes.

In Fig. 2.64 we have plotted the impulse responses for the LS optimized when assuming both time-domain and frequency domain filtering structures with truncation of the frequency domain coefficients to reduce the complexity. We have depicted in Fig. 2.65 the subcarrier frequency responses.

2.5.4 EGF and IOTA Filters

The prototypes presented so far, namely, RRC, Lapped and Frequency sampling based, have very good spectral properties, i.e. a good stop band attenuation or good spectral localization. The price to be paid is a long impulse response, i.e. a bad time localization. There is a class of prototype design that strives to find an optimum or a configurable trade-off between time and frequency localization. The IOTA filter belongs to this class of time-frequency localized prototypes and was initially proposed in [48]. It was later shown in [63], [3] and [67] that the IOTA belongs to a more general class of time-frequency localized filters called EGF.

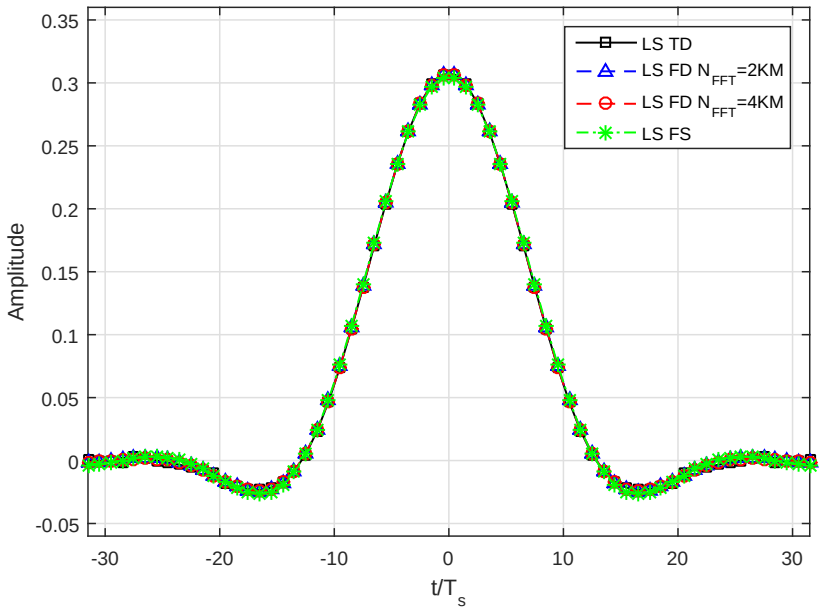

Fig. 2.64. Impulse responses of the optimum LS prototype filter for $K = 4$, $M = 16$ and different frequency truncation.

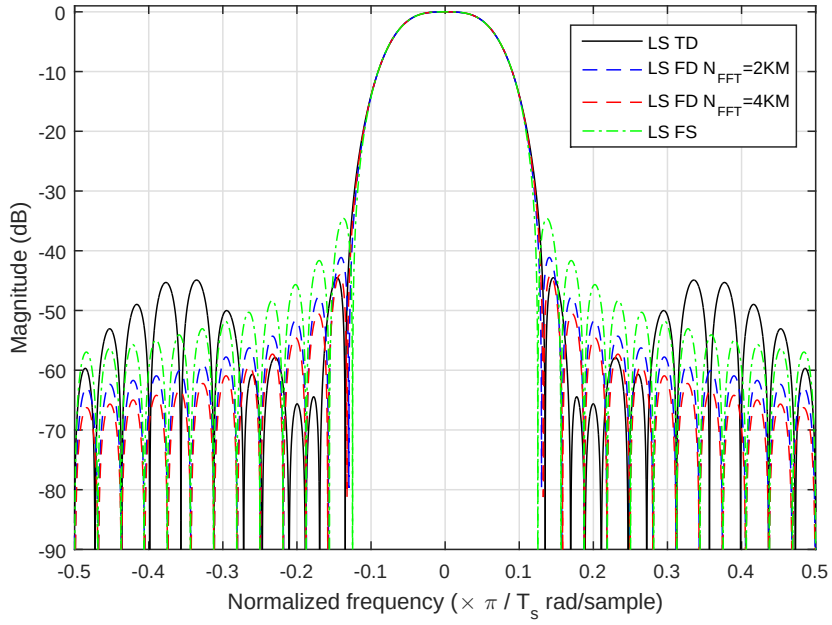

Fig. 2.65. Frequency response of the optimum LS prototype filter for $K = 4$, $M = 16$ and different frequency truncation.

In EGF based FBMC it is assumed that the OQAM symbols are transmitted in a symbol period of τ_0 and that the subcarrier spacing is nu_0. In order to fulfill the requirements for orthogonality and allow at least an NPR behavior, it is assumed that the product $\tau_0\nu_0 = \frac{1}{2}$ needs to remain constant.

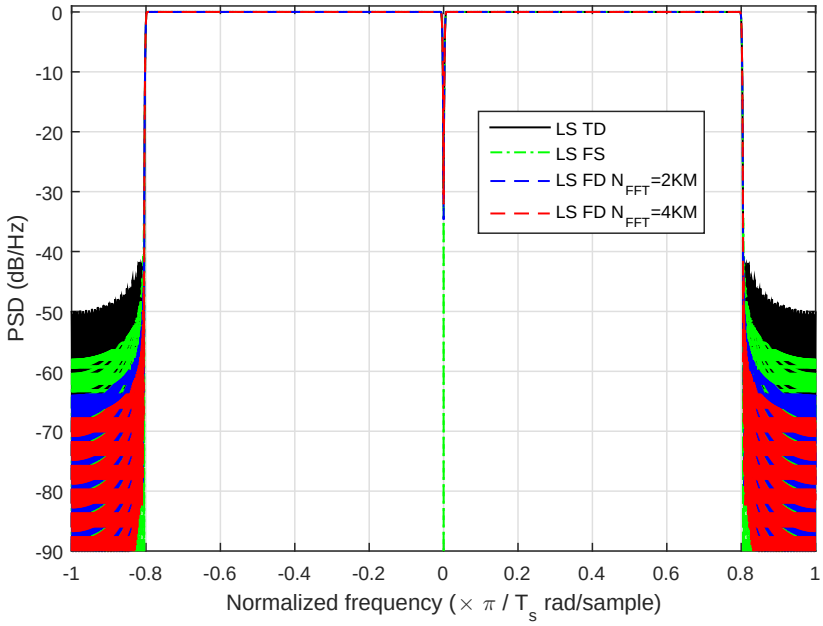

Fig. 2.66. PSD of the optimum LS prototype filter for $K = 4$, $M = 256$, $M_{\mathrm{f}} = 204$ and different frequency truncation.

The design of the EGFs starts with the definition of a basic Gaussian function in the time domain as follows

$$g_\alpha(t) = (2\alpha)^{\frac{1}{4}} \mathrm{e}^{-\alpha\pi t^2}. \tag{2.81}$$

The parameter α determines how fast the function decays, in this case, in the time-domain. It is worth noting that the Fourier transform of a Gaussian function is also Gaussian. The Gaussian cannot guarantee a NPR behavior if directly employed in FBMC systems, i.e. there would be strong ICI and ISI.

In [48, 63, 67] the authors proposed to apply an orthogonalization operation to the basic Gaussian function, which is defined as

$$\mathfrak{O}_{\tau_0}\left\{g_\alpha(t)\right\} = \frac{g_\alpha(t)}{\sqrt{\tau_0 \sum_{k=-\infty}^{\infty} |g_\alpha(t - k\tau_0)|^2}}. \tag{2.82}$$

After that a Fourier transform is applied, followed by another similar orthogonalization procedure in the frequency domain function and, finally, by an inverse Fourier transform. The prototype is the given by

$$h_{\mathrm{P}}(t) = \mathcal{F}^{-1}\left\{\mathfrak{O}_{\nu_0}\left\{\mathcal{F}\left\{\mathfrak{O}_{\tau_0}\left\{g_\alpha(t)\right\}\right\}\right\}\right\}. \tag{2.83}$$

In [63, 67] the authors have shown that a closed form expression for the prototype can be obtained for the parameter $0.528\nu_0^2 \leq \alpha \leq 1/(0.528\nu_0^2)$. This closed form solution and its approx-

imation are given by

$$h_{\mathrm{P}}(t) = \frac{1}{2}\left(\sum_{k=0}^{\infty} d_{k,\alpha,\nu_0}\left[g_\alpha\left(t+\frac{k}{\nu_0}\right)+g_\alpha\left(t-\frac{k}{\nu_0}\right)\right]\right)\sum_{l=0}^{\infty} d_{l,1/\alpha,\tau_0}\cos\left(2\pi l\frac{t}{\tau_0}\right), \tag{2.84}$$

$$\approx \frac{1}{2}\left(\sum_{k=0}^{K} d_{k,\alpha,\nu_0}\left[g_\alpha\left(t+\frac{k}{\nu_0}\right)+g_\alpha\left(t-\frac{k}{\nu_0}\right)\right]\right)\sum_{l=0}^{K} d_{l,1/\alpha,\tau_0}\cos\left(2\pi l\frac{t}{\tau_0}\right), \tag{2.85}$$

where the coefficients d_k and its approximation are given by

$$d_{k,\alpha,\nu_0} = \sum_{l=0}^{\infty} a_{k,l}\mathrm{e}^{-\left(\frac{\alpha\pi}{2\nu_0^2}\right)l}, \quad 0 \le k \le \infty, \tag{2.86}$$

$$\approx \sum_{j=0}^{j_k} b_{k,j}\mathrm{e}^{-\left(\frac{\alpha\pi}{2\nu_0^2}\right)(2j+k)}, \quad 0 \le k \le K, \tag{2.87}$$

The values for the constants $b_{k,j}$ are given in Table V of [68] and will not be reproduced here.

We can then further sample $h_{\mathrm{P}}(t)$ at a period given by $t = n\frac{1}{M\nu_0}$. The resulting discrete time approximation of the EGF is then given by

$$h_{\mathrm{P},n} = \frac{1}{2}\left(\sum_{k=0}^{K} d_{k,\alpha,\nu_0}\left[g_\alpha\left(n\frac{1}{M\nu_0}+\frac{k}{\nu_0}\right)+g_\alpha\left(n\frac{1}{M\nu_0}-\frac{k}{\nu_0}\right)\right]\right)\sum_{l=0}^{K} d_{l,1/\alpha,\tau_0}\cos\left(ln\frac{4\pi}{M}\right), \tag{2.88}$$

and, finally, we truncate the impulse response length by taking $-KM/2 \le n \le KM/2$. The IOTA filter is a special case of the EGF when $\alpha = 1$ and $\tau_0 = \nu_0 = \frac{1}{\sqrt{2}}$. Comparing to our conventional FBMC systems, the IOTA based system has an OQAM symbol period which is $1/\sqrt{2}$ shorter and a subcarrier spacing which is $\sqrt{2}$ further apart.

In Fig. 2.67, we depict the impulse response of the IOTA function when a time domain structure is assumed and the corresponding one when frequency domain filtering structures are assumed. The corresponding subcarrier frequency response for the IOTA functions is shown in Fig. 2.68.

In Fig. 2.69 we show the PSD when employing the IOTA prototype for the time and frequency domain realization structures.

2.5.5 Prototype Filters Comparison and Discussion

We can now perform an overall numerical comparison among the various prototype filters just presented. Our analysis is based on the assumption that for each filter the impulse response is provided as a start point, independent of which design method was employed, which also corresponds to the assumption that a time domain filtering polyphase decompositions based structure.

We will first show here a comparison of the impulse responses, the subcarrier frequency responses and the PSD for a selection of parameters. Then we further discuss the overall properties of each filter and qualitatively compare them.

In Fig. 2.70, we show the impulse responses for $K = 4$ ($K = 2$ for ELT), $M = 16$, $\rho = 1$ and $\alpha = 1$. The subcarrier frequency responses are compared in Fig. 2.71 also $K = 4$ ($K = 2$ for ELT), $M = 16$, $\rho = 1$ and $\alpha = 1$. Finally, we have the PSD in Fig. 2.72 for $K = 4$ ($K = 2$ for ELT), $M = 256$, $M_{\mathrm{f}} = 204$ $\rho = 1$ and $\alpha = 1$.

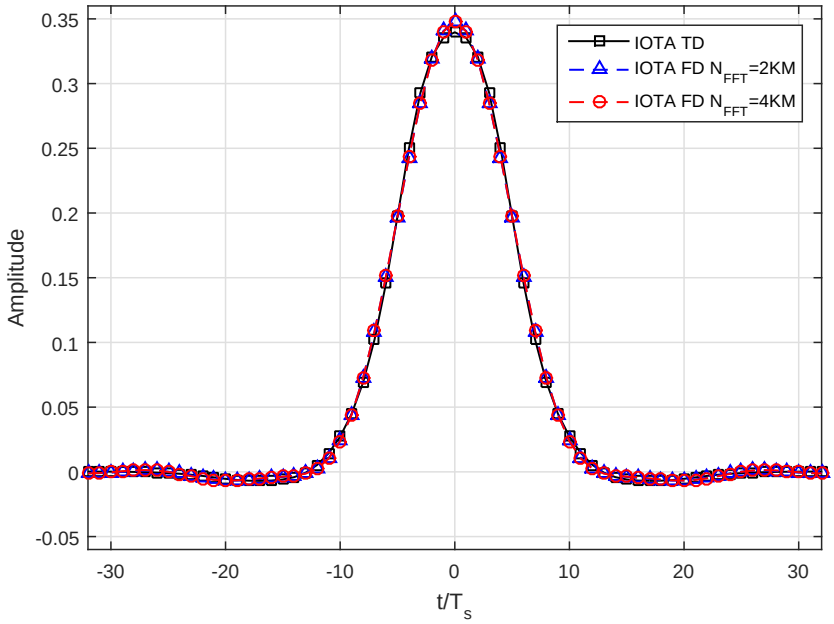

Fig. 2.67. Impulse responses of the IOTA prototype filter for $K = 4$, $M = 16$, $\alpha = 1$ and different frequency truncation.

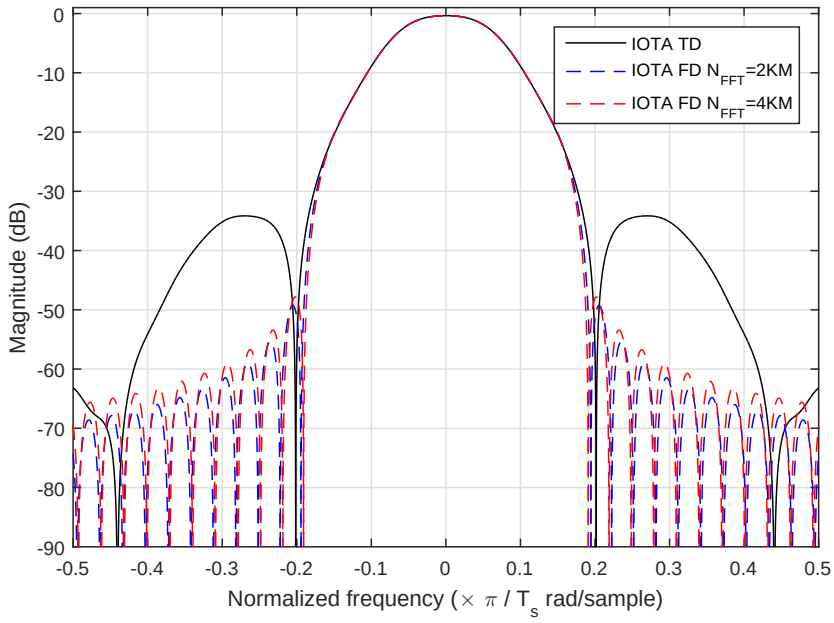

Fig. 2.68. Frequency response of the IOTA prototype filter for $K = 4$, $M = 16$, $\alpha = 1$ and different frequency truncation.

From the numerical comparisons in Figs. 2.70, 2.71 and 2.72, we can observe the classical trade-off between time domain and frequency concentration. Moreover, the impulse responses of the filters have different decays, what reflects on a very diverse stop-band behavior.

We can also characterize the filters according toPR or NPR properties, design methodology, number of parameters and the flexibility to chose their length and frequency behavior. We can then summarize the different filters considered as follows:

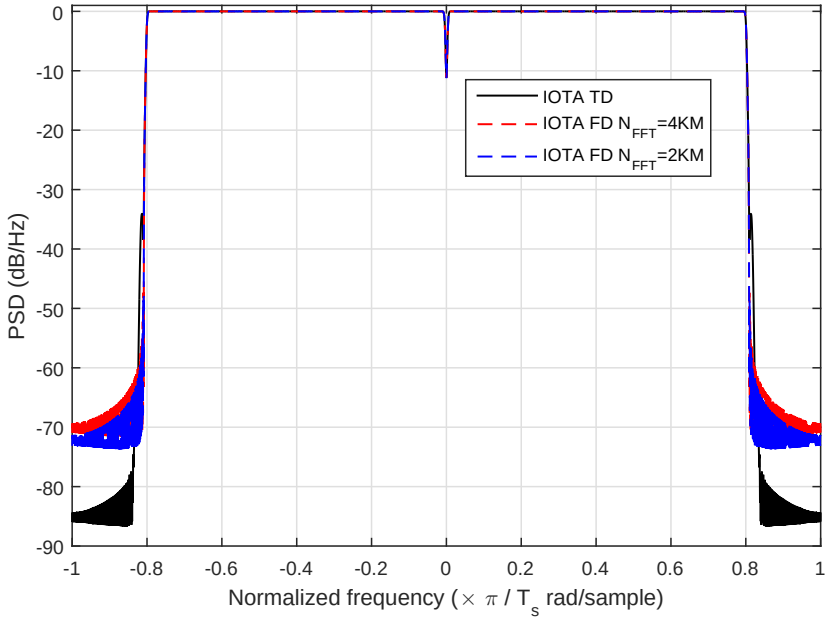

Fig. 2.69. PSD of the IOTA prototype filter for $K = 4$, $M = 256$, $M_{\mathrm{f}} = 204$, $\alpha = 1$ and different frequency truncation.

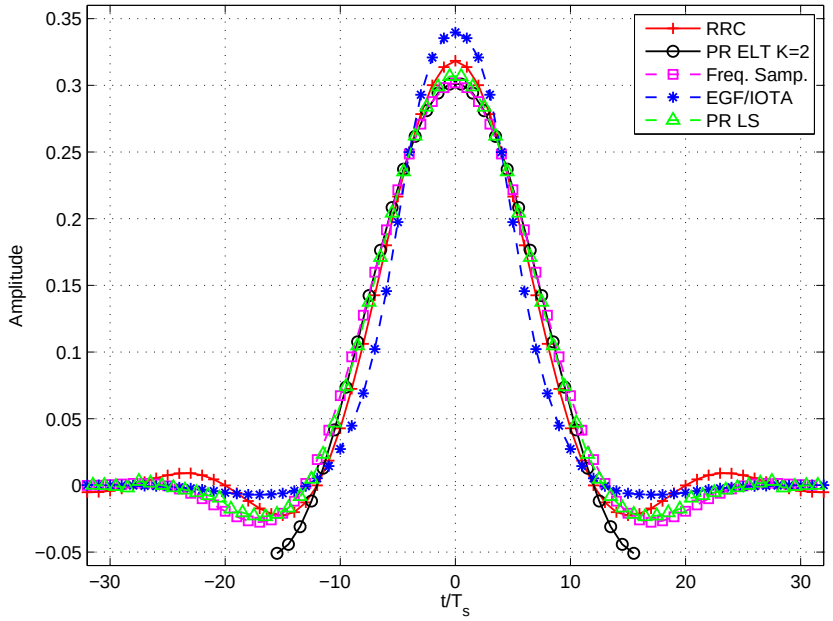

Fig. 2.70. Impulse responses of the different prototype filters for $K = 4$ ($K = 2$ for ELT), $M = 16$, $\rho = 1$, $\alpha = 1$.

- RRC has a simple design with few parameters and a closed form. Moreover, it has a flexible choice of the filter length and roll-off factor. It is of NPR class and presents a low flexibility on the choice of the stop-band attenuation, which will depend on the length and roll-off factor.
- Frequency sampling according to Martin-Bellanger provides a high stop-band attenuation, has a simple design with closed form and few parameters. It is of NPR class and presents low flexibility on the choice of filter length ($K < 5$) and on the frequency behavior.

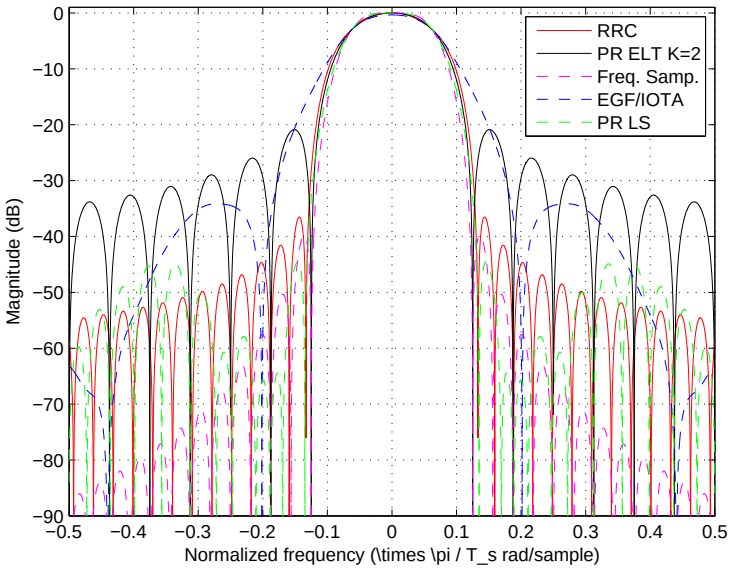

Fig. 2.71. Frequency responses of the different prototype filters for $K = 4$ ($K = 2$ for ELT), $M = 16$, $\rho = 1$, $\alpha = 1$.

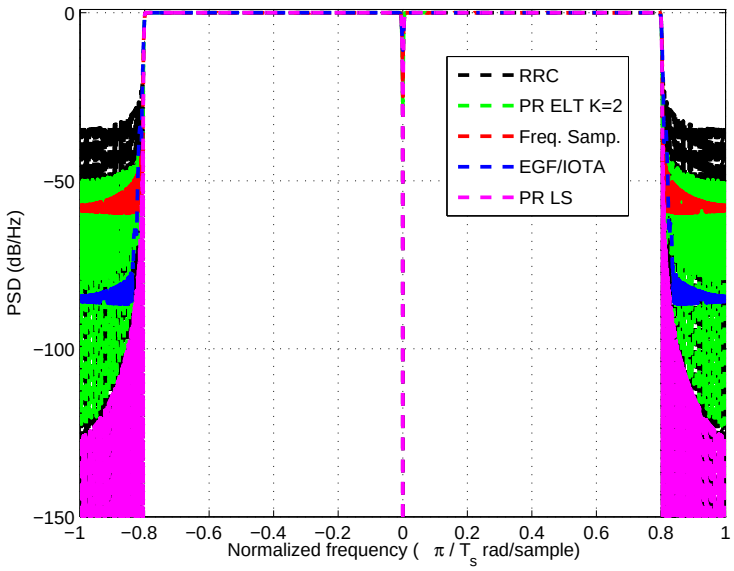

Fig. 2.72. PSD of the different prototype filters for $K = 4$ ($K = 2$ for ELT), $M = 256$, $M_{\mathrm{f}} = 204$ $\rho = 1$ and $\alpha = 1$.

- Extended Lapped has a simple design with closed form and few parameters. If is of PR class but has low flexibility on the choice of filter length ($K = 2$), on the choice of the filter length and on the frequency behavior.
- Optimized prototype (LS, Minimax, Peak-constrained, etc.) fulfills PR constraints and is flexible on the choice of parameters, filter length and frequency behavior. On the downside, it has no closed form and has a more complicated design involving numerical optimization.

- EGF and IOTA fulfills PR constraints. It has flexible choice of filter length, but the length will not influence much time and frequency behavior, because it optimizes the trade-off between time and frequency concentration. It has no closed form, a complicated design, no flexibility on the choice of frequency behavior.

From the analysis and comparison of the different filters the following points have to be considered when choosing a specific prototype for a given application:

- Filters from PR class can be realized in any structure without loosing their original time and frequency domain characteristics.
- Filters from NPR class may not keep the original time and frequency characteristics.
- Depending on the application and scenario an improve concentration in time or in frequency may be desired. For example, in wireless communications an improved frequency concentration is favored if frequency synchronization is an issue. When short chunks of data are transmitted or quick switches between different directions of a Time-Division Duplex (TDD) system, shorter filter with quicker decay is desired.
- If multiple subcarrier bandwidths have to be supported, a high flexibility is desired on the choice of the filter length as well as the frequency behavior.

3. Channel Estimation

3.1 Introduction

In wireless systems, channel estimation is not a trivial but a very important and critical task. Channel estimation in OFDM already poses a number of challenges and has a direct influence on the overall performance of the system. The CP provides some help to simplify channel estimation in OFDM-based wireless links. In FBMC, channel estimation is even more challenging than OFDM due to the lack of a CP—or any guard interval—and the longer subcarrier pulse shaping employed. A symbol sample observed at the output of a receiver's subcarrier with index m in a certain time sampling with index n is a function of the proceeding and subsequent symbols in that same subcarrier, and of the symbols transmitted in the adjacent subcarriers, i.e. the received samples contain ISI and ICI. In CP-OFDM, the received symbols transmitted in different time and frequency resources are assumed to be decoupled, if the CP is long enough—longer than the channel impulse response—and the system is well synchronized in time and frequency.

In most of the literature on channel estimation schemes for FBMC, a low frequency selectivity is assumed. In that case the overlapping in time and frequency of adjacent symbols can be neglected. The book chapter in [46] provides a review of a number of channel estimation methods for FBMC including in part the methods presented in this chapter. The approach presented in this chapter assumes a high frequency selectivity.

In this chapter, we will introduce and employ for the channel estimation two different subcarrier models, which we call narrowband and broadband. The narrowband subchannel model can be considered the FBMC-equivalent of the frequently used subcarrier model for CP-OFDM. In the case of FBMC, a narrowband model is typically useful when a small number of subcarriers are occupied or employed, or even only one single carrier is of interest for the receiver. This scenario is especially envisioned when a large subcarrier spacing—or subchannel bandwidth—is considered, for example, to reduce the sensitivity to phase noise and carrier frequency offset and/or to reduce the latency for mission critical applications. When a large number of subcarriers are occupied, the channel estimation based on the broadband subcarrier model results in less parameters to be estimated and, consequently, is more spectrally efficient.

After presenting the two models, we will describe different methodologies to perform channel estimation. We will present estimators that do not require knowledge of the noise variance and also no knowledge of the covariance matrix of the channel. In addition, we present methods that consider the knowledge of one or both covariances. We will also show the performance loss when more spectrally efficient estimation is performed, i.e. when a small number of training or reference symbols are employed relative to the number of observations, taking into account the spreading of the symbols in time due to the long pulse shaping.

3.2 Subcarrier System Models

The subcarrier or subchannel model of the FBMC/OQAM system is depicted in Fig. 3.1, where the fact that there is no significant interference coming from subcarriers further apart than the immediate adjacent ones is explored, because the prototypes are designed to have sufficient stop-band attenuation for the frequencies corresponding to those subcarriers.

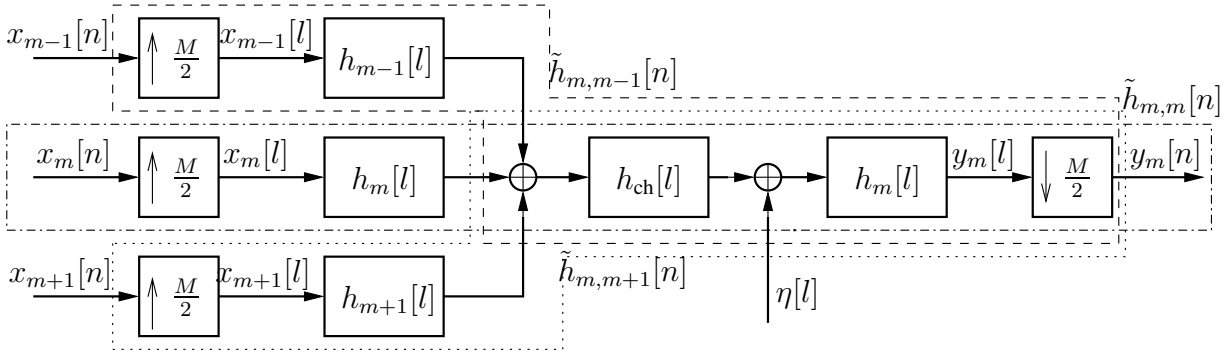

Fig. 3.1. Subcarrier model for the FBMC/OQAM system.

The overall composed impulse responses $\tilde{h}_{m,\ell}[n]$ are obtained by first convolving the AFB subfilter with the SFB subfilter and with the channel and then sub-sampling by $\frac{M}{2}$, i.e.

$$\tilde{h}_{m,\ell}\left[n\frac{M}{2}\right] = h_m[l] * h_\ell[l] * h_{\text{ch}}[l], \quad \text{for } \ell = m-1, m, m+1, \tag{3.1}$$

where $*$ stands for discrete-time linear convolution [26, 59]. The resulting impulse response has $L_{\tilde{h}} = \lceil \frac{2L_{\text{P}}+L_{\text{ch}}-2}{M/2} \rceil$ coefficients, where L_{ch} is the number of coefficients of the impulse response of the frequency selective propagation channel.

3.2.1 Narrowband CIR Model

The narrowband subchannel model considers that one channel impulse response is observed in a per-subcarrier basis. This model is analogous to the approach followed for the conventional CP-OFDM, in which case the impulse response reduces to a single coefficient and is a common approach in practical implementations of multicarrier systems, for example, LTE and Long-Term Evolution-Advanced (LTE-A).

Let us assume that a per-subcarrier equalizer (linear MMSE [77] or decision feedback [10, 75]) should be employed and that a per-subcarrier channel estimator is sufficient for the purpose of designing the equalizer. We will initially make no differentiation between training or reference symbols and the data symbols contained not only in the subcarrier under observation but also in their two neighbors. Later we will define the input sequences more exactly and separate between training and data carrying ones.

To perform the per-subcarrier channel estimation, we will model the multipath channel viewed at each subcarrier as a narrowband channel with a short impulse response and represent it at the sampling rate of the OQAM symbols, namely twice the QAM symbol rate, that is $2/T$. This approach is sometimes called structured channel estimation [7, 11].

We define now the impulse responses

$$h_{m,\ell}[l] = h_m[l] * h_\ell[l], \tag{3.2}$$

which have $(2L_\text{P}-1)$ coefficients and are the convolutions of AFB subfilters $h_m[l]$ with SFB subfilters $h_\ell[l]$, with $\ell = m-1, m, m+1$. Then we sub-sample $h_{m,\ell}[l]$ by $\frac{M}{2}$, i.e. we take only every $l = n\frac{M}{2}$ sample of the composed filter, what results in a total of $L_h = \left\lceil \frac{2L_\text{P}-1}{M/2} \right\rceil$ coefficients[1]. Moreover, we define a narrowband subchannel impulse response $h_{\text{ch},m}[n]$ with $L_{\text{ch},m}$ coefficients, which we would like to estimate. We can then redraw the subcarrier model in Fig. 3.1 to the one shown in Fig. 3.2. It is worth noting that the order of $h_{\text{ch},m}[n]$ is not necessarily the same

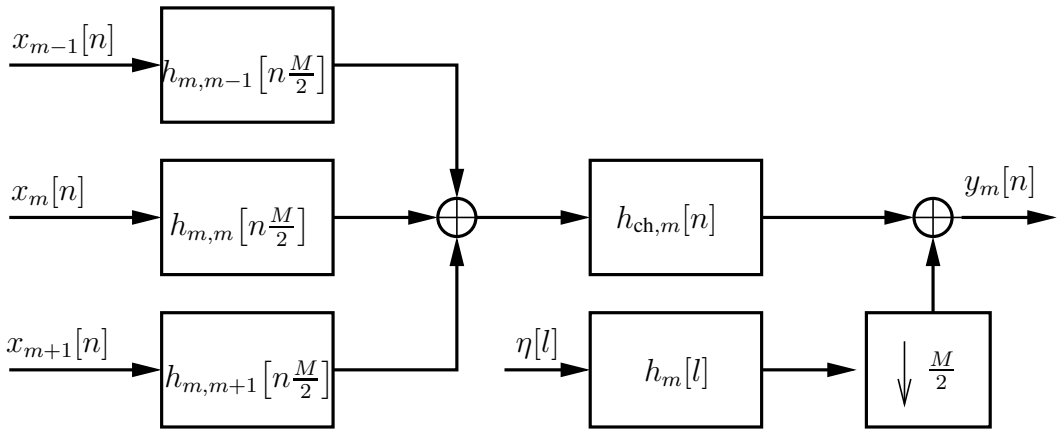

Fig. 3.2. Subcarrier model of Fig. 3.1 reformulated for narrowband channel estimation.

for all subcarriers because the frequency selectivity may vary on different portions of the overall spectrum. Moreover, $L_{\text{ch},m}$ cannot be obtained by just dividing L_ch by $\frac{M}{2}$, although the two values are somehow dependent on each other [2], i.e. a larger L_ch implies in a larger $L_{\text{ch},m}$ and vice versa.

Based on the diagram in Fig. 3.2, we can express $y_m[n]$ the output of the AFB in m-th subcarrier in the OQAM rate of $2/T$, i.e. before the OQAM destaggering, as

$$y_m[n] = (h_{m,m}[n] * x_m[n] + h_{m,m-1}[n] * x_{m-1}[n] + h_{m,m+1}[n] * x_{m+1}[n]) * h_{\text{ch},m}[n] + \eta_m[n], \tag{3.3}$$

where $\eta_m[n\frac{M}{2}] = h_m[l] * \eta[l]$.

We can then arrange the signal received at subcarrier m in an observations vector

$$\mathbf{y}_m[n] = \begin{bmatrix} y_m[n] & y_m[n-1] & \cdots & y_m[n-L_\text{o}+1] \end{bmatrix}^\text{T} \in \mathbb{C}^{L_\text{o}}, \tag{3.4}$$

which is then defined as

$$\mathbf{y}_m[n] = \left(\mathbf{X}_m[n]\mathbf{H}_{m,m} + \mathbf{X}_{m-1}[n]\mathbf{H}_{m,m-1} + \mathbf{X}_{m+1}[n]\mathbf{H}_{m,m+1}\right)\mathbf{h}_{\text{ch},m} + \mathbf{\Gamma}_m\boldsymbol{\eta}[l], \tag{3.5}$$

where $\mathbf{h}_{\text{ch},m} \in \mathbb{C}^{L_{\text{ch},m}}$ contains the coefficients of the mth sub-channel impulse response.

The Toeplitz matrices $\mathbf{H}_{m,\ell} \in \mathbb{C}^{L_{h'} \times L_{\text{ch},m}}$ contain the composed subfilter impulse responses, with the new overall subchannel impulse response including the narrowband channel having $L_{h'} = L_h + L_{\text{ch},m} - 1$ coefficients, and can be calculated as[3]

$$\mathbf{H}_{m,\ell} = \sum_{i=1}^{L_{h'}} \mathbf{e}_i \mathbf{h}_{m,\ell}^\text{T} \mathbf{D}_i, \tag{3.6}$$

[1] In the common case of $L_\text{P} = KM$ we get $L_h = 4K$ and for $L_\text{P} = KM+1$ we get $L_h = 4K+1$

[2] The exact physical and mathematical relation between $L_{\text{ch},m}$ and L_ch has not been deeply studied in the framework of this work and remains as a topic for future research.

[3] The definition of the matrices $\mathbf{H}_{m,\ell}$ results in a transposed of the so-called convolution matrix.

where $\mathbf{h}_{m,\ell} \in \mathbb{C}^{L_h}$ contains the coefficients of the impulse response $h_{m,\ell}[n]$, vector $\mathbf{e}_i \in \{0,1\}^{L_{h'}}$ has the i-th element equal to one and the other elements equal to zero, and matrix $\mathbf{D}_i \in \{0,1\}^{L_h \times L_{\text{ch},m}}$ is defined as

$$\mathbf{D}_i = \begin{bmatrix} \mathbf{0}_{L_h \times (i-1)} & \mathbf{I}_{L_h} & \mathbf{0}_{L_h \times (L_{h'}-i)} \end{bmatrix}, \tag{3.7}$$

where $\mathbf{0}_{(i-1)\times L_h} \in \{0\}^{(i-1)\times L_h}$ is the all zero matrix and $\mathbf{I}_{L_h} \in \{0,1\}^{L_h \times L_h}$ is the identity matrix.

The Hankel matrices $\mathbf{X}_\ell[n] \in \mathbb{C}^{L_\text{o} \times L_{h'}}$ are obtained from the input sequences in each subcarrier

$$\mathbf{X}_\ell[n] = \sum_{j=1}^{L_{h'}} \mathbf{D}_j \mathbf{O}_\ell \mathbf{x}_\ell^\text{R}[n] \mathbf{e}_j^\text{T}, \tag{3.8}$$

where $\mathbf{x}_\ell^\text{R}[n] \in \mathbb{R}^{L_x}$ is a purely real version of $\mathbf{x}_\ell[n] \in \mathbb{C}^{L_x}$, which contain $L_x = L_{h'} + L_\text{o} - 1$ samples of the input sequence of symbols $x_\ell[n]$ in subcarrier ℓ, and vector $\mathbf{e}_i \in \{0,1\}^{L_{h'}}$ has the i-th element equal to one and the other elements equal to zero.

Matrix $\mathbf{D}_j \in \{0,1\}^{L_\text{o} \times L_x}$ is defined as

$$\mathbf{D}_j = \begin{bmatrix} \mathbf{0}_{L_\text{o} \times (j-1)} & \mathbf{I}_{L_\text{o}} & \mathbf{0}_{L_\text{o} \times (L_{h'}-j)} \end{bmatrix} \tag{3.9}$$

and selects the part of $\mathbf{x}_\ell^\text{R}[n]$ that appear in each column of $\mathbf{X}_\ell[n]$ and $\mathbf{O}_\ell = \text{diag}([..., 1, \text{j}, 1, \text{j}, ...])$ represents the alternation between purely real and purely imaginary symbols of the OQAM staggering.

Matrix $\mathbf{\Gamma}_m$ is defined as

$$\mathbf{\Gamma}_m = \begin{bmatrix} h_{m,0} & h_{m,1} & \dots & h_{m,L_\text{P}-1} & \mathbf{0}^\text{T}_{L_\text{o}\frac{M}{2}} & \\ \mathbf{0}^\text{T}_{\frac{M}{2}} & h_{m,0} & h_{m,1} & \dots & h_{m,L_\text{P}-1} & \mathbf{0}^\text{T}_{(L_\text{o}-1)\frac{M}{2}} \\ \mathbf{0}^\text{T}_{M} & h_{m,0} & h_{m,1} & \dots & h_{m,L_\text{P}-1} & \mathbf{0}^\text{T}_{(L_\text{o}-2)\frac{M}{2}} \\ \vdots & \vdots & \vdots & \ddots & & \\ \mathbf{0}^\text{T}_{(L_\text{o}-1)\frac{M}{2}} & h_{m,0} & h_{m,1} & \dots & h_{m,L_\text{P}-1} & \mathbf{0}^\text{T}_{\frac{M}{2}} \end{bmatrix} \in \mathbb{C}^{L_\text{o} \times (L_\text{P} + \lceil \frac{M}{2} L_\text{o} \rceil)} \tag{3.10}$$

and is obtained by taking each $\frac{M}{2}$-th row of the convolution matrix constructed with the analysis filter impulse response $h_m[l]$. This is the reason why the vector $\boldsymbol{\eta}[l] \in \mathbb{C}^{(L_\text{P} + \lceil \frac{M}{2} L_\text{o} \rceil)}$, which contains Additive White Gaussian Noise (AWGN) samples with zero mean and variance σ_η^2, is defined at the high sampling rate M/T. Furthermore, we denote the vector with the filtered noise samples $\boldsymbol{\eta}_m[n] = \mathbf{\Gamma}_m \eta[l]$.

We can now define the matrix

$$\mathbf{S}_m[n] = \mathbf{S}_{\text{u},m}[n] + \mathbf{U}_m[n] \tag{3.11}$$

$$= \mathbf{X}_m[n]\mathbf{H}_{m,m} + \mathbf{X}_{m-1}[n]\mathbf{H}_{m,m-1} + \mathbf{X}_{m+1}[n]\mathbf{H}_{m,m+1}, \tag{3.12}$$

where $\mathbf{S}_{\text{u},m}[n] = \mathbf{X}_m[n]\mathbf{H}_{m,m}$ and $\mathbf{U}_m[n] = \mathbf{X}_{m-1}[n]\mathbf{H}_{m,m-1} + \mathbf{X}_{m+1}[n]\mathbf{H}_{m,m+1}$. Resulting in the following compact sub-carrier model for the narrowband sub-channel estimation

$$\mathbf{y}_m[n] = \mathbf{S}_{\text{u},m}[n]\mathbf{h}_{\text{ch},m} + \mathbf{U}_m[n]\mathbf{h}_{\text{ch},m} + \boldsymbol{\eta}_m[n] \tag{3.13}$$

$$= \mathbf{S}_m[n]\mathbf{h}_{\text{ch},m} + \boldsymbol{\eta}_m[n] \tag{3.14}$$

We can observe that even if the propagation channel between SFB and AFB contains a single complex tap, the filters will spread the effect over multiple symbols.

In the special case of low frequency and time selectivity, i.e. large coherence bandwidth and time, the channel impulse response in have very low order compared to the M. We can assume that $L_{\text{ch},m} = 1$ and $L_{\text{o}} = 1$ to use the following simplified notation

$$y_m[n] = \left(\mathbf{x}_m^T[n]\mathbf{h}_{m,m} + \mathbf{x}_{m-1}^T[n]\mathbf{h}_{m,m-1} + \mathbf{x}_{m+1}^T[n]\mathbf{h}_{m,m+1}\right) h_{\text{ch},m} + \eta_m[n], \tag{3.15}$$

where the vectors $\mathbf{x}_\ell^T[n]$ contain the first L_h elements of the first row of $\mathbf{X}_\ell^T[n]$ and $\mathbf{h}_{m,\ell}$ is defined as in (3.6) and corresponds to the first L_h elements of the first column of $\mathbf{H}_{m,\ell}$. We assume that the $\tau_h + 1$-th element of $\mathbf{h}_{m,m}$ is one, i.e. $\mathbf{e}_{\tau_h+1}^{\text{T}}\mathbf{h}_{m,m} = 1$, which is the middle coefficient of the impulse response $h_{m,m}[n]$[4]. We can further develop the expression to

$$y_m[n] = \left(x_m[n-\tau_h] + (\mathbf{x}'_m)^T[n]\mathbf{h}'_{m,m} + \mathbf{x}_{m-1}^T[n]\mathbf{h}_{m,m-1} + \mathbf{x}_{m+1}^T[n]\mathbf{h}_{m,m+1}\right) h_{\text{ch},m} + \eta_m[n], \tag{3.16}$$

where $(\mathbf{x}'_m)^T[n]$, resp. $\mathbf{h}'_{m,m}$, is $\mathbf{x}_m^T[n]$, resp. $\mathbf{h}'_{m,m}$, with the $\tau_h + 1$ element removed. Due to the OQAM staggering, we can assume that $x_m[n-\tau_h]$ is purely real. We can then define

$$\text{j}u_m[n] = (\mathbf{x}'_m)^T[n]\mathbf{h}'_{m,m} + \mathbf{x}_{m-1}^T[n]\mathbf{h}_{m,m-1} + \mathbf{x}_{m+1}^T[n]\mathbf{h}_{m,m+1}, \tag{3.17}$$

and show that

$$\sigma_u^2 = \sigma_x^2\left(||\mathbf{h}'_{m,m}||_2^2 + ||\mathbf{h}_{m,m-1}||_2^2 + ||\mathbf{h}_{m,m+1}||_2^2\right). \tag{3.18}$$

Then we obtain the compact form

$$y_m[n] = \left(x_m[n-\tau_h] + \text{j}u_m[n]\right) h_{\text{ch},m} + \eta_m[n]. \tag{3.19}$$

We can further extend this expression and consider that the single tap channel is time variant at the resolution of n. By using a CP-OFDM-like notation we can finally write

$$y_{m,n} = \left(x_{m,n-\tau_h} + \text{j}u_{m,n}\right) h_{\text{ch},m,n} + \eta_{m,n}. \tag{3.20}$$

3.2.2 Broadband CIR Model

We will consider now a model to be used when we would like to estimate the broadband channel impulse response $h_{\text{ch}}[l]$ defined in the higher sampling rate as shown in Fig. 3.1. We start by redrawing the subcarrier model of Fig. 3.1 in the simplified form shown in Fig. 3.3.

The signal $y_m[n]$ contains the downsampled AFB output samples in the OQAM symbol rate $2/T$ and is defined as

$$y_m[n] = \tilde{h}_{m,m}[n] * x_m[n] + \tilde{h}_{m,m-1}[n] * x_{m-1}[n] + \tilde{h}_{m,m+1}[n] * x_{m+1}[n] + \eta_m[n], \tag{3.21}$$

where $\tilde{h}_{m,\ell}[n]$ are the downsampled impulse responses with $L_{\tilde{h}}$ that result from the convolution of SFB subfilter $h_\ell[n]$, AFB subfilter $h_m[n]$ and broadband frequency selective channel $h_{\text{ch}}[l]$ as defined in (3.1). The signal $\eta_m[n]$ corresponds to the downsampled filtered noise.

[4]For the case $L_{\text{P}} = KM$ we get $\tau_h = 2K - 1$ and for the case $L_{\text{P}} = KM + 1$ we get $\tau_h = 2K$

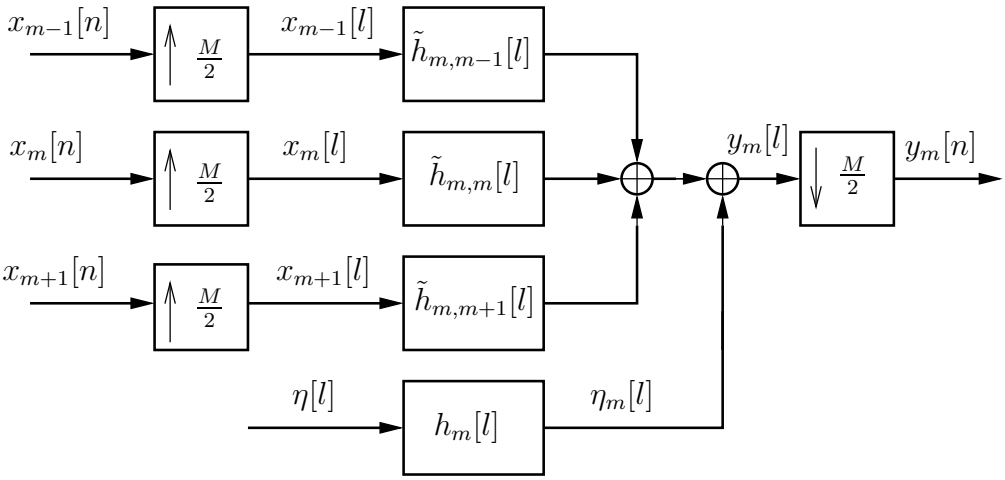

Fig. 3.3. Subcarrier model of Fig. 3.1 reformulated for broadband channel estimation.

We can then arrange the signal received at subcarrier m in an observations vector

$$\mathbf{y}_m[n] = \begin{bmatrix} y_m[n] & y_m[n-1] & \cdots & y_m[n-L_\mathrm{o}+1] \end{bmatrix}^\mathrm{T} \in \mathbb{C}^{L_\mathrm{o}}, \tag{3.22}$$

which is then defined as

$$\mathbf{y}_m[n] = \mathbf{X}_m[n]\tilde{\mathbf{h}}_{m,m} + \mathbf{X}_{m-1}[n]\tilde{\mathbf{h}}_{m,m-1} + \mathbf{X}_{m+1}[n]\tilde{\mathbf{h}}_{m,m+1} + \mathbf{\Gamma}_m\boldsymbol{\eta}[l], \tag{3.23}$$

where the Hankel matrices $\mathbf{X}_\ell[n] \in \mathbb{C}^{L_\mathrm{o}\times L_{\tilde{h}}}$ are obtained from the input sequences in each subcarrier

$$\mathbf{X}_\ell[n] = \sum_{j=1}^{L_{\tilde{h}}} \mathbf{D}_j\mathbf{O}_\ell\mathbf{x}_\ell^\mathrm{R}[n]\mathbf{e}_j^\mathrm{T}, \tag{3.24}$$

where $\mathbf{x}_\ell^\mathrm{R}[n] \in \mathbb{R}^{L_x}$ is a purely real version of $\mathbf{x}_\ell[n] \in \mathbb{C}^{L_x}$, which now contain $L_x = L_{\tilde{h}} + L_\mathrm{o} - 1$ samples of the input sequence of symbols $x_\ell[n]$ in subcarrier ℓ, and vector $\mathbf{e}_i \in \{0,1\}^{L_{\tilde{h}}}$ has the i-th element equal to one and the other elements equal to zero.

Matrix $\mathbf{D}_j \in \{0,1\}^{L_\mathrm{o}\times L_x}$ is defined as

$$\mathbf{D}_j = \begin{bmatrix} \mathbf{0}_{L_\mathrm{o}\times(j-1)} & \mathbf{I}_{L_\mathrm{o}} & \mathbf{0}_{L_\mathrm{o}\times(L_{\tilde{h}}-j)} \end{bmatrix} \tag{3.25}$$

and selects the part of $\mathbf{x}_\ell^\mathrm{R}[n]$ that appears in each column of $\mathbf{X}_\ell[n]$ and $\mathbf{O}_\ell = \mathrm{diag}([..., 1, \mathrm{j}, 1, \mathrm{j}, ...])$ represents the alternation between purely real and purely imaginary symbols of the OQAM staggering.

Vectors $\tilde{\mathbf{h}}_{m,\ell} \in \mathbb{C}^{L_{\tilde{h}}}$ contain the coefficients of the overall subchannel impulse responses $\tilde{h}_{m,\ell}[n]$ and can be expressed as

$$\tilde{\mathbf{h}}_{m,\ell} = \tilde{\mathbf{H}}_{m,\ell}\mathbf{h}_\mathrm{ch}, \tag{3.26}$$

where vector $\mathbf{h}_\mathrm{ch} \in \mathbb{C}^{L_\mathrm{ch}}$ contain the coefficients of the impulse response of the broadband propagation channel $h_\mathrm{ch}[l]$.

Matrices $\tilde{\mathbf{H}}_{m,\ell} \in \mathbb{C}^{L_{\tilde{h}}\times L_\mathrm{ch}}$ are defined as

$$\tilde{\mathbf{H}}_{m,\ell} = \mathbf{J}_{\frac{M}{2}}\bar{\mathbf{H}}_{m,\ell} = \begin{bmatrix} h_{m,\ell}[0] & 0 & 0 & \dots \\ h_{m,\ell}[M/2] & h_{m,\ell}[M/2-1] & h_{m,\ell}[M/2-2] & \dots \\ h_{m,\ell}[M] & h_{m,\ell}[M-1] & h_{m,\ell}[M-2] & \dots \\ \vdots & \vdots & \vdots & \ddots \end{bmatrix}, \tag{3.27}$$

where $\bar{\mathbf{H}}_{m,\ell} \in \mathbb{C}^{(2L_{\text{P}}-1)\times L_{\text{ch}}}$ is the convolution matrix obtained with the coefficients of $h_{m,\ell}[l]$, $\mathbf{J}_{\frac{M}{2}}$ represents the downsampling by $\frac{M}{2}$ and is defined as

$$\mathbf{J}_{\frac{M}{2}} = \begin{bmatrix} \mathbf{e}_1^{\text{T}} \\ \mathbf{e}_{\frac{M}{2}+1}^{\text{T}} \\ \vdots \\ \mathbf{e}_{(L_{\tilde{h}}-1)\frac{M}{2}+1}^{\text{T}} \end{bmatrix} \tag{3.28}$$

with $\mathbf{e}_q \in \{0,1\}^{(2L_{\text{P}}-1)}$, and the result is that we take each $\frac{M}{2}$-th row of the convolution matrix of $\bar{\mathbf{H}}_{m,\ell}$.

We can now rewrite (3.23) as

$$\mathbf{y}_m[n] = (\mathbf{X}_m[n]\tilde{\mathbf{H}}_{m,m} + \mathbf{X}_{m-1}[n]\tilde{\mathbf{H}}_{m,m-1} + \mathbf{X}_{m+1}[n]\tilde{\mathbf{H}}_{m,m+1})\mathbf{h}_{\text{ch}} + \mathbf{\Gamma}_m\boldsymbol{\eta}[l], \tag{3.29}$$

Again similar to the narrowband model, we define $\mathbf{S}_m[n] = \mathbf{S}_{\text{u},m}[n] + \mathbf{U}_m[n] = \mathbf{X}_m[n]\tilde{\mathbf{H}}_{m,m} + \mathbf{X}_{m-1}[n]\tilde{\mathbf{H}}_{m,m-1} + \mathbf{X}_{m+1}[n]\tilde{\mathbf{H}}_{m,m+1}$, where $\mathbf{S}_{\text{u},m}[n] = \mathbf{X}_m[n]\tilde{\mathbf{H}}_{m,m}$ and $\mathbf{U}_m[n] = \mathbf{X}_{m-1}[n]\tilde{\mathbf{H}}_{m,m-1} + \mathbf{X}_{m+1}[n]\tilde{\mathbf{H}}_{m,m+1}$. We then get for each observed subcarrier

$$\begin{aligned} \mathbf{y}_m[n] &= \mathbf{S}_m[n]\mathbf{h}_{\text{ch}} + \mathbf{\Gamma}_m\boldsymbol{\eta}[l] && (3.30) \\ &= (\mathbf{S}_{\text{u},m}[n] + \mathbf{U}_m[n])\mathbf{h}_{\text{ch}} + \mathbf{\Gamma}_m\boldsymbol{\eta}[l]. && (3.31) \end{aligned}$$

We finally stack M_{o} vectors with the outputs of the M_{o} observed subcarriers we obtain

$$\begin{bmatrix} \mathbf{y}_0[n] \\ \mathbf{y}_1[n] \\ \vdots \\ \mathbf{y}_{M_{\text{o}}-1}[n] \end{bmatrix} = \begin{bmatrix} \mathbf{S}_0[n] \\ \mathbf{S}_1[n] \\ \vdots \\ \mathbf{S}_{M_{\text{o}}-1}[n] \end{bmatrix} \mathbf{h}_{\text{ch}} + \begin{bmatrix} \mathbf{\Gamma}_0 \\ \mathbf{\Gamma}_1 \\ \vdots \\ \mathbf{\Gamma}_{M_{\text{o}}-1} \end{bmatrix} \boldsymbol{\eta}[l], \tag{3.32}$$

$$\begin{aligned} \mathbf{y}[n] &= \mathbf{S}[n]\mathbf{h}_{\text{ch}} + \tilde{\boldsymbol{\eta}}[n] \\ &= (\mathbf{S}_{\text{u}}[n] + \mathbf{U}[n])\mathbf{h}_{\text{ch}} + \tilde{\boldsymbol{\eta}}[n]. && (3.33) \end{aligned}$$

It should be noted that the vectors $\mathbf{y}_m[n]$ that are collected into $\mathbf{y}[n]$ do not need to belong to contiguous subcarriers. This means that the observations can be sparsely taken in the subcarrier domain. This allows the use of preambles that are not full in the sense that they can be frequency multiplexed with data sequences. In this way, a higher spectral efficiency is obtained by reducing the number of training symbols transmitted in the whole training block. In the simulation results, an example of this situation is presented.

3.2.3 Broadband-Narrowband CIR Transformation

We describe here how to obtain many narrowband channel impulse responses given one single broadband channel impulse response.

The narrowband channel observed in each subcarrier can calculated from the broadband channel by the transformation $\mathbf{h}_{\text{ch},m} = \mathbf{B}_m\mathbf{h}_{\text{ch}}$. Thereby, the following definition holds

$$\mathbf{B}_m = \begin{bmatrix} \mathbf{I}_{L_{\text{ch},m}} & \mathbf{0}_{B1} \end{bmatrix} \mathbf{W}^{\text{H}}_{L_{\text{ch},m}M_i} \begin{bmatrix} \mathbf{0}_{B2} & \mathbf{I}_{L_{\text{ch},m}M_i} & \mathbf{0}_{B3} \end{bmatrix} \mathbf{W}_{N_{\text{f}}} \begin{bmatrix} \mathbf{I}_{L_{\text{ch}}} \\ \mathbf{0}_{B4} \end{bmatrix},$$

where $\mathbf{W}_{N_\mathrm{f}}$ is an N_f-DFT matrix, $N_\mathrm{f} = ML_{\mathrm{ch},m}M_i$, $\mathbf{0}_{B1} \in \{0\}^{L_{\mathrm{ch},m}\times(L_{\mathrm{ch},m}(M_i-1))}$, $\mathbf{0}_{B2} \in \{0\}^{(L_{\mathrm{ch},m}M_i)\times(mL_{\mathrm{ch},m}M_i)}$, $\mathbf{0}_{B3} \in \{0\}^{(L_{\mathrm{ch},m}M_i)\times((M-1-m)L_{\mathrm{ch},m}M_i)}$, $\mathbf{0}_{B4} \in \{0\}^{(N_\mathrm{f}-L_\mathrm{ch})\times L_\mathrm{ch}}$, M_i is a resolution factor for the calculation's resolution of the $\mathbf{h}_{\mathrm{ch},m}$.

As a consequence we can rewrite (3.13) as follows

$$\mathbf{y}_m = \mathbf{S}'_m\mathbf{B}_m\mathbf{h}_\mathrm{ch} + \mathbf{\Gamma}_m\boldsymbol{\eta}, \tag{3.34}$$

and similar to (3.33) we can write $\mathbf{y} = \mathbf{S}'\mathbf{h}_\mathrm{ch} + \boldsymbol{\eta}$, with $\mathbf{S}'^{\mathrm{T}} = \left[\mathbf{B}_0^{\mathrm{T}}\mathbf{S}_0'^{\mathrm{T}} \quad \mathbf{B}_1^{\mathrm{T}}\mathbf{S}_1'^{\mathrm{T}} \quad .. \quad \mathbf{B}_{M_\mathrm{o}-1}^{\mathrm{T}}\mathbf{S}_{M_\mathrm{o}-1}'^{\mathrm{T}}\right]^{\mathrm{T}}$.

The narrowband to broadband transformation can be performed by stacking the $\mathbf{h}_{\mathrm{ch},m}$ into a long vector and multiplying it by a stacking of the inverse of matrix $\mathbf{B}_m$.

3.3 Narrowband CIR Estimation

Now that we have introduced the two models, namely, narrowband and broadband, we can derive various explicit estimators for the FBMC system. In this section we present four estimators based on the narrowband model. The first three estimators assume that given an observation vector at the receiver side in one specific subcarrier m, at least L_x subsequent symbols in subcarriers $m-1$, m and $m+1$ are known, i.e. they are reference or pilot symbols. The fourth estimator assumes that only part of those L_x symbols are known and the other contain unknown information at the receiver, for example, payload data.

3.3.1 Per-subcarrier LS Estimation

A first and very common estimator is the LS estimator. This channel estimation is employed when there is no knowledge of statistics of the noise and of the channel.

The objective function here is given by

$$\hat{\mathbf{h}}_{\mathrm{ch},m} = \underset{\mathbf{h}_{\mathrm{ch},m}\in\mathbb{C}^{L_{\mathrm{ch},m}}}{\operatorname{argmin}} \|\mathbf{y}_m - \mathbf{S}_m\mathbf{h}_{\mathrm{ch},m}\|_2^2. \tag{3.35}$$

The solution to the LS problem above is straightforward and given by

$$\hat{\mathbf{h}}_{\mathrm{ch},m} = \left(\mathbf{S}_m^{\mathrm{H}}\mathbf{S}_m\right)^{-1}\mathbf{S}_m^{\mathrm{H}}\mathbf{y}_m. \tag{3.36}$$

It is worth noting that the inverse contain information that is assumed to be known at the receiver side and can be calculated offline. However, as many narrowband channels need to be estimated as the number of receiving subcarriers.

3.3.2 Per-subcarrier ML Estimation

Another classical estimator that we will apply to the FBMC system is the ML estimator, which typically provide better performance than the LS estimator for low SNR scenarios. The ML estimation can be employed when the variance of the noise, i.e. its statistics, is known to the receiver, but the statistics of the channel are not known. The noise variance can be estimated on previous procedures typically employed in the receiver chain, such as synchronization or some preamble detection.

We can see that in the linear model of (3.13) that the noise is zero mean Gaussian distributed with covariance matrix $\mathbf{R}_{\eta,m} = \sigma^2 \mathbf{\Gamma}_m \mathbf{\Gamma}_m^{\mathrm{H}}$ and the observation $\mathbf{y}_m$ given $\mathbf{h}_{\mathrm{ch},m}$ is Gaussian distributed. The ML estimate of $\mathbf{h}_{\mathrm{ch},m}$ is thus given by

$$\hat{\mathbf{h}}_{\mathrm{ch},m} = \arg \max_{\mathbf{h}_{\mathrm{ch},m} \in \mathbb{C}^{L_{\mathrm{ch},m}}} p(\mathbf{y}_m | \mathbf{h}_{\mathrm{ch},m}) = \arg \min_{\mathbf{h}_{\mathrm{ch},m}} J(\mathbf{h}_{\mathrm{ch},m}), \tag{3.37}$$

where

$$J(\mathbf{h}_{\mathrm{ch},m}) = (\mathbf{y}_m - \mathbf{S}_m \mathbf{h}_{\mathrm{ch},m})^{\mathrm{H}} \mathbf{R}_{\eta,m}^{-1} (\mathbf{y}_m - \mathbf{S}_m \mathbf{h}_{\mathrm{ch},m}) . \tag{3.38}$$

Then the ML estimate of the narrowband multipath channel in each subcarrier is given by

$$\hat{\mathbf{h}}_{\mathrm{ch},m} = \left(\mathbf{S}_m^{\mathrm{H}} \mathbf{R}_{\eta,m}^{-1} \mathbf{S}_m\right)^{-1} \mathbf{S}_m^{\mathrm{H}} \mathbf{R}_{\eta,m}^{-1} \mathbf{y}_m. \tag{3.39}$$

It was shown in [7, 11] that the latter estimator works fine provided enough training is employed in the subcarriers m and $m \pm 1$. We should note that the subchannel length, $L_{h_{\mathrm{ch},m}}$, is a design parameter of the estimator. It can be different for each subcarrier depending on how frequency selective the channel is for the corresponding portion of the spectrum.

3.3.3 Per-subcarrier MMSE Estimation

The last classical estimator we would like to introduce for the narrowband subcarrier model of FBMC systems is the MMSE. This channel estimation can be employed when both the noise and the channel statistics are known to the receiver. This knowledge can be obtained by various means, for example, by some longer term averaging or using preambles.

If we assume that the power delay profile of the sub-channel impulse response is known a priori, then we can easily calculate the covariance matrix of $\mathbf{h}_{\mathrm{ch},m}$, here called $\mathbf{R}_{\mathbf{h}_{\mathrm{ch},m}}$. The MMSE estimator has the following objective

$$\hat{\mathbf{h}}_{\mathrm{ch},m} = \underset{\mathbf{h}_{\mathrm{ch},m} \in \mathbb{R}^{L_{\mathrm{ch},m}}}{\operatorname{argmin}} \ \mathrm{E}\left[\|\mathbf{y}_m - \mathbf{S}_m \mathbf{h}_{\mathrm{ch},m}\|_2^2\right] . \tag{3.40}$$

The resulting estimator is then given by

$$\hat{\mathbf{h}}_{\mathrm{ch},m} = \mathbf{R}_{\mathbf{h}_{\mathrm{ch},m}} \mathbf{S}_m^{\mathrm{H}} \left[\mathbf{S}_m \mathbf{R}_{\mathbf{h}_{\mathrm{ch},m}} \mathbf{S}_m^{\mathrm{H}} + \mathbf{R}_{\eta,m}\right]^{-1} \mathbf{y}_m. \tag{3.41}$$

The MMSE estimator will typically provide even better performance than the ML estimator at lower SNR.

3.3.4 Per-subcarrier ML Estimation via EM

In this fourth channel estimator, we assume that the input sequence in the subcarrier m is known, i.e. it is a training or pilot sequence, but the input sequences in subcarriers $m-1$ and $m+1$ are unknown, i.e. they may be carrying payload data or just unknown sequences.

The entries of $\mathbf{S}_{\mathrm{u},m}$ in (3.13) are a result of the convolution between the training sequence in subcarrier m and the resulting subcarrier filter—synthesis convolved with analysis—in the same subcarrier. Although the resulting filter has a purely real impulse response when the prototype has a purely real impulse response, the resulting convolution with the OQAM staggered training sequence results in a complex valued sequence. Consequently all entries of $\mathbf{S}_{\mathrm{u},m}$ are complex

valued. In contrast, the entries of $\mathbf{U}_m$ are alternatingly purely real and purely imaginary valued, because in addition to the OQAM symbols in subcarriers $m-1$ and $m+1$ also the impulse response between the two adjacent subcarriers has alternating real and imaginary coefficients, also resambling an real and imaginary staggering. As a consequence, the interference term $\mathbf{U}_m$ has improper statistics [66] and one way to estimate it is by employing Widely Linear (WL) processing.

Now, one can rewrite the observation vector in (3.13) on each subcarrier as

$$\mathbf{y}_m = \mathbf{S}_{\mathrm{u},m}\mathbf{h}_{\mathrm{ch},m} + \mathbf{H}_m\mathbf{u}_m + \boldsymbol{\eta}_m = \mathbf{S}_{\mathrm{u},m}\mathbf{h}_{\mathrm{ch},m} + \mathbf{H}'_m\mathcal{O}_m\mathbf{H}_{\mathrm{u},m}\mathbf{x}_{\mathrm{u},m} + \boldsymbol{\eta}_m \tag{3.42}$$

where now we assume that the vector $\mathbf{u}_m \in \mathbb{R}^{L_{h'}}$, or equivalently $\mathbf{x}_{\mathrm{u},m}$, in each subcarrier is unknown, $\mathbf{u}_m = \mathbf{H}_{\mathrm{u},m}\mathbf{x}_{\mathrm{u},m}$ and $\mathbf{H}_m = \mathbf{H}'_m\mathcal{O}_m$, where $\mathbf{H}'_m$ is the convolution matrix associated to the m-th narrowband channel impulse response, i.e. $\mathbf{h}_{\mathrm{ch},m}$. For convenience, we define

$$\mathcal{O}_m = \begin{cases} \mathrm{diag}([1, \mathrm{j}, 1, ...]), & \text{for } m \text{ even} \\ \mathrm{diag}([\mathrm{j}, 1, \mathrm{j}, ...]), & \text{for } m \text{ odd.} \end{cases} \tag{3.43}$$

Note that in this case $\mathbf{H}_{\mathrm{u},m} \in \mathbb{R}^{L_{h'} \times 2L_x}$ is a purely real matrix related to the matrices $\mathbf{H}_{m,m-1}$ and $\mathbf{H}_{m,m+1}$ in (3.5).

Although the exact values of $\mathbf{u}_m$ are unknown, its statistics are typically known, for example, if it contains QAM symbols. We define then an interference covariance matrix as

$$\mathbf{R}_{u,m} = \frac{\sigma_x^2}{2}\mathbf{H}_{\mathrm{u},m}\mathbf{H}_{\mathrm{u},m}^{\mathrm{H}}, \tag{3.44}$$

where we assume that $\mathbf{x}_{\mathrm{u},m}$ is i.i.d. and Gaussian distributed with zero mean and variance $\sigma_x^2/2$. This is typically a good approximation although $\mathbf{x}_{\mathrm{u},m}$ elements are symbols taken from a finite constellation.

For the linear model of (3.42), the ML estimator has no closed form solution due to the unknown or interference components, and an efficient way to implement it is to employ the iterative EM algorithm [55].

The EM algorithm works here as follows: Before the first iteration, a rough ML channel estimate is obtained by ignoring the interference and only considering the known training sequence in the observed subcarrier m. This estimate is given by

$$\hat{\mathbf{h}}_{m,0} = (\mathbf{S}_{\mathrm{u},m}^{\mathrm{H}}\mathbf{R}_{\eta,m}^{-1}\mathbf{S}_{\mathrm{u},m})^{-1}\mathbf{S}_{\mathrm{u},m}^{\mathrm{H}}\mathbf{R}_{\eta,m}^{-1}\mathbf{y}_m. \tag{3.45}$$

Then, the iterative process starts, where for each iteration i, the algorithm involves two steps: the E-step and the M-step. In the E-step, an approximation of the ML objective function (here its derivative) is obtained by taking the expected value of it conditioned on the channel estimated in the iteration before and on the observation sequence, as follows

$$\begin{aligned} \mathrm{E}_{\mathbf{u}|\mathbf{y},\mathbf{h}_{\mathrm{ch},m,i}}\left[\frac{\partial J(\mathbf{h}_{\mathrm{ch},m,i})}{\partial \mathbf{h}_{\mathrm{ch},m,i}^{\mathrm{H}}}\right] &= \big[\mathbf{S}_{\mathrm{u},m}^{\mathrm{H}}\mathbf{R}_{\eta,m}^{-1}\mathbf{S}_{\mathrm{u},m} + \mathbf{S}_{\mathrm{u},m}^{\mathrm{H}}\mathbf{R}_{\eta,m}^{-1}\mathrm{E}[\mathbf{U}_m] + \mathrm{E}[\mathbf{U}_m]^{\mathrm{H}}\mathbf{R}_{\eta,m}^{-1}\mathbf{S}_{\mathrm{u},m} \\ &\quad + \mathrm{E}[\mathbf{U}_m^{\mathrm{H}}\mathbf{R}_{\eta,m}^{-1}\mathbf{U}_m]\big]\,\mathbf{h}_{\mathrm{ch},m,i} - (\mathbf{S}_{\mathrm{u},m} + \mathrm{E}[\mathbf{U}_m])^{\mathrm{H}}\mathbf{R}_{\eta,m}^{-1}\mathbf{y}_m. \end{aligned} \tag{3.46}$$

We can show that the result is a function of $\mathrm{E}[\mathbf{u}_m]$ and $\mathrm{E}[\mathbf{U}_m^{\mathrm{H}}\mathbf{R}_{\eta,m}^{-1}\mathbf{U}_m]$. $\mathrm{E}[\mathbf{u}_m] = \hat{\mathbf{u}}_{m,i}$ can be viewed as an instantaneous estimate of the interference term $\mathbf{u}_m$ in the i-th iteration.

To express the last expectation in (3.46) also in terms of the estimate $\hat{\mathbf{u}}_i$, one has first to write the matrix $\mathbf{U}_m$ as a function of vector $\mathbf{u}_m$ as

$$\mathbf{U}_m = \sum_{j=1}^{L_{\mathrm{ch},m}} \mathbf{D}_j \mathcal{O}_m \mathbf{u}_m \mathbf{e}_j^T, \tag{3.47}$$

where $\mathbf{D}_j = \begin{bmatrix} \mathbf{0}_{j-1} & \mathbf{I}_{L_\mathrm{o}} & \mathbf{0}_{L_{\mathrm{h}'}-L_\mathrm{o}-j} \end{bmatrix}$ is a matrix that selects L_o rows of $\mathbf{u}_m$ and $\mathbf{e}_j \in \{0,1\}^{L_{\mathrm{ch},m}}$ is a vector with one in the j-th row and the rest of its elements are zero. Then we plug(3.47) in the expected value

$$\begin{aligned}
\mathrm{E}\left[\mathbf{U}_m^{\mathrm{H}} \mathbf{R}_{\eta,m}^{-1} \mathbf{U}_m\right] &= \mathrm{E}\left[\sum_{l=1}^{L_{\mathrm{ch},m}} \mathbf{e}_l \mathbf{u}_m^{\mathrm{T}} \mathcal{O}_m^{\mathrm{H}} \mathbf{D}_l^{\mathrm{T}} \mathbf{R}_{\eta,m}^{-1} \sum_{j=1}^{L_{\mathrm{ch},m}} \mathbf{D}_j \mathcal{O}_m \mathbf{u}_m \mathbf{e}_j^{\mathrm{T}}\right] \\
&= \sum_{l=1}^{L_{\mathrm{ch},m}} \mathbf{e}_l \sum_{j=1}^{L_{\mathrm{ch},m}} \mathrm{E}\left[\mathbf{u}_m^{\mathrm{T}} \mathcal{O}_m^{\mathrm{H}} \mathbf{D}_l^{\mathrm{T}} \mathbf{R}_{\eta,m}^{-1} \mathbf{D}_j \mathcal{O}_m \mathbf{u}_m\right] \mathbf{e}_j^{\mathrm{T}} \\
&= \sum_{l=1}^{L_{\mathrm{ch},m}} \mathbf{e}_l \sum_{j=1}^{L_{\mathrm{ch},m}} \mathrm{tr}\left\{\mathcal{O}_m^{\mathrm{H}} \mathbf{D}_l^{\mathrm{T}} \mathbf{R}_{\eta,m}^{-1} \mathbf{D}_j \mathcal{O}_m \mathrm{E}\left[\mathbf{u}_m \mathbf{u}_m^{\mathrm{T}}\right]\right\} \mathbf{e}_j^{\mathrm{T}}.
\end{aligned} \tag{3.48}$$

Furthermore, we can develop the expression

$$\mathrm{E}\left[\mathbf{u}_m \mathbf{u}_m^{\mathrm{T}}\right] = \mathbf{R}_{\epsilon,m,i} + \mathrm{E}[\mathbf{u}_m]\mathrm{E}[\mathbf{u}_m]^{\mathrm{T}} = \mathbf{R}_{\epsilon,m,i} + \hat{\mathbf{u}}_{m,i} \hat{\mathbf{u}}_{m,i}^{\mathrm{T}}, \tag{3.49}$$

where $\mathbf{R}_{\epsilon,m,i}$ is the covariance matrix of the estimation error of $\mathbf{u}_m$ in the i-th iteration. Consequently, we get

$$\begin{aligned}
\mathrm{E}\left[\mathbf{U}_m^{\mathrm{H}} \mathbf{R}_{\eta,m}^{-1} \mathbf{U}_m\right] &= \sum_{l=1}^{L_{\mathrm{ch},m}} \mathbf{e}_l \sum_{j=1}^{L_{\mathrm{ch},m}} \mathrm{tr}\left\{\mathcal{O}_m^{\mathrm{H}} \mathbf{D}_l^{\mathrm{T}} \mathbf{R}_{\eta,m}^{-1} \mathbf{D}_j \mathcal{O}_m \mathbf{R}_{\epsilon,m,i}\right\} \mathbf{e}_j^{\mathrm{T}} + \mathrm{E}\left[\mathbf{U}_m\right]^{\mathrm{H}} \mathbf{R}_{\eta,m}^{-1} \mathrm{E}\left[\mathbf{U}_m\right], \\
&= \mathbf{\Psi}_{m,i} + \mathrm{E}\left[\mathbf{U}_m\right]^{\mathrm{H}} \mathbf{R}_{\eta,m}^{-1} \mathrm{E}\left[\mathbf{U}_m\right],
\end{aligned} \tag{3.50}$$

where we applied the definition $[\mathbf{\Psi}_{m,i}]_{j,l} = \mathrm{tr}\left\{\mathcal{O}_m^{\mathrm{H}} \mathbf{D}_j^{\mathrm{T}} \mathbf{R}_{\eta,m}^{-1} \mathbf{D}_l \mathcal{O}_m \mathbf{R}_{\epsilon,m,i}\right\}$. Finally, we can find the expression for the E-step as

$$\begin{aligned}
\mathrm{E}_{\mathbf{u}_m|\mathbf{y}_m,\mathbf{h}_{\mathrm{ch},m,i}}\left[\frac{\partial J(\mathbf{h}_{\mathrm{ch},m,i})}{\partial \mathbf{h}_{\mathrm{ch},m,i}^{\mathrm{H}}}\right] &= \left(\left(\mathbf{S}_{\mathrm{u},m} + \hat{\mathbf{U}}_{m,i}\right)^{\mathrm{H}} \mathbf{R}_{\eta,m}^{-1} \left(\mathbf{S}_{\mathrm{u},m} + \hat{\mathbf{U}}_{m,i}\right) + \mathbf{\Psi}_{m,i}\right) \mathbf{h}_{\mathrm{ch},m,i} \\
&\quad - \left(\mathbf{S}_{\mathrm{u},m} + \hat{\mathbf{U}}_{m,i}\right)^{\mathrm{H}} \mathbf{R}_{\eta,m}^{-1} \mathbf{y}_m.
\end{aligned} \tag{3.51}$$

Given that an estimate of $\mathbf{h}_{\mathrm{ch},m,i}$ and the training sequence are known, one can subtract $\mathbf{S}_{\mathrm{u},m}\hat{\mathbf{h}}_{\mathrm{ch},m,i}$ from the observations vector to make an estimate of the interference vector $\mathbf{u}_m$. Then the resulting vector can be processed using an MMSE estimator. As mentioned previously, the interference vector is composed of purely real and purely imaginary terms, and for that a WL MMSE estimator [66] can be employed as follows

$$\mathrm{E}[\mathbf{u}_{m,i}] = \hat{\mathbf{u}}_{m,i} = 2\,\mathbb{R}\mathrm{e}\left\{\boldsymbol{\mathcal{W}}_m^{\mathrm{H}} \left(\mathbf{y}_m - \mathbf{S}_{\mathrm{u},m}\hat{\mathbf{h}}_{\mathrm{ch},m,i}\right)\right\}, \tag{3.52}$$

where the estimator matrix is given by

$$\boldsymbol{\mathcal{W}}_m = \left(\mathbf{R}_{y,m} - \mathbf{P}_{y,m}^{\mathrm{T}}\mathbf{R}_{y,m}^{-\mathrm{T}}\mathbf{P}_{y,m}^{\mathrm{H}}\right)^{-1}\left(\mathbf{R}_{uy,m}^{\mathrm{H}} - \mathbf{P}_{y,m}^{\mathrm{T}}\mathbf{R}_{y,m}^{-\mathrm{T}}\mathbf{P}_{uy,m}^{\mathrm{H}}\right), \tag{3.53}$$

the following definitions for the covariance matrices hold

$$\mathbf{R}_{y,m} = \hat{\mathbf{H}}_{m,i}\mathbf{R}_{u,m}\hat{\mathbf{H}}_{m,i}^{\mathrm{H}} + \mathbf{R}_{\eta,m}, \text{ and } \mathbf{R}_{uy,m} = \mathbf{R}_{u,m}\hat{\mathbf{H}}_{m,i}^{\mathrm{H}}, \tag{3.54}$$

and the pseudo-covariance matrices are defined by

$$\mathbf{P}_{y,m} = \hat{\mathbf{H}}_{m,i}\mathbf{R}_{u,m}\hat{\mathbf{H}}_{m,i}^{\mathrm{T}}, \text{ and } \mathbf{P}_{uy,m} = \mathbf{R}_{u,m}\hat{\mathbf{H}}_{m,i}^{\mathrm{T}}, \tag{3.55}$$

and $\hat{\mathbf{H}}_{m,i} = \hat{\mathbf{H}}'_{m,i}\mathcal{O}_m$, where $\hat{\mathbf{H}}'_{m,i}$ is a convolution matrix containing the estimated subchannel impulse response $\hat{\mathbf{h}}_{\mathrm{ch},m,i}$. The corresponding covariance matrix of the estimation error is given by

$$\mathbf{R}_{\epsilon,m,i} = \mathbf{R}_{u,m} - 2\,\mathbb{R}\mathrm{e}\left\{\boldsymbol{\mathcal{W}}_m\mathbf{R}_{uy,m}^{\mathrm{H}}\right\}. \tag{3.56}$$

Finally, the M-step is performed, where $J(\mathbf{h}_{m,i})$ is minimized, resulting in a new channel estimate to be used in the next iteration $i+1$

$$\hat{\mathbf{h}}_{\mathrm{ch},m,i+1} = \left(\left(\mathbf{S}_{\mathrm{u},m} + \hat{\mathbf{U}}_{m,i}\right)^{\mathrm{H}}\mathbf{R}_{\eta,m}^{-1}\left(\mathbf{S}_{\mathrm{u},m} + \hat{\mathbf{U}}_{m,i}\right) + \boldsymbol{\Psi}_{m,i}\right)^{-1}\left(\mathbf{S}_{\mathrm{u},m} + \hat{\mathbf{U}}_{m,i}\right)^{\mathrm{H}}\mathbf{R}_{\eta,m}^{-1}\mathbf{y}_m. \tag{3.57}$$

The alternate estimation of $\mathbf{u}_m$ and $\mathbf{h}_{\mathrm{ch},m}$ is then repeated for N_{EM} iterations until convergence is achieved.

3.3.5 Simulation Results

The simulation results reported here are from the numerical performance evaluation of the narrowband EM-based ML sub-channel estimator. An ITU Veh-A channel was employed as channel model, at a bandwidth of 10 MHz and sampling rate $M/T = 15.36$ MHz. The FBMC/OQAM system was employed with $M = 256$ subcarriers, from which 210 were occupied with training and data symbols, with the rest being inactive. The resulting subcarrier spacing is 60 kHz. The prototype is an RRC filter with $K = 4$ (of length $L_{\mathrm{P}} = 1025$) and roll-off one. With this configuration and scenario, $L_{\mathrm{ch},m} = 5$ taps for the narrowband multipath sub-channels and $L_{\mathrm{e}} = 5$ taps for the corresponding per-subcarrier equalizers were seen to be sufficient for all subcarriers. Preamble-based channel estimation was performed, with L_{o} observations per subcarrier. This corresponds to a training sequence of $L_x = 19 + L_{\mathrm{o}}$ FBMC symbols. 16-QAM was adopted for FBMC/OQAM and 32-QAM for CP-OFDM. Moreover, the CP length was $L_{\mathrm{cp}} = 64$. With this combination of constellation size and CP length, the two systems achieve the same data throughput. For the training sequences, pseudorandom QPSK symbols were employed. Monte-Carlo simulations were run on 200 channel realizations for different E_{b}/N_0. For calculating the bit error rate (BER), 100 FBMC data symbols were transmitted after training.

In Fig. 3.4, the NMSE of the narrowband channel estimation as a function of E_{b}/N_0 is depicted for different number of observation L_{o} and for different numbers of iterations N_{EM}. Also the results for the ML narrowband channel estimation with known training on the adjacent subcarriers, i.e. no ICI, are shown as references. We can observe a considerable loss in NMSE for the EM

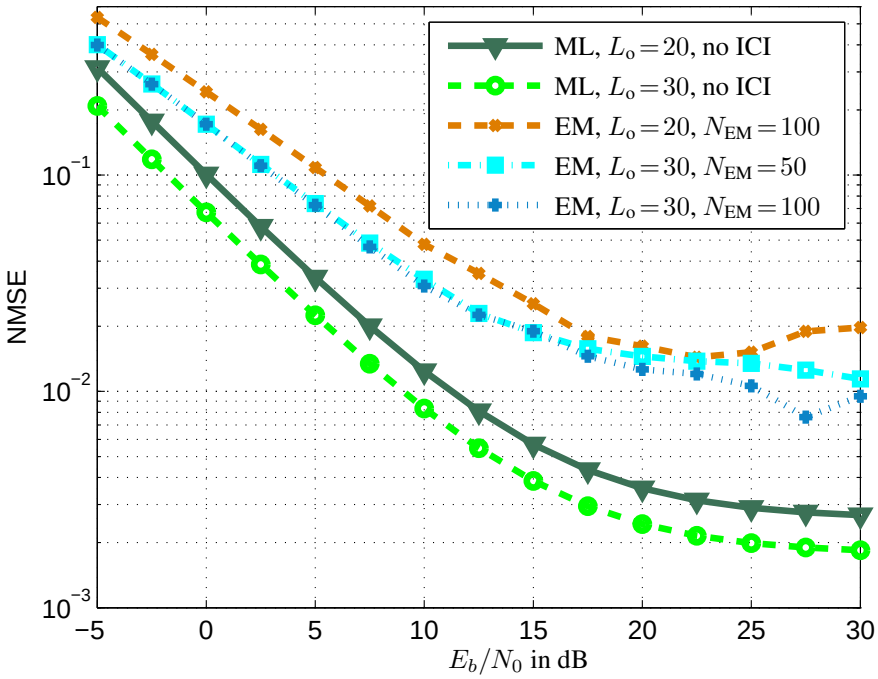

Fig. 3.4. NMSE as a function of E_b/N_0 for ML estimator, different number of observations and EM iterations.

based estimator that increases with the E_b/N_0. The coresponding BER as a function of E_b/N_0 is shown in Fig. 3.5. The results for perfect channel state information for both FBMC and OFDM are included for comparison and as references. We can observe that for the BER the gap between the two estimation methods is not so high as the NMSE curves show. We can also note that for sufficiently many observations and iterations, very good estimates of the subchannels can be achieved for a broad range of E_b/N_0. Regarding the convergence of the algorithm, it was observed in the experiments that it practically always provides a stable solution after a certain number of iterations.

3.4 Broadband CIR Estimation

Now based on the linear model in (3.33) and analogous to the previous section on narrowband channel estimation, we will provide here also the four estimators, i.e. the LS, ML, MMSE and ML combined with EM algorithm.

3.4.1 LS Estimation

The optimization for the LS estimation for the broadband model is given by

$$\hat{\mathbf{h}}_\mathrm{ch} = \underset{\mathbf{h}_\mathrm{ch} \in \mathbb{C}^{L_\mathrm{ch}}}{\operatorname{argmin}} \|\mathbf{y} - \mathbf{S}\mathbf{h}_\mathrm{ch}\|_2^2 \tag{3.58}$$

we have the estimate

$$\hat{\mathbf{h}}_\mathrm{ch} = \left(\mathbf{S}^\mathrm{H}\mathbf{S}\right)^{-1} \mathbf{S}^\mathrm{H}\mathbf{y}. \tag{3.59}$$

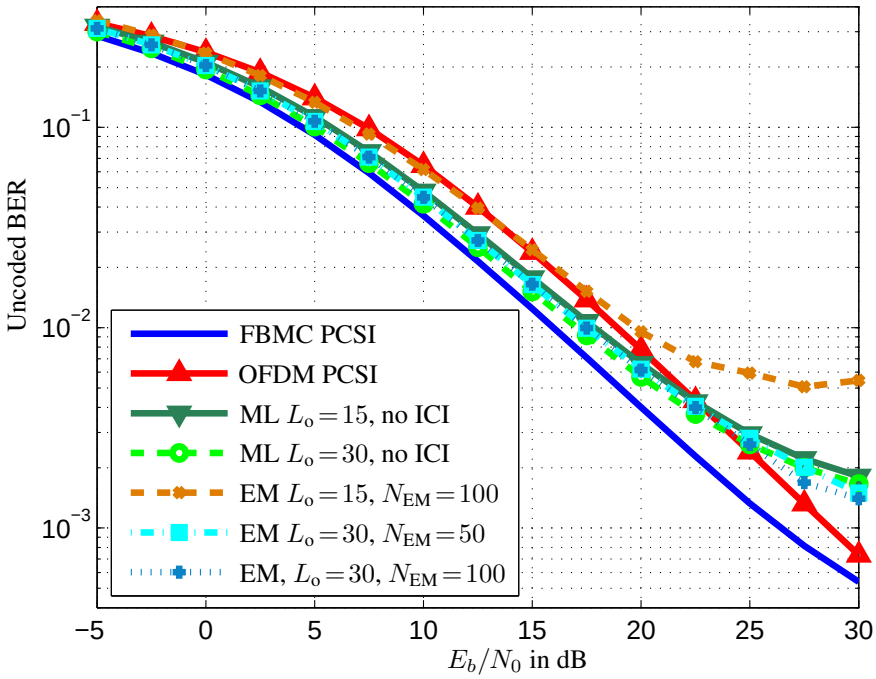

Fig. 3.5. Uncoded BER as a function of E_b/N_0 for ML estimator, different number of observations and EM iterations.

The covariance matrix of the estimation error $\boldsymbol{\Delta}\hat{\mathbf{h}}_{\text{ch}} = (\hat{\mathbf{h}}_{\text{ch}} - \mathbf{h}_{\text{ch}})$ broadband LS estimator is given by

$$\mathbf{R}_{\boldsymbol{\Delta}\hat{\mathbf{h}}_{\text{LS}}} = \mathrm{E}\left[\boldsymbol{\Delta}\hat{\mathbf{h}}_{\text{ch}}\boldsymbol{\Delta}\hat{\mathbf{h}}_{\text{ch}}^{\text{H}}\right] = \left(\mathbf{S}^{\text{H}}\mathbf{S}\right)^{-1} \tag{3.60}$$

The theoretical MSE of the broadband LS estimator, that in this case it is equal to the Cramér-Rao Lower Bound (CRLB) is given by

$$\epsilon_{\text{LS}} = \frac{\sigma^2 M_{\text{f}}}{M}\,\mathrm{tr}\left\{\mathbf{R}_{\boldsymbol{\Delta}\hat{\mathbf{h}}_{\text{LS}}}\right\} = \frac{\sigma^2 M_{\text{f}}}{M}\,\mathrm{tr}\left\{\left(\mathbf{S}^{\text{H}}\mathbf{S}\right)^{-1}\right\}, \tag{3.61}$$

where M_{f} is the total number of subcarriers occupied with either data or training. In practical deployment of FBMC $M_{\text{f}} < M$ to take advantage of the spectral containment of the prototype filter and to leave a band-guard to the adjacent channel, similar to what is also done in CP-OFDM. In this case, $\mathbf{R}_{\boldsymbol{\Delta}\hat{\mathbf{h}}_{\text{LS}}}$ will become ill-conditioned, i.e. the ratio between the largest and the smallest eingenvalue becomes too large. The intuitive explanation is that we are not able to estimate the channel in the region of the spectrum where there is neither training nor data transmitted, i.e. there is no excitation our sounding signal in those regions of the channel. In this case the calculation of the inverse will explode and some numerical measure has to be taken.

We have decided to utilize a pseudo-inverse with the help of the Singular Value Decomposition (SVD) as a measure to mitigate the numerical overrun of the inverse. The total number of singular values of $\mathbf{R}_{\boldsymbol{\Delta}\hat{\mathbf{h}}_{\text{LS}}}$ is L_{ch}—its dimensions are $L_{\text{ch}} \times L_{\text{ch}}$—and it can be proven that only $N_{\text{SV}} = \left\lceil \frac{L_{\text{ch}} M_{\text{f}}}{M} \right\rceil$ singular values need to be inverted to obtain the best theoretical MSE performance. As a consequence, for the theoretical MSE only the sum of the inverted singular values need to be performed. Later, in the simulation results, we will show the effect of the use of the pseudo-inverse in the measured MSE.

3.4.2 ML Estimation

We can see that in (3.33) the noise vector $\boldsymbol{\eta}$ is Gaussian distributed with zero mean and covariance matrix $\mathbf{R}_\eta = \sigma_\nu^2 \boldsymbol{\Gamma}\boldsymbol{\Gamma}^{\mathrm{H}} = \mathrm{diag}(\mathbf{R}_{\eta,0}, \mathbf{R}_{\eta,1}, ..., \mathbf{R}_{\eta,M_\mathrm{o}-1})$ and the observation $\mathbf{y}$ given $\mathbf{h}_{\mathrm{ch}}$ is then Gaussian distributed. The ML estimate of $\mathbf{h}_{\mathrm{ch}}$ in this case is given by

$$\begin{aligned}\hat{\mathbf{h}}_{\mathrm{ch}} &= \arg \max_{\mathbf{h}_{\mathrm{ch}} \in \mathbb{C}^{L_{\mathrm{ch}}}} p(\mathbf{y}|\mathbf{h}_{\mathrm{ch}}) = \arg \min_{\mathbf{h}_{\mathrm{ch}}} J(\mathbf{h}_{\mathrm{ch}}), \\ &= \left(\mathbf{S}^{\mathrm{H}}\mathbf{R}_\eta^{-1}\mathbf{S}\right)^{-1} \mathbf{S}^{\mathrm{H}}\mathbf{R}_\eta^{-1}\mathbf{y}, \end{aligned} \tag{3.62}$$

where

$$J(\mathbf{h}_{\mathrm{ch}}) = (\mathbf{y} - \mathbf{S}\mathbf{h}_{\mathrm{ch}})^{\mathrm{H}}\mathbf{R}_\eta^{-1}(\mathbf{y} - \mathbf{S}\mathbf{h}_{\mathrm{ch}}) \tag{3.63}$$

and we assume here that $(\mathbf{S}^{\mathrm{H}}\mathbf{R}_\eta^{-1}\mathbf{S})$ is non-singular. Moreover, the covariance matrix of the estimation error $\boldsymbol{\Delta}\hat{\mathbf{h}}_{\mathrm{ch}} = (\hat{\mathbf{h}}_{\mathrm{ch}} - \mathbf{h}_{\mathrm{ch}})$ of the broadband ML estimator is given by

$$\mathbf{R}_{\boldsymbol{\Delta}\hat{\mathbf{h}}_{\mathrm{ch}}} = \mathrm{E}\left[\boldsymbol{\Delta}\hat{\mathbf{h}}_{\mathrm{ch}}\boldsymbol{\Delta}\hat{\mathbf{h}}_{\mathrm{ch}}^{\mathrm{H}}\right] = \left(\mathbf{S}^{\mathrm{H}}\mathbf{R}_\eta^{-1}\mathbf{S}\right)^{-1}. \tag{3.64}$$

As a consequence, the theoretical MSE of the broadband ML estimator is given by

$$\epsilon_{\mathrm{ML}} = \frac{\sigma^2 M_{\mathrm{f}}}{M} \mathrm{tr}\left\{\mathbf{R}_{\boldsymbol{\Delta}\hat{\mathbf{h}}_{\mathrm{ch}}}\right\}. \tag{3.65}$$

When multicarrier systems like FBMC or CP-OFDM are deployed, the number of subcarriers filled with data and training M_{f} is smaller than M, in order to allow for upsampling, filtering and D/A conversion. Even if all M_{f} subcarriers are only filled with training symbols, the estimation of the broadband CIR can only be performed in a fraction of its total frequency response. As a consequence $(\mathbf{S}^{\mathrm{H}}\mathbf{R}_\eta^{-1}\mathbf{S})$ will become ill conditioned or, most probably, singular. The reason is that the portions of the channel frequency response that are not excited cannot and need not be reliably estimated.

To solve this problem we define the downsampled (DS) broadband CIR vector $\mathbf{h}_{\mathrm{DS}} \in \mathbb{C}^{L_{h_{\mathrm{DS}}}}$ that can be estimated in the occupied spectrum. Then we define the linear transformation $\mathbf{h}_{\mathrm{ch}} = \mathbf{A}\mathbf{h}_{\mathrm{DS}}$, that performs a fractionally upsampling of $\mathbf{h}_{\mathrm{DS}}$ by a factor of $L_{\mathrm{frac}} = L_{\mathrm{ch}}/L_{h_{\mathrm{DS}}}$, where $L_{h_{\mathrm{DS}}} = \lfloor \frac{M_{\mathrm{f}}}{M} L_{\mathrm{ch}} \rfloor$. This operation is performed in three steps: upsampling by a factor of L_{ch}, low-pass filtering and downsampling by a factor $L_{h_{\mathrm{DS}}}$. Mathematically, this can be described by

$$\mathbf{A} = \mathbf{J}_{\mathrm{DS}}^{A} \begin{bmatrix} \mathbf{0}_A & \mathbf{I}_{L_{h_{\mathrm{DS}}} L_h} & \mathbf{0}_A \end{bmatrix} \mathbf{H}_{\mathrm{int}} \mathbf{J}_{\mathrm{US}} \in \mathbb{R}^{L_h \times L_{h_{\mathrm{DS}}}}, \tag{3.66}$$

where $\mathbf{J}_{\mathrm{DS}}^{A}$ is a downsampling matrix with its ℓ-th row given by $\mathbf{e}_q^T \in \{0,1\}^{(L_{h_{\mathrm{DS}}} L_{\mathrm{ch}})}$ for $q = (\ell - 1)L_{h_{\mathrm{DS}}} + 1$ and $\ell \in \{1, 2, ..., L_{\mathrm{ch}}\}$, $\mathbf{J}_{\mathrm{US}}$ is an upsampling matrix with its ℓ-th column given by $\mathbf{e}_q \in \{0,1\}^{(L_{h_{\mathrm{DS}}} L_{\mathrm{ch}})}$ for $q = (\ell - 1)L_{\mathrm{ch}} + 1$ and $\ell \in \{1, 2, ..., L_{h_{\mathrm{DS}}}\}$, $\mathbf{H}_{\mathrm{int}} \in \mathbb{R}^{(L_{\mathrm{DS}} L_{\mathrm{ch}} + 2(d_g - 1)) \times (L_{h_{\mathrm{DS}}} L_h)}$ is a convolution matrix obtained from the interpolation filter $\mathbf{g}_{\mathrm{int}} \in \mathbb{R}^{2d_g - 1}$, $\mathbf{0}_A \in \{0\}^{(L_{h_{\mathrm{DS}}} L_{\mathrm{ch}}) \times (d_g - 1)}$. $g_{\mathrm{int}}[n]$ is taken as an FIR approximation of a raised cosine (RC) filter with a sharp roll-off $\alpha = 0.001$, transfer function degree of $L_{g_{\mathrm{int}}} = 10 L_{h_{\mathrm{DS}}} L_{\mathrm{ch}}$ and group delay $d_g = 5L_{h_{\mathrm{DS}}} + 1$.

By substituting $\mathbf{h} = \mathbf{A}\mathbf{h}_{\mathrm{DS}}$ in (3.33) we can calculate the new ML estimator to obtain

$$\hat{\mathbf{h}}_{\mathrm{DS}} = \left(\mathbf{A}^{\mathrm{H}}\mathbf{S}^{\mathrm{H}}\mathbf{R}_\eta^{-1}\mathbf{S}\mathbf{A}\right)^{-1} \mathbf{A}^{\mathrm{H}}\mathbf{S}^{\mathrm{H}}\mathbf{R}_\eta^{-1}\mathbf{y}, \tag{3.67}$$

where now $\left(\mathbf{A}^{\mathrm{H}}\mathbf{S}^{\mathrm{H}}\mathbf{R}_\eta^{-1}\mathbf{S}\mathbf{A}\right)$ is neither ill conditioned nor singular and the corresponding MSE is given by

$$\epsilon_{\mathrm{DS}} = \frac{\sigma_\nu^2 M_{\mathrm{f}}}{M} \mathrm{tr}\left\{\left(\mathbf{A}^{\mathrm{H}}\mathbf{S}^{\mathrm{H}}\mathbf{R}_\eta^{-1}\mathbf{S}\mathbf{A}\right)^{-1}\right\}. \tag{3.68}$$

3.4.3 MMSE Estimation

Let us here also assume that the power delay profile of the broadband impulse response is known a priori. In other words, the covariance matrix of $\mathbf{h}_{\text{ch}}$, here called $\mathbf{R}_{\mathbf{h}_{\text{ch}}}$, is provided to the channel estimator. This can be done via estimation of the matrix from other reference symbols or other source of information about the environment. In this case, another alternative is to minimize the MSE of the channel estimation, which is formulated as

$$\hat{\mathbf{h}}_{\text{ch}} = \underset{\mathbf{h}_{\text{ch}} \in \mathbb{C}^{L_{\text{ch}}}}{\operatorname{argmin}} \, \mathrm{E}\left[\|\mathbf{y} - \mathbf{S}\mathbf{h}_{\text{ch}}\|_2^2\right]. \tag{3.69}$$

By solving (3.69), one can find that the MMSE solution for the broadband channel estimation is expressed as

$$\hat{\mathbf{h}}_{\text{ch}} = \mathbf{R}_{\mathbf{h}_{\text{ch}}}\mathbf{S}^{\text{H}}\left(\mathbf{S}\mathbf{R}_{\mathbf{h}_{\text{ch}}}\mathbf{S}^{\text{H}} + \mathbf{R}_{\eta}\right)^{-1}\mathbf{y}. \tag{3.70}$$

Finally, the MSE of the broadband MMSE estimator is given by

$$\begin{aligned}\epsilon_{\text{MMSE}} &= \operatorname{tr}\left\{\mathbf{R}_{\boldsymbol{\Delta}\hat{\mathbf{h}}_{\text{ch}}}\right\} \\ &= \operatorname{tr}\left\{\left(\mathbf{I}_{L_{\text{ch}}} - \mathbf{R}_{\mathbf{h}_{\text{ch}}}\mathbf{S}^{\text{H}}\left(\mathbf{S}\mathbf{R}_{\mathbf{h}_{\text{ch}}}\mathbf{S}^{\text{H}} + \frac{\sigma^2 M_{\text{f}}}{M}\mathbf{R}_{\eta}\right)^{-1}\mathbf{S}\right)\mathbf{R}_{\mathbf{h}_{\text{ch}}}\right\}.\end{aligned} \tag{3.71}$$

In the case of the broadband MMSE estimator, there is no conditioning problem for the matrix that has to be inverted, at least for typical E_b/N_0 values. Only for very high E_b/N_0 values some numerical measure has to be taken, for example, the SVD approach mentioned for the LS estimator can be used.

3.4.4 Simulation Results Comparing LS, ML and MMSE Estimators

For the simulations, the same scenario is considered as previously, where the length of $\mathbf{h}_{\text{ch}}$ is $L_{\text{ch}} = 36$. Of the $M = 256$ subcarriers, either all or only 111 were carrying training signals. As previously, QPSK pseudo-random training sequences were employed, of length $L_x = L_{\text{o}} + 19$ symbols were employed. The parameter M_{e} gives the distance (in frequency) between neighboring pilot subcarriers. It thus denotes how densely or sparsely were the subcarriers occupied with training sequences. Thus, $M_{\text{e}} = 1$ means that all 210 subcarriers are used for the estimation while $M_{\text{e}} = 7$ implies that only 37 subcarriers were used as pilot tones.

In Fig. 3.6, the MSE performance of the LS, ML and MMSE estimators and for a different number of observations is depicted. As expected the MMSE provides the best MSE performance and increasing the number of subcarriers—reducing M_{e}—used for channels significantly improves the performance. It is worth noting that we have reduced the number of observations L_{o} in the last case.

We show some simulation results for the case $M_{\text{f}} = 210$ in Fig. 3.7. In this case only $N_{\text{SV}} = \lceil \frac{L_h M_{\text{f}}}{M} \rceil = 30$ singular values are inverted. One can see the error floor because of the bad approximation of the inverse.

Again for $M_{\text{f}} = 210$, in Fig. 3.8 we have also employed the pseudo-inverse, but now $N_{\text{SV}} = 32$. We can see there that the simulated MSE is closer to the CRLB for wider range of E_b/N_0

In Fig. 3.9, the result of equalizing these channels with the WL MMSE equalizer of [75, 77] of length 5 and with 16-QAM data is shown. Again, in this plot the perfect CSI case is included for the sake of the comparison.

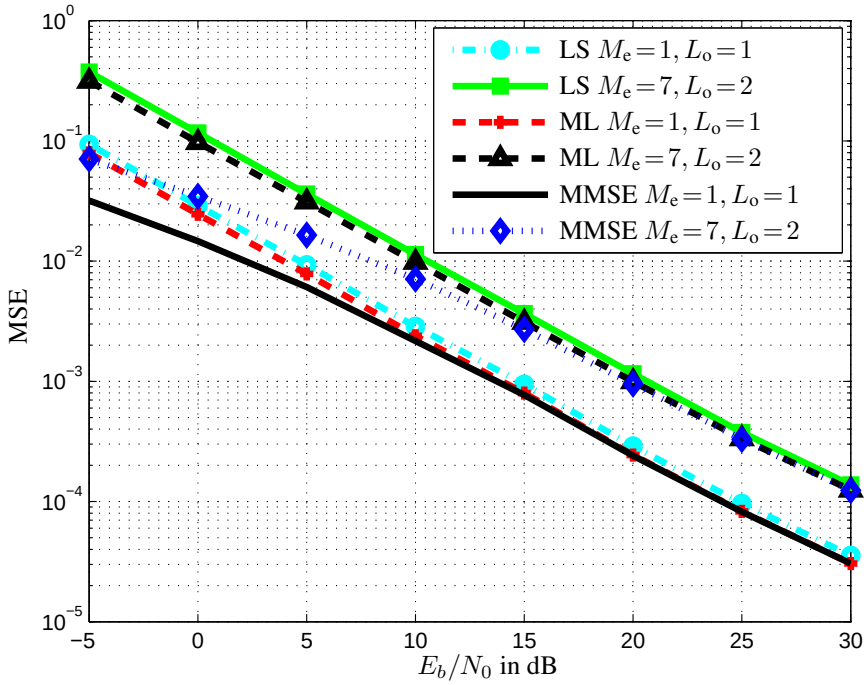

Fig. 3.6. MSE as a function of E_b/N_0 for different estimators and training parameters.

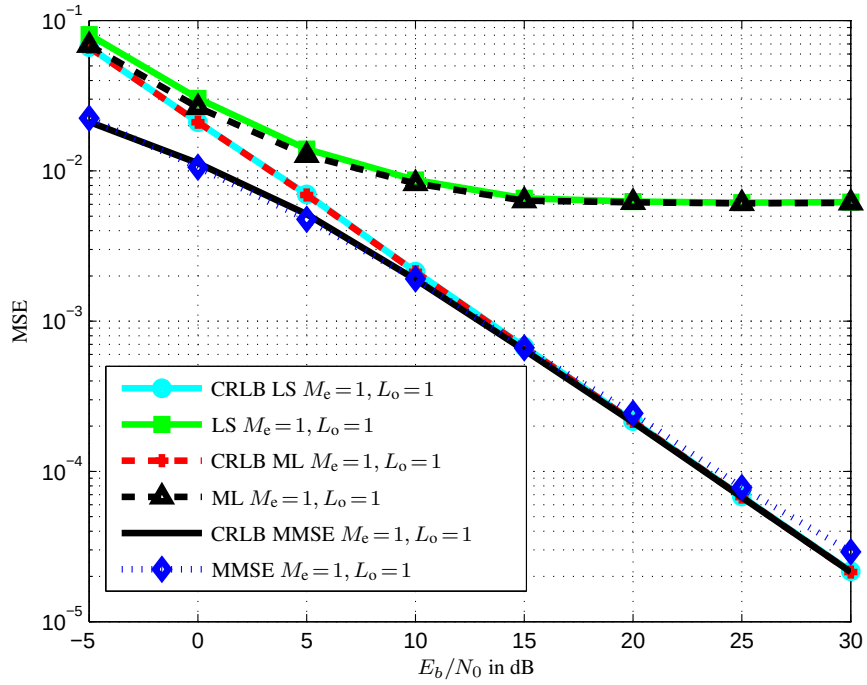

Fig. 3.7. MSE as a function of E_b/N_0 for $M_\mathrm{f} = 210$ and $N_\mathrm{SV} = 30$

3.4.5 ML Channel Estimation via EM

We now assume that the $\mathbf{U}_m$s in (3.33) are unknown, this means that the subcarriers adjacent to the ones with training contain data. Moreover, in Section 3.3.4 and in [6] we have employed the

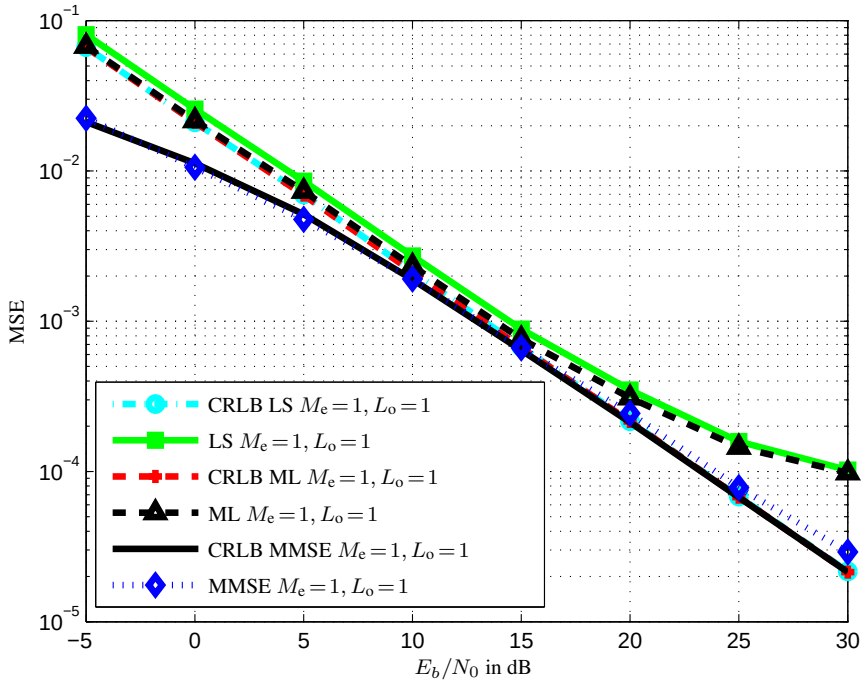

Fig. 3.8. MSE as a function of E_b/N_0 for $M_\mathrm{f} = 210$ and $N_\mathrm{SV} = 32$

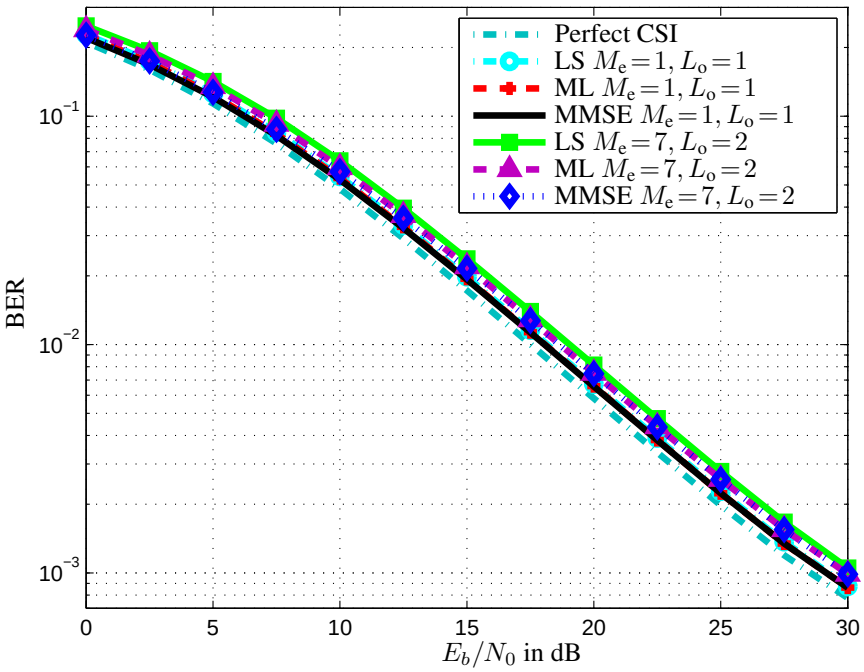

Fig. 3.9. BER as a function of E_b/N_0 for different estimators and parameters

subcarrier model where a narrowband propagation channel was estimated in each subcarrier. Now we modify the subcarrier observations vector to contain a mix of two models: for the training or

reference symbols part we take the broadband model and for the unknown symbols part we will take the narrowband model.

Now, we can rewrite the observations vector in (3.29) obtained for each subcarrier at the receiver as

$$\begin{aligned}\mathbf{y}_m &= \mathbf{S}_{\mathrm{u},m}\mathbf{h}_{\mathrm{ch}} + \mathbf{U}_m\mathbf{h}_{\mathrm{ch}} + \boldsymbol{\eta}_m \\ &= \mathbf{S}_{\mathrm{u},m}\mathbf{h}_{\mathrm{ch}} + \mathbf{U}'_m\mathbf{h}_{\mathrm{ch},m} + \boldsymbol{\eta}_m, \\ &= \mathbf{S}_{\mathrm{u},m}\mathbf{h}_{\mathrm{ch}} + \mathbf{U}'_m\mathbf{B}_m\mathbf{h}_{\mathrm{ch}} + \boldsymbol{\eta}_m, \\ &= \mathbf{S}_{\mathrm{u},m}\mathbf{h}_{\mathrm{ch}} + \mathbf{H}_m\mathbf{u}'_m + \boldsymbol{\eta}_m \\ &= \mathbf{S}_{\mathrm{u},m}\mathbf{h}_{\mathrm{ch}} + \mathbf{H}_m\mathbf{H}_{\mathrm{u},m}\mathbf{x}_{\mathrm{u},m} + \boldsymbol{\eta}_m, \end{aligned} \tag{3.72}$$

where $\mathbf{H}_m \in \mathbb{C}^{L_{\mathrm{o}} \times L_{\tilde{g}'}}$, with $L_{\tilde{g}'} = L_{\mathrm{ch},m} + L_{\bar{g}'} - 1$ and $L_{\bar{g}'} = \lceil \frac{2L_{\mathrm{P}}-1}{M/2} \rceil$, is a convolution matrix obtained from the narrowband propagation channel $\mathbf{h}_{\mathrm{ch},m} \in \mathbb{C}^{L_{\mathrm{ch},m}}$ observed in each subcarrier that is calculated from the broadband channel by the transformation $\mathbf{h}_{\mathrm{ch},m} = \mathbf{B}_m\mathbf{h}_{\mathrm{ch}}$. Thereby, the following definition holds

$$\mathbf{B}_m = \begin{bmatrix}\mathbf{I}_{L_{\mathrm{ch},m}} & \mathbf{0}_{B1}\end{bmatrix} \mathbf{F}^{\mathrm{H}}_{L_{\mathrm{ch},m}M_i} \begin{bmatrix}\mathbf{0}_{B2} & \mathbf{I}_{L_{\mathrm{ch},m}M_i} & \mathbf{0}_{B3}\end{bmatrix} \mathbf{F}_{N_{\mathrm{f}}} \begin{bmatrix}\mathbf{I}_{L_{\mathrm{ch}}} \\ \mathbf{0}_{B4}\end{bmatrix},$$

with $\mathbf{F}_{N_{\mathrm{f}}}$ being an N_{f}-DFT matrix, $N_{\mathrm{f}} = ML_{\mathrm{ch},m}M_i$, $\mathbf{0}_{B1} \in \{0\}^{L_{\mathrm{ch},m}\times(L_{\mathrm{ch},m}(M_i-1))}$, $\mathbf{0}_{B2} \in \{0\}^{(L_{\mathrm{ch},m}M_i)\times(kL_{\mathrm{ch},m}M_i)}$, $\mathbf{0}_{B3} \in \{0\}^{(L_{\mathrm{ch},m}M_i)\times((M-1-k)L_{\mathrm{ch},m}M_i)}$, $\mathbf{0}_{B4} \in \{0\}^{(N_{\mathrm{f}}-L_{\mathrm{ch}})\times L_{\mathrm{ch}}}$, M_i is a resolution factor for the calculation's precision of the $\mathbf{h}_{\mathrm{ch},m}$s.

Moreover, the following equalities hold

$$\mathbf{U}_m\mathbf{h}_{\mathrm{ch}} = \mathbf{U}'_m\mathbf{B}_m\mathbf{h}_{\mathrm{ch}} = \mathbf{U}'_m\mathbf{h}_{\mathrm{ch},m} = \mathbf{H}_m\mathbf{u}'_m = \mathbf{H}_m\mathbf{H}_{\mathrm{u},m}\mathbf{x}_{\mathrm{u},m}, \tag{3.73}$$

where $\mathbf{U}'_m$ is a Hankel matrix obtained for the narrowband subcarrier model. Note that $\mathbf{H}_{\mathrm{u},m} \in \mathbb{C}^{L_{\tilde{g}'}\times 2L'_{\mathrm{t}}}$ and $\mathbf{x}_{\mathrm{u},m} \in \mathbb{C}^{2L'_{\mathrm{t}}}$, where $L'_{\mathrm{t}} = L_{\tilde{g}'} + L_{\mathrm{o}} - 1$.

Stacking all the subcarrier observations, we get

$$\begin{aligned}\begin{bmatrix}\mathbf{y}_0 \\ \mathbf{y}_1 \\ \vdots \\ \mathbf{y}_{M_{\mathrm{o}}-1}\end{bmatrix} &= \begin{bmatrix}\mathbf{S}_{\mathrm{u},0} \\ \mathbf{S}_{\mathrm{u},1} \\ \vdots \\ \mathbf{S}_{\mathrm{u},M_{\mathrm{o}}-1}\end{bmatrix}\mathbf{h} + \mathbf{H}_{\mathrm{E}}\begin{bmatrix}\mathbf{u}'_0 \\ \mathbf{u}'_1 \\ \vdots \\ \mathbf{u}'_{M_{\mathrm{o}}-1}\end{bmatrix} + \begin{bmatrix}\boldsymbol{\Gamma}_0 \\ \boldsymbol{\Gamma}_1 \\ \vdots \\ \boldsymbol{\Gamma}_{M_{\mathrm{o}}-1}\end{bmatrix}\boldsymbol{\nu}, \\ \mathbf{y} &= \mathbf{S}_{\mathrm{u}}\mathbf{h}_{\mathrm{ch}} + \mathbf{H}_{\mathrm{E}}\mathbf{u}' + \boldsymbol{\eta} \\ &= \mathbf{S}_{\mathrm{u}}\mathbf{h}_{\mathrm{ch}} + \mathbf{U}\mathbf{h}_{\mathrm{ch}} + \boldsymbol{\eta}, \end{aligned} \tag{3.74}$$

where $\mathbf{U} = [\mathbf{B}_0^{\mathrm{T}}\mathbf{U}_0'^{\mathrm{T}}, \mathbf{B}_1^{\mathrm{T}}\mathbf{U}_1'^{\mathrm{T}}, ..., \mathbf{B}_{M_{\mathrm{o}}-1}^{\mathrm{T}}\mathbf{U}_{M_{\mathrm{o}}-1}'^{\mathrm{T}}]^{\mathrm{T}}$ and $\mathbf{H}_{\mathrm{E}} = \mathrm{diag}(\mathbf{H}_0, \mathbf{H}_1, ..., \mathbf{H}_{M_{\mathrm{o}}-1})$.

Although the exact values of $\mathbf{u}'_m$ are unknown, their statistics are known. We then define the interference covariance and pseudo-covariance matrices as $\mathbf{R}_{u,m} = \frac{\sigma_d^2}{2}\mathbf{H}_{\mathrm{u},m}\mathbf{H}_{\mathrm{u},m}^{\mathrm{H}}$ and $\mathbf{P}_{u,m} = \frac{\sigma_d^2}{2}\mathbf{H}_{\mathrm{u},m}\mathrm{diag}(1,-1,1,...)\mathbf{H}_{\mathrm{u},m}^{\mathrm{T}}$, where $\mathbf{x}_{\mathrm{u},m}$ was assumed to be i.i.d. and Gaussian distributed with zero mean and variance $\sigma_d^2/2$. This is usually a good approximation, although $\mathbf{x}_{\mathrm{u},m}$ is composed of symbols taken from a finite constellation set.

For the linear model of (3.74), the ML estimator has no closed form solution due to the unknow component and one way to calculate it is by employing the iterative EM algorithm [55], that works

here as follows: Before the first iteration, an initial channel estimate is performed by ignoring $\mathbf{U}$. This estimate is given by

$$\hat{\mathbf{h}}_{\text{ch},0} = (\mathbf{S}_{\text{u}}^{\text{H}}\mathbf{R}_{\eta}^{-1}\mathbf{S}_{\text{u}})^{-1}\mathbf{S}_{\text{u}}^{\text{H}}\mathbf{R}_{\eta}^{-1}\mathbf{y}. \tag{3.75}$$

Then, the iterative process starts. For each iteration i, the algorithm is divided into two steps: the E-step and the M-step. In the E-step, an approximation of the ML function (here its derivative) is obtained by taking its expected value conditioned on the channel estimate in the iteration before and the observed sequence, as follows

$$\begin{aligned}\mathrm{E}\left[\left.\frac{\partial J(\mathbf{h}_{\text{ch},i})}{\partial \mathbf{h}_{\text{ch},i}^{\text{H}}}\right| \mathbf{y}, \mathbf{h}_{\text{ch},i}\right] &= \left(\mathbf{S}_{\text{u}}^{\text{H}}\mathbf{R}_{\eta}^{-1}(\mathbf{S}_{\text{u}} + \mathrm{E}[\mathbf{U}]) + \mathrm{E}[\mathbf{U}]^{\text{H}}\mathbf{R}_{\eta}^{-1}\mathbf{S}_{\text{u}} + \mathrm{E}\left[\mathbf{U}^{\text{H}}\mathbf{R}_{\eta}^{-1}\mathbf{U}\right]\right)\mathbf{h}_{\text{ch},i} \\ &\quad - (\mathbf{S}_{\text{u}} + \mathrm{E}[\mathbf{U}])^{\text{H}}\mathbf{R}_{\eta}^{-1}\mathbf{y}.\end{aligned}$$

The result is a function of $\mathrm{E}[\mathbf{U}]$ and $\mathrm{E}[\mathbf{U}^{\text{H}}\mathbf{R}_{\eta}^{-1}\mathbf{U}]$, and $\mathrm{E}[\mathbf{U}]$ is a function of $\mathrm{E}[\mathbf{u}]$. $\mathrm{E}[\mathbf{u}] = \hat{\mathbf{u}}_i$ is actually an estimate of the interference term $\mathbf{u}$ in the i-th iteration. Furthermore, one can show that

$$\mathrm{E}[\mathbf{U}^{\text{H}}\mathbf{R}_{\eta}^{-1}\mathbf{U}] = \sum_{m=0}^{M_{\text{o}}-1}\mathrm{E}[\mathbf{U}_m^{\text{H}}\mathbf{R}_{\eta,m}^{-1}\mathbf{U}_m] = \sum_{m=0}^{M_{\text{o}}-1}\mathbf{B}_m^{\text{H}}\mathrm{E}[\mathbf{U}_m'^{\text{H}}\mathbf{R}_{\eta,m}^{-1}\mathbf{U}_m']\mathbf{B}_m.$$

To express the above expectation also in terms of the estimate $\hat{\mathbf{u}}_i$, one first has to write the matrix $\mathbf{U}_m'$ as a function of the vector $\mathbf{u}_m'$ as $\mathbf{U}_m' = \sum_{\ell=1}^{L_{\text{ch},m}}\mathbf{D}_\ell\mathbf{u}_m'\mathbf{e}_\ell^T$, where $\mathbf{D}_\ell = \begin{bmatrix}\mathbf{0}_{D1} & \mathbf{I}_{L_{\text{o}}} & \mathbf{0}_{D2}\end{bmatrix}$ is a matrix that selects L_{o} rows of $\mathbf{u}_m'$, $\mathbf{0}_{D1} \in \{0\}^{L_{\text{o}}\times(\ell-1)}$, $\mathbf{0}_{D2} \in \{0\}^{L_{\text{o}}\times(L_{\text{ch},m}-\ell)}$ and $\mathbf{e}_\ell \in \{0,1\}^{L_{\text{ch},m}}$. We then obtain

$$\begin{aligned}\mathrm{E}\left[\mathbf{U}_m'^{\text{H}}\mathbf{R}_{\eta,m}^{-1}\mathbf{U}_m'\right] &= \mathrm{E}\left[\sum_{\lambda=1}^{L_{\text{ch}}}\mathbf{e}_\lambda\mathbf{u}_m'^{\text{H}}\mathbf{D}_\lambda^{\text{T}}\mathbf{R}_{\eta,m}^{-1}\sum_{\ell=1}^{L_{\text{ch}}}\mathbf{D}_\ell\mathbf{u}_m'\mathbf{e}_\ell^{\text{T}}\right] \\ &= \sum_{\lambda=1}^{L_{\text{ch}}}\mathbf{e}_\lambda\sum_{\ell=1}^{L_{\text{ch}}}\mathrm{E}\left[\mathbf{u}_m'^{\text{H}}\mathbf{D}_\lambda^{\text{T}}\mathbf{R}_{\eta,m}^{-1}\mathbf{D}_\ell\mathbf{u}_m'\right]\mathbf{e}_\ell^{\text{T}} \\ &= \sum_{\lambda=1}^{L_{\text{ch}}}\mathbf{e}_\lambda\sum_{\ell=1}^{L_{\text{ch}}}\mathrm{tr}\left\{\mathbf{D}_\lambda^{\text{T}}\mathbf{R}_{\eta,m}^{-1}\mathbf{D}_\ell\mathrm{E}\left[\mathbf{u}_m'\mathbf{u}_m'^{\text{H}}\right]\right\}\mathbf{e}_\ell^{\text{T}}.\end{aligned}$$

Furthermore,

$$\mathrm{E}\left[\mathbf{u}_m'\mathbf{u}_m'^{\text{H}}\right] = \mathbf{R}_{\epsilon,m,i} + \mathrm{E}[\mathbf{u}_m']\mathrm{E}[\mathbf{u}_m']^{\text{H}} = \mathbf{R}_{\epsilon,m,i} + \hat{\mathbf{u}}_{m,i}'\hat{\mathbf{u}}_{m,i}'^{\text{H}}, \tag{3.76}$$

where $\mathbf{R}_{\epsilon,m,i}$ is the covariance matrix of the estimation error of $\mathbf{u}_m'$ in the i-th iteration. Consequently, we obtain

$$\mathrm{E}\left[\mathbf{U}_m'^{\text{H}}\mathbf{R}_{\eta,m}^{-1}\mathbf{U}_m'\right] = \mathbf{\Psi}_{m,i} + \mathrm{E}[\mathbf{U}_m']^{\text{H}}\mathbf{R}_{\eta,m}^{-1}\mathrm{E}[\mathbf{U}_m'], \tag{3.77}$$

with $[\mathbf{\Psi}_{m,i}]_{\ell,\lambda} = \mathrm{tr}\left\{\mathbf{D}_\ell^{\text{T}}\mathbf{R}_{\eta,m}^{-1}\mathbf{D}_\lambda\mathbf{R}_{\epsilon,m,i}\right\}$. Then it follows that

$$\begin{aligned}\mathrm{E}[\mathbf{U}^{\text{H}}\mathbf{R}_{\eta}^{-1}\mathbf{U}] &= \sum_{m=0}^{M_{\text{o}}-1}\mathbf{B}_m^{\text{H}}\left(\mathbf{\Psi}_{m,i} + \mathrm{E}[\mathbf{U}_m']^{\text{H}}\mathbf{R}_{\eta,m}^{-1}\mathrm{E}[\mathbf{U}_m']\right)\mathbf{B}_m, \\ &= \mathbf{\Psi}_i + \hat{\mathbf{U}}_i^{\text{H}}\mathbf{R}_{\eta}^{-1}\hat{\mathbf{U}}_i,\end{aligned} \tag{3.78}$$

where $\hat{\mathbf{U}}_i^{\mathrm{H}}\mathbf{R}_\eta^{-1}\hat{\mathbf{U}}_i = \sum_{m=0}^{M_\mathrm{o}-1}\mathbf{B}_m^{\mathrm{H}}\hat{\mathbf{U}}_{m,i}'^{\mathrm{H}}\mathbf{R}_{\eta,m}^{-1}\hat{\mathbf{U}}_{m,i}'\mathbf{B}_m$, and $\boldsymbol{\Psi}_i = \sum_{m=0}^{M_\mathrm{o}-1}\mathbf{B}_m^{\mathrm{H}}\boldsymbol{\Psi}_{m,i}\mathbf{B}_m$.

Finally, we define $\hat{\mathbf{S}}_i = \mathbf{S}_\mathrm{u} + \hat{\mathbf{U}}_i$ and write

$$\mathrm{E}\left[\left.\frac{\partial J(\mathbf{h}_{\mathrm{ch},i})}{\partial \mathbf{h}_{\mathrm{ch},i}^{\mathrm{H}}}\right| \mathbf{y}, \mathbf{h}_{\mathrm{ch},i}\right] = \left(\hat{\mathbf{S}}_i^{\mathrm{H}}\mathbf{R}_\eta^{-1}\hat{\mathbf{S}}_i + \boldsymbol{\Psi}_i\right)\mathbf{h}_{\mathrm{ch},i} - \hat{\mathbf{S}}_i^{\mathrm{H}}\mathbf{R}_\eta^{-1}\mathbf{y}.$$

Given the estimate of $\mathbf{h}_\mathrm{ch}$ and the training, one can estimate $\mathbf{u}'$. It can be shown that the entries of $\mathbf{u}'$ are alternating purely real and purely imaginary, because in addition to the OQAM data signals in subcarriers $m-1$ and $m+1$ also the impulse response from the two adjacent subcarriers have alternating real and imaginary coefficients. As a consequence, the interference term $\mathbf{u}_m'$ has improper statistics and the following Widely Linear MMSE [66] estimator can be employed

$$\mathrm{E}[\mathbf{u}_i'] = \hat{\mathbf{u}}_i' = \mathbf{W}_1\mathbf{y}_u + \mathbf{W}_2\mathbf{y}_u^*, \tag{3.79}$$

where $\mathbf{y}_u = \mathbf{y} - \mathbf{S}\hat{\mathbf{h}}_i \approx \hat{\mathbf{H}}_{\mathrm{E},i}\mathbf{u}' + \boldsymbol{\eta}$,

$$\begin{aligned}\mathbf{W}_1 &= (\mathbf{R}_{uy_u} - \mathbf{P}_{uy_u}\mathbf{R}_{y_u}^{-*}\mathbf{P}_{y_u}^*)(\mathbf{R}_{y_u} - \mathbf{P}_{y_u}\mathbf{R}_{y_u}^{-*}\mathbf{P}_{y_u}^*)^{-1},\\ \mathbf{W}_2 &= (\mathbf{P}_{uy_u} - \mathbf{R}_{uy_u}\mathbf{R}_{y_u}^{-1}\mathbf{P}_{y_u})(\mathbf{R}_{y_u}^* - \mathbf{P}_{y_u}^*\mathbf{R}_{y_u}^{-1}\mathbf{P}_{y_u})^{-1},\end{aligned}$$

while $\mathbf{R}_{y_u} = \hat{\mathbf{H}}_{\mathrm{E},i}\mathbf{R}_u\hat{\mathbf{H}}_{\mathrm{E},i}^{\mathrm{H}} + \mathbf{R}_\eta$, and $\mathbf{R}_{uy_u} = \mathbf{R}_u\hat{\mathbf{H}}_{\mathrm{E},i}^{\mathrm{H}}$. The pseudo-covariance matrices are given by $\mathbf{P}_{y_u} = \hat{\mathbf{H}}_{\mathrm{E},i}\mathbf{P}_u\hat{\mathbf{H}}_{\mathrm{E},i}^{\mathrm{T}}$ and $\mathbf{P}_{uy_u} = \mathbf{P}_u\hat{\mathbf{H}}_{\mathrm{E},i}^{\mathrm{T}}$, where $\mathbf{R}_u = \mathrm{diag}(\mathbf{R}_{u,0}, ..., \mathbf{R}_{u,M_\mathrm{o}-1})$, and correspondingly for $\mathbf{P}_u$. One can see that all covariance matrices are block diagonal and the estimation of $\mathbf{u}'$ in (3.79) is equivalent to estimating the $\mathbf{u}_m'$s subcarrier-wise.

The corresponding error covariance is given by

$$\mathbf{R}_{\epsilon,i} = \mathbf{R}_u - \mathbf{W}_1\mathbf{R}_{uy_u}^{\mathrm{H}} - \mathbf{W}_2\mathbf{P}_{uy_u}^{\mathrm{H}}, \tag{3.80}$$

where $\mathbf{R}_{\epsilon,i} = \mathrm{diag}(\mathbf{R}_{\epsilon,0,i}, \mathbf{R}_{\epsilon,1,i}, ..., \mathbf{R}_{\epsilon,M_\mathrm{o}-1}, i)$.

Finally, the M-step is performed, where $J(\mathbf{h}_{\mathrm{ch},i})$ is minimized, resulting in the new channel estimate

$$\begin{aligned}\hat{\mathbf{h}}_{\mathrm{ch},i+1} &= \mathbf{A}\hat{\mathbf{h}}_{\mathrm{DS},i}\\ &= \mathbf{A}(\mathbf{A}^{\mathrm{H}}(\hat{\mathbf{S}}_i^{\mathrm{H}}\mathbf{R}_\eta^{-1}\hat{\mathbf{S}}_i + \boldsymbol{\Psi}_i)\mathbf{A})^{-1}\mathbf{A}^{\mathrm{H}}\hat{\mathbf{S}}_i^{\mathrm{H}}\mathbf{R}_\eta^{-1}\mathbf{y},\end{aligned}$$

where $\mathbf{A}$ was defined in (3.66) and we employ the ML estimator from (3.67). The estimation of $\mathbf{u}$ (E-Step) and $\mathbf{h}_\mathrm{ch}$ (M-Step) are then repeated N_EM-times until convergence is achieved.

3.4.5.1 Simulation Results

For the performance simulations, the parameters were $M = 256$, $M_\mathrm{f} = 210$, $K = 4$ and an RRC prototype with roll-off one. The total signal bandwidth is 12.6 MHz and the sampling rate is $M/T = 15.36$ MHz, giving a subcarrier bandwidth of 60 kHz and a symbol duration of $T = 16.67$ μs. The channel model was the ITU-Vehicular A without mobility. The CIR duration is $L_h = 36$ samples.

The observations were taken from every 4-th subcarrier. Then we can consider two cases: for a known $\mathbf{u}$, 158 subcarriers are filled with training and the rest with unknown symbols, while for unknown $\mathbf{u}$, only 53 subcarriers are filled with training and the rest with further unknown symbols.

We have used random QPSK training symbols. The NMSE of the channel estimation was averaged over 100 channel realizations, each was also averaged over 10 training sequences and, for each training, averaged over 10 noise realizations. In Fig. 3.10, the theoretical and numerical NMSEs for the different estimators are depicted as a function of E_s/N_0. Further parameters are $L_o = 4$ and for the ML-EM algorithm $L_{ch,m} = 3$. The theoretical NMSE and the curve where $\mathbf{u}$ is known

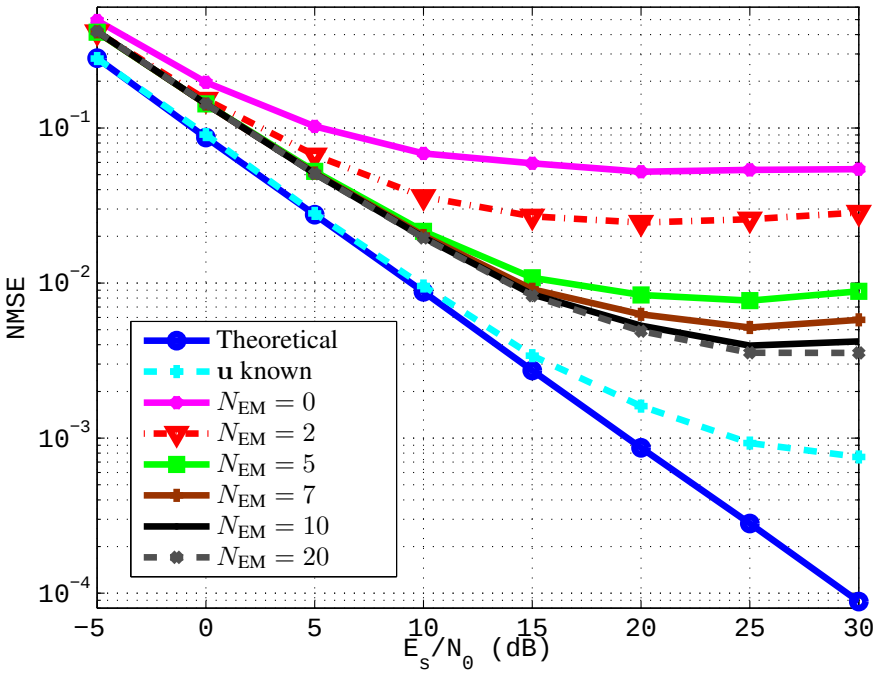

Fig. 3.10. NMSE as a function of E_s/N_0.

show a lower bound on the NMSE performance. The curve for $N_{EM} = 0$ shows an upper bound, since there the interference from data carrying subcarriers degrades the estimation performance. The ML-EM curves show the performance for $N_{EM} = 2, 5, 7, 10$ and 20 iterations. One can see that for 10 and 20 iterations the performance is nearly the same, showing that no more than 10 iterations are necessary. A great improvement compared to 0 iterations is achieved and a low level of MSE is achieved.

3.4.6 Spectrally Efficient CIR Estimation

One can see that the model in (3.33) is dependent on the inputs of three adjacent subcarriers and, in addition to that, the number of input symbols to generate $\mathbf{X}_\ell$ is dependent on the prototype length L_P, on the CIR length L_h, and on the number observations L_o collected at the receiver side. Usually, the length of the training should be as short as possible and not necessarily depend on all those factors. Actually, it is usually desired to have short training sequences distributed over the time vs. frequency plane, as for example in LTE standards. In this way one could consider that short training sequences are interpolated in the frequency axis by data subcarriers and data symbols which are transmitted immediately before and after the training sequences, without any guard intervals (or empty subcarriers) neither in time nor in frequency.

Let us now define the desired training sequence length $L_t < L_x$ and the constants $L_{d1} = \lfloor \frac{L_x - L_t}{2} \rfloor$ and $L_{d2} = \lceil \frac{L_x - L_t}{2} \rceil$. Then, we decompose $\mathbf{X}_\ell = \mathbf{X}_{t,\ell} + \mathbf{X}_{d,\ell}$, where $\mathbf{X}_{t,\ell}$ is generated

from the vector $\left[\mathbf{0}_{L_{\text{d1}}}^{\text{T}} \quad \mathbf{x}_{\text{t},\ell}^{\text{T}} \quad \mathbf{0}_{L_{\text{d1}}}^{\text{T}}\right]^{\text{T}} \in \mathbb{C}^{L_x}$ containing training symbols and $\mathbf{X}_{\text{d},\ell}$ is generated from the vector $\left[\mathbf{x}_{\text{d1},\ell}^{\text{T}} \quad \mathbf{0}_{L_{\text{t}}}^{\text{T}} \quad \mathbf{x}_{\text{d2},\ell}^{\text{T}}\right]^{\text{T}} \in \mathbb{C}^{L_x}$ containing data symbols, with $\mathbf{x}_{\text{t},\ell} \in \mathbb{C}^{L_{\text{t}}}$, $\mathbf{x}_{\text{d1},\ell} \in \mathbb{C}^{L_{\text{d1}}}$ and $\mathbf{x}_{\text{d2},\ell} \in \mathbb{C}^{L_{\text{d2}}}$. The reason for this choice of the values of L_{d1} and L_{d2} is that the prototype filter IR is symmetric and its energy is concentrated in the coefficients in the middle of the IR.

We further define the following observations vector as a function of two input terms: a training dependent and an interference dependent one

$$\mathbf{y}_m = (\mathbf{S}_{\text{u},m} + \mathbf{U}_m)\mathbf{h}_{\text{ch}} + \mathbf{\Gamma}_m \boldsymbol{\nu}, \tag{3.81}$$

where for the model in (3.33) one can clearly see that $\mathbf{U}_m = \mathbf{0}$. Then, three cases can be considered for an spectral efficient channel estimation: (3.33)

- Case 1, ICI limited estimation: $\mathbf{X}_{m+1} = \mathbf{X}_{\text{d},m+1}$ and $\mathbf{X}_{m-1} = \mathbf{X}_{\text{d},m-1}$ contain only data symbols and $\mathbf{X}_m = \mathbf{X}_{\text{t},m}$ is fully filled with training, so that the following definitions hold $\mathbf{S}_m = \mathbf{X}_{\text{t},m}\bar{\mathbf{H}}_{m,m}$ and $\mathbf{U}_m = \mathbf{X}_{\text{d},m-1}\bar{\mathbf{H}}_{m,m-1} + \mathbf{X}_{\text{d},m+1}\bar{\mathbf{H}}_{m,m+1}$.
- Case 2, ISI limited estimation: We use the decomposition of $\mathbf{X}_\ell$ to get the matrices $\mathbf{S}_m = \sum_{\ell=m-1}^{m+1} \mathbf{X}_{\text{t},\ell}\bar{\mathbf{H}}_{m,\ell}$ and $\mathbf{U}_m = \sum_{\ell=m-1}^{m+1} \mathbf{X}_{\text{d},\ell}\bar{\mathbf{H}}_{m,\ell}$.
- Case 3, ICI and ISI limited estimation: We decompose only $\mathbf{X}_m$ to get the matrices $\mathbf{S}_m = \mathbf{X}_{\text{t},m}\bar{\mathbf{H}}_{m,m}$ and $\mathbf{U}_m = \mathbf{X}_{\text{d},m}\bar{\mathbf{H}}_{m,m} + \mathbf{X}_{\text{d},m-1}\bar{\mathbf{H}}_{m,m-1} + \mathbf{X}_{\text{d},m+1}\bar{\mathbf{H}}_{m,m+1}$.
  Similar to (3.33) the observations can be stacked to get

$$\mathbf{y} = (\mathbf{S}_{\text{u}} + \mathbf{U})\mathbf{h}_{\text{ch}} + \boldsymbol{\eta}. \tag{3.82}$$

The estimator in (3.67) can then be employed and, for the moment, the interference term $\mathbf{U}\mathbf{h}_{\text{ch}}$ is just ignored. In Section 3.4.5, [6] and [5] we have proposed methods to iteratively estimate the $\mathbf{h}_{\text{ch}}$ and $\mathbf{U}$ for the Case 1 based on the EM algorithm and we have shown that the estimation quality can be significantly improved. Extensions for the cases 2 and 3 are also possible, but were not considered in this work.

3.4.6.1 Simulation Results

For the performance evaluations, the parameters were $M = 256$, $M_{\text{f}} = 156$, $K = 4$ and the prototype was an RRC filter with roll-off one. The total signal bandwidth is 12.6 MHz and the sampling rate is $M/T = 15.36$ MHz, giving a subcarrier bandwidth of 60 kHz and a symbol duration of $T = 16.67$ μs. The channel model was the ITU-Vehicular A without mobility. The CIR duration is $L_{\text{ch}} = 36$ samples.

The observations were taken from every 4-th subcarrier, resulting in $M_{\text{o}} = 39$ observations subcarriers. For Cases 1 and 3, only those 39 subcarriers are filled with training or reference symbols. 117 subcarriers are filled with training symbols for the interference free estimation and for Case 2. All the other subcarriers in all cases are filled with random Quadrature Phase-Shift Keying (QPSK) symbols, which are assumed as unknown at the receiver. Moreover, we have used random QPSK training symbols with symbol period T. The NMSE $\bar{\epsilon} = \frac{\text{E}[\epsilon_{\text{DS}}]}{\text{E}[\|\mathbf{h}_{\text{DS}}\|]}$ of the channel estimation was averaged over 100 channel realizations, each was also averaged over 10 training sequences and, for each training, averaged over 10 noise realizations.

In Fig. 3.11, we show simulation results for both broadband and narrowband models for $L_{\text{o}} = 4$ observations. For Cases 2 and 3, the training length in the $T/2$ period is $L_{\text{t}} = 4$, which is equivalent to two QAM symbols in the period T. For the narrowband model, we have used $L_{h_m} = 3$ for each subcarrier. We can see that the interference worsens the performance of both channel estimators

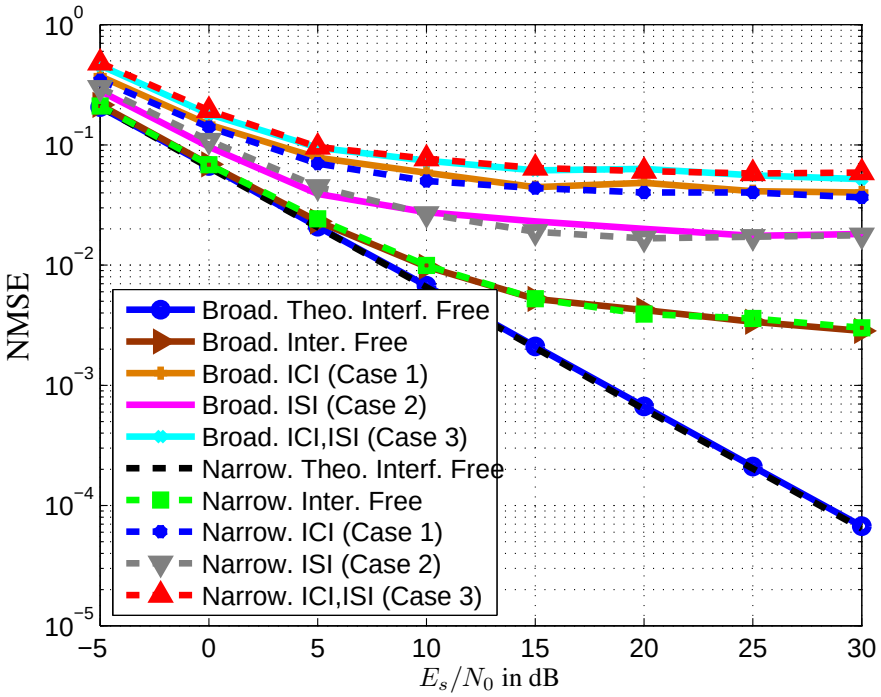

Fig. 3.11. MSE as a function of E_s/N_0 for $L_t = 4$.

as expected. The use of different models seems to make no difference in the results for this set of parameters.

One extreme example is shown in Fig. 3.12, where the main difference is for Cases 2 and 3, where the training length is now $L_t = 2$ in the $T/2$ period, what is equivalent to one QAM symbol in each training subcarrier. Here the training length is minimal and, for the three cases, one can see that both broadband and narrowband based models show the same performance when the interference is ignored.

To better illustrate the effect of longer training sequences, we show in Fig. 3.13 an example where $L_t = 6$, i.e. three QAM symbols long. It is possible to see that the performances for Cases 1 and 3 gets very close to each other, because the ISI in this case becomes negligible compared to the ICI, which dominates also over the noise for a wide range of E_s/N_0. It is also possible to see that Case 2 gets very close to the interference free case for the broadband based model and for the narrowband not that much. The reason for that is the length of the necessary interference free training length for this model. If we extend the training to $L_t = 8$—corresponding to four QAM symbols in period T—the result becomes identical to the interference free one for the same parameters.

3.5 Summary and Discussion

In this Chapter we have presented two basic approaches for channel estimation in FBMC systems. The first one is based on a narrowband modeling of the propagation channel, i.e. an impulse response per subcarrier is estimated per subcarrier. The equalizer that is then designed also per subcarrier will then utilize the corresponding impulse response. The narrowband approach assumes that training symbols are inserted in each subcarrier utilized for the estimation. In the subcarriers

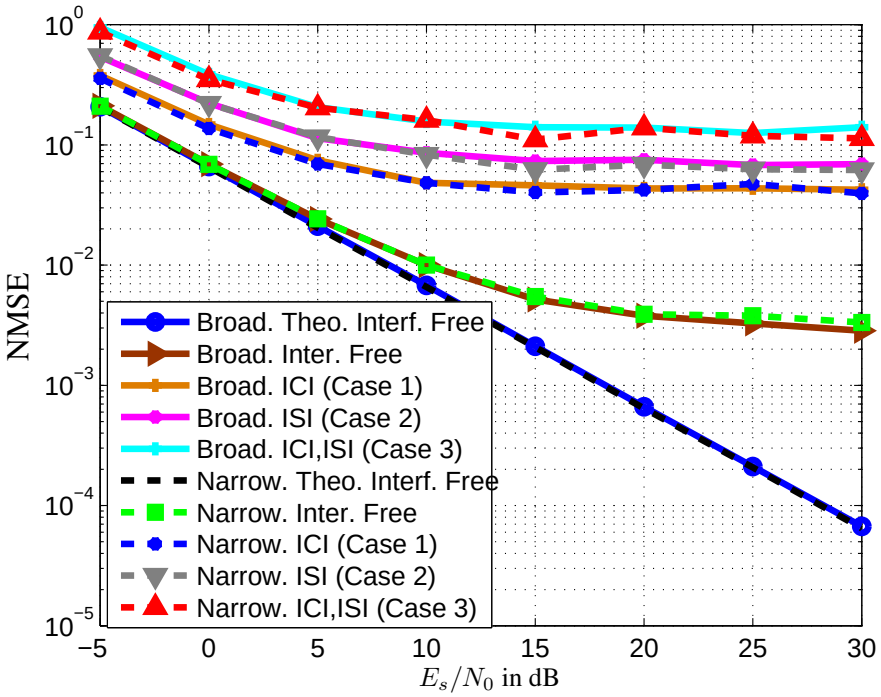

Fig. 3.12. MSE as a function of E_s/N_0 for $L_t = 2$.

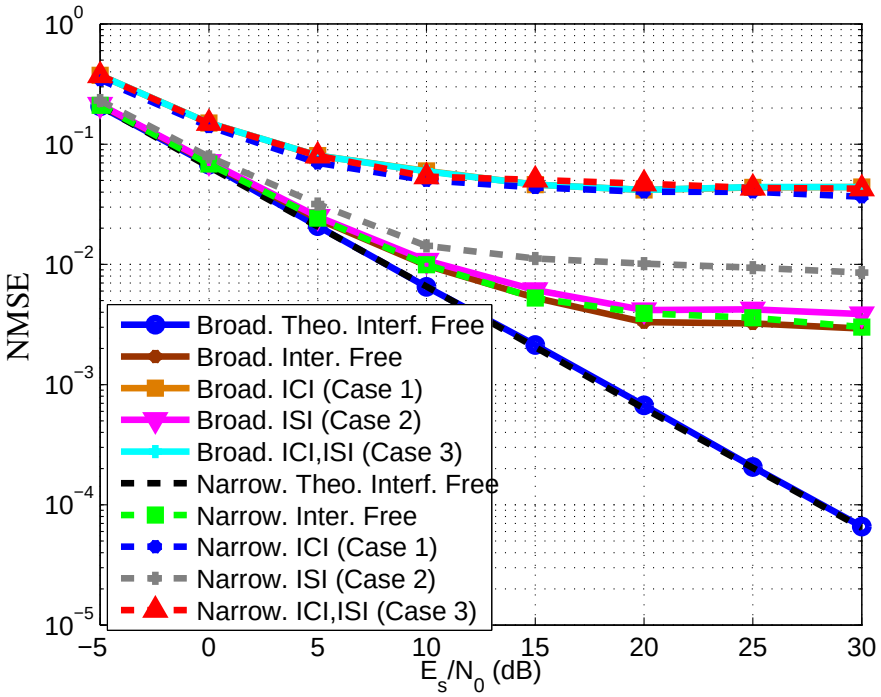

Fig. 3.13. MSE as a function of E_s/N_0 for $L_t = 6$.

where no training symbols are inserted, the estimation can be done by applying an interpolation in the frequency axis for each of the coefficients in an analogous way as frequently employed in CP-OFDM. If the channel presents time variations and the training symbols are periodically

transmitted, two alternatives can be envisioned to obtain a more accurate estimation in the interval between training symbols: the use of adaptive algorithms or also a one dimensional interpolation for each of the coefficients of the impulse responses.

The second approach is based on a broadband model of the propagation channel, where one single impulse response is estimated and can be employed in the design of the equalizer of all active subcarriers. Not all active subcarriers need to have training symbols inserted, but it is assumed that they are uniformly distributed across the subcarriers with a distance that depends on the level of frequency selectivity.

The choice between narrowband or broadband approach will depend on different characteristics of the system, the environment, complexity and required spectral efficiency. The narrowband approach presents some similarities to the conventional channel estimation in CP-OFDM and may employ a per sub-carrier parallel processing during the estimation. Depending on the level of frequency selectivity and for a given total number of active subcarrier, different levels of spectral efficiency can be achieved for narrowband or broadband, since the total number of training symbols necessary to achieve a certain performance may be different.

For both narrowband and broadband approaches, we have presented the EM based ML estimation that assumes that training symbols are only inserted in the observations subcarriers and their adjacent can convey data symbols. This improves the spectral efficiency at the cost of higher complexity for the estimation.

Finally, we also presented three conventional objectives for the design utilizing both narrowband and broadband approach, namely LS, ML and MMSE. The LS objective is the simplest one and does not require any information about the statistics of the noise, resulting in a very low complexity to calculate the estimation matrix. The ML estimation requires knowledge about the statistics of the noise, which requires a higher complexity to obtain the estimation matrix, but provides better performance than the LS objective for low noise levels. The MMSE objective requires knowledge about the statistics of both noise and channel, but will provide the best performance in low SNR scenarios.

From the comparison discussed above, it becomes clear that the choice between LS, ML and MMSE will basically depend on the computational capabilities, availability of noise and channel statistics, and SNR level. It is worth noting that in this work we have presented the EM based estimation only based on the ML estimator, but this can be further extended for the MMSE objective.

4. Equalizer and Precoder Design

4.1 Introduction

One of the main advantages of MultiCarrier Modulation (MCM) schemes for broadband wireless communications is their robustness to multi-path propagation[1] channels, stemming from the fact that they divide the channel spectrum in very narrow subbands and, in the extreme case, no frequency selectivity, i.e., only flat fading, is observed in each of them. For an increased spectral efficiency, most practical MCM schemes have their subbands overlapped in frequency. In CP-OFDM, ISI and ICI can be completely removed if the CP is at least as long as the channel delay spread. Thus, at the expense of reducing the spectral efficiency due to the CP redundancy, the subchannels corresponding to the different subbands are completely decoupled. The equalization in CP-OFDM then becomes trivial and can be performed by a single complex multiplication per subcarrier, giving rise to the so-called single-tap equalizer. Usually this is of the Zero Forcing (ZF) type, which directly inverts the frequency response of the channel at each subcarrier. More sophisticated equalizers, such as the MMSE one, are adopted if the noise and channel statistics are known or estimated.

FBMC/OQAM systems do not have to employ a CP and they can enjoy (real-field) orthogonality in ideal propagation scenarios. This also means that full orthogonality exists, by considering the QAM symbols before the OQAM staggering at the SFB and after OQAM de-staggering at the AFB, as originally proved for PR MDFT FilterBank (FB) [43] and later for FBMC/OQAM systems in [68]. In other words, the so-called self-interference can easily be removed by the OQAM de-staggering. For realistic propagation scenarios, where channel distortions are present, the symbols received at the AFB output are contaminated by both ISI and ICI, which are channel-induced. With mildly frequency selective channels, a single-tap equalizer, like the one presented in Section 4.2.1, should be sufficient to compensate for the channel effects and minimize both kinds of interference. However, with moderate to highly frequency selective channels, more elaborate equalizers have to be used, which will also increase the receiver complexity. Such equalizers can be designed and implemented in the time or the frequency domain, and they have the ability to compensate also for time and phase shifts.

Another advantage of FBMC/OQAM systems, apart from the CP-free transmission, is that they provide a flexibility in choosing the subcarrier spacing. In usual cases where a higher symbol rate per subcarrier is necessary to reduce latency or frequency offset/phase noise are relevant impairments, a higher subcarrier bandwidth (large subcarrier spacing) can be considered. The consequences of this include an increase in the complexity of the per-subcarrier equalization due to

[1] We mainly refer to wireless channels here although MCM and the solutions presented in this chapter could also be employed in broadband wireline systems, e.g., in Digital Subscriber Line (DSL), power line, and fiber optics communications, where frequency selective channels are also involved.

the larger number of taps required. In other practical cases, where a higher granularity in frequency domain is desired, a higher PAPR can be tolerated[2], and a longer symbol duration can be accepted, narrower subbands (smaller subcarrier spacing) can be considered. Then equalizers of low complexity can be employed, with the single-tap one being the simplest possible.

A first solution to compensate for the effects of multi-path propagation in FBMC/OQAM systems was presented in [33], where it was shown that it is possible to completely eliminate ISI, ICI, compensate for time deviations and demodulating carrier phase deviations if a per-subcarrier $T/2$-spaced[3] equalizer with a sufficient number of taps is employed, where T is the symbol period. The equalizer coefficients are computed using an MMSE steepest descent adaptive algorithm. The analytical solution for the multi-tap equalizer presented in Section 4.2.2 shares many objectives and properties with the one in [33]. It is worth mentioning that in [33] two structures for the implementation of the fractionally-spaced equalizer are introduced, which correspond to the equalizer operating at the $2/T$ or the $1/T$ sampling rate. Much later, in [79], both fractionally- and symbol-spaced adaptive steepest descent equalizers were proposed. In the non-fractionally-spaced case, three equalizers per subcarrier, which combine the output of the subcarrier of interest and its neighbors and are placed after the OQAM de-staggering, are employed to remove ISI and ICI. In the fractionally-spaced case, also three equalizers per subcarrier are employed and two variants are provided: with and without the OQAM destagering in the adaptation loop. In [57], a combined equalization and echo cancellation solution was presented, where a fractionally-spaced FIR filter for the equalization and another for the echo cancellation part are employed. For the latter, a preprocessing before the FIR filter is included to emulate the SFB- and AFB-equivalent response. The per-subcarrier equalization for odd-stacked FBMC/OQAM systems was revisited in [37], where specific equalizer structures were presented to compensate for different levels of frequency selectivity. In [35], an equalizer similar with the one presented in Section 4.2.2 was designed so as to cope with ICI from all subcarriers and channel time selectivity. An evaluation of the spectral efficiency as a function of the time and frequency spread was performed and showed that the MMSE multi-tap equalizer significantly increases spectral efficiency. To improve the robustness to ISI and ICI, a combination of Walsh-Hadamard transform with FBMC/OQAM was proposed in [2]. The effect of the transform is to spread the symbols over all subcarriers, resulting in frequency diversity. An MMSE equalizer was employed at the receiver. It is worth mentioning here that frequency diversity can also be achieved by combining bit-interleaved channel coding and the equalization schemes presented in this chapter. The authors in [56] performed an analysis of ISI and ICI and proposed a new equalizer structure that uses the interference effect in a positive way. A single-tap ZF equalizer before OQAM de-staggering is combined with an interference estimation and cancellation scheme applied after the de-staggering, on a per-subcarrier basis.

For mildly frequency selective channels, the classical single-tap ZF equalizer, applied before the OQAM destaggering, was compared to two alternative equalizers in [45]: a dispersion receiver, where the AFB is designed to match SFB-plus-channel and ZF equalization is then applied, and an interference-free receiver, which pre-processes the received signal before the AFB, to transform the equivalent channel to one with purely real or imaginary Channel Frequency Response (CFR), thus allowing the interference to be completely eliminated. It was shown that all three receivers behave

[2]It should be noted that, while the subcarrier spacing directly affects the number of active subcarriers in the used frequency band, also the PAPR properties become an important concern in the FBMC/OQAM system dimensioning.

[3]We refer here to a fractionally-spaced equalizer because its inputs are the signals before the OQAM de-staggering or complex symbols before the Pulse Amplitude Modulation (PAM) demodulation, depending on which subcarrier model is employed.

similarly for mildly frequency selective channels. If the channel dispersion increases, the first one presents better performance than the other two. In [40], also for mildly frequency selective channels and considering channel coding, a method for calculating the Log-Likelihood Ratio (LLR) values was derived for the specific OQAM signaling in FBMC systems when single-tap ZF equalizers are employed. More recently, a single-tap equalizer that maximizes the Signal-to-Interference Ratio (SIR) was derived in [53], again for mildly frequency selective channels. It was shown that the maximum SIR criterion leads to improved performance compared to the ZF one. The authors of [69] propose a per subchannel joint equalizer and AFB filter design method based on maximizing SINR. They follow an iterative two-step approach, where in the first step the equalizer and in the second step the Receiver (RX) prototype filter are optimized, in an alternating manner. The convergence of the algorithm is proved and an extension to MIMO is also introduced.

The design of the equalizer should take into account the signal model according to the location of the equalizer. If a time-domain filtering, like when the polyphase network based structure is employed, the equalizer is typically located in each subcarrier after the FFT and before the OQAM staggering - although as shown in Chapter 2 equalizer and OQAM destaggering can be combined to reduce the complexity. In this case, the corresponding subcarrier filtering should be considered during the equalizer design. While if a frequency domain filtering is employed, the equalizer can be placed in two different positions: after the subcarrier frequency domain filtering and before the OQAM de-staggering; or before - or jointly realized - with the subcarrier frequency domain filtering. For the first location, the design and implementation should be identical to those used in the polyphase based structure. In the second case, the design of the equalizer can be performed by only considering the FFT operation and the proceeding serial-to-parallel or block overlapped serial-to-parallel operation. The AFB filter does not need to be considered during the design, although the equalizer and frequency domain filter coefficients can be combined in one multiplier.

The book chapter in [4] provides a further review of existing channel equalization schemes for FBMC.

4.2 SISO Equalization and Precoding

4.2.1 Single-tap MMSE Linear Equalizer Design

For mildly frequency selective channels or, in other words, transmission scenarios where the subcarrier bandwidth is small compared to the coherence bandwidth of the channel, a single-tap complex equalizer per subcarrier can be employed, similarly with CP-OFDM systems. Moreover, it can be assumed, as it is common in MC systems, that the coherence time of the channel covers at least one MC symbol. With these assumptions, FBMC/OQAM systems have a similar complexity for their equalization with conventional CP-OFDM, with the difference that the pulse shaping and the OQAM scheme modify the system model. This needs to be taken into account in order not to have a poor equalization performance. ISI and ICI limit the performance of the ZF equalizer. Hence, in the following, a single-tap MMSE equalizer is developed so as to take into account the effect of the pulse shaping and the OQAM modulation properties.

The pulse shaping at the mth subcarrier, $m = 0, 1, \ldots, M-1$, is given by (see also Section 2.3)

$$h_m[l] = h_{\mathrm{P}}[l] \mathrm{e}^{\mathrm{j}\frac{2\pi}{M} m \left(l - \frac{L_{\mathrm{P}}-1}{2}\right)}, \quad l = 0, 1, \ldots, L_{\mathrm{P}} - 1, \tag{4.1}$$

where $h_{\mathrm{P}}[l]$ is the (symmetric and unit energy) prototype filter impulse response with L_{P} coefficients, M is the (even) number of subcarriers and K is the time overlapping factor. The latter

should be kept as small as possible so as not only to limit the complexity but also to reduce the time-domain spreading of the symbols and the transceiver latency. A typical value is $K = 4$ and the roll-off factor of the prototype filter is usually set to one. Thus, $h_m[l]$ has a non-negligible overlap in frequency only with its two adjacent filters. Observe that the subcarrier filter response in (4.1) is the paraconjugate of itself, namely $h_m^*[L_\mathrm{P} - 1 - l] = h_m[l]$.

The subcarrier model commonly adopted for a single-tap equalizer design is described in (3.20) and relies on the assumption that the channel is sufficiently slowly varying in frequency and time that its CFR is (almost) invariant over the first-order Time-Frequency (T-F) neighborhood of the given Frequency-Time (F-T) point, (m, n). Then (3.20) applies and the AFB output at subcarrier m and time instant n can be written as

$$y_{m,n} \approx h_{\mathrm{ch},m,n}(x_{m,n-\tau_h} + \mathrm{j}u_{m,n}) + \eta_{m,n}, \tag{4.2}$$

where the PAM symbol $x_{m,n}$ contains the information of interest, $\mathrm{j}u_{m,n}$ stands for the interference contributed by its T-F neighbors, and $\eta_{m,n}$ is the corresponding noise component. Consider the complex-valued single-tap equalizer $w_{m,n}$. The real part of its output is taken to yield an estimate of $x_{m,n}$[4]

$$\begin{aligned}\tilde{x}_{m,n-\tau_h} = \mathbb{R}\mathrm{e}\{w_{m,n}y_{m,n}\} &= w_{m,n}^{(\mathrm{R})}y_{m,n}^{(\mathrm{R})} - w_{m,n}^{(\mathrm{I})}y_{m,n}^{(\mathrm{I})} \\ &= \bar{\mathbf{w}}_{m,n}^{\mathrm{T}}\left(\bar{\mathbf{H}}_{\mathrm{ch},m,n}\bar{\mathbf{x}}_{m,n} + \bar{\boldsymbol{\eta}}_{m,n}\right),\end{aligned} \tag{4.3}$$

where

$$\begin{aligned}\bar{\mathbf{x}}_{m,n} &= \begin{bmatrix} x_{m,n-\tau_h} & u_{m,n}\end{bmatrix}^{\mathrm{T}} \\ \bar{\mathbf{H}}_{\mathrm{ch},m,n} &= \begin{bmatrix} h_{\mathrm{ch},m,n}^{(\mathrm{R})} & -h_{\mathrm{ch},m,n}^{(\mathrm{I})} \\ h_{\mathrm{ch},m,n}^{(\mathrm{I})} & h_{\mathrm{ch},m,n}^{(\mathrm{R})}\end{bmatrix} \\ \bar{\mathbf{w}}_{m,n} &= \begin{bmatrix} w_{m,n}^{(\mathrm{R})} & w_{m,n}^{(\mathrm{I})}\end{bmatrix}^{\mathrm{T}} \\ \bar{\boldsymbol{\eta}}_{m,n} &= \begin{bmatrix} \eta_{m,n}^{(\mathrm{R})} & \eta_{m,n}^{(\mathrm{I})}\end{bmatrix}^{\mathrm{T}} \\ &= \begin{bmatrix} \mathbf{h}_m^{(\mathrm{R})} & \mathbf{h}_m^{(\mathrm{I})} \\ -\mathbf{h}_m^{(\mathrm{I})} & \mathbf{h}_m^{(\mathrm{R})}\end{bmatrix}^{\mathrm{T}} \begin{bmatrix} \boldsymbol{\eta}^{(\mathrm{R})} \\ \boldsymbol{\eta}^{(\mathrm{I})}\end{bmatrix} = \bar{\boldsymbol{\mathcal{H}}}_m\bar{\boldsymbol{\eta}},\end{aligned} \tag{4.4}$$

with $\mathbf{h}_m \in \mathbb{C}^{L_\mathrm{P}}$ containing the coefficients of the analysis filter impulse response of the mth subcarrier and $\boldsymbol{\eta} \in \mathbb{C}^{L_\mathrm{P}}$ containing samples of the noise that is added to the channel output. The noise is assumed zero mean white Gaussian with variance σ_η^2. The AFB output noise, $\eta_m[n]$, is then also Gaussian with zero mean but colored and has the same variance σ_η^2, because we assume unitary filters.

The ZF equalizer is a first and straightforward solution for single-tap equalization, that has been extensively employed in the literature [45]. Similarly to CP-OFDM, the ZF equalizer is given by $w_{m,n} = 1/h_{\mathrm{ch},m,n}$. But it may not be the best possible option to be employed here, because of the existing interference, which strongly limits its performance and because it does not take the influence of the filters into account. Another solution frequently used in practice[5] is the Linear

[4] The decomposition into real-valued vectors and matrices shown here was first introduced in the context of OQAM equalizers in [70], for Single-Carrier (SC) systems.

[5] Although the ZF is the mostly commonly encountered solution in the CP-OFDM literature, in practical implementations, such as in LTE, it is the MMSE that is more often adopted.

Minimum Mean Squared Error (LMMSE) equalizer, which must take into account the statistics of the interference and of the noise, in addition to the properties of the OQAM signaling. The latter solution is given by

$$\begin{aligned}\bar{\mathbf{w}}_{m,n}^{\text{opt}} &= \underset{\bar{\mathbf{w}}_{m,n}}{\operatorname{argmin}} \, \mathrm{E}\left\{|\tilde{x}_{m,n-\tau_h} - x_{m,n-\tau_h}|^2\right\} \\ &= \left(\bar{\mathbf{H}}_{\text{ch},m,n} \begin{bmatrix} 1 & 0 \\ 0 & \frac{\sigma_u^2}{\sigma_x^2} \end{bmatrix} \bar{\mathbf{H}}_{\text{ch},m,n}^{\mathrm{T}} + \frac{\sigma_\eta^2}{2\sigma_x^2} \bar{\boldsymbol{\mathcal{H}}}_m \bar{\boldsymbol{\mathcal{H}}}_m^{\mathrm{T}} \right)^{-1} \begin{bmatrix} h_{\text{ch},m,n}^{(\mathrm{R})} \\ h_{\text{ch},m,n}^{(\mathrm{I})} \end{bmatrix}, \end{aligned} \tag{4.5}$$

where σ_d^2 and σ_u^2 are the variances of the input symbols and the interference term, respectively. Recalling the variance of the interference σ_u^2 from (3.18), where it only depends on the prototype filter. The complex single-tap equalizer is then obtained by de-stacking the two components of $\bar{\mathbf{w}}_{m,n}$ into its real and imaginary parts. An efficient implementation of the single-tap equalizer, which combines it with the OQAM de-staggering was presented in 2.4.3.

4.2.2 Multi-tap Linear MMSE Equalizer Design

Multi-tap equalizers can be divided into two basic categories depending on how they are computed and realized. On a per-subcarrier basis, equalizer design and implementation can be performed both in the time and frequency domains. Moreover, the computation of the equalizer coefficients does not impose a specific structure to be adopted. This also means that, during the design step, a specific structure can be assumed, which is not exactly the implemented one. For example, in [37], the authors base the design of the equalizers on the frequency responses of the channel and the FB prototype, but the implementation is primarily based on time domain real and complex valued FIR filters. On the other hand, in the FS-FBMC structure [14] or in the equalizers presented in [62], multiple frequency bins per subcarrier are assumed, the equalizer is designed in the frequency domain and implemented as one complex multiplier per frequency bin. Clearly, one multiplier per frequency bin is not the same as a single tap per subcarrier presented previously and can also address frequency selectivity at the subchannel level. The frequency domain design can also follow ZF or MMSE criteria.

This section focuses on classical Tap Delay Line (TDL) structure-based design. One or more equalizers per subcarrier are represented as FIR filters and their coefficients are then computed. It is worth noting that, a TDL or any other structure can be implemented. That is, other FIR filter structures, such as polyphase based, non-recursive lattice, CORDIC-based, etc., can be employed for the equalizer operation. One example is the efficient polyphase based structure presented in Section 2.4.3. Moreover, the design that follows can be also effectively implemented in the frequency domain, as long as the number of frequency bins is the same as the number of equalizer taps in the time domain.

In an FBMC/OQAM system, the SFB combines the M complex-valued QAM input signals $x_m[k] = x_m[2n] + \mathrm{j}x_m[2n-1]$, $m = 0, 1, \ldots, M-1$, generated at a rate of $1/T$, into a single complex-valued signal $x_{\text{SFB}}[l]$ of a higher sampling rate, $1/T_s = M/T$. The signal is transmitted to the receiver through a frequency selective channel, and white Gaussian noise is added. In our system, M corresponds to the total number of subcarriers available and M_{u} is the number of subcarriers used for transmission. The AFB separates the received signal back into its M_{f} components at the lower rate $1/T$ per subcarrier. A subcarrier model that can be used to design multi-tap equalizers is given in Figure 4.1. $\mathcal{O}_\ell$ and $\mathcal{O}'_\ell$ represent the staggering and de-staggering operations, respectively.

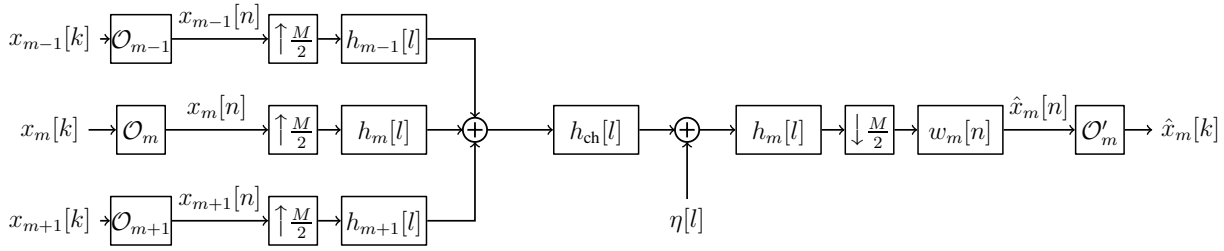

Fig. 4.1. Subcarrier model for the multi-tap equalizer design.

The first operation in the SFB is the OQAM staggering of each input $x_\ell[k]$ that generated the output sequence $\mathbf{x}_\ell[n]$ as

$$\mathbf{x}_\ell[n] = \begin{cases} \begin{bmatrix} x'_\ell[n] & \mathrm{j}x'_\ell[n-1] & x'_\ell[n-2] & \cdots \end{bmatrix}^{\mathrm{T}}, & m+n \text{ is odd,} \\ \begin{bmatrix} \mathrm{j}x'_\ell[n] & x'_\ell[n-1] & \mathrm{j}x'_\ell[n-2] & \cdots \end{bmatrix}^{\mathrm{T}}, & m+n \text{ is even.} \end{cases} \tag{4.6}$$

The input symbol $x_\ell[k]$ is split into its real $x_\ell^{(\mathrm{R})}[k] = x'_\ell[2n]$ and j times its imaginary $\mathrm{j}x_\ell^{(\mathrm{I})}[k] = \mathrm{j}x'_\ell[2n-1]$ parts and up-sampled by a factor of two. Then depending on the parity of the subcarrier index that we observe, either $x'_\ell[n]$ or $\mathrm{j}x'_\ell[n]$ is delayed by exactly $T/2$ samples and finally these components are added together. At the receiver, the AFB applies OQAM de-staggering to reconstruct the complex QAM $\hat{x}_m[k]$ symbols from the equalizer outputs $\hat{x}_m[2n]$ and $\hat{x}_m[2n-1]$ at the observed subcarrier m and time slot n.

To have a simple notation for the system in Figure 4.1, we define the following filtering and downsampling operation, $\tilde{h}_{m,\ell}[n] = (h_m[l] * h_{\text{ch}}[l] * h_\ell[l])\ |_{l=n\frac{M}{2}}$. This represents the overall impulse response from subcarrier ℓ at the SFB to subcarrier m at the AFB, with $\ell \in \{m-1, m, m+1\}$. The resulting filter has $L_{\tilde{h}} = \left\lceil \frac{2L_{\text{P}}+L_{\text{ch}}-2}{M/2} \right\rceil$ coefficients. Moreover, we define the transposed convolution matrix $\mathbf{H}_{m,\ell} \in \mathbb{R}^{L_{\text{eq}} \times (L_{\tilde{h}}+L_{\text{eq}}-1)}$ generated from the impulse response $\tilde{h}_{m,\ell}[n]$, where L_{eq} is the number of taps of the equalizer. Furthermore, we assume the channel impulse response $h_{\text{ch}}[l]$ or an estimate is available.

Also here, we work with a purely real notation and therefore define a purely real input sequence as $\mathbf{x}'_\ell[n]$, where the relation $\mathbf{x}_\ell[n] = \mathbf{J}_{\ell,n}\mathbf{x}'_\ell[n]$ holds with

$$\mathbf{J}_{\ell,n} = \begin{cases} \mathrm{diag}\begin{bmatrix} 1 & \mathrm{j} & 1 & \mathrm{j} & \cdots \end{bmatrix}, & \ell+n \text{ is odd,} \\ \mathrm{diag}\begin{bmatrix} \mathrm{j} & 1 & \mathrm{j} & 1 & \cdots \end{bmatrix}, & \ell+n \text{ is even.} \end{cases} \tag{4.7}$$

This extracts the imaginary constants j from the input signal. We then multiply the transposed convolution matrix of $h_{m,\ell}[n]$ from the right by $\mathbf{J}_{\ell,n}$ and obtain $\mathbf{H}'_{m,\ell} = \mathbf{H}_{m,\ell}\mathbf{J}_{\ell,n}$. Hence we can write

$$\hat{x}_m[n] = \bar{\mathbf{w}}_m^{\mathrm{T}} \left(\bar{\mathbf{H}}'_{m,m}\mathbf{x}'_m[n] + \bar{\mathbf{H}}'_{m,m-1}\mathbf{x}'_{m-1}[n] + \bar{\mathbf{H}}'_{m,m+1}\mathbf{x}'_{m+1}[n] + \mathbf{\Gamma}_m\bar{\boldsymbol{\eta}} \right), \tag{4.8}$$

where we define

$$\begin{aligned}
\mathbf{x}'_\ell[n] &\in \mathbb{R}^{(L_{\tilde{h}}+L_{\text{eq}}-1)\times 1},\\
\bar{\mathbf{H}}'_{m,\ell} &= \begin{bmatrix}(\mathbf{H}'_{m,\ell})^{(\text{R})}\\ (\mathbf{H}'_{m,\ell})^{(\text{I})}\end{bmatrix} \in \mathbb{R}^{(2L_{\text{eq}})\times(L_{\tilde{h}}+L_{\text{eq}}-1)},\\
&\text{with } \ell \in \{m-1,\ m,\ m+1\},\\
\bar{\mathbf{w}}_m &= \begin{bmatrix}\mathbf{w}_m^{(\text{R})}\\ \mathbf{w}_m^{(\text{I})}\end{bmatrix} \in \mathbb{R}^{(2L_{\text{eq}})\times 1},\\
\mathbf{\Gamma}_m &= \begin{bmatrix}(\check{\mathbf{H}}_m)^{(\text{R})} & -(\check{\mathbf{H}}_m)^{(\text{I})}\\ (\check{\mathbf{H}}_m)^{(\text{I})} & (\check{\mathbf{H}}_m)^{(\text{R})}\end{bmatrix} \in \mathbb{R}^{(2L_{\text{eq}})\times 2(L_{\text{eq}}+L_{\tilde{h}}-1)} \text{ and}\\
\bar{\boldsymbol{\eta}} &= \begin{bmatrix}\boldsymbol{\eta}^{(\text{R})}\\ \boldsymbol{\eta}^{(\text{I})}\end{bmatrix} \in \mathbb{R}^{2(L_{\text{eq}}+L_{\tilde{h}}-1)\times 1}.
\end{aligned} \tag{4.9}$$

The matrix $\check{\mathbf{H}}_m$ is obtained by taking every $\frac{M}{2}$th row of the convolution matrix generated from the AFB subfilter impulse response $h_m[l]$.

We make here the usual assumption that the input symbols are independent and identically distributed (i.i.d.) and Gaussian distributed, although they belong in reality to a discrete alphabet. As a result, the covariance matrix of $\mathbf{x}'_\ell[n]$ can be expressed as $\text{E}\left[\mathbf{x}'_\ell[n]\mathbf{x}'^{\text{T}}_\ell[n]\right] = \sigma_d^2\mathbf{I}$ and, again, the noise vector $\boldsymbol{\eta}$ at the AFB input has covariance $\sigma_\eta^2\mathbf{I}$.

The multi-tap MMSE equalizer is given by [77]

$$\begin{aligned}
\bar{\mathbf{w}}_m^{\text{opt}} &= \underset{\bar{\mathbf{w}}_m}{\text{argmin}}\ \text{E}\left\{|\hat{x}_{m,n} - x_{m,n-\nu}|^2\right\}\\
&= \left(\sum_{\ell=m-1}^{m+1} \bar{\mathbf{H}}'_{m,\ell}(\bar{\mathbf{H}}'_{m,\ell})^{\text{T}} + \frac{\sigma_\eta^2}{2\sigma_x^2}\mathbf{\Gamma}_m\mathbf{\Gamma}_m^{\text{T}}\right)^{-1} \bar{\mathbf{H}}'_{m,m}\mathbf{e}_{\nu+1}.
\end{aligned} \tag{4.10}$$

The vector $\mathbf{e}_{\nu+1} \in \{0,1\}^{(L_{\tilde{h}}+L_{\text{eq}}-1)\times 1}$ contains a unity at the $(\nu+1)$th position and ν is the equalizer delay typically chosen as $\nu = 2K + \lceil L_{\text{eq}}/2\rceil$. It can be easily proved that separately solving for real or imaginary symbols gives the same result. Moreover, there is a number of solutions in the literature to simplify the matrix inversion above in order to reduce the costs of its implementation.

An efficient implementation of the multi-tap equalizer, which combines it with the OQAM de-staggering was presented in 2.4.3.

4.2.2.1 Bias Removal

Given an equalizer impulse response for each subchannel, it can be shown that the MSE at its output is given by

$$\text{MSE}_m^{\text{eq}} = \sigma_x^2(1 - \bar{\mathbf{w}}_m^{\text{T}}\bar{\mathbf{H}}_{m,m}\mathbf{e}_{\nu+1}). \tag{4.11}$$

On the other hand, the output of the MMSE equalizer is given by

$$\hat{x}_m[n] = \alpha_m(x_m[n-\nu] + \text{ISI}_m + \text{ICI}_m + \eta_m[n]), \tag{4.12}$$

where ISI_m and ICI_m are the residual intersymbol and intercarrier interference, respectively, while the factor $\alpha_m = \text{E}[\hat{x}_m[n]|x_m[n-\nu]]/x_m[n-\nu] < 1$ is related to the bias inserted by this equalizer,

as it is well-known that the linear MMSE equalizer is biased. Consequently, it can be demonstrated that the SINR at the output of the MMSE LE is [24]

$$\mathrm{SINR}_m = \frac{\sigma_x^2}{\mathrm{MSE}_m} - 1. \tag{4.13}$$

Moreover, as shown in [24], the bias is defined as

$$\alpha_m = \frac{1}{1 + (\mathrm{SINR}_m)^{-1}}. \tag{4.14}$$

A simple way to force the MMSE equalizer to become unbiased is by simply multiplying its output by α_k^{-1}. As a result, the bias removal coefficient is given by

$$\alpha_m^{-1} = \frac{\sigma_d^2}{\sigma_d^2 - \mathrm{MSE}_m} \tag{4.15}$$

It is worth noting that although the bias removal reduces the symbol estimation error, it increases the MSE in each subchannel. The new MSE becomes

$$\mathrm{MSE}_{m,U} = \frac{1}{\alpha_k}\mathrm{MSE}_m = \frac{\sigma_d^2 \mathrm{MSE}_m}{\sigma_d^2 - \mathrm{MSE}_m}$$

Furthermore, we would like to comment that in the case of CP-OFDM, the trivial one-tap MMSE unbiased equalizer is equal to the zero forcing equalizer. The latter is widely accepted as the standard one-tap equalizer for CP-OFDM.

4.2.2.2 MLSE Receiver

In the classical literature of receivers for frequency selective channels, the MLSE equalizer is referred as the optimal receiver [61]. In addition to completely mitigating the ISI, those receivers make use of the time diversity inserted by the multipath channel. The main drawback and an obstacle to practical use of the MLSE is its computational complexity.

Let us now consider the more sophisticated MLSE equalization for the FBMC system in order to compare with the more practical MMSE solution previously presented. The optimal MLSE receiver should take into account the output of all subchannels to find the most likely input symbols. The problem is that this joint ML decoding among all subcarriers is computationally infeasible. Nevertheless, since there is overlap only between contiguous subchannels, the complexity can be reduced by using a two-dimensional Viterbi-like detector, but it still remains much more complex than a per-subchannel detector.

Therefore, for simplicity, the interference from the adjacent subcarriers is assumed to be Gaussian distributed, which means that we separately perform a suboptimal MLSE on each subcarrier. Furthermore, we ignore the fact the ICI is colored. In that case, the MLSE rule is only related to the impulse response $\tilde{h}_{m,m}[n]$, whose length is denoted by $L_{\tilde{h}}$. For the case of Offset Quadrature Phase-Shift Keying (OQPSK) modulation, the trellis has $2^L_{\tilde{h}}$ states with only two possible transitions per state since the detection is carried out on a real representation of the data. The MLSE selects the input sequence $\hat{x}_m[0], ..., \hat{x}_m[B]$ of length $(B+1)$ that minimizes the cost

$$\mathcal{C}_m[B] = \sum_{\mu=0}^{B} \left| y_m[\mu] - \sum_{n=0}^{L_{\tilde{h}-1}} x'_m[\mu - n]\tilde{h}_{m,m}\prime[n] \cdot \mathbb{I}(\mu - n) \right|^2, \tag{4.16}$$

where

$$\mathbb{I}(n) = \begin{cases} 1 & \text{for } n \text{ even}, \\ \mathrm{j} & \text{for } n \text{ odd}. \end{cases} \tag{4.17}$$

Hereby, the case distinction follows from the OQAM constellation structure and we assume the subcarrier index m to be odd. For even m, we just have to reverse the definition of $\mathbb{I}(n)$. More precisely, the MLSE rule (4.16) can be computed sequentially using the Viterbi algorithm as

$$\mathcal{C}_m[\mu] = \mathcal{C}_m[\mu-1] + \left| y_m[\mu] - \sum_{n=0}^{L_{\tilde{h}-1}} x'_m[\mu-n]\bar{h}_{m,m}[\mu,n] \right|^2, \tag{4.18}$$

where $\bar{h}_{m,m}[\mu,n]$ represents a time-variant impulse response given by

$$\bar{h}_{m,m}[\mu,n] = \begin{cases} \tilde{h}_{m,m}[n] & \text{for } m \text{ even}, \\ \mathrm{j}\tilde{h}_{m,m}[n] & \text{for } m \text{ odd}, \end{cases} \tag{4.19}$$

and $x'_m[n] \in \{\pm 1\}$ for the OQPSK case. In other words, the added single squared error term at time m to the cost at time $m-1$ has to be computed differently, depending on whether m is even or odd.

4.2.2.3 Numerical Results

In our simulations we have considered the FBMC system described in Chapter 2. The prototype was obtained by the frequency sampling method described in [13]. The channel between synthesis and analysis FBs is modeled as an FIR filter to reproduce the effects of multipath propagation encountered in wireless communication environments. For the matter of comparison, we have employed at the receiver both MLSE and Unbiased MMSE linear equalizer to compensate for the frequency selectivity of the channel.

In the first example we have employed the parameters in Table 4.1. Fig. 4.2 shows a comparison

Parameter	Value
Modulation	QPSK
Total number of subchannels	$M = 128$
Data filled subchannels	$M_{\mathrm{f}} = 96$
Subchannel spacing	$\Delta f = 87.2$ kHz
Total bandwidth	$\mathrm{BW} = 10$ MHz
Sampling period	$T_{\mathrm{s}} = 89.28$ ns
Equalizer length	$L_{\mathrm{eq}} = 21$
Channel model	ITU Vehicular B static
RMS delay spread	$\tau_{\mathrm{RMS}} = 4\,\mu$s
Symbols per subchannel	100
Channel realizations	100

Table 4.1. Parameters for BER comparison of FBMC receivers

of the uncoded BER between the MMSE Linear Equalizer and two variants of the MLSE equalizer. The curve denoted MLSE ICI corresponds to the case where the ICI is not removed before the

sequence estimation, but just seen as Gaussian noise. The curve denoted MLSE corresponds to the case where ICI is completely removed from the received signal unrealistically assuming that the receiver perfectly knows it. This is consequently a performance lower bound for a feasible MLSE.

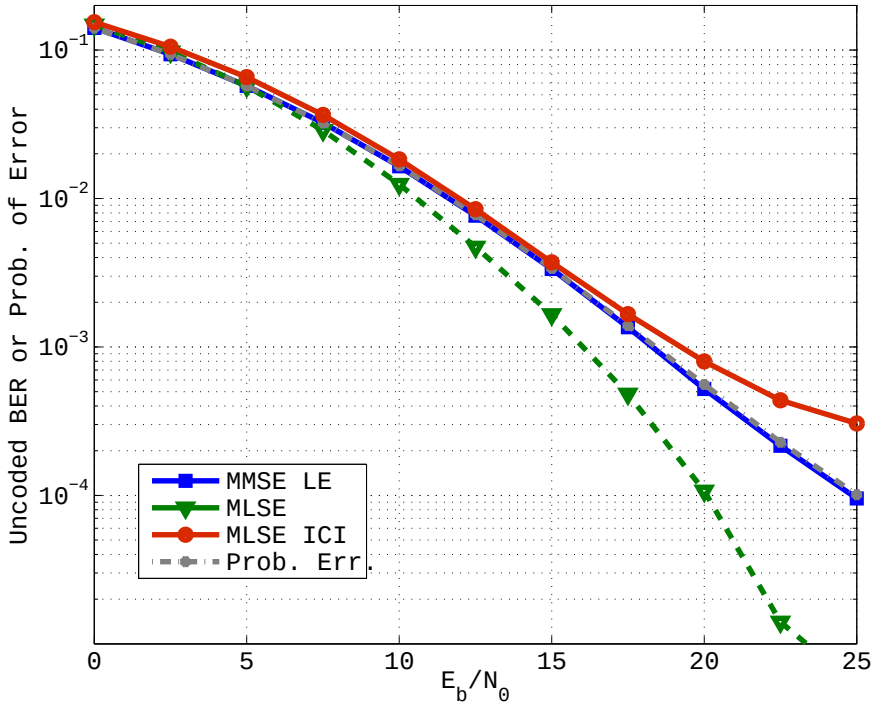

Fig. 4.2. Uncoded BER comparison between MMSE Linear Equalizer and MLSE. Parameterization from Table 4.1.

The analytical probability of error is also depicted in Fig. 4.2. For this computation, we have assumed that the sum of the residual ISI, ICI and noise at the output of the equalizer are Gaussian distributed. Consequently the probability of error was calculated for an AWGN channel on each subchannel and for each channel realization. The variance of that interference-plus-noise source is given by the MSE in Eq. (4.11).

We can see that for low values of E_b/N_0 (Energy per bit over the one sided noise power spectral density) both MMSE and MLSE equalizers present similar results, only for higher values of E_b/N_0, the MLSE without ICI presents significant improvements. Clearly, this improved performance comes at the price of an impractical increase in the computational complexity.

As a second example, we have considered a comparison between the coded and uncoded BER for both FBMC employing 16-QAM and CP-OFDM employing 32-QAM. We have used a convolutional encoder and a soft decoder. All the other parameters are shown in Table 4.2 and the results are depicted in Fig. 4.3. By choosing different QAM alphabets both systems will possess the same spectral efficiency in bits/Hz. It should be clear that CP-OFDM loses in spectral efficiency proportionally to the length of the CP.

From the simulation in Fig. 4.3 it is possible to see that the FBMC system allows a reduction of 2.5 dB in the transmitted power to achieve the same data rate and BER performance of a similar CP-OFDM system.

Parameter	Value
Total number of subchannels	$M = 1024$
Data filled subchannels	$M_{\mathrm{f}} = 768$
Subchannel spacing	$\Delta f = 10.9$ kHz
Total bandwidth	$\mathrm{BW} = 10$ MHz
Sampling period	$T_{\mathrm{s}} = 89.28$ ns
CP length	$T_{\mathrm{CP}} = 22.85\,\mu$s $(1/4)$
Equalizer length	$L_{\mathrm{eq}} = 5$
Channel model	ITU Vehicular B static
RMS delay spread	$\tau_{\mathrm{RMS}} = 4\,\mu$s
Symbols per subchannel	1000
Channel realizations	200
Code rate, R	$1/2$
Code polynomials	$1 + D^1 + D^2 + D^3 + D^6$
	$1 + D^2 + D^3 + D^5 + D^6$
Type of decoder	Max-log-MAP algorithm

Table 4.2. Parameters for BER comparison between FBMC and CP-OFDM

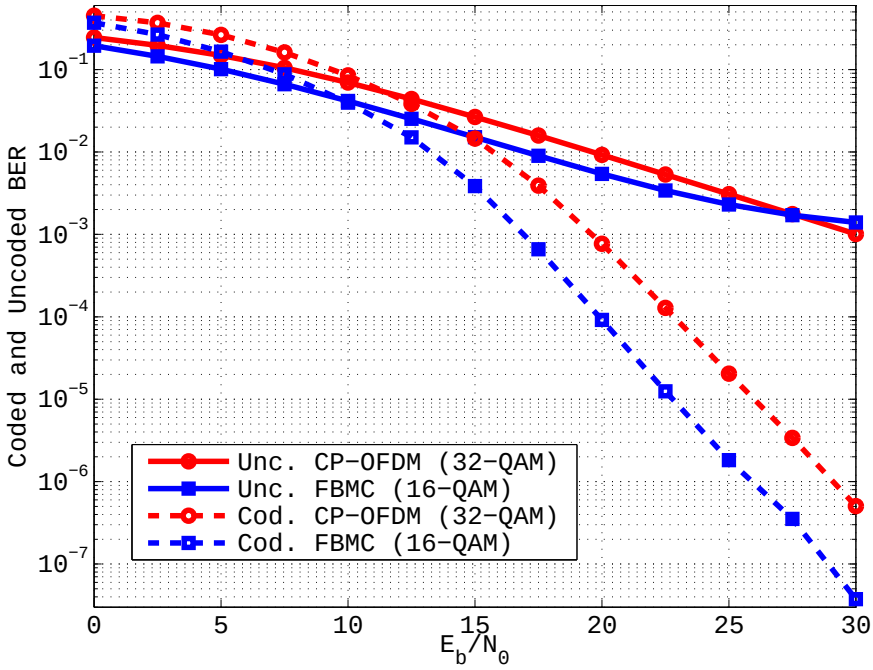

Fig. 4.3. Uncoded and coded BER comparison between FBMC with LE and OFDM

4.2.3 Precoder Design based on MSE Duality Transformations

In scenarios where the channel impulse response is known at the transmitter side, it is usually preferred to employ a precoder instead of or complementary to an equalizer. The precoder has the advantage that it will not color nor amplify the noise like the equalizer does, so that the symbol detection can be performed with the white noise assumption. Other advantage is in case the transmitter has more computational capability and has performed the estimation of the dual channel during

the reception or obtained as feedback from the receiver. An example is when an infrastructure network node communicates via a wireless channel with a mobile device with low computational capability, for example, a low power IoT device.

A block diagram with the subcarrier model for the linear precoder design is shown in Fig. 4.4, where $b_\ell[n]$ are the impulse responses of the precoders that have L_{pre} coefficients. The precoder needs to be designed in a way that the transmit power is limited, otherwise, depending on the channel conditions the precoder may try to amplify the transmit signal above the capabilities of the hardware where it is implemented and saturation will occur. That is why the single coefficient $\bar{w}_m^{(\text{pre})} \in \mathbb{R}_+$ needs to be employed at the AFB.

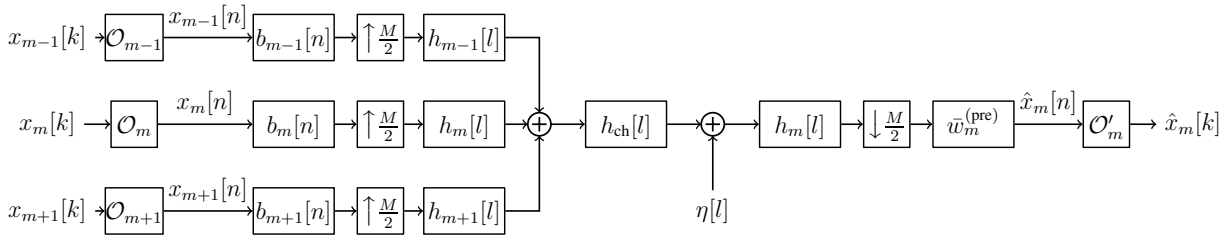

Fig. 4.4. Subcarrier model for the multi-tap precoder design.

We can then write the signal at the output of the AFB and before the OQAM destaggering as

$$\hat{x}_m[n] = \bar{w}_m^{(\text{pre})} \left(\sum_{\ell=m-1}^{m+1} \bar{\mathbf{b}}_\ell^{\text{T}} \bar{\mathbf{H}}'_{m,\ell} \mathbf{x}'_\ell[n] + \Re\left\{ \mathbf{h}_m^{\text{H}} \bar{\boldsymbol{\eta}} \right\} \right), \tag{4.20}$$

where the matrices and vectors employed here are similarly or identically defined as in (4.9).

Based on the subcarrier model presented, we can calculate the MSE per subcarrier as a function of the precoders and the subcarrier subfilters as follows

$$\text{MSE}_m^{\text{pre}} = \sigma_x^2 \left(\left(\bar{w}_m^{(\text{pre})}\right)^2 \sum_{\ell=m-1}^{m+1} \bar{\mathbf{b}}_\ell^{\text{T}} \bar{\mathbf{H}}'_{m,\ell} \bar{\mathbf{H}}'^{\,\text{T}}_{m,\ell} \bar{\mathbf{b}}_m + 1 - 2\bar{w}_m^{(\text{pre})} \bar{\mathbf{b}}_\ell^{\text{T}} \bar{\mathbf{H}}'_{m,m} \mathbf{e}_{\nu+1} \right) + \left(\bar{w}_m^{(\text{pre})}\right)^2 \sigma_\eta^2 ||\mathbf{h}_{\text{P}}||_2^2. \tag{4.21}$$

where $||\mathbf{h}_{\text{P}}||_2^2$ is the norm of the prototype filter. We can observe that the MSE is a function not only of the precoders of the subcarrier under consideration but also of the precoders of the adjacent subcarriers. If we would like to design the precoders to minimize this MSE, we would need to jointly minimize for all subcarriers, which consecutively overlap. This would be increase the dimensions of the problem in a impractical and unnecessary way.

One way to still minimize the MSE and calculate the precoder on a subcarrier basis is to employ the MSE duality [36, 54]. Instead of directly designing the precoders, an equalizer of the dual subcarrier system is firstly designed an then a duality transformation is employed to obtain the coefficients of the precoder. A basic assumption of the duality transformation is that the transmit power remains preserved, i.e. the transmit power of the system employing precoders is the same as of the dual system employing equalizers.

The first step is to calculate the MMSE equalizer as described in Section 4.2.2. Then we need to make the MSE from the precoder system equal to the one of the dual equalizer system. Here we have two possibilities: make the sum of the MSE along all subcarriers equal or make the individual subcarrier MSE equal. Those two possibilities translate in two different duality transformations that we describe in detail in the next sections.

4.2.3.1 Sum-MSE Duality Transformation

This duality transformation preserves the sum of the MSE and is the simplest one, since a single scaling factor is required which leads to a relatively low computational complexity. We first define the relation between equalizer and precoder with a real valued positive scaling factor such that

$$\bar{\mathbf{b}}_m = \gamma \bar{\mathbf{w}}_m \quad \text{and} \quad \bar{w}_m^{(\text{pre})} = \gamma^{-1}. \tag{4.22}$$

The sum of the MSE along all subcarriers are set equal for precoder and equalizer as follows

$$\sum_{m=0}^{M_\text{f}-1} \text{MSE}_m^\text{pre} = \sum_{m=0}^{M_\text{f}-1} \text{MSE}_m^\text{eq}. \tag{4.23}$$

We plug (4.22) into (4.21), employ it together with the MSE definition from 4.11, and solve for γ to get the following expression

$$\gamma^2 = \frac{M_\text{f}\sigma_\eta^2 ||\mathbf{h}_\text{P}||_2^2}{\sum_{m=0}^{M_\text{f}-1} \sigma_x^2 \left(\bar{\mathbf{w}}_\ell^\text{T} \bar{\mathbf{H}}'_{m,m} \mathbf{e}_{\nu+1} - \sum_{\ell=m-1}^{m+1} \bar{\mathbf{w}}_\ell^\text{T} \bar{\mathbf{H}}'_{m,\ell} \bar{\mathbf{H}}'^\text{T}_{m,\ell} \bar{\mathbf{w}}_m \right)}. \tag{4.24}$$

This method spreads the transmit power across the subcarriers as required by the channel frequency response. The disadvantage of this method arises if the MSE of certain subcarriers is disproportionately large. This leads to these subcarriers obtaining a greater amount of transmit power at the cost of reduced power in subcarriers with better channel conditions. This is also known as the inverse water filling solution.

4.2.3.2 Per-Subcarrier MSE Duality Transformation

In this transformation the MSE per subcarrier is preserved and results in an individual scaling factor for each subcarrier. We define the relation between equalizer and precoder with a real-valued scaling factor per subcarrier such that

$$\bar{\mathbf{b}}_m = \gamma_m \bar{\mathbf{w}}_m \quad \text{and} \quad \bar{w}_m^{(\text{pre})} = \gamma_m^{-1} \tag{4.25}$$

The individual MSE expressions per subcarrier equal as follows

$$\text{MSE}_m^\text{pre} = \text{MSE}_m^\text{eq}, \quad \text{for } m = 0, ..., M_\text{f} - 1 \tag{4.26}$$

By making the appropriate substitutions we end-up with the following system of equations

$$\mathbf{T} \begin{bmatrix} \gamma_0^2 \\ \gamma_1^2 \\ \vdots \\ \gamma_{M_\text{f}-1}^2 \end{bmatrix} = M_\text{f}\sigma_\eta^2 ||\mathbf{h}_\text{P}||_2^2 \mathbf{1}_{M_\text{f}} \tag{4.27}$$

where the tridiagonal matrix $\mathbf{T}$ is given by

$$[\mathbf{T}]_{m,\ell} = \begin{cases} -\sigma_x^2 \bar{\mathbf{w}}_{m-1}^\text{T} \bar{\mathbf{H}}'_{m-1,m-1} \bar{\mathbf{H}}'^\text{T}_{m-1,m-1} \bar{\mathbf{w}}_{m+1} & \text{for } \ell = m-1 \\ \sigma_x^2 \left(\bar{\mathbf{w}}_\ell^\text{T} \bar{\mathbf{H}}'_{m,m} \mathbf{e}_{\nu+1} - \bar{\mathbf{w}}_m^\text{T} \bar{\mathbf{H}}'_{m,m} \bar{\mathbf{H}}'^\text{T}_{m,m} \bar{\mathbf{w}}_m \right) & \text{for } \ell = m \\ -\sigma_x^2 \bar{\mathbf{w}}_{m+1}^\text{T} \bar{\mathbf{H}}'_{m+1,m+1} \bar{\mathbf{H}}'^\text{T}_{m+1,m+1} \bar{\mathbf{w}}_{m+1} & \text{for } \ell = m+1 \\ 0 & \text{elsewhere.} \end{cases} \tag{4.28}$$

We get a linear system of equations for M_f scaling factors, which results in a higher computational complexity than a Sum-MSE transformation. Now the transmit power is not spread amongst the subcarriers but instead we normalize the filter in each subcarrier.

4.2.4 Multi-tap Linear Maximum SINR Equalizer Design

An alternative equalizer design to the MMSE solution described in Section 4.2.2 is to maximize the SINR. In this solution we can also compensate for ICI in addition to ISI.

We start by defining the effective channel experienced by the specific symbol being equalized such that

$$\bar{\mathbf{h}}_m^{\prime(\text{eff})} = \bar{\mathbf{H}}^{\prime}_{m,m}\mathbf{e}_{\nu+1}. \tag{4.29}$$

With that we can express the power of the signal of interest as

$$\text{SP}_m = \text{E}\left[|\bar{\mathbf{w}}_m^{\text{T}}\bar{\mathbf{h}}_m^{\prime(\text{eff})}|^2\right] = \bar{\mathbf{w}}_m^{\text{T}}\bar{\mathbf{h}}_m^{\prime(\text{eff})}\bar{\mathbf{h}}_m^{\prime(\text{eff}),\text{T}}\bar{\mathbf{w}}_m. \tag{4.30}$$

Now we define the temporal spread, i.e. the coefficients of the ISI, by $\bar{\mathbf{H}}^{\prime(\text{ISI})}_{m,m} = \bar{\mathbf{H}}^{\prime}_{m,m}\left(\mathbf{I}_{L_{\tilde{h}}} - \mathbf{e}_{\nu+1}\mathbf{e}_{\nu+1}^{\text{T}}\right)$ in order to calculate the ISI power at the output of the equalizer as follows

$$\text{ISI}_m = \text{E}\left[|\bar{\mathbf{w}}_m^{\text{T}}\bar{\mathbf{H}}^{\prime(\text{ISI})}_{m,m}\mathbf{x}^{\prime}_m[n]|^2\right] = \sigma_x^2\bar{\mathbf{w}}_m^{\text{T}}\bar{\mathbf{H}}^{\prime(\text{ISI})}_{m,m}\bar{\mathbf{H}}^{\prime(\text{ISI}),\text{T}}_{m,m}\bar{\mathbf{w}}_m. \tag{4.31}$$

Furthermore, we can define the ICI power after equalization as

$$\begin{aligned}\text{ICI}_m &= \text{E}\left[|\bar{\mathbf{w}}_m^{\text{T}}\bar{\mathbf{H}}^{\prime}_{m,m-1}\mathbf{x}^{\prime}_{m-1}[n]|^2\right] + \text{E}\left[|\bar{\mathbf{w}}_m^{\text{T}}\bar{\mathbf{H}}^{\prime}_{m,m+1}\mathbf{x}^{\prime}_{m+1}[n]|^2\right] &(4.32)\\ &= \sigma_x^2\bar{\mathbf{w}}_m^{\text{T}}\left(\bar{\mathbf{H}}^{\prime}_{m,m-1}\bar{\mathbf{H}}^{\prime\,\text{T}}_{m,m-1} + \bar{\mathbf{H}}^{\prime}_{m,m+1}\bar{\mathbf{H}}^{\prime\,\text{T}}_{m,m+1}\right)\bar{\mathbf{w}}_m. &(4.33)\end{aligned}$$

Finally, we define the noise power in the equalizer output such that

$$\mathcal{N}_m = \text{E}\left[|\bar{\mathbf{w}}_m^{\text{T}}\mathbf{\Gamma}_m\bar{\boldsymbol{\eta}}|^2\right] = \sigma_\eta^2\bar{\mathbf{w}}_m^{\text{T}}\mathbf{\Gamma}_m\mathbf{\Gamma}_m^{\text{T}}\bar{\mathbf{w}}_m. \tag{4.34}$$

The optimum equalizer in the sense of maximizing the SINR is given by

$$\bar{\mathbf{w}}_m^{\text{opt}} = \underset{\bar{\mathbf{w}}_m}{\text{argmax}}\,\text{SINR}_m = \underset{\bar{\mathbf{w}}_m}{\text{argmax}}\,\frac{\text{SP}_m}{\text{ISI}_m + \text{ICI}_m + \mathcal{N}_m}, \tag{4.35}$$

which after performing the corresponding substitutions results in the following expression

$$\text{SINR}_m = \frac{\bar{\mathbf{w}}_m^{\text{T}}\left(\bar{\mathbf{h}}_m^{\prime(\text{eff})}\bar{\mathbf{h}}_m^{\prime(\text{eff}),\text{T}}\right)\bar{\mathbf{w}}_m}{\bar{\mathbf{w}}_m^{\text{T}}\left(\bar{\mathbf{H}}^{\prime(\text{ISI})}_{m,m}\bar{\mathbf{H}}^{\prime(\text{ISI}),\text{T}}_{m,m} + \bar{\mathbf{H}}^{\prime}_{m,m-1}\bar{\mathbf{H}}^{\prime\,\text{T}}_{m,m-1} + \bar{\mathbf{H}}^{\prime}_{m,m+1}\bar{\mathbf{H}}^{\prime\,\text{T}}_{m,m+1} + \frac{\sigma_\eta^2}{\sigma_x^2}\mathbf{\Gamma}_m\mathbf{\Gamma}_m^{\text{T}}\right)\bar{\mathbf{w}}_m} \tag{4.36}$$

If we then define the matrix $\bar{\mathbf{A}} = \bar{\mathbf{h}}_m^{\prime(\text{eff})}\bar{\mathbf{h}}_m^{\prime(\text{eff}),\text{T}}$ and further define

$$\bar{\mathbf{C}} = \bar{\mathbf{H}}^{\prime(\text{ISI})}_{m,m}\bar{\mathbf{H}}^{\prime(\text{ISI}),\text{T}}_{m,m} + \bar{\mathbf{H}}^{\prime}_{m,m-1}\bar{\mathbf{H}}^{\prime\,\text{T}}_{m,m-1} + \bar{\mathbf{H}}^{\prime}_{m,m+1}\bar{\mathbf{H}}^{\prime\,\text{T}}_{m,m+1} + \frac{\sigma_\eta^2}{\sigma_x^2}\mathbf{\Gamma}_m\mathbf{\Gamma}_m^{\text{T}}, \tag{4.37}$$

we get the following simple equation for the SINR

$$\text{SINR}_m = \frac{\bar{\mathbf{w}}_m^{\text{T}}\bar{\mathbf{A}}\bar{\mathbf{w}}_m}{\bar{\mathbf{w}}_m^{\text{T}}\bar{\mathbf{C}}\bar{\mathbf{w}}_m} \tag{4.38}$$

The solution for the SINR equalizer is then given by the matrix pencil $(\bar{\mathbf{A}}, \bar{\mathbf{C}})$, which means that the equalizer vector $\bar{\mathbf{w}}_m^{\text{opt}}$ is the principal eigenvector corresponding to the maximum eigenvalue of the matrix $\bar{\mathbf{C}}^{-1}\bar{\mathbf{A}}$ from the solution of a generalized eigenvalue decomposition.

We should note here that an SINR duality similar to the MSE duality we previously presented also exist and can be employed for a dual precoder design.

4.2.5 Multi-tap Linear Maximum SLR Precoder Design

This is a precoder design method that allows us to obtain the precoder coefficients directly without the use of a duality transformation. The maximization of the SLR for the precoder is analogous to the maximization of the SINR equalizer design, but instead of considering the ICI from the subcarriers $m-1$ and $m+1$ that contaminates the subcarrier of interest m, it considers the leakage from the subcarrier m into its adjacent subcarriers $m-1$ and $n+1$.

The solution looks very similar to the SINR equalizer solution, where the optimum precoder per subcarrier is given by

$$\bar{\mathbf{b}}_m^{\text{opt}} = \underset{\bar{\mathbf{b}}_m}{\text{argmax}}\, \text{SLR}_m = \underset{\bar{\mathbf{b}}_m}{\text{argmax}}\, \frac{\text{SP}_m^{(\text{pre})}}{\text{ISI}_m^{(\text{pre})} + \text{ICI}_m^{(\text{leak})}}. \tag{4.39}$$

We just need first to define $\text{SP}_m^{(\text{pre})}$, i.e. the power of the signal of interest as

$$\text{SP}_m^{(\text{pre})} = \bar{\mathbf{b}}_m^{\text{T}} \bar{\mathbf{h}}_m^{\prime(\text{eff})} \bar{\mathbf{h}}_m^{\prime(\text{eff}),\text{T}} \bar{\mathbf{b}}_m. \tag{4.40}$$

Second we define the ISI power as

$$\text{ISI}_m^{(\text{pre})} = \sigma_x^2 \bar{\mathbf{b}}_m^{\text{T}} \bar{\mathbf{H}}_{m,m}^{\prime(\text{ISI})} \bar{\mathbf{H}}_{m,m}^{\prime(\text{ISI}),\text{T}} \bar{\mathbf{b}}_m \tag{4.41}$$

Third, we define the sum of the contributions from subcarrier m to the ICI in each of the adjacent subcarriers $m-1$ and $m+1$, i.e. the sum of the leakage from subcarrier m as

$$\begin{aligned} \text{ICI}_m^{(\text{leak})} &= \text{E}\left[|\bar{\mathbf{b}}_m^{\text{T}} \bar{\mathbf{H}}'_{m-1,m} \mathbf{x}'_m[n]|^2\right] + \text{E}\left[|\bar{\mathbf{b}}_m^{\text{T}} \bar{\mathbf{H}}'_{m+1,m} \mathbf{x}'_m[n]|^2\right] & (4.42)\\ &= \sigma_x^2 \bar{\mathbf{b}}_m^{\text{T}} \left(\bar{\mathbf{H}}'_{m-1,m} \bar{\mathbf{H}}^{\prime\,\text{T}}_{m-1,m} + \bar{\mathbf{H}}'_{m+1,m} \bar{\mathbf{H}}^{\prime\,\text{T}}_{m+1,m}\right) \bar{\mathbf{b}}_m. & (4.43) \end{aligned}$$

By performing the corresponding substitutions we obtain the following SLR expression

$$\text{SLR}_m = \frac{\bar{\mathbf{b}}_m^{\text{T}} \bar{\mathbf{h}}_m^{\prime(\text{eff})} \bar{\mathbf{h}}_m^{\prime(\text{eff}),\text{T}} \bar{\mathbf{b}}_m}{\bar{\mathbf{b}}_m^{\text{T}} \left(\bar{\mathbf{H}}_{m,m}^{\prime(\text{ISI})} \bar{\mathbf{H}}_{m,m}^{\prime(\text{ISI}),\text{T}} + \bar{\mathbf{H}}'_{m-1,m} \bar{\mathbf{H}}^{\prime\,\text{T}}_{m-1,m} + \bar{\mathbf{H}}'_{m+1,m} \bar{\mathbf{H}}^{\prime\,\text{T}}_{m+1,m}\right) \bar{\mathbf{b}}_m} = \frac{\bar{\mathbf{b}}_m^{\text{T}} \bar{\mathbf{A}} \bar{\mathbf{b}}_m}{\bar{\mathbf{b}}_m^{\text{T}} \bar{\mathbf{C}}' \bar{\mathbf{b}}_m} \tag{4.44}$$

The solution for the SLR precoder is then given by the matrix pencil $(\bar{\mathbf{A}}, \bar{\mathbf{C}}')$, which is similar to the SINR equalizer, but with the corresponding interference elements.

4.2.6 Further SISO Equalizer and Precoder Design Extensions

The linear multitap equalizers and precoders based on the MMSE criteria presented in this chapter can be further extended following different directions. In [10] the linear MMSE equalizers were extended to non-linear MMSE decision feedback equalizers. Later in [39] the MSE duality was employed to transform the Decision Feedback Equalizer (DFE) into a Tomlinson-Harashima Precoder (THP). The non-linear equalizers and precoders are especially useful for very high frequency selectivity inside one subcarrier. This scenario may occur when the subcarrier spacing is very large and the propagation channel has large multipath

Another natural extension is the combination of multitap equalizer with multitap precoder. In this case a joint design, which is usually iterative, needs to be employed. For this joint design, the MSE duality can also be employed.

The equalizers and precoders design described in this chapter always assume perfect channel knowledge, i.e. the impulse responses contained no error. In reality the channel impulse response needs to be estimated, for example, using the methods presented in the previous chapter. Depending on the technique used for the channel estimation, the statistics of the estimation may become available. Those statistics can be employed for the calculation of the equalizer or precoder to end-up with robust design.

4.2.7 Summary and Discussion

In this section we have presented different strategies to design equalizers for SISO FBMC systems. In the case of equalizer design the MMSE and SINR objectives will require the same knowledge about channel and noise. Nevertheless, the final calculation of the equalizer coefficients employ a different types of calculations and the choice among them will in principle depend on the specifics of the computational capability, especially if specialized hardware is available. Typically, the MMSE equalizer will provide slightly better BER results compared to SINR, although not shown in this work. The MLSE equalizer will typically provide the best BER performance but its complexity may be prohibitive and has not been well studied in FBMC systems. In this work we have employed an idealized MLSE to see what is the higher bound in performance if such an equalizer could be employed.

For the choice of the precoder design we have presented two fundamental variants: one based on the MSE duality, where the precoder is indirectly obtained from a dual equalizer and an SLR, where the precoder is directly designed and is analogous to the SINR equalizer. The SLR will typically provide worse results for low SNR, because the statistics of the noise and its power are not taken into account. It is worth noting that there also exist a SINR duality, such that the precoder can also be indirectly calculated from a dual equalizer.

4.3 Extension to MU-MIMO Equalizer and Precoder Design

The equalizers and, more importantly, the precoders presented in this chapter can be further extended to scenarios where multiple mobile stations with one or more antennas communicate with a base station with many antennas.

In [58] a method for the precoder design in a MU-Multiple-Input Single-Output (MISO) scenario is presented, where a modified MMSE is utilized as objective function. The MSE in subcarrier m is added to the power of the contributions from subcarrier m to the ICI in subcarriers $m-1$ and $m+1$, resulting in a sum of MSE with leakage. The work further extend the result for a joint precoder and equalizer design.

In [22] extensions of the MMSE precoder from [58] and from the SLR precoder for MU-MIMO scenarios is presented. The first one being an iterative solution and in both cases an MRC receiver is employed at the mobile station.

In [23] a precoder design based on maximum Signal-to-Leakage-plus-Noise Ratio (SLNR) criteria combined with an equalizer design based on the zero-forcing criteria are applied to multi-streaming MU-MIMO scenarios.

In [17] the MSE duality was applied for the precoder and equalizer designs in MU-MISO scenarios. In addition to the two MSE duality transformations presented in this chaper two other transformations exist from the base station perspective. When the dimension number of users is introduced the sum MSE among the users has to be considered for each of the two dualities pre-

sented in this chapter. The same authors further extended those results in an internal report, where the non-linear THP precoder designed to improve the separation of the users in cases where the number of users approximate the number of transmit antennas.

In [18], the algorithms to design precoders introduced in [17] are further extended for MU-MIMO scenarios, where mobile stations also employ multiple antennas. An iterative design is introduced and two MSE duality transforms need to be performed in an alternating manner, either form the mobile or from the base station.

Further extensions to all those precoder and equalizer design methods applied to MIMO scenarios include multi-streaming, robust design when channel knowledge is imperfect, effects of quantization at the antenna ports, massive number of antennas and compact antenna arrays. In [19, 32, 47, 80], further MIMO aspects and design methods, including for multi-user environment, are reviewed and presented in detail.

5. Concluding Remarks

Multicarrier systems have already found their path into wired and wireless communications standards and technology. Cyclic Prefix based Orthogonal Frequency Division Multiplexing (CP-OFDM) is currently the mostly deployed and well studied multicarrier system among all. Its simplicity from both theoretical and practical implementation perspectives have helped an easy acceptance among researchers, technologists and business persons. Due to the use of the CP, its poor spectral properties, sensitivity to synchronization errors and inflexibility in changing the subcarrier bandwidth, CP-OFDM do not provide the spectral and energy efficiency, robustness and the adaptability necessary for advanced wired and wireless technology.

Filter Bank based Multicarrier (FBMC) systems provide on the other hand an effective alternative to CP-OFDM. FBMC systems based on Offset-Quadratude Amplitude Modulation (OQAM), in particular, have properties which allows to fulfil a number of the requirements for advanced wireless communications. Due to the lack of CP and the orthogonal or near-orthogonal overlapping of the subcarriers, an improved spectral and energy efficiency is achieved. The use of a pulse shaping in each subcarrier tailored to fulfil stricter frequency and time domain requirements allows to improve the spectral containment and increase the robustness to synchronization errors. Furthermore, the pulse shaping can be flexibly chosen to convey the transmission of different categories of communications traffic.

This dissertation covered different aspects of FBMC systems based on OQAM with the objective to bring further maturity to this combination of classical digital signal processing building blocks and pave its way into wireless standards and future technology.

In the first part, the basic theory and fundamental operations of FBMC systems were presented. Different structures for the realization of the system were derived. They allow to efficiently perform the per-subcarrier filtering, modulation and combination of all subcarrier signals. The presentation of the structures was followed by a complexity analysis and comparison. Finally, some options for the choice of the filter employed in each subcarrier were presented.

In the second part, different procedures for the estimation of the propagation channel under which the system operates were shown. In addition to the need of schemes that differ from the ones used in CP-OFDM, FBMC systems also require appropriate subcarrier signal models that are tailored to the channel estimation scheme chosen. Two basic models were presented: a first one that considers a per-subcarrier estimation of a narrowband channel and a second that considers an estimation of the broadband propagation channel by collecting observations of multiple subcarriers. Then channel estimation algorithms that are adapted to each of the corresponding model were derived and also different levels of knowledge of the channel and noise statistics were considered.

In the final part, methods to compensate and mitigate the effects of the propagation channel are presented. The channel equalization or precoding in FBMC systems also has to be adapted to the

underlying signal model. Then different methods based on different objectives were presented for both equalizer and precoder design. An extension from systems which involve single antenna at the transmitter and single antenna at the receiver, to systems with multiple antennas on both sides is also discussed in this work.

Bibliography

[1] Project PHYDYAS FP7-ICT 211887.

[2] M. Al-Attraqchi, S. Boussakta, and S. Le Goff. An enhanced OFDM/OQAM system exploiting Walsh-Hadamard transform. In *Proc. IEEE VTC-Spring 2011*, Budapest, Hungary, May 2011.

[3] M Alard, C Roche, and P Siohan. A new family of function with a nearly optimal time-frequency localization. *Technical Report of the RNRT Project Modyr*, 1999.

[4] L. G. Baltar, P. Chevalier, M. Renfors, J. Yli-Kaakinen, J. Louveaux, X. Mestre, F. Bader, and V. Savaux. Chapter 12 - FBMC channel equalization techniques. In M. Renfors, X. Mestre, E. Kofidis, and F. Bader, editors, *Orthogonal Waveforms and Filter Banks for Future Communication Systems*, pages 299–337. Academic Press, 2017.

[5] L. G. Baltar, T. Laas, M. Newinger, A. Mezghani, and J. A. Nossek. Enhancing spectral efficiency in advanced multicarrier techniques: A challenge. In *Proceedings of the 22nd European Signal Processing Conference (EUSIPCO-2014)*, Lisbon, Portugal, September 2014.

[6] L. G. Baltar, A. Mezghani, and J. A. Nossek. EM based per-subcarrier ML channel estimation for filter bank multicarrier systems. In *Proc. of the 10-th Int. Symposium on Wireless Comm. Systems ISWCS 2013*, pages 1–5, August 2013.

[7] L. G. Baltar and J. A. Nossek. Multicarrier systems: A comparison between filter bank based and cyclic prefix based OFDM. In *17th International OFDM Workshop 2012 (InOWo 12)*, Aug. 2012.

[8] L. G. Baltar, F. Schaich, M. Renfors, and J. A. Nossek. Computational complexity analysis of advanced physical layers based on multicarrier modulation. In *Proc. Future Network & Mobile Summit (FutureNetw)*, pages 1–8, 2011.

[9] L. G. Baltar, D. S. Waldhauser, and J. A. Nossek. Out-of-band radiation in multicarrier systems: A comparison. In *Multi-Carrier Spread Spectrum 2007*, pages 107–116. Springer, 2007.

[10] L. G. Baltar, D. S. Waldhauser, and J. A. Nossek. MMSE subchannel decision feedback equalization for filter bank based multicarrier systems. In *Proc. IEEE Int. Symp. Circuits and Systems ISCAS 2009*, pages 2802–2805, Taipei, Taiwan, May 2009.

[11] L.G. Baltar, M. Newinger, and J.A. Nossek. Structured subchannel impulse response estimation for filter bank based multicarrier systems. In *Wireless Communication Systems (ISWCS), 2012 International Symposium on*, pages 191 –195, aug. 2012.

[12] P. Banelli, S. Buzzi, G. Colavolpe, A. Modenini, F. Rusek, and A. Ugolini. Modulation formats and waveforms for 5G networks: Who will be the heir of OFDM?: An overview of alternative modulation schemes for improved spectral efficiency. *IEEE Signal Process. Mag.*, 31(6):80–93, 2014.

[13] M. Bellanger. Specification and design of a prototype filter for filter bank based multicarrier transmission. In *Proc. IEEE ICASSP 2001*, Salt Lake City, UT, May 2001.

[14] M. Bellanger. FS-FBMC: A flexible robust scheme for efficient multicarrier broadband wireless access. In *Proc. IEEE GLOBECOM 2012*, Anaheim, CA, December 3-7 2012.

[15] M. Bellanger. FS-FBMC: An alternative scheme for filter bank based multicarrier transmission. In *2012 5th International Symposium on Communications, Control and Signal Processing*, pages 1–4, May 2012.

[16] M. Bellanger, D. Le Ruyet, D. Roviras, M. Terré, J. A. Nossek, L. G. Baltar, Q. Bai, D. Waldhauser, M. Renfors, T. Ihalainen, et al. FBMC physical layer: A primer. *PHYDYAS, January*, 2010.

[17] O. D. Candido, L. G. Baltar, A. Mezghani, and J. A. Nossek. SIMO/MISO MSE-Duality for Multi-User FBMC with Highly Frequency Selective Channels. In *Proc. WSA 2015; 19th Int. ITG Workshop Smart Antennas*, pages 1–7, March 2015.

[18] O. D. Candido, S. A. Cheema, L. G. Baltar, M. Haardt, and J. A. Nossek. Downlink Precoder and Equalizer Designs for Multi-User MIMO FBMC/OQAM. In *Proc. WSA 2016; 20th Int. ITG Workshop Smart Antennas*, pages 1–8, March 2016.

[19] M. Caus, X. Mestre, D. Gregoratti, A. I. Pérez-Neira, M. Haardt, Y. Cheng, and L. G. Baltar. Chapter 13 - MIMO-FBMC transceivers. In M. Renfors, X. Mestre, E. Kofidis, and F. Bader, editors, *Orthogonal Waveforms and Filter Banks for Future Communication Systems*, pages 341–374. Academic Press, 2017.

[20] R. W. Chang. Synthesis of band-limited orthogonal signals for multichannel data transmission. *The Bell System Technical Journal*, 45:1775–1796, December 1966.

[21] R. W. Chang and R. A. Gibby. A theoretical study of performance of an orthogonal multiplexing data transmission scheme. *IEEE Trans. on Communication Technology*, COM-16(4):529–540, August 1968.

[22] Y. Cheng, L. G. Baltar, M. Haardt, and J. A. Nossek. Precoder and equalizer design for multi-user MIMO FBMC/OQAM with highly frequency selective channels. In *Proc. Speech and Signal Processing (ICASSP) 2015 IEEE Int. Conf. Acoustics*, pages 2429–2433, April 2015.

[23] Y. Cheng, M. Haardt, L. G. Baltar, and J. A. Nossek. Downlink per-user multi-streaming for FBMC/OQAM based multi-user MIMO with highly frequency selective channels. In *Proc. WSA 2015; 19th Int. ITG Workshop Smart Antennas*, pages 1–6, March 2015.

[24] J. M. Cioffi, G. P. Dudevoir, M. Vedat Eyuboglu, and G. D. Forney. MMSE decision-feedback equalizers and coding. I. Equalization results. *IEEE Transactions on Communications*, 43(10):2582–2594, October 1995.

[25] I. Daubechies and W. Sweldens. Factoring wavelet transforms into lifting steps. *J. Fourier Anal. Appl*, 4:247–269, 1998.

[26] P. S. R. Diniz, E. A. B. da Silva, and S. L. Netto. *Digital Signal Processing: System Analysis and Design*. E-Libro. Cambridge University Press, 2010.

[27] N. J. Fliege. Orthogonal multiple carrier data transmission. *European Transactions on Telecommunications*, 3(3):255–264, May-June 1992.

[28] N. J. Fliege. *Multirate Digital Signal Processing*. Wiley, Chichester,U.K., 1994.

[29] M. B. Furtado. *Filter Bank Based FIR Transceiver Optimization Applied to Fixed and Mobile Digital Communications*. PhD thesis, COPPE/Federal University of Rio de Janeiro, Rio de Janeiro, Brazil, September 2006. In portuguese.

[30] M. B. Furtado, P. S. R. Diniz, and S. L. Netto. Numerically efficient optimal design of cosine-modulated filter banks and transmultiplexers with peak-constrained least-squares behavior. *IEEE Trans. on Circuits and Systems I*, 52(3):597–608, March 2005.

[31] M. B. Furtado, P. S. R. Diniz, and S. L. Netto. On the design of high-complexity cosine-modulated transmultiplexers based on the frequency-response masking approach. *IEEE Trans. on Circuits and Systems I*, 52(11):2413–2426, November 2005.

[32] M. Haardt, Y. Cheng, F. Rottenberg, J. Louveaux, and E. Kofidis. Chapter 16 - FBMC distributed and cooperative systems. In M. Renfors, X. Mestre, E. Kofidis, and F. Bader, editors, *Orthogonal Waveforms and Filter Banks for Future Communication Systems*, pages 421–440. Academic Press, 2017.

[33] B. Hirosaki. An analysis of automatic equalizers for orthogonally multiplexed QAM systems. *IEEE Transactions on Communications*, COM-28(1):73–83, January 1980.

[34] B. Hirosaki. An orthogonally multiplexed QAM system using the discrete fourier transform. *IEEE Transactions on Communications*, COM-29(7):982–989, July 1981.

[35] N. Holte. MMSE equalization of OFDM/OQAM systems for channels with time and frequency dispersion. In *Proc. IEEE WCSP 2009*, Nanjing, China, November 2009.

[36] R. Hunger, M. Joham, and W. Utschick. On the MSE-duality of the broadcast channel and the multiple access channel. *WSA*, 57(2):698–713, 2009.

[37] T. Ihalainen, T. H. Stitz, M. Rinne, and M. Renfors. Channel equalization in filter bank based multicarrier modulation for wireless communications. *EURASIP Journal on Advances in Signal Processing*, 2007. doi: 10.1155/2007/49389.

[38] Tero Ihalainen, Tobias Hidalgo Stitz, and Markku Renfors. Efficient per-carrier channel equalizer for filter bank based multicarrier systems. In *Proc. IEEE Int. Symp. Circuits and Systems*, pages 3175–3178, Kobe, Japan, May 2005.

[39] H. Jedda, L. G. Baltar, O. De Candido, A. Mezghani, and J. A. Nossek. DFE/THP duality for FBMC with highly frequency selective channels. In *Proc. 23rd European Signal Processing Conf. (EUSIPCO)*, pages 2127–2131, Nice, France, August 2015.

[40] S. Jo and J. S. Seo. Efficient LLR calculation for FBMC. *IEEE Commun. Lett.*, 19(10):1834–1837, October 2015.

[41] K. D. Kammeyer, U. Tuisel, and H. Bochmann. Digital multicarrier-transmission of audio signals over mobile radio channels. *European Transactions on Telecommunications*, 3(3), May-June 1992.

[42] T. Karp and N. J. Fliege. Computationally efficient realization of MDFT filter banks. In *Proc. 8th European Signal Processing (EUSIPCO '96)*, volume 1, pages 336–365, Tampere, Finland, February 1996.

[43] T. Karp and N.J. Fliege. Modified DFT filter banks with perfect reconstruction. *IEEE Trans. Circuits Syst. II*, 46(11):1404–1414, November 1999.

[44] T. Karp, A. Mertins, and T. Q. Nguyen. Efficiently VLSI-realizable prototype filters for modulated filter banks. In *Acoustics, Speech, and Signal Processing, 1997. ICASSP-97., 1997 IEEE International Conference on*, volume 3, pages 2445–2448, 1997.

[45] D. Katselis, E. Kofidis, and S. Theodoridis. On OFDM/OQAM receivers. In *Proc. EUSIPCO 2012*, Bucharest, Romania, August 2012.

[46] E. Kofidis, L. G. Baltar, X. Mestre, F. Bader, and V. Savaux. Chapter 11 - FBMC Channel Estimation Techniques. In M. Renfors, X. Mestre, E. Kofidis, and F. Bader, editors, *Orthogonal Waveforms and Filter Banks for Future Communication Systems*, pages 257–297. Academic Press, 2017.

[47] E. Kofidis, M. Renfors, J. Louveaux, X. Mestre, D. Gregoratti, D. Le Ruyet, and R. Zakaria. Chapter 14 - MIMO-FBMC Receivers. In M. Renfors, X. Mestre, E. Kofidis, and F. Bader, editors, *Orthogonal Waveforms and Filter Banks for Future Communication Systems*, pages 375–406. Academic Press, 2017.

[48] B. Le Floch, M. Alard, and C. Berrou. Coded orthogonal frequency division multiplex. *Proc. IEEE*, 83(6):982–996, June 1995.

[49] R. M. Lerner. Band-pass filters with linear phase. *Proceedings of the IEEE*, 52(3):249–268, March 1964.

[50] H. S. Malvar. *Signal processing with lapped transforms*. Artech Hause, Norwood, MA, 1992.

[51] P. Marsch, Ö. Bulakci, O. Queseth, and M. Boldi, editors. *5G System Design: Architectural and Functional Considerations and Long Term Research*. Wiley, 2018.

[52] K. W. Martin. Small side-lobe filter design for multitone data-communication applications. *IEEE Transactions on Circuits and Systems II: Analog and Digital Signal Processing*, 45(8):1155–1161, August 1998.

[53] D. Mattera and M. Tanda. Optimum single-tap per-subcarrier equalization for OFDM/OQAM systems. *Digital Signal Process.*, 49:148–161, November 2016.

[54] A. Mezghani, M. Joham, R. Hunger, and W. Utschick. Transceiver design for multi-user MIMO systems. In *International ITG Workshop on Smart Antennas*, 2006. Ulm, Germany.

[55] T.K. Moon. The expectation-maximization algorithm. *Signal Processing Magazine, IEEE*, 13(6):47–60, 1996.

[56] G. Ndo, H. Lin, and P. Siohan. FBMC/OQAM equalization: Exploiting the imaginary interference. In *Proc. IEEE PIMRC 2012*, Sydney, Australia, September 2012.

[57] S. Nedic. An unified approach to equalization and echo cancellation in OQAM-based multicarrier data transmission. In *Proc. IEEE GLOBECOM 1997*, Phoenix, AZ, November 1997.

[58] M. Newinger, L. G. Baltar, A. L. Swindlehurst, and J. A. Nossek. MISO broadcasting fbmc system for highly frequency selective channels. In *Proc. WSA 2014; 18th Int. ITG Workshop Smart Antennas*, pages 1–7, March 2014.

[59] A. V. Oppenheim, R. W. Schafer, and J. R. Buck. *Discrete-time signal processing*. Prentice-Hall, Upper Saddle River, NJ, EUA, second edition, 1997.

[60] A. W. Paeth. A fast algorithm for general raster rotation. In *Proceedings of Graphics Interface and Vision Interface '86*, GI '86, pages 77–81, Toronto, Ontario, Canada, 1986. Canadian Man-Computer Communications Socitey.

[61] J. G. Proakis. *Digital communications*. McGraw-Hill, New York, NY, 4th edition, 2001.

[62] M. Renfors and J. Yli-Kaakinen. Channel equalization in fast-convolution filter bank based receivers for professional mobile radio. In *Proc. European Wireless 2014; 20th European Wireless Conf*, pages 1–5, Barcelona, Spain, May 2014.

[63] C. Roche and P. Siohan. A family of extended Gaussian functions with a nearly optimal localization property. In *Multi-carrier spread-spectrum*, pages 179–186. Springer, 1997.

[64] B. R. Saltzberg. Performance of an efficient parallel data transmission system. *IEEE Transactions on Communication Technology*, COM-15(6):805–811, December 1967.

[65] T. Saramäki. A generalized class of cosine-modulated filter banks. In *Proc. TICSP Workshop on Transforms and Filter Banks*, pages 336–365, Tampere, Finland, Jun. 1998.

[66] P. J. Schreier and L. L. Scharf. *Statistical Signal Processing of Complex-Valued Data - The Theory of Improper and Noncircular Signals*. Cambridge University Press, 2010.

[67] P. Siohan and C. Roche. Cosine-modulated filterbanks based on extended Gaussian functions. *IEEE Transactions on Signal Processing*, 48(11):3052–3061, November 2000.

[68] P. Siohan, C. Siclet, and N. Lacaille. Analysis and Design of OFDM/OQAM Systems Based on Filterbank Theory. *IEEE Trans. Signal Process.*, 50(5):1170–1183, May 2002.

[69] S. M. J. Asgari Tabatabaee and H. Zamiri-Jafarian. Per-subchannel joint equalizer and receiver filter design in OFDM/OQAM systems. *IEEE Trans. Signal Process.*, 64(19):5094–5105, October 2016.

[70] J. C. Tu. Optimum MMSE equalization for staggered modulation. In *Proc. IEEE ACSSC 1993*, Pacific Grove, CA, November 1993.

[71] P. P. Vaidyanathan. *Multirate Systems and Filter Banks*. Prentice-Hall, Englewood Cliffs, NJ, 1993.

[72] A. Viholainen. *Modulated Filter Bank Design for Communications Signal Processing*. Tampere University of Technology, 2004.

[73] A. Viholainen, J. Alhava, and M. Renfors. Efficient implementation of complex modulated filter banks using cosine and sine modulated filter banks. *EURASIP Journal on Advances in Signal Processing*, 2006(1):058564, 2006.

[74] A. Viholainen, T. H. Stitz, J. Alhava, and et al. Complex modulated critically sampled filter banks based on cosine and sine modulation. In *Proc. IEEE Int. Symp. Circuits and Systems*, pages 833–836, Scottsdale, EUA, May 2002.

[75] D. S. Waldhauser. *Multicarrier Systems Based on Filter Banks*. Ph.D. thesis (Technische Universität München), Shaker Verlag, Aachen, 2009.

[76] D. S. Waldhauser, L. G. Baltar, and J. A. Nossek. Comparison of Filter Bank Based Multicarrier Systems with OFDM. In *Proc. IEEE Asia-Pacific Conference on Circuits and Systems*, pages 976–979, Singapore, December 2006.

[77] D. S. Waldhauser, L. G. Baltar, and J. A. Nossek. MMSE subcarrier equalization for filter bank based multicarrier systems. In *Proc. IEEE 9th Workshop Signal Processing Advances in Wireless Communications SPAWC 2008*, pages 525–529, Recife, Brazil, July 2008.

[78] S. B. Weinstein and Paul M. Ebert. Data transmission by frequency-division multiplexing using the discrete fourier transform. *IEEE Trans. on Communication Technology*, COM-19(5):628–634, October 1971.

[79] T. Wiegand and N. J. Fliege. Equalizers for transmultiplexers in orthogonal multiple carrier data transmission. In *Proc. European Signal Processing Conference*, volume 2, pages 1211–1214, Trieste, Italy, September 1996. EURASIP.

[80] R. Zakaria, D. Le Ruyet, and M. Renfors. Chapter 15 - Space-Time Coding for FBMC. In M. Renfors, X. Mestre, E. Kofidis, and F. Bader, editors, *Orthogonal Waveforms and Filter Banks for Future Communication Systems*, pages 407–419. Academic Press, 2017.

List of Acronyms

3GPP	3rd Generation Partnership Project
ADSL	Asymmetric Digital Subscriber Line
AFB	Analysis Filter Bank
AWGN	Additive White Gaussian Noise
BER	Bit Error Rate
CFR	Channel Frequency Response
CIR	Channel Impulse Response
CMFB	Cosine Modulated Filter Bank
CP	Cyclic Prefix
CP-OFDM	Cyclic Prefix Orthogonal Frequency-Division Multiplexing
CRLB	Cramér-Rao Lower Bound
DFE	Decision Feedback Equalizer
DFT	Discrete Fourier Transform
DSL	Digital Subscriber Line
EGF	Extended Gaussian Function
ELT	Extended Lapped Transform
EM	Expectation Maximization
EMFB	Exponentially Modulated Filter Banks
FB	FilterBank
FBMC	Filter Bank MultiCarrier
FBMC/OQAM	Filter Bank Multicarrier Systems with Offset-QAM subcarrier modulation
FD-FBMC	Frequency Domain FBMC/OQAM
FDM	Frequency-Division Multiplexing
FDMA	Frequency-Division Multiple Access
FFT	Fast Fourier Transform
FIR	Finite Impulse Response
FMT	Filtered Multitone
FS-FBMC	Frequency Spread FBMC/OQAM
F-T	Frequency-Time
i.i.d.	independent and identically distributed
IEEE	Institute of Electrical and Electronics Engineers
ICI	Inter-carrier Interference
IDFT	Inverse Discrete Fourier Transform
IFFT	Inverse Fast Fourier Transform
IoT	Internet of Things

IOTA	Isotropic Orthogonal Transform Algorithm
ISI	Inter-symbol Interference
LE	Linear Equalizer
LLR	Log-Likelihood Ratio
LMMSE	Linear Minimum Mean Squared Error
LTE	Long-Term Evolution
LS	Least Squares
LTE	Long-Term Evolution
LTE-A	Long-Term Evolution-Advanced
MC	MultiCarrier
MCM	MultiCarrier Modulation
MDFT	Modified Discrete Fourier Transform
MIMO	Multiple-Input Multiple-Output
MISO	Multiple-Input Single-Output
ML	Maximum Likelihood
MLSE	Maximum Likelihood Sequence Estimation
MMSE	Minimum Mean-Squared Error
MSE	Mean-Squared Error
MU	Multi-User
NMSE	Normalized Mean-Squared Error
NPR	Near Perfect Reconstruction
OA	Overlap-Add
OFDM	Orthogonal Frequency-Division Multiplexing
OQAM	Offset Quadrature Amplitude Modulation
OQPSK	Offset Quadrature Phase-Shift Keying
OS	Overlap-Save
PAM	Pulse Amplitude Modulation
PAPR	Peak-to-Average Power Ratio
PR	Perfect Reconstruction
PSD	Power Spectral Density
QAM	Quadrature Amplitude Modulation
QPSK	Quadrature Phase-Shift Keying
RC	Raised Cosine
RRC	Square Root Raised Cosine
RX	Receiver
SBC	Sub-band Coding
SC	Single-Carrier
SFB	Synthesis Filter Bank
SINR	Signal-to-Interference-plus-Noise Ratio
SIR	Signal-to-Interference Ratio
SISO	Single-Input Single-Output
SLNR	Signal-to-Leakage-plus-Noise Ratio
SLR	Signal-to-Leakage Ratio
SMFB	Sine Modulated Filter Bank
SNR	Signal-to-Noise Ratio
SVD	Singular Value Decomposition

TDD	Time-Division Duplex
TDL	Tap Delay Line
T-F	Time-Frequency
THP	Tomlinson-Harashima Precoder
TMUX	Transmultiplexer
VDSL	Very-high-bit-rate digital subscriber line
WL	Widely Linear
ZF	Zero Forcing